Multiscale Modeling and Simulation of Deformation Accumulation in Fault Networks

Dissertation
zur Erlangung des Grades eines
Doktors der Naturwissenschaften

eingereicht am
Fachbereich Mathematik und Informatik
der Freien Universität Berlin

vorgelegt von
Joscha Podlesny

Berlin
2021

Betreuer:	Prof. Dr. Ralf Kornhuber	(Freie Universität Berlin)
Erstgutachter:	Prof. Dr. Ralf Kornhuber	(Freie Universität Berlin)
Zweitgutachter:	Prof. Dr. Alexander Mielke	(Weierstraß Institut Berlin)
Drittgutachter:	Prof. Dr. Onno Oncken	(GFZ Potsdam)

Tag der Disputation: 22. Juni 2022

Selbstständigkeitserklärung nach § 7 Absatz 4 der Promotionsordnung

Ich erkläre gegenüber der Freien Universität Berlin, dass ich die vorliegende Dissertation selbstständig und ohne Benutzung anderer als der angegebenen Quellen und Hilfsmittel angefertigt habe. Die vorliegende Arbeit ist frei von Plagiaten. Alle Ausführungen, die wörtlich oder inhaltlich aus anderen Schriften entnommen sind, habe ich als solche kenntlich gemacht. Diese Dissertation wurde in gleicher oder ähnlicher Form noch in keinem früheren Promotionsverfahren eingereicht. Mit einer Prüfung meiner Arbeit durch ein Plagiatsprüfungsprogramm erkläre ich mich einverstanden.

Datum Unterschrift (Joscha Podlesny)

Acknowledgments

The preparation of this thesis has been a challenging undertaking in many aspects and would not have been possible without the generous and selfless support from a variety of people. First and foremost, I would like to thank my supervisor Prof. Dr. Ralf Kornhuber, not only for his guidance and advice regarding mathematical topics, but also for fostering an open, empathic environment for learning and personal growth. Another much appreciated facilitator of this atmosphere is Prof. Dr. Carsten Gräser, whose open ear for questions and tireless, patient pursuit of understanding lead to many insightful mathematical discussions. Dr. Martin Heida was an inspiring source for conversations and ideas concerning projections on fractal function spaces. Special recognition goes to my collaborators Dr. Matthias Rosenau and Dr. Michael Rudolf from GFZ Potsdam. They supplied valuable geoscientific expertise and intuition for the dynamics of the lithosphere and especially earthquake and rupture processes. Their eagerness for interdisciplinary cooperation has been a pleasure to experience.

Furthermore, I am much obliged to my colleagues and friends at the department of mathematics, who welcomed me sincerely, eased the transition into the world of academic research and accompanied me throughout this endeavor with words and deeds. Last, I am especially grateful for my friends, family and partner as well as their abundant encouragement, sympathy and emotional support during these exciting times.

This research has been funded by Deutsche Forschungsgemeinschaft (DFG) through grant CRC 1114 "Scaling Cascades in Complex Systems", Project Number 235221301, Project B01 "Fault networks and scaling properties of deformation accumulation".

Contents

1 Introduction

The lithosphere is the rigid, outermost layer of the Earth and consists of the crust and upper mantle. It is divided into separate, distinct tectonic plates, which are rigid but deform elastically and through brittle failure during very long periods of geologic time. The tectonic plates ride on the underlying weaker, hotter, deeper and comparatively more ductile part of the upper mantle—the asthenosphere. In contrast to the lithosphere, the asthenosphere deforms viscously under stress and accommodates strain through plastic deformation. The dynamics of tectonic plates are attributed to an interplay of various phenomena like convection caused by lateral density variations in the mantle, the motion of the seafloor away from spreading ridges due to differences in topography, changes in density of the crust as it ages and cools, as well as varying tidal forces generated by the Sun and Moon. The induced relative motion of multiple tectonic plates identifies three major types of plate boundaries.

Divergent boundaries feature two plates sliding apart from each other, while typically producing new ocean basin. Examples of divergent boundaries include active zones of mid-ocean ridges such as the Mid-Atlantic Ridge or East Pacific Rise as well as continent-to-continent rifting sites like the East African Rift. Convergent boundaries exhibit two plates sliding toward each other and either colliding or one plunging underneath the other in a subduction zone. The collision of continental lithosphere, where neither mass is subducted, leads to a compression, folding, and uplift of plate edges, which can be observed in the Himalayas and Alps. The Andes mountain range in South America and Japanese island arc are instances of ocean-to-continent and ocean-to-ocean subduction zones, respectively. Transform boundaries are characterized by plates grinding past each other and plate area neither being created nor destroyed, e.g. the San Andreas Fault in California.

In general, the dynamics at the plate boundaries give rise to geological events like earthquakes, see Figure 1.1, and the development of topographic features such as mountains, volcanoes, oceanic trenches, and mid-ocean ridges. Due to their large area of impact in short time periods, earthquakes are historically the most hazardous of these phenomena in terms of economic damage, devastation of infrastructure and threat to human life. For example, the 2011 Tōhoku undersea megathrust earthquake occurred in the Pacific ocean east of the Tōhoku region in Japan with a magnitude of approximately $9.1\,\mathrm{M_w}$, lasted 6 minutes and triggered a tsunami causing the Fukushima Daiichi nuclear disaster [60]. The earthquake and its aftermath cost about $20,000$ people their lives and an estimated US$ 235 billion in economic damage making it the single most expensive natural disaster in recorded history [71].

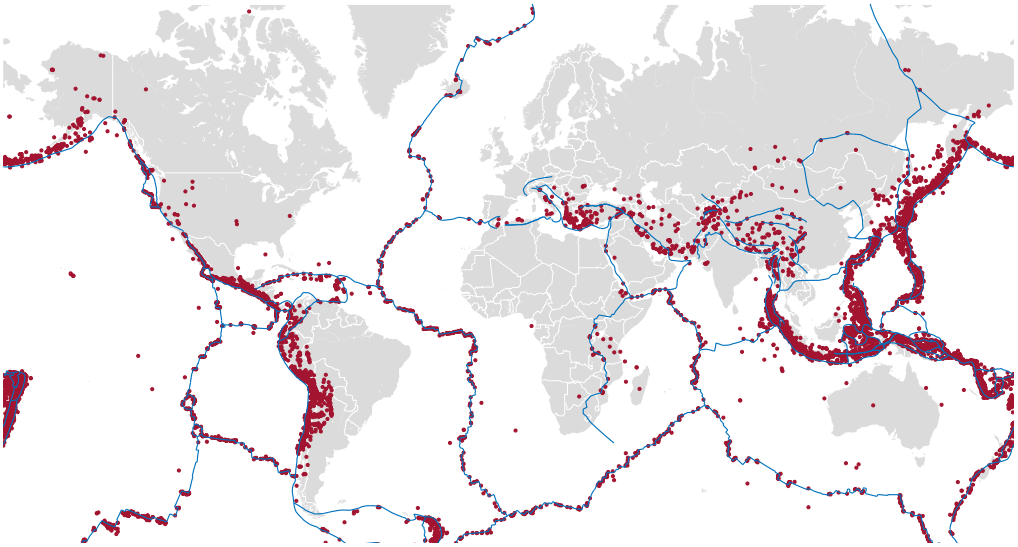

Figure 1.1: Tectonic plate boundaries (blue) and epicenters (red) of earthquakes between 01.01.2000 and 31.12.2020 with magnitudes of at least 5.5 M_w.[1]

Fault networks in the lithosphere

Lithospheric faults are structural discontinuities in Earth's lithosphere, are thin relative to the surrounding rock and commonly approximated as locally planar. Compared to the rather homogeneous surrounding rock, faults possess different physical properties and are host to phenomena like lubrication due to water, which alter the overall behavior of the system and play a crucial role in understanding and describing its dynamics. Faults are not distributed homogeneously over the entire lithosphere, but occur in multiscale spatial clusters called fault zones or fault networks that are typically situated at plate boundaries. Spatial scales range from fractures in grains ($\sim 10^{-6}$ m) over rocks ($\sim 10^{1}$ m) all the way up to tectonic plates ($\sim 10^{6}$ m). Figure 1.2 exemplifies part of the scale range occurring around the San Andreas Fault in Southern California and illustrates these clusters typically featuring "self-similar" geometries over many orders of magnitude. Fault networks develop in regions of high strain with preexisting weaknesses due to material contrasts or large differences in compressive stresses over millions of years. On these geological time scales, crack formation through brittle fracture, fault opening and healing lead to an ever changing geometry.

[1] Data source: U.S. Geological Survey, Earthquake Hazards Program, 2017, Advanced National Seismic System (ANSS) Comprehensive Catalog of Earthquake Events and Products.

[2] Data Source: U.S. Geological Survey, 2014 National Seismic Hazard Maps fault sources, accessed October 8, 2021, at `https://earthquake.usgs.gov/static/lfs/nshm/qfaults/hazfaults2014.zip`.

[3] Data Source: U.S. Geological Survey and California Geological Survey, Quaternary fault and fold database for the United States, accessed October 8, 2021, at `https://earthquake.usgs.gov/static/lfs/nshm/qfaults/Qfaults_GIS.zip`.

[4] Retrieved from `http://www.sanandreasfault.org/Palmdale_Road_Cut.jpg` on October 8, 2021.

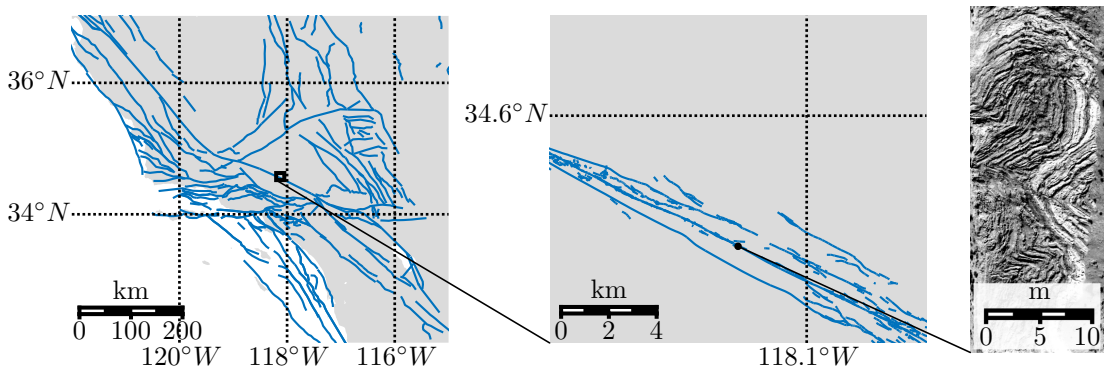

Figure 1.2: Exemplary range of spatial scales occurring around the San Andreas fault showing Southern California[2], the greater Palmdale region[3] and picture of a roadside cut[4] with increasing resolution from left to right.

Fault slip and the seismic cycle

Fault surfaces possess asperities—a geometric roughness—that cause friction forces along the interface. Static friction locks bulk material separated by a fault in place, while strain builds up, which eventually leads to stresses exceeding the friction force causing relative displacement or slip. Lithospheric earthquake activity, i.e. seismic fault slip, fault creep and slow earthquakes are the major slip mechanisms accommodating strain and releasing stress along faults. In the geosciences, the frictional behavior of these processes is predominantly described by rate-and-state friction (RSF) models [14, 110, 112]. In the following, the focus will be on earthquake and rupture processes, where faults unlock suddenly and slide rapidly on timescales of seconds to minutes relieving built-up strain.

During such an event, energy is released in form of seismic waves. On Earth's surface, this manifests as rapid displacement and disruption of the ground, which may trigger secondary natural disasters like tsunamis, landslides, volcanic activity or nuclear accidents. Seismic activity occurs at all plate boundaries and varies in intensity as well as frequency depending on the type of relative displacement (divergent, convergent, transform) and the location of the hypocenter. Cyclic strain accumulation by far field stresses leads to a clustering of earthquakes in space and time [5]. Nonetheless, the average dynamics of the plate boundary dominate the effects of local slip instabilities in the long run.
In 1910, Reid [111] observed that earthquakes rupture the same part of a fault repeatedly and delineated seismic activity as three characteristic phases coined the *seismic cycle* sketched in Figure 1.3:

- interseismic phase: It is a period between earthquakes of relative tectonic quiescence with slow accumulation of elastic strain, while faults are (partially) locked due to friction.
- coseismic phase: Once stresses exceed the friction force, a seismogenic fault patch unlocks and built-up strain is suddenly released by rapid shallow slip (earthquake).

- postseismic slip: During days up to years after an earthquake, further seismic activity in the vicinity of the initial rupture continues to relieve strain (aftershocks) and postseismic slip eventually relaxes back to interseismic levels by slow deep slip activity on ductile segments of the fault.

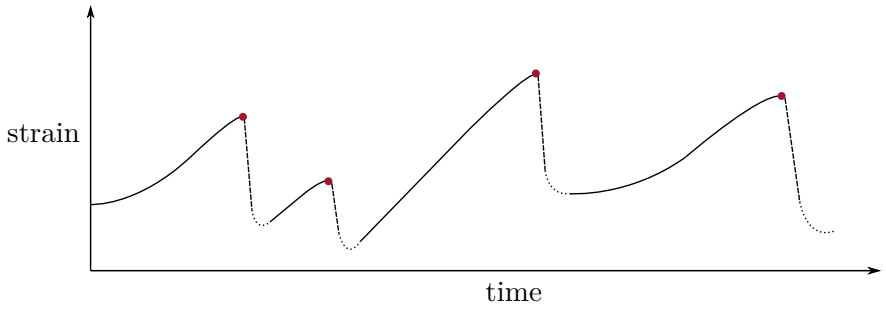

Figure 1.3: Sketch of qualitative strain accumulation and release at a single fault during interseismic (line), coseismic (dashed) and postseismic (dotted) phases of the seismic cycle, where a red dot indicates the occurrence of an earthquake.

As the terminology implies, it was believed that the seismic cycle indeed described a periodic phenomenon and could be harnessed to predict future rupture events. This may be true for isolated, single faults in a controlled laboratory setting, however, for natural earthquakes accurate quantitative prediction of time, location and magnitude beyond statistical statements is currently an unsurmounted challenge. Extrinsic factors such as other faults, different active fault zones interacting with each other and deformation or otherwise dependent material properties are very demanding to quantify [5]. This was demonstrated by the failure to forecast the 2004 Sumatra–Andaman and 2011 Tōhoku earthquakes [51]. Therefor, humanity relies on identifying characteristic precursor phenomena that warn of immediately impending earthquakes. For instance, seismic warning systems may register pressure waves preceding usually more destructive shear and Rayleigh waves.

Multiscale character of seismic fault slip

It has become evident over the course of this chapter, that there is an entire continuum of spatiotemporal scales involved in earthquake and rupture processes. Insights from experiments and geophysical (analogue) modeling suggest that grain sizes in fractured rock [93, 126] as well as fragmentation due to tectonic deformation [116] are distributed in a fractal sense, i.e. grain sizes and interfaces adhere to an exponential law. Their interplay contributes to complex dynamics in earth's lithosphere and is host to phenomena on time scales of seconds, e.g. earthquakes, all the way to plate tectonics and evolving fault networks over millions of years.
Moreover, geoscientific evidence hints at seismic fault slip exhibiting multiscale characteristics in terms of total earthquake magnitudes and slip velocities, whose statistics are described by empirical power laws. Measuring the strength of earthquakes using the Richter magnitude, which is determined by the logarithm of the amplitude of seismic waves, and recording the number of occurrences in a set period of time and region reveals scale invariant earthquake statistics over ten orders of

magnitude as expressed by the Gutenberg-Richter law. Here, scale invariance means that scaling the argument of the power law by a constant simply multiplies the original relation by a constant factor. Omori's law establishes a qualitatively similar relation of magnitude and frequency of aftershocks with respect to the time passed after the main rupture. These laws may be valid and have predictive power for earthquake recurrence on a global scale, but individual faults may produce very different statistics [14].

The scarcity of large earthquakes with recurrence times of hundreds thousands of years and incompleteness of paleoseismic, historical and instrumental record lead to a fundamental lack of insight into the multiscale, spatiotemporal interaction of different faults and fault networks, as noted by Goldfinger et al. in [51]. This thesis represents parts of an interdisciplinary simulation strategy pursued in project B01 of the Collaborative Research Center 1114. As a first step towards reliable earthquake prediction and quantitative hazard analysis, the focus will be on the mathematical modeling and efficient simulation of prototypical, layered fault networks on short time scales covering few seismic cycles. On the considered time intervals, the geometry of the fault networks is assumed to be invariant.

Outline

In Chapter 2, this exposition begins by establishing a layered fault system consisting of m bodies with viscoelastic Kelvin-Voigt rheology and $m-1$ non-intersecting faults featuring rate-and-state friction as proposed by Dieterich [38] and Ruina [114]. The individual bodies are assumed to experience small viscoelastic deformations, but possibly large relative tangential displacements. Thereafter, a variational formulation, its discretization and the construction of a numerical solver are introduced extending ideas originally developed for the simulation of a subduction zone modeled by unilateral frictional contact between a rigid foundation and deformable slider in [102]. Following Rothe's approach, semi-discretization in time with the classical Newmark scheme yields a sequence of continuous, coupled, spatial velocity and state problems for each time step, that are decoupled by means of a fixed point iteration, cf. [102]. Subsequently, the focus will be on discretizing and solving the ensuing velocity problems parametrized with given state using linear finite elements and a dual mortar discretization of the non-penetration constraints [130, 132, 133]. This discretization ansatz entails a hierarchical decomposition of the discrete solution space, that enables the localization of the non-penetration condition as well as friction nonlinearity leading to a convex minimization problem with a nonsmooth, block-separable friction functional. Exploiting the block-separability of the problem, a variant of the *Truncated Nonsmooth Newton Multigrid* (TNNMG) method [55, 53, 56] is constructed for the solution of the corresponding algebraic problems. It is globally convergent due to nonlinear, block Gauß–Seidel type smoothing and employs nonsmooth Newton and multigrid ideas to enhance robustness and efficiency of the overall method. A key step in the TNNMG algorithm is the efficient computation of a correction obtained from a linearized, inexact Newton step.

Although the layered fault system possesses multiple spatial scales, it is not envisioned to model the full range of spatial scales and thus the multiscale nature observed in geological settings as depicted in Figure 1.2. Thence, Chapter 3 addresses the construction and analysis of efficient numerical methods for the solution of variational problems, that are structurally similar to the ones arising in the linearized correction step of the TNNMG method, but incorporate the full spatial complexity in terms of truly multiscale fractal interface networks. In particular, the object of study are scalar, linear, self-adjoint, elliptic variational problems involving linear jump contributions across interfaces. One outcome of this investigation is the effect of approximating fractal interface networks by truncating finer scales—the strategy employed in Chapter 2 implicitly.
In the spirit of [61], a sequence of faults $(\Gamma_l)_{l\in\mathbb{N}}$ is ordered from "strong" to "weak" by introducing an exponential scaling of the resistance to jumps across Γ_l and thus decreasing discontinuities. The limiting fractal interface network Γ contains all faults Γ_l, $l \in \mathbb{N}$. After defining a suitable fractal function space $\mathcal{H}$ for the multiscale interface network Γ with assumptions on its shape regularity and fractal character, fractal interface problems in $\mathcal{H}$ will be considered. Their multiscale character exceeds the usual lack of smoothness commonly present in multiscale problems, because the solution space $\mathcal{H}$ depends on the fractal geometry which is not accessible by a fixed, classical finite element space. Introducing K-scale problems for approximating, K-scale spaces $\mathcal{H}_K \subset \mathcal{H}$ containing jumps across the faults Γ_l, $1 \leq l \leq K$, suitable piecewise linear finite element spaces $\mathcal{S}_K \subset \mathcal{H}_K$ for the approximation of the k-scale problems will be investigated.
The next Section 3.2 contains the main contribution of this thesis. Therein, suitable projections $\Pi : \mathcal{H} \to \mathcal{S}_K$ with approximation and stability properties will be constructed and analyzed relying on local Poincaré inequalities and a trace lemma following standard ideas published by Carstensen [22] and Verfürth [129]. This endeavor is complicated by the presence of jump terms. For instance, counterexamples show that it is not possible to bound jumps of local averages by jumps of the original functions, which leads to strong assumptions on the locality of Γ. Thereafter, the projections Π are applied in the construction and analysis of a LOD-type multiscale discretization with optimal error estimates in the spirit of [76, 89] and subspace correction methods going back to Xu [134] and Yserentant [136], that are mesh- and scale-independent. This chapter is concluded by numerical experiments with increasingly complex interface networks less and less covered by theory, that illustrate the theoretical results and the applicability of the approach beyond their limits.

Finally, the previous findings are applied to geological fault systems in a series of numerical experiments in Chapter 4. The properties and performance of the TNNMG variant presented in Chapter 2, whose linear correction is obtained inexactly by a standard multigrid V-cycle, will be assessed in a generic 2-body spring slider setting with deformable foundation and slider. Last, in the context of the layered fault system, the scaling properties of the proposed method will be investigated with respect to the number of faults.

2 Numerical simulation of geological fault networks

It is well-established in the geosciences, that lithospheric earthquake activity is one of the slip mechanisms accommodating strain and releasing stress along fault networks as described by rate-and-state friction (RSF) models [14, 110, 112]. The computational simulation of earthquake and rupture dynamics constitutes an integral part of seismic hazard assessment and has therefore quite a history in the field (see, e.g., [4, 10, 30, 85] and the references cited therein). For typical applications in the geosciences, it is imperative to be able to handle realistic geometries with high computational efficiency. In the literature, there is a wide range of numerical methods implementing the dynamics of earthquake rupture of which the following paragraphs provide a brief excerpt.

Finite difference schemes as investigated in [32] exhibit mesh-independent convergence in practice, but suffer from the inherent difficulty to resolve complex geometries and usually operate on tensor product grids. Spectral element methods [47] leverage high degree piecewise polynomial basis functions to discretize the solution space in order to achieve a very high order of accuracy. On the other hand, resolving complicated (fault) geometries poses a major challenge, especially for hexahedral elements in three space dimensions, compared to the flexibility of finite element approaches. De la Puente [104] introduced a numerical method for simulating wave propagation and dynamic rupture based on a discontinuous Galerkin (DG) discretization in space combined with arbitrary high-order derivatives (ADER) time integration [124]. Subsequently, it was extended to three space dimensions [96] and integrated into the software package SeisSol (see [70] and the references cited therein). SeisSol is optimized for high performance computing on parallel clusters and has experienced widespread application to, e.g., a subduction zone in the context of the 2004 Sumatra-Andaman earthquake [128], a strike-slip fault and the 1992 Landers earthquake [62] as well as weak crustal faults and the 2016 Kaikōura earthquake cascade [127].

A conceptually different class of approaches is based on viscous fluid flows incorporating faults through plasticity models. Here, faults are no longer resolved exactly by the computational grid as sharp interfaces, but represented in a diffuse way. Some of the corresponding numerical algorithms have been implemented in publicly available software packages, e.g. Slim3d [103] and Aspect [7, 83], and applied successfully to various geological settings including subduction zones [49, 63, 122] and strike-slip faults [31]. This ansatz is well-suited for modeling complex fault geometries, that change over time, and thus for simulating temporal multiscale aspects over longer time scales of minutes to millions of years. However, their mathematical structure, e.g. Stokes problems with saddle point structure [103], is more complicated and

computationally more demanding due to currently less efficient numerical solvers for the arising algebraic problems.

This chapter commences with a short introduction to continuum mechanics, the mathematical modeling of viscoelastic Kelvin-Voigt rheologies as well as non-penetration of bodies and rate-and-state friction as envisioned by Dieterich [38] and Ruina [114]. Based on these concepts and ideas from [102] for unilateral frictional contact, a layered fault system consisting of m bodies and $m-1$ non-intersecting faults with rate-and-state friction will be developed and guide the rest of the exposition. The individual bodies are assumed to experience small viscoelastic deformations, but possibly large relative tangential displacements. Following ideas for the variational formulation of RSF presented therein, a weak formulation of this model problem will be discretized using Rothe's approach. Time discretization with the classical Newmark scheme leads to a sequence of continuous spatial problems for each time step. These spatial problems consist of coupled velocity—thus rate—and state problems, that will be decoupled by means of a fixed point iteration, cf. [102]. The resulting state problem for given rate is discretized in space using piecewise constant functions, which entails a spatial decomposition into independent scalar subproblems that can be solved with bisection. On the other hand, obtaining a discretization and approximation of a solution to the rate problems parametrized with given state is much more involved. Using linear finite elements and a dual mortar discretization of the non-penetration constraints suggested and analyzed in [130, 132, 133] yields fully discrete rate problems. A major advantage of this approach is that it entails a hierarchical decomposition of the discrete solution space into a subspace with weak zero jump across the faults and a subspace containing the relative velocities at the faults. Then, computing normal and tangential relative velocities across the faults, which is essential for evaluating the non-penetration and friction contributions, can be done in the appropriate subspace. Motivated by this decomposition, a suitable basis transformation localizes the non-penetration condition to pointwise constraints at the faults. Subsequent lumping of the friction nonlinearity gives a convex minimization problem with a nonsmooth, block-separable friction functional. Due to this structure, a nonlinear block Gauß–Seidel type relaxation method converges globally albeit with quickly diminishing convergence rates for finer and finer meshes. The *Truncated Nonsmooth Newton Multigrid* (TNNMG) method builds on the global convergence of this smoothing iteration and augments it with nonsmooth Newton and multigrid techniques to accelerate convergence. It is designed for problems with block-separable, nonsmooth functionals and typically exhibits mesh independent convergence rates. Gräser and Sander [56] contributed a variant for non-scalar problems, whose application to the fully discrete rate problems concludes this chapter.
Much of the content presented here is subject of an upcoming publication [54].

2.1 Contact mechanics

The following section introduces basic concepts, that are fundamental to the mathematical modeling of a layered fault system. First, a continuum mechanical description of viscoelasticity with small bodywise deformations is stated before non-penetration is modeled in a regime of large relative displacements at the contact boundary. Last, a Dieterich-Ruina model of rate-and-state friction is established.

2.1.1 Stress and strain

Consider an open, bounded, connected set $\Omega \subset \mathbb{R}^d$, $d \in \{2, 3\}$. The closure $\overline{\Omega}$ of the set Ω represents the volume occupied by an undeformed body, i.e. its stress-free equilibrium state in the absence of external forces, and is called the *reference configuration*. Its boundary is denoted by $\partial\Omega$ and assumed to be composed of two disjoint subsets Γ^D and Γ^N, where Γ^D has nonzero $(d-1)$-dimensional Hausdorff measure and $\partial\Omega = \overline{\Gamma}^D \cup \overline{\Gamma}^N$ holds. Along the Dirichlet boundary Γ^D, the body is fixed in space, while it is subject to surface forces on the Neumann boundary Γ^N. Moreover, let us assume that $\partial\Omega$ is piecewise Lipschitz continuous, thus leading to the existence of an outward unit normal vector field $n : \partial\Omega \to \mathbb{R}^d$ almost everywhere on $\partial\Omega$ [27].

When surface and volume forces act on a body, it will deform and attain a new equilibrium given by a *deformation* function

$$y : \overline{\Omega} \to \mathbb{R}^d,$$

that maps points in the reference configuration to their respective positions in the deformed one. In order to avoid unphysical self-penetration, this function is assumed to be orientation-preserving in $\overline{\Omega}$ and injective on Ω.

With the canonical basis $\{e_1, \dots, e_d\}$ in $\mathbb{R}^d$ and the representation

$$y = \sum_{i=1}^{d} y_i e_i$$

of the deformation, the *deformation gradient* is defined as

$$\nabla y = \begin{pmatrix} \frac{\partial y_1}{\partial x_1} & \cdots & \frac{\partial y_1}{\partial x_d} \\ \vdots & \ddots & \vdots \\ \frac{\partial y_d}{\partial x_1} & \cdots & \frac{\partial y_d}{\partial x_d} \end{pmatrix} \tag{2.1.1}$$

for all $x \in \Omega$. The deformation gradient $\nabla y(x)$ is invertible for all $x \in \Omega$, since the deformation y is orientation-preserving, i.e., it holds

$$\det \nabla y(x) > 0 \quad \forall x \in \Omega.$$

Rather than in absolute terms, deformation can be phrased as a *displacement* function

$$u : \Omega \to \mathbb{R}^d, \quad u(x) = y(x) - x \tag{2.1.2}$$

relative to the reference configuration. This characterization is frequently used in the setting of linear elasticity and will be employed throughout the rest of the exposition.

Although the deformation gradient characterizes local deformations with first order accuracy, it is not a suitable strain measure, since it is not invariant under rigid-body motions, i.e. translation and rotation [27]. This motivates the definition of the right *Green-St. Venant strain tensor*

$$\boldsymbol{E} : \Omega \to \mathbb{S}^d, \quad \boldsymbol{E}(x) = \tfrac{1}{2}\left(\nabla u(x) + (\nabla u(x))^T + (\nabla u(x))^T \nabla u(x)\right), \tag{2.1.3}$$

where $\mathbb{S}^d$ is the space of symmetric second-order tensors in $\mathbb{R}^d$, that remedies this shortcoming [27].

Assuming *infinitesimal deformations*, i.e. the displacement gradient ∇u is infinitesimally small compared to unity, the quadratic term in (2.1.3) can be neglected, which yields the *linearized strain tensor*

$$\boldsymbol{\varepsilon} = \tfrac{1}{2}\left(\nabla u + (\nabla u)^T\right),$$

which is invariant under translations, but not rotations.

The *Euler-Cauchy stress principle* establishes the existence of a symmetric stress tensor field $\boldsymbol{\sigma} : \overline{\Omega} \to \mathbb{S}^d$ encoding internal forces that arise due to boundary conditions or external loading, e.g. by compression, tension, shear, torsion, or bending. For any sub-volume $V \subset \Omega$, the traction force acting on its boundary ∂V with outer unit normal field n is induced by the surrounding material and given by the *Cauchy stress vector*

$$t = \boldsymbol{\sigma} n \quad \text{ on } \partial V. \tag{2.1.4}$$

Until this point, the previous continuum mechanical description of bodies and their deformation is a general framework and does not incorporate any specific materials. In a concrete setting, materials and their properties are characterized by a given constitutive relation, that quantifies the stress dependence on strain.

A material is called *elastic*, if the stress $\boldsymbol{\sigma}$ at a point $x \in \Omega$ depends only on the deformation gradient at x and possibly on x itself, i.e.

$$\boldsymbol{\sigma}(x) = \hat{\boldsymbol{\sigma}}(\nabla u(x), x). \tag{2.1.5}$$

A material is called *homogeneous*, if (2.1.5) does not depend on its second argument. It is called *isotropic*, if it behaves the same "in all directions", i.e.,

$$\hat{\boldsymbol{\sigma}}(FQ, x) = \hat{\boldsymbol{\sigma}}(F, x) \quad \forall F \in \mathbb{R}^{d\times d}_{+} \quad \forall Q \in \mathrm{SO}(d),$$

where $\mathbb{R}^{d\times d}_{+}$ denotes the set of real $d \times d$ matrices with positive determinant and $\mathrm{SO}(d)$ the group of rotations.

Under the infinitesimal deformation assumption and in the regime of linear elasticity, higher order strain contributions are negligible and stress $\boldsymbol{\sigma}$ depends linearly on strain $\boldsymbol{\varepsilon}$

$$\boldsymbol{\sigma}(u) = \boldsymbol{B}\boldsymbol{\varepsilon}(u),$$

with the fourth-order elasticity tensor $\boldsymbol{B}$. This proportionality factor is also called the Hooke tensor and a higher dimensional analog of the 1-D spring constant known from basic physical model problems like the harmonic oscillator.

Kelvin-Voigt model

On the spatiotemporal scales of interest, the lithosphere exhibits a reversible, viscoelastic behavior, i.e. such solids deform elastically under external stresses like a spring, but the elastic response may be delayed by a Newtonian (viscous) damper. In this setting, the Kelvin-Voigt model of linear viscoelasticity is a common choice, see, e.g., [101, 102]. Its constitutive law augments the linearly elastic model (2.1.1) by a viscosity term and relates stress and strain according to the linear first-order differential equation

$$\boldsymbol{\sigma}(u) = \boldsymbol{A}\dot{\boldsymbol{\varepsilon}}(u) + \boldsymbol{B}\boldsymbol{\varepsilon}(u),$$

where $\boldsymbol{A}$ and $\boldsymbol{B}$ denote viscosity and elasticity tensors. For the remainder, these tensors are assumed to possess the symmetry properties

$$\boldsymbol{A}_{ijkl} = \boldsymbol{A}_{klij}, \qquad \boldsymbol{A}_{ijkl} = \boldsymbol{A}_{jikl}, \qquad \boldsymbol{B}_{ijkl} = \boldsymbol{B}_{klij}, \qquad \boldsymbol{B}_{ijkl} = \boldsymbol{B}_{jikl}$$

such that the stress tensor $\boldsymbol{\sigma}(u)$ and the bilinear forms induced by $\boldsymbol{A}$ and $\boldsymbol{B}$ are symmetric. If the material is homogeneous and isotropic, the inherent geometric symmetries enforce the above symmetry of the tensors.
In general, the material gradually relaxes to its undeformed state, when stress is reduced. If constant stress is applied, the material deforms at a decreasing rate, asymptotically approaching the steady-state strain.

2.1.2 Non-penetration

Modeling frictional contact requires a mathematical notion of bodies that are in contact, but not penetrating one another. In the established literature, there are numerous approaches enforcing such non-penetration. Especially early contributions assume a discrete setting with a suitable triangulation of the contact boundary. Some of these descriptions rely on the existence of outer normal fields [13, 66], where others manage to avoid them at the cost of additional constraints per face on the contact boundary [69]. This section introduces a variant of a continuum-based model first proposed by Laursen and Simo [86]. It leads to weak formulations and subsequent finite element discretizations in a natural fashion and is thus widely applied in modern approaches to elastic contact problems. The following presentation is based on Wohlmuth and Krause [133] as well as [54].

Consider two viscoelastic bodies represented by two disjoint domains $\Omega_1, \Omega_2 \subset \mathbb{R}^d$, $d = 2, 3$, with piecewise Lipschitz continuous boundaries $\partial\Omega_i$, $i = 1, 2$, that are in contact along a common interface and slide against each other. Denote with u_i their respective configurations. The boundaries $\partial\Omega_i$ can be decomposed into three pairwise disjoint parts, namely the Dirichlet boundary Γ_i^D, the Neumann boundary Γ_i^N and the common contact boundary $\Gamma^F = \Gamma_{1,2}^F = \overline{\Omega}_1 \cap \overline{\Omega}_2$ (see Figure 2.1). Let us suppose, that Γ^F is compactly contained in $\partial\Omega_i \backslash \overline{\Gamma}_i^D$, i.e. there is a compact set K such that

$$\overline{\Gamma}^F \subset K \subset \partial\Omega_i \backslash \overline{\Gamma}_i^D. \tag{2.1.6}$$

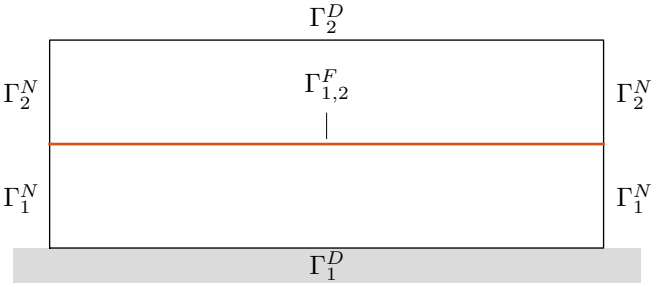

Figure 2.1: Spring slider configuration with deformable foundation.

Denoting $v = (v_1, v_2)$ with $v_i : \Omega_i \to \mathbb{R}^d$, $i = 1, 2$, the restrictions of v to Γ^F—possibly in the sense of traces—from the top Ω_2 and the bottom Ω_1 are identified by v_T and v_B, respectively, via

$$v_T = v_2|_{\Gamma^F}, \quad v_B = v_1|_{\Gamma^F}.$$

Let $n = (n_1, n_2)$ and refer with $n_i \in \mathbb{R}^d$ to the outward unit normal to Ω_i, $i = 1, 2$. For the top and bottom normals on Γ^F, it holds $n_B = -n_T$.

Although individual bodies are assumed to experience small interior viscoelastic displacements as per the previous section, their relative tangential displacements may be large after many seismic cycles. Hence, the contact conditions cannot be formulated only with respect to the reference configuration, but must take the actual, possibly large, relative displacements into account, i.e., phrased in terms of the deformed bodies. Considering a sufficiently smooth displacement field

$$u = (u_1, u_2), \qquad u_i : \Omega_i \to \mathbb{R}^d$$

where u_i is the displacement of the body Ω_i, $i = 1, 2$, the corresponding deformations are given by $\mathrm{Id} + u_i$ and the deformed bodies by $(\mathrm{Id} + u_i)(\Omega_i)$. Thus, in the deformed configuration, the deformed contact boundary is obtained by

$$\gamma^u = (\mathrm{Id} + u_B)(\Gamma^F) \cap (\mathrm{Id} + u_T)(\Gamma^F),$$

and its pullback to the bottom and top reference configurations yields

$$\Gamma_B^{F,u} = (\mathrm{Id} + u_B)^{-1}(\gamma^u) \subset \Gamma^F, \qquad \Gamma_T^{F,u} = (\mathrm{Id} + u_T)^{-1}(\gamma^u) \subset \Gamma^F.$$

Then, there is a parameterization of the bottom reference boundary $\Gamma_B^{F,u}$ over the top reference boundary $\Gamma_T^{F,u}$ via the bijective contact mapping

$$\pi^u : \Gamma_T^{F,u} \to \Gamma_B^{F,u}, \qquad \pi^u = (\mathrm{Id} + u_B)^{-1} \circ (\mathrm{Id} + u_T),$$

that assigns each point $x \in \Gamma_T^{F,u}$ to the unique point $y \in \Gamma_B^{F,u}$ with which it coincides in the deformed configuration, i.e. it holds $(\mathrm{Id} + u_T)(x) = (\mathrm{Id} + u_B)(y)$. Using the contact mapping, there are parameterizations of the deformed contact boundary γ^u over $\Gamma_T^{F,u}$ via $\mathrm{Id} + u_T = (\mathrm{Id} + u_B) \circ \pi^u$ and over $\Gamma_B^{F,u}$ via $\mathrm{Id} + u_B = (\mathrm{Id} + u_T) \circ (\pi^u)^{-1}$, respectively. Figure 2.2 shows the deformation-dependent quantities, that were just introduced, and illustrates the contact mapping π^u.

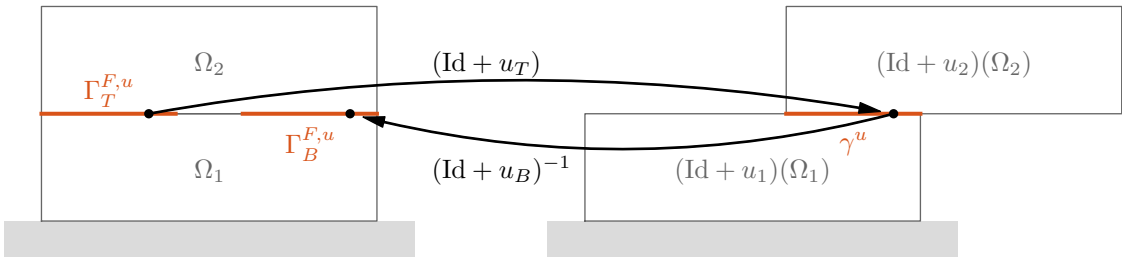

Figure 2.2: Illustration of the contact mapping π^u parameterizing $\Gamma_B^{F,u}$ over $\Gamma_T^{F,u}$ in the reference configuration (left) via the deformed contact boundary γ^u (right).

For any piecewise defined scalar or vector field

$$v = (v_1, v_2) \in H^1(\Omega_1)^k \times H^1(\Omega_2)^k$$

with $k = 1$ or $k = d$, let us define the jump of v across the deformed contact boundary γ^u on the top reference boundary $\Gamma_T^{F,u}$ according to

$$[v]^u = v_T - v_B \circ \pi^u \qquad \text{on } \Gamma_T^{F,u}.$$

Contact conditions, and in particular the non-penetration condition, as well as the friction law will be incorporated in terms of constraints on the normal and tangential components of displacements and velocities on the deformed contact boundary γ^u. In order to construct this decomposition, let us introduce an outer normal field $n^u(x)$ to the deformed body $(\mathrm{Id}+u_i)(\Omega_i)$, $i = 1, 2$, at the point $(\mathrm{Id}+u_i)(x)$, $x \in \Gamma_T^{F,u}$, that has been pulled back to the reference configuration i.e. $n^u(x)$ is obtained as the pullback of an oriented normal field of the deformed contact boundary $\gamma^u = (\mathrm{Id}+u_T)(\Gamma_T^{F,u})$ to $\Gamma_T^{F,u}$ using the map $(\mathrm{Id}+u_T)^{-1}$. Then, any vector field on $\Gamma_T^{F,u}$ is decomposed into its normal and tangential components with respect to the deformed configuration by

$$v = v_t + v_n n^u, \qquad v_n = v \cdot n^u, \qquad v_t = v - v_n n^u.$$

By this construction, the decomposition depends on the deformation-dependent normal field n^u of the deformed top body $(\mathrm{Id}+u_2)(\Omega_2)$ and not on the normal field of the reference bodies Ω_i.

Requiring that the relative displacement of the deformed bodies Ω_i, $i = 1, 2$, is tangential to the actual contact boundary γ^u per the closed-fault condition

$$[u]_n^u = [u]^u \cdot n^u = 0 \tag{2.1.7}$$

on $\Gamma_T^{F,u}$ ensures non-penetration and prohibits fault opening.

Remark 2.1.1. Above notions, especially the non-penetration condition, are phrased with respect to the top boundary $\Gamma_T^{F,u}$. Due to the geometric symmetry, there are analogous concepts in terms of the bottom boundary $\Gamma_B^{F,u}$, see [54]. However, the upcoming approach to mathematical modeling and the subsequent discretization will not be independent of this choice.

Remark 2.1.2. This setting can be extended to scenarios allowing gaps between the two bodies. Usually, an additional contact mapping Φ, e.g. the closest point [133] or normal projection [125], is used to identify points on the (deformed) contact boundaries. Based on this choice, a gap function $g_\Phi : \Gamma_T^{F,u} \to \mathbb{R}$ and relative displacement $[u]_\Phi^u$ can be defined leading to a more general non-penetration constraint. The upcoming analysis, discretization and subsequent numerical approach cover this slight modification without conceptual differences.

The closed-fault condition imposes kinetic constraints on the physical system that are further augmented by the stress balance on $\Gamma_T^{F,u}$ according to Newton's third law

$$(\boldsymbol{\sigma}(u)n)_T = -\omega^u(\boldsymbol{\sigma}(u)n)_B \circ \pi^u, \tag{2.1.8}$$

where $\boldsymbol{\sigma}(u)$ denotes the stress tensor on $\Omega = \Omega_1 \cup \Omega_2$. In particular, the stress $(\boldsymbol{\sigma}(u)n)_B$ represents a force per surface area. Thus, changing the area element via the pullback to $\Gamma_T^{F,u}$ with π^u requires an additional scaling by the weighting factor $\omega^u = \sqrt{\det((D\pi^u)^T D\pi^u + n_T \otimes n_T)}$, that is associated with this transformation. Again, the stress field $(\boldsymbol{\sigma}(u)n)_T$ can be decomposed into normal and tangential components

$$\sigma_n(u) = (\boldsymbol{\sigma}(u)n)_T \cdot n^u, \qquad \sigma_t(u) = (\boldsymbol{\sigma}(u)n)_T - \sigma_n(u)n^u,$$

on the top side, such that $(\boldsymbol{\sigma}(u)n)_T = \sigma_t + \sigma_n n^u$ holds. Frequently, σ_n is referred to as the normal stress and σ_t as the shear stress. The shear stress σ_t encodes the frictional response and will be discussed in the next section.

Remark 2.1.3. Since there are only small, interior deformations inside the individual bodies by assumption, the stress vector $(\boldsymbol{\sigma}(u)n)_T$ is determined for the reference normal n_T, whereas its decomposition into normal and shear stress is carried out in terms of the deformed configuration and its corresponding normal n^u, which is necessitated by a possibly large relative displacement of the two bodies.

2.1.3 Friction

Friction is the force at the contact interface Γ^F that opposes the relative lateral motion of two bodies sliding against each other. Exempting molecular friction, friction captures the effective, macroscopic response arising from the interaction of microscale surface features known as asperities. Experiments by Rabinowicz [109, 108, 107] showed that these kinds of slip systems exhibit two frictional regimes. First, static friction signifies a stationary (interseismic) state without any relative motion of the two bodies at the friction interface. Once the system has been loaded by stress accumulation sufficiently to overcome static friction, it enters an active, sliding (coseismic) state of dynamic friction.

As early as the 15th to 18th centuries, experimental studies investigated elementary properties of dynamic friction and lead to the following empirical laws.

Amontons' Laws: The force of friction is

- independent of the projected area of contact
- proportional to the applied load.

The former implies that friction is a local process at every point on the surface of contact, whereas the latter postulates the existence of a scalar μ called the *friction coefficient* relating tangential and normal stresses as per

$$|\sigma_t| = \mu \, |\sigma_n| \, . \tag{2.1.9}$$

Any friction law based on these assumptions needs to provide an explicit representation of the friction coefficient. Choosing a suitable friction law is a modeling decision and depends on the physical system and phenomena one wants to simulate.

The simplest choice for the friction coefficient is a constant $\mu \geq 0$. Assuming collinearity of relative tangential velocity and shear stress in addition, i.e.,

$$- \, |\sigma_t| \, [\dot{u}]_t^u = |[\dot{u}]_t^u| \, \sigma_t, \tag{2.1.10}$$

Tresca friction postulates the relation

$$- \, \sigma_t = \mu \, |\sigma_n| \, \frac{[\dot{u}]_t^u}{|[\dot{u}]_t^u|}, \text{ if } [\dot{u}]_t^u \neq 0, \quad \text{and} \quad |\sigma_t| \leq \mu \, |\sigma_n| \, , \text{ if } [\dot{u}]_t^u = 0. \tag{2.1.11}$$

with a deformation-independent normal stress $\sigma_n = \sigma_n(u)$. Note that in this simplest of settings, the frictional response is independent of the sliding velocity.

Dieterich-Ruina model of rate-and-state friction

Observations from natural earthquakes and rock friction experiments uncovered a dependence of typical dynamical parameters on slip distance, slip velocity, normal stress, and their histories. For example, for rock surfaces and fault gouge, the stress needed to overcome static friction and transition to dynamic slipping depends on hold time. Marone [90] and Dieterich [39] attributed this phenomenon to a time dependent healing effect, that alters asperities such that the effective area of contact grows. Then, in the regime of dynamic friction, rock surfaces and fault gouges demonstrate characteristic velocity weakening, i.e. the friction coefficient decreases as the sliding velocity increases [38]. Moreover, velocity step tests indicate a non-linear relaxation-type response of stress to sudden jumps in velocity (see Dieterich [35]).

The empirical rate-and-state friction framework pioneered by Dieterich [38] and Ruina [114] is able to model these features. It is a versatile model and is not only applicable to rock friction [36, 37] but also the frictional behavior of soils, engineered structures and abrasive processes [64, 119]. Assuming collinearity of relative tangential velocity and shear stress (2.1.10) as well as a deformation-independent normal stress $\sigma_n = \sigma_n(u)$, cf. Tresca friction, the dynamic friction relation between shear and normal stresses reads

$$- \, \sigma_t = [\mu(|[\dot{u}]_t^u| \, , \theta) \, |\sigma_n| + C] \, \frac{[\dot{u}]_t^u}{|[\dot{u}]_t^u|}, \tag{2.1.12}$$

where C denotes a cohesion parameter, and introduces a friction coefficient μ now depending on the relative tangential velocity as well as a state field θ encoding the history of dynamic sliding. Setting $V = |[\dot{u}]_t^u|$, the friction coefficient is typically given by

$$\mu(V,\theta) = \mu_0 + a \log \frac{V}{V_0} + b \log \frac{V_0 \theta}{L} \tag{2.1.13}$$

and positive parameters μ_0, a, b, V_0 and $L \in \mathbb{R}$ (see Dieterich [35] and the references therein). Relying on experiments, these frictional parameters are fitted to the observed frictional response caused by a velocity perturbance. The reference friction μ_0 is measured at reference speed V_0. The friction parameter a quantifies the immediate response to a velocity perturbance, whereas b is the difference between peak response given by a and the new steady state level of friction. The critical slip distance L is related to the characteristic slip distance over which the relaxation from peak to new steady state friction occurs. All of these parameters are material dependent (consult [64, 35, 90] for more in depth information on these parameters and their respective effects).

Note that (2.1.13) is nonphysical and meaningless for very small velocities V, since $\mu(V,\theta) \to -\infty$ for $V \to 0$ and fixed θ. This deficit has been remedied by means of regularization or truncation in the literature. Reformulating (2.1.13) with the sign-change velocity V_θ, for which smaller velocities lead to negative and thus inadmissible friction coefficients, leads to

$$\mu(V,\theta) = a \log \frac{V}{V_\theta}, \qquad V_\theta = V_0 \exp\left(-\frac{\mu_0 + b \log(\theta V_0/L)}{a}\right). \tag{2.1.14}$$

The regularized law [18] replaces the first equation of (2.1.14) by

$$\mu_{\mathrm{r}}(V,\theta) = a \sinh^{-1} \frac{V}{2V_\theta}, \tag{2.1.15}$$

and the truncated law [102] by

$$\mu_{\mathrm{t}}(V,\theta) = a \log^+ \frac{V}{V_\theta}, \qquad \log^+ x = \begin{cases} \log x, & \text{if } x \geq 1 \\ 0, & \text{otherwise.} \end{cases} \tag{2.1.16}$$

In practice, both versions differ so little that the actual choice is of no consequence.

The state variable θ, however, displays a characteristic evolution over time. Dieterich and Kilgore interpreted it as a characteristic time measuring the nature of the respective contact dynamics [39]. It can be used to incorporate complex, time-dependent phenomena implicitly, e.g., fault healing or fault lubrication due to frictional melting or water in the pore space, that are crucial for natural rupture processes.

The *aging law* introduced by Dieterich [36, 114] approximates the state evolution according to

$$\dot{\theta} = 1 - \frac{V}{L}\theta. \tag{2.1.17}$$

The state evolves with ongoing slip and during hold times of stationary contact, i.e., θ increases for $V = 0$. Thus, it captures effects due to contact aging and healing processes implicitly.

In contrast, Ruina's *slip law* [114] given by

$$\dot{\theta} = -\frac{V}{L}\theta \log \frac{V}{L}\theta \tag{2.1.18}$$

only leads to a frictional response during slip. Both state equations feature increasing states θ for decreasing slip rates V and vice versa. A state evolution due to the aging law attains the new frictional steady state slower than the slip law. Moreover, the slip law is able to approximate an initially strong decay of shear stress better, that occurs in some experiments [88]. Again, the choice of a suitable state evolution is a modeling decision.

Remark 2.1.4. At present, there is a fundamental lack of understanding regarding the rigorous derivation of rate-and-state friction from first principles. It is a purely heuristic model that is obtained by geoscientific experiments and the observation of natural processes. Nonetheless, there has been progress in the mathematical modeling of simpler frictional settings.
Mielke and Roubíček [92] investigated the coupling of finite-strain elasticity and plasticity in the context of unilateral frictionless contact. Moreover, Mielke introduced a finite-dimensional model for rate-and-state friction in a single fault setting, that is thermodynamically consistent in the sense of the GENERIC framework (see [91] and references therein).
Recently, Cheng and Spiers [26] developed a physical model describing the frictional behavior of a system with strong rate-and-state characteristics (carbonate fault gouge) on the microscale. The microscale is represented by granular beads that are tightly packed in a "honey comb"-like structure and do not roll or fracture, but slide over one another. It was suggested that two competing processes of dilatation due to shear-induced granular flow and compaction by intergranular pressure solution (a mechanism of bulk deformation and pore volume change) augmented by thermodynamical considerations give rise to full rate-and-state-type behavior qualitatively similar to experiments. The authors believe their model to capture the key mechanisms and physics underlying rate-and-state-type behavior and the rate-and-state friction law. However, it is a matter of future research how to obtain macroscopic rate-and-state parameters, e.g. a and b, from this approach and thus transition from micro- to macroscale.

2.2 Subdifferential friction law and state evolution

Following Pipping, Sander and Kornhuber [102], let us reformulate the rate-and-state friction law and state evolution as subdifferential inclusions in order to facilitate their incorporation into a variational formulation of the upcoming model problem 2.3.1. For this purpose, the Dieterich-Ruina model of friction will be restated in terms of a

transformed state variable $\alpha = \log(\theta V_0/L)$. Thus, the friction coefficient, formerly given by (2.1.14), becomes

$$\mu(V,\alpha) = a \log \frac{V}{V_\alpha}, \qquad V_\alpha = V_0 \exp\left(-\frac{\mu_0 + b\alpha}{a}\right), \tag{2.2.1}$$

whereas the state evolution due to aging (2.1.17) and slip law (2.1.18) read

$$-\dot{\alpha} = \frac{V - V_0\, e^{-\alpha}}{L}, \quad -\dot{\alpha} = \frac{V}{L}\left(\alpha + \log\frac{V}{V_0}\right), \tag{2.2.2}$$

respectively.

The first objective is to phrase the friction law (2.1.12) as a subdifferential inclusion. Consider the convex, non-decreasing functional $\phi(\cdot,\alpha) : \mathbb{R}^d \to \mathbb{R}$ corresponding to the truncation of μ in (2.1.16)

$$\phi(v,\alpha) = \begin{cases} a\,|\sigma_n|\,(|v| \log(|v|/V_\alpha) - |v| + V_\alpha) + C\,|v|\,, & |v| \geq V_\alpha \\ C\,|v|\,, & \text{otherwise.} \end{cases} \tag{2.2.3}$$

Then, using the collinearity assumption (2.1.10) as well as the chain rule leads to

$$-\sigma_t \in \partial_{[\dot{u}]_t^u} \phi([\dot{u}]_t^u, \alpha)$$

or equivalently

$$\sigma_t(x) \cdot (v - [\dot{u}]_t^u(x)) + \phi(v,\alpha) \geq \phi([\dot{u}]_t^u(x), \alpha) \qquad \forall v \in \mathbb{R}^d \tag{2.2.4}$$

at any $x \in \Gamma_T^{F,u}$.

Lastly, a subdifferential inclusion representing the state evolution of α will be developed. Rewriting Dieterich's law with a suitable function $\psi_d(\alpha, V)$, it becomes

$$-\dot{\alpha} = \frac{d}{d\alpha}\psi_d(\alpha,V), \qquad \psi_d(\alpha,V) = \frac{V}{L}\alpha + e^{-\alpha} \tag{2.2.5}$$

while Ruina's law turns into

$$-\dot{\alpha} = \frac{d}{d\alpha}\psi_r(\alpha,V), \qquad \psi_r(\alpha,V) = \frac{V}{L}\left(\frac{1}{2}\alpha^2 + \log\left(\frac{V}{L}\right)\alpha\right). \tag{2.2.6}$$

Both $\psi(\,\cdot\,,V) = \psi_d(\,\cdot\,,V)$ or $\psi(\,\cdot\,,V) = \psi_r(\,\cdot\,,V)$ are convex, hence yielding the subdifferential inclusion $-\dot{\alpha} \in \partial_\alpha \psi(\alpha,V)$, or equivalently

$$\dot{\alpha}(x) \cdot (\beta - \alpha(x)) + \psi(\beta,V) \geq \psi(\alpha(x),V) \qquad \forall \beta \in L^2(\Gamma_T^{F,u}) \tag{2.2.7}$$

at any $x \in \Gamma_T^{F,u}$. Additionally, $-\dot{\alpha} = 0$ prescribes a constant state α on $\Gamma^F \setminus \Gamma_T^{F,u}$, where no contact occurs.

2.3 Layered fault system with rate-and-state friction

Building on the previous insights, let us develop a mathematical model describing a geological structure consisting of a deformable body with reference configuration $\Omega \subset \mathbb{R}^d$, $d = 2, 3$, that is split into m viscoelastic sub-bodies $\Omega_i \subset \Omega$, $i = 1, \dots, m$, by a system of non-intersecting faults, i.e. it holds

$$\overline{\Omega} = \bigcup_{i=1}^{m} \overline{\Omega}_i.$$

These bodies are assumed to be non-empty, bounded Lipschitz domains, to not penetrate each other, and to be layered in the sense that at most two sub-bodies are in contact at any point in $\mathbb{R}^d$ (no crosspoints), see, e.g., Figure 2.3 for an illustration with $m = 5$ bodies and $m - 1 = 4$ faults.

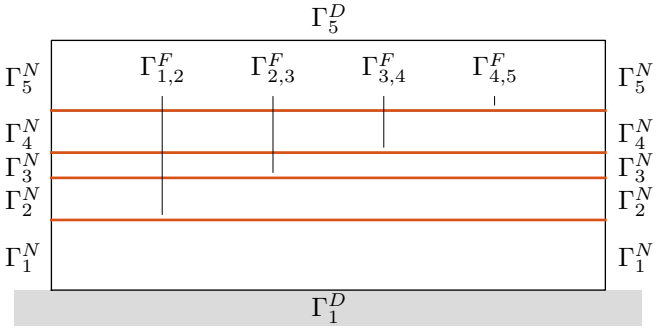

Figure 2.3: Layered fault system with $m = 5$ bodies and $m - 1 = 4$ faults.

Consequently, there is an ordering of all sub-bodies, such that there exist possible contact interfaces $\Gamma_{i,i+1}^F = \overline{\Omega}_i \cap \overline{\Omega}_{i+1}$, $i = 1, \dots, m-1$, while all other intersections of sub-bodies are empty.
The next objective is to extend concepts and notation introduced in the previous sections to this m body setting. As described in Section 2.1.2, the boundary $\partial\Omega_i$ of Ω_i is decomposed into Dirichlet Γ_i^D, Neumann Γ_i^N and contact $\Gamma_i^F = \Gamma_{i-1,i}^F \cup \Gamma_{i,i+1}^F$ parts according to $\partial\Omega_i = \Gamma_i^D \cup \Gamma_i^N \cup \Gamma_i^F$, where $\Gamma_{0,1}^F = \Gamma_{m,m+1}^F = \varnothing$ is set for notational convenience. Let us denote

$$\Gamma^D = \bigcup_{i=1}^{m} \Gamma_i^D, \quad \Gamma^N = \bigcup_{i=1}^{m} \Gamma_i^N, \quad \Gamma^F = \bigcup_{i=1}^{m-1} \Gamma_{i,i+1}^F.$$

For any $v = (v_1, \dots, v_m)$ with $v_i : \Omega_i \to \mathbb{R}^d$, $i = 1, \dots, m$, the restrictions of v to Γ^F—possibly in the sense of traces—from the top Ω_{i+1} and bottom Ω_i of the the individual faults $\Gamma_{i,i+1}^F$, are identified by $v_T = (v_{T,1}, \dots, v_{T,m-1})$ and $v_B = (v_{B,1}, \dots, v_{B,m-1})$, respectively, via

$$v_{T,i} = v_{i+1}|_{\Gamma_{i,i+1}^F}, \quad v_{B,i} = v_i|_{\Gamma_{i,i+1}^F}, \quad i = 1, \dots, m-1.$$

On occasion, it will prove helpful to regard these top and bottom restrictions as functions v_T and v_B defined piecewise on Γ^F by $v_T|_{\Gamma_{i,i+1}^F} = v_{T,i}$ and $v_B|_{\Gamma_{i,i+1}^F} = v_{B,i}$, $i = 1, \dots, m-1$. Moreover, let $n = (n_1, \dots, n_m)$ and refer with $n_i \in \mathbb{R}^d$ to the

outward unit normal to Ω_i, $i = 1, \dots m$. For the top $n_T = (n_{T,1}, \dots, n_{T,m-1})$ and bottom normals $n_B = (n_{B,1}, \dots, n_{B,m-1})$ on Γ^F, it holds $n_B = -n_T$.

Suppose that a body force f, e.g. gravity, acts on all of Ω, while the Neumann boundary Γ^N is subject to surface forces f^N. On the Dirichlet boundary Γ^D, the velocity $\dot{u}(t)$ and displacement fields $u(t)$ of the deformable body Ω are prescribed at all times $t > 0$ and set to $u(t) = \dot{u}(t) = 0$ for notational simplicity. The concepts, that will be developed hereafter, can be generalized to the inhomogeneous case. All boundary forces are assumed to be compressive, meaning that no fault opening occurs and adjacent bodies Ω_i and Ω_{i+1}, $i = 1, \dots, m-1$ remain in contact throughout the entire evolution.

Considering a sufficiently smooth displacement field

$$u = (u_1, \dots, u_m), \qquad u_i : \Omega_i \to \mathbb{R}^d$$

where u_i is the displacement of the body Ω_i, $i = 1, \dots, m$, the corresponding deformations are given by $\mathrm{Id} + u_i$ and the deformed bodies by $(\mathrm{Id} + u_i)(\Omega_i)$. Recall that the interior displacements u_i inside each body Ω_i are assumed to be small, while their relative displacement may be large. Furthermore, the associated deformations are assumed to be small, such that different faults $\Gamma^F_{i,i+1}$ do not get in contact after deformation. Then, the deformed contact boundary γ^u, its pullback to the bottom $\Gamma^{F,u}_B$ and top $\Gamma^{F,u}_T$ reference configurations as well as the parameterization of the bottom reference boundary $\Gamma^{F,u}_B$ over the top reference boundary $\Gamma^{F,u}_T$ via the bijective contact mapping π^u can literally be defined as in Section 2.1.2.

For any piecewise defined scalar or vector field

$$v = (v_1, \dots, v_m) \in H^1(\Omega_1)^k \times \cdots \times H^1(\Omega_m)^k$$

with $k = 1$ or $k = d$, let us define the jump of v across the deformed contact boundary γ^u on the top reference boundary $\Gamma^{F,u}_T$ according to

$$[v]^u = v_T - v_B \circ \pi^u \qquad \text{on } \Gamma^{F,u}_T. \tag{2.3.1}$$

Again, a decomposition of any vector field on $\Gamma^{F,u}_T$ into normal and tangential components with respect to the deformed contact boundary γ^u is constructed in terms of an outer normal field n^u to the deformed bodies $(\mathrm{Id} + u_i)(\Omega_i)$, $i = 1, \dots, m$, that has been pulled back to the reference configuration, according to

$$v = v_t + v_n n^u, \qquad v_n = v \cdot n^u, \qquad v_t = v - v_n n^u.$$

To be precise, n^u is obtained as the pullback of an oriented normal field of the deformed contact boundary $\gamma^u = (\mathrm{Id} + u_T)(\Gamma^{F,u}_T)$ to $\Gamma^{F,u}_T$ using the map $(\mathrm{Id} + u_T)^{-1}$.

The extension of the closed-fault condition establishes that the relative displacement of the deformed bodies Ω_i and Ω_{i+1}, $i = 1, \dots, m-1$, is tangential to the actual contact boundary γ^u per

$$[u]^u_n = [u]^u \cdot n^u = 0$$

on $\Gamma_T^{F,u}$ and ensures non-penetration as well as prohibits fault opening. Together with the previous assumptions, the normal relative velocity vanishes as well, i.e. it holds

$$[\dot{u}]^u \cdot n^u = 0 \tag{2.3.2}$$

on $\Gamma_T^{F,u}$. Thus, the jump of the relative tangential velocity across Γ^F satisfies

$$[\dot{u}]_t^u = [\dot{u}]^u - ([\dot{u}]^u \cdot n^u)n^u = [\dot{u}]^u \quad \text{on } \Gamma_T^{F,u}.$$

Hereafter, the superscript indicating the deformation-dependence of the jump terms will mostly be dropped and $[\,\cdot\,] = [\,\cdot\,]^u$ written instead.
The stress balance (2.1.8) carries over to the layered fault system and reads

$$(\boldsymbol{\sigma}(u)n)_T = -\omega^u(\boldsymbol{\sigma}(u)n)_B \circ \pi^u \tag{2.3.3}$$

on $\Gamma_T^{F,u}$ with the stress tensor $\boldsymbol{\sigma}(u)$ on Ω. Using $[\dot{u}]_t^u = [\dot{u}]^u$ and decomposing the stress field $(\boldsymbol{\sigma}(u)n)_T = \sigma_t + \sigma_n n^u$ into normal and tangential components

$$\sigma_n(u) = (\boldsymbol{\sigma}(u)n)_T \cdot n^u, \qquad \sigma_t(u) = (\boldsymbol{\sigma}(u)n)_T - \sigma_n(u)n^u,$$

on $\Gamma_T^{F,u}$, a rate-and-state friction law with a state-dependent convex functional $\phi(\cdot,\alpha)$ and a state evolution with a second convex functional $\psi(\cdot,V)$ for given relative slip rate $V = |[\dot{u}]^u|$, cf. Section 2.2, are prescribed on $\Gamma_T^{F,u}$. As all faults $\Gamma_{i,i+1}^F$, $i = 1,\dots,m-1$, hold the same, scale-invariant friction law, possible spatial multiscale features are solely induced by the number m of bodies Ω_i and their respective size.

Let us fix a final time $T > 0$. Based on balance of momentum and Cauchy's stress principle, the deformation of a viscoelastic body Ω of Kelvin–Voigt material with a layered system of faults Γ^F and rate-and-state friction is governed by the following formal set of equations and boundary conditions.

Problem 2.3.1 (Layered fault system with rate-and-state friction, cf. [54])**.** *Find*

$$u\colon\ \Omega \times [0,T] \to \mathbb{R}^d \quad \textit{and} \quad \alpha\colon\ \Gamma^F \times [0,T] \to \mathbb{R}$$

such that

$$\boldsymbol{\sigma}(u) = \boldsymbol{A}\boldsymbol{\varepsilon}(\dot{u}) + \boldsymbol{B}\boldsymbol{\varepsilon}(u) \qquad \text{in } \Omega\backslash\Gamma^F \qquad \textit{(Kelvin–Voigt material)} \tag{2.3.4}$$

$$\operatorname{div}\boldsymbol{\sigma}(u) + f = \rho\ddot{u} \qquad \text{in } \Omega\backslash\Gamma^F \qquad \textit{(balance of momentum)} \tag{2.3.5}$$

with boundary conditions,

$$u = \dot{u} = 0 \qquad \text{on } \Gamma^D \qquad \textit{(Dirichlet condition)}$$

$$\boldsymbol{\sigma}(u)n = f^N \qquad \text{on } \Gamma^N \qquad \textit{(Neumann condition)}$$

frictional contact conditions,

$$[\dot{u}]^u \cdot n^u = 0 \qquad \text{on } \Gamma_T^{F,u} \qquad \textit{(closed-fault condition)}$$

$$(\boldsymbol{\sigma}(u)n)_T = -\omega^u(\boldsymbol{\sigma}(u)n)_B \circ \pi^u \qquad \text{on } \Gamma_T^{F,u} \qquad \textit{(stress balance)}$$

$$-\sigma_t \in \partial_{[\dot{u}]^u}\phi([\dot{u}]^u, \alpha) \qquad \text{on } \Gamma_T^{F,u} \qquad \textit{(state-dependent friction law)}$$

contact state condition,

$$-\dot{\alpha} \in \partial_\alpha \psi(\alpha, |[\dot{u}]^u|), \qquad \text{on } \Gamma_T^{F,u} \qquad \textit{(rate-dependent state law)}$$

and non-contact interface conditions

$$-\dot{\alpha} = 0 \qquad \text{on } \Gamma^F \backslash \Gamma_T^{F,u} \quad \textit{(non-contact state condition)}$$

$$(\boldsymbol{\sigma}(u)n)_T = 0 \qquad \text{on } \Gamma^F \backslash \Gamma_T^{F,u} \quad \textit{(top Neumann condition)}$$

$$(\boldsymbol{\sigma}(u)n)_B = 0 \qquad \text{on } \Gamma^F \backslash \Gamma_B^{F,u} \quad \textit{(bottom Neumann condition)}$$

holds for all $t \in [0,T]$ with viscosity and elasticity tensors $\boldsymbol{A}$ and $\boldsymbol{B}$, body forces f as well as a constant material density $\rho > 0$. Additionally, initial conditions are imposed on the displacement u, velocity $\dot{u}$ and state α.

Remark 2.3.2. This is an extension of the model presented in [102], where a single deformable body in contact with a rigid foundation and unilateral rate-and-state friction on the contact interface was considered. Note that the main adaptation is to replace the tangential velocity relative to the fixed rigid foundation by the relative tangential velocity of adjacent deformable bodies.

In principle, fault opening can be incorporated into the model by replacing (2.3.2) with the non-penetration condition $[u]^u \cdot n^u \leq 0$ on $\Gamma_T^{F,u}$ and dynamically freezing or thawing rate-and-state friction as described by the sudifferential inclusions, when faults open or close, i.e. adjacent bodies lose or come in contact to one another, respectively.

2.4 Weak formulation

A weak formulation typically represents a variational principle that a physical system satisfies. It encodes the notion of minimizing a physical or abstract energy to obtain a solution and is formally derived by multiplying the strong form with a suitable test function, then integrating over the domain, and applying integration by parts. By the integrals and the last step transfering derivatives to the test function, necessary assumptions on the regularity of solutions are relaxed. Moreover, appropriate solution and test spaces are chosen such that the arising integrals are well-defined.

With the Hilbert space $\mathcal{H} = H^1(\Omega_1)^d \times \cdots \times H^1(\Omega_m)^d$ and the canonical inner product $(v,w)_{\mathcal{H}} = \sum_{i=1}^m (v_i, w_i)_{H^1(\Omega_i)^d}$, $v_i, w_i \in H^1(\Omega_i)$, $i = 1, \ldots, m$, let us introduce the closed linear subspace

$$\mathcal{H}_0 = \left\{ v \in \mathcal{H} \,:\, v = 0 \text{ on } \Gamma^D \right\}$$

of admissible displacements and velocities satisfying the Dirichlet boundary conditions. In the closed affine subspace

$$\mathcal{H}_0^u = \left\{ v \in \mathcal{H}_0 \,:\, [v]^u \cdot n^u = 0 \right\}, \tag{2.4.1}$$

the closed-fault condition in form of the normal jump condition (2.3.2) is fulfilled with respect to sufficiently smooth u in addition.

Assuming that the viscosity and elasticity tensors $\boldsymbol{A}$ and $\boldsymbol{B}$ are uniformly elliptic in the sense that the bilinear forms induced by $\boldsymbol{A}(x)$ and $\boldsymbol{B}(x)$ on the space of symmetric $d \times d$ matrices are elliptic with constants independent of $x \in \Omega$, the bilinear forms

$$a(v,w) = \int_{\Omega\setminus\Gamma^F} \boldsymbol{A}\boldsymbol{\varepsilon}(v) \colon \boldsymbol{\varepsilon}(w)\,dx, \quad b(v,w) = \int_{\Omega\setminus\Gamma^F} \boldsymbol{B}\boldsymbol{\varepsilon}(v) \colon \boldsymbol{\varepsilon}(w)\,dx, \qquad v,w \in \mathcal{H}_0,$$

where the symbol : denotes the tensor contraction, are well-defined. Moreover, let us introduce the linear functional

$$\ell(v) = \int_\Omega f v\,dx + \int_{\Gamma^N} f^N v\,ds, \qquad v \in \mathcal{H}_0.$$

Following the usual steps of inserting the stress–strain relation of the material law (2.3.4) into the balance of momentum (2.3.5), testing with functions $v - \dot{u}$, integrating by parts, using the symmetry of $\boldsymbol{\sigma}(u)$ and taking the boundary conditions on Γ^D and Γ^N into account formally leads to

$$\begin{aligned} &\langle \rho\ddot{u},\, v - \dot{u}\rangle + a(\dot{u}, v-\dot{u}) + b(u, v-\dot{u}) - \ell(v-\dot{u}) \\ &= \int_{\Gamma^F} (\boldsymbol{\sigma}(u)n)_T \cdot (v-\dot{u})_T\,ds + \int_{\Gamma^F} (\boldsymbol{\sigma}(u)n)_B \cdot (v-\dot{u})_B\,ds \end{aligned}$$

for all $v \in \mathcal{H}_0$ and $t \in (0,T)$, where $\langle\cdot,\cdot\rangle$ denotes the pairing of $\mathcal{H}_0$ and its dual $\mathcal{H}_0^*$. Using the non-contact interface conditions $(\boldsymbol{\sigma}(u)n)_T = 0$ on $\Gamma^F \setminus \Gamma_T^{F,u}$ and $(\boldsymbol{\sigma}(u)n)_B = 0$ on $\Gamma^F\setminus\Gamma_B^{F,u}$, the definition of jumps (2.3.1), the integral transformation from $\Gamma_B^{F,u}$ to $\Gamma_T^{F,u}$, and the stress balance (2.3.3), the right hand side reduces to

$$\begin{aligned} &\int_{\Gamma_T^{F,u}} (\boldsymbol{\sigma}(u)n)_T \cdot (v-\dot{u})_T\,ds + \int_{\Gamma_B^{F,u}} (\boldsymbol{\sigma}(u)n)_B \cdot (v-\dot{u})_B\,ds \\ &= \int_{\Gamma_T^{F,u}} (\boldsymbol{\sigma}(u)n)_T \cdot \Big([v-\dot{u}]^u + (v-\dot{u})_B \circ \pi^u \Big) + \omega^u \Big((\boldsymbol{\sigma}(u)n)_B \cdot (v-\dot{u})_B \Big) \circ \pi^u\,ds \\ &= \int_{\Gamma_T^{F,u}} (\boldsymbol{\sigma}(u)n)_T \cdot [v-\dot{u}]^u\ ds. \end{aligned} \tag{2.4.2}$$

For given state α, let us consider the convex functional Φ^u on $\mathcal{H}_0$ defined by

$$\Phi^u(\,\cdot\,,\alpha) = \int_{\Gamma_T^{F,u}} \phi([\,\cdot\,]^u, \alpha)\,ds \tag{2.4.3}$$

with the convex functional ϕ from (2.2.3). Then, any $v \in \mathcal{H}_0^u \subset \mathcal{H}_0$ satisfies the closed-fault condition (2.3.2) and using the decomposition $(\boldsymbol{\sigma}(u)n)_T = \sigma_t + \sigma_n n^u$, the closed-fault condition $[v-\dot{u}]^u \cdot n^u = 0$ on $\Gamma_T^{F,u}$ and the subdifferential friction law (2.2.4) results in the estimate

$$\int_{\Gamma_T^{F,u}} (\boldsymbol{\sigma}(u)n)_T \cdot [v-\dot{u}]^u\ ds \geq \Phi^u(\dot{u},\alpha) - \Phi^u(v,\alpha). \tag{2.4.4}$$

Finally, the weak form of the rate equation is obtained by inserting (2.4.4) into (2.4.2)

$$\langle \rho\ddot{u},\, v-\dot{u}\rangle + a(\dot{u}, v-\dot{u}) + b(u, v-\dot{u}) + \Phi^u(v,\alpha) - \Phi^u(\dot{u},\alpha) \geq \ell(v-\dot{u}) \quad \forall v \in \mathcal{H}_0^u.$$

On the other hand, for given velocity $\dot{u} \in \mathcal{H}_0^u$ and thus given rate $V = |[\dot{u}]^u|$, let us define the convex functional Ψ^u on $L^2(\Gamma^F)$ by

$$\Psi^u(\,\cdot\,, \dot{u}) = \int_{\Gamma_T^{F,u}} \psi(\,\cdot\,, |[\dot{u}]^u|)\, ds \tag{2.4.5}$$

with the convex functional ψ taken from the state law (2.2.7) and test the subdifferential state evolution with $\beta \in L^2(\Gamma^F)$ to obtain its weak formulation

$$(\dot{\alpha}, \beta-\alpha)_{L^2(\Gamma^F)} + \Psi^u(\beta, \dot{u}) - \Psi^u(\alpha, \dot{u}) \geq 0 \qquad \forall \beta \in L^2(\Gamma^F).$$

Although Ψ^u is defined on $L^2(\Gamma^F)$, it only depends on values of α on the contact boundary $\Gamma_T^{F,u}$. Therefore, the above weak state evolution intrinsically fulfills the non-evolution condition $-\dot{\alpha} = 0$ on the non-contact boundary $\Gamma^F \backslash \Gamma_T^{F,u}$. Consequently, the weak formulation of the coupled rate-and-state friction problem 2.3.1 reads as follows.

Problem 2.4.1 (Weak formulation, cf. [54])**.** *Find a sufficiently smooth*

$$u \in H^1((0,T), \mathcal{H}_0) \cap H^2((0,T), \mathcal{H}_0^*) \text{ and } \alpha \in H^1((0,T), L^2(\Gamma^F))$$

such that $\dot{u} \in \mathcal{H}_0^u$ *holds and*

$$\begin{aligned} \langle \rho\ddot{u},\, v-\dot{u}\rangle + a(\dot{u}, v-\dot{u}) + b(u, v-\dot{u}) + \Phi^u(v,\alpha) - \Phi^u(\dot{u},\alpha) &\geq \ell(v-\dot{u}) \quad \forall v \in \mathcal{H}_0^u \\ (\dot{\alpha}, \beta-\alpha)_{L^2(\Gamma^F)} + \Psi^u(\beta, \dot{u}) - \Psi^u(\alpha, \dot{u}) &\geq 0 \qquad \forall \beta \in L^2(\Gamma^F) \end{aligned}$$

is satisfied for almost all $t \in (0,T)$ *with initial conditions*

$$u(0) = u_0, \quad \dot{u}(0) = \dot{u}_0, \quad \alpha(0) = \alpha_0$$

and given $u_0, \dot{u}_0 \in \mathcal{H}_0^{u_0}$ *and* $\alpha_0 \in L^2(\Gamma^F)$.

A generic choice of initial conditions, which is consistent with the Dirichlet boundary conditions, is the equilibrium configuration consisting of vanishing velocities $\dot{u}_0 = 0$ and an initial displacement u_0, that is obtained as the solution of the stationary problem

$$u_0 \in \mathcal{H}_0^{u_0} : \qquad b(u_0, v) = \ell(v) \qquad \forall v \in \mathcal{H}_0^{u_0}. \tag{2.4.6}$$

In the numerical simulations conducted in Chapter 4, the solution of (2.4.6) is approximated by one step of a fixed point iteration over the geometric nonlinearity, i.e. u_0 is computed as the unique solution (up to tangential rigid body motions) of the linear problem on $\mathcal{H}_0^{u_0^0}$, where the initial iterate is given by $u_0^0 = 0$.

Remark 2.4.2. A precise characterization of the solution space for the deformations u is subject to further research on the existence and uniqueness of solutions for this weak coupled rate-and-state friction problem. However, Pipping [100] showed the existence of long-time solutions in a setting with unilateral frictional contact of a single deformable body with a rigid foundation and Dieterich's aging law.

2.5 Semi-discretization in time

Until this point, the coupled variational RSF Problem 2.4.1 is continuous both in time and space. In this section, time-discrete approximations of its parametrized rate and state subproblems will be considered proceeding similarly to [102], before deriving fully discrete versions after spatial discretization in Section 2.6. This time-then-space discretization ansatz is called *Rothe's method* [113]. As will be demonstrated, discretization in time leads to an elliptic boundary value problem in function space in each time step. In principle, for each stationary problem, the subsequent spatial discretization using finite elements and the associated finite element space can easily be chosen differently, e.g. varying grids, ansatz functions, polynomial degrees. This is advantageous for a priori and a posteriori error analysis, which is why this approach is particularly suited for adaptivity and is thus a common choice in the FE community.

Rate problem with given state For contact problems, there is a plethora of time integration methods, see e.g. [87] for an overview. In the setting of dynamic contact problems, the classical Newmark scheme or variants thereof are the most prevalent options due to their consistency and stability properties in the absence of contact. Assuming that the time interval $[0,T]$ is partitioned into N subintervals $[t_{n-1},t_n]$, $n=1,\dots,N$, with $0=t_0<\dots<t_N=T$ and uniform step size $\tau=\tau_n=t_n-t_{n-1}$, the classical Newmark discretization of the weak rate problem 2.4.1 for given state $\alpha\in L^2(\Gamma^F)$ is based on the extended mean value theorem approximating first and second derivatives and reads

$$\begin{aligned}\dot{u}_n &= \dot{u}_{n-1}+\tau\left((1-\gamma)\ddot{u}_{n-1}+\gamma\ddot{u}_n\right)\\ u_n &= u_{n-1}+\tau\dot{u}_{n-1}+\tfrac{\tau^2}{2}\left((1-2\beta)\ddot{u}_{n-1}+2\beta\ddot{u}_n\right)\end{aligned}$$

with spatial approximations $u_n=u(t_n)$, $\dot{u}_n=\dot{u}(t_n)$ and $\ddot{u}_n=\ddot{u}(t_n)$, $0<n\leq N$ as well as parameters $0\leq\gamma\leq 1$ and $0\leq 2\beta\leq 1$.

It is a one-step method, meaning that it only uses information from its immediate predecessor to compute an approximation of the solution at the next time step. Hence, it is fully described by the time step size and a time-stepping procedure from arbitrary initial data to the next time step.
In the absence of contact, the Newmark scheme is second-order consistent for $\gamma=\frac{1}{2}$ and unconditionally stable for $2\beta\geq\frac{1}{2}(\gamma+\frac{1}{2})^2$. A typical choice is $2\beta=\gamma=\frac{1}{2}$, where the scheme coincides with the trapezoidal rule and is energy conserving [59].
In case of contact, the classical Newmark scheme is known to exhibit some shortcomings. Although it is energy conserving, if the actual contact boundary is invariant during the time step [87], the energy is not guaranteed to remain bounded during time integration in general. Moreover, artificial oscillations in the contact stresses, displacements and velocities at the contact boundary may occur due to an unfavorable interplay of space and time discretizations or due to a violation of the persistency condition, i.e. the relative velocity in normal direction at the contact boundary has to vanish. Several modifications of the classical scheme are suggested in the literature to overcome these drawbacks (see Krause & Walloth [82] and the references cited therein for an overview and comparison).

In particular, the contact-stabilized Newmark scheme originally presented by Deuflhard et al. in [34] and further improved in Klapproth [72] features additional dissipation in case of contact in order to prevent energy blow-up as well as guarantee physical contact forces and relative velocities at the contact boundary. Moreover, there is extensive theory on this variant including consistency results [74] and adaptive time step control [73] for the frictionless case.

However, as the focus of this thesis is on the resolution of the spatial multiscale aspects of the problem, the classical scheme with $2\beta = \gamma = \frac{1}{2}$, i.e.

$$\begin{aligned} \dot{u}_n &= \dot{u}_{n-1} + \tfrac{\tau}{2}\left(\ddot{u}_{n-1} + \ddot{u}_n\right) \\ u_n &= u_{n-1} + \tau \dot{u}_{n-1} + \left(\tfrac{\tau}{2}\right)^2 \left(\ddot{u}_{n-1} + \ddot{u}_n\right) \end{aligned}$$

for $n = 1, \ldots, N$, will be used in the remainder, cf. [102]. Solving the first equation for $\ddot{u}_n$ makes

$$\ddot{u}_n = \tfrac{2}{\tau}\left(\dot{u}_n - \dot{u}_{n-1}\right) - \ddot{u}_{n-1} \tag{2.5.1}$$

and inserting into the second yields

$$u_n = u_{n-1} + \tfrac{\tau}{2}\left(\dot{u}_{n-1} + \dot{u}_n\right). \tag{2.5.2}$$

Then, inserting into the weak rate inequality in problem 2.4.1 at fixed time $t = t_n$ and evaluating the deformation-dependent closed-fault condition as well as the friction law with respect to u_{n-1} results in the spatial variational inequality

$$\dot{u}_n \in \mathcal{H}_0^{u_{n-1}}: \quad a_n(\dot{u}_n, v - \dot{u}_n) + \Phi^{u_{n-1}}(v, \alpha) - \Phi^{u_{n-1}}(\dot{u}_n, \alpha) \geq \ell_n(v - \dot{u}_n) \tag{2.5.3}$$

for all $v \in \mathcal{H}_0^{u_{n-1}}$ and $n = 1, \ldots, N$, where

$$a_n(v, w) = \tfrac{2}{\tau}(\rho v, w) + a(v, w) + \tfrac{\tau}{2} b(v, w) \tag{2.5.4}$$

with the canonical $L^2(\Omega)$ inner product $(\cdot, \cdot)$ and

$$\ell_n(v) = \ell(v) + (\rho \ddot{u}_{n-1}, v) + \tfrac{2}{\tau}(\rho \dot{u}_{n-1}, v) - \tfrac{\tau}{2} b(\dot{u}_{n-1}, v) - b(u_{n-1}, v).$$

So far, $\ddot{u}_0$ has not been prescribed in the continuous problem 2.4.1. In case the initial configuration manifests acceleration towards equilibrium, it can be computed by solving

$$\ddot{u}_0 \in \mathcal{H}_0: \quad (\rho \ddot{u}_0, v) + a(\dot{u}_0, v) + b(u_0, v) = \ell(v) \qquad \forall v \in \mathcal{H}_0 \tag{2.5.5}$$

in general. However, if the system starts in equilibrium, this initial acceleration equates to $\ddot{u}_0 = 0$.

Remark 2.5.1. By evaluating the jump terms $[\,\cdot\,]^u$, the contact boundary $\Gamma_T^{F,u}$, and the contact mapping π^u with respect to the deformation $(\mathrm{Id} + u_{n-1})(\Gamma^F)$ associated with the previous time step, the geometric nonlinearity incorporating large (relative) deformations of the contact boundary is eliminated. Hence, in each time step, the variational inequality (2.5.3) is to be solved on the affine subspace $\mathcal{H}_0^{u_{n-1}} \subset \mathcal{H}_0$.

In (2.5.3), $\dot{u}_n$ is the sole unknown for given state α. Due to the symmetry of the bilinear form $a_n(\cdot,\cdot)$, its positive definiteness and the convexity of $\Phi(\cdot,\alpha)$, this variational inequality is equivalent to the minimization problem

$$\dot{u}_n \in \mathcal{H}_0^{u_{n-1}}: \qquad \mathcal{J}(\dot{u}_n,\alpha) \leq \mathcal{J}(v,\alpha) \qquad \forall v \in \mathcal{H}_0^{u_{n-1}} \tag{2.5.6}$$

with the generic energy functional

$$\mathcal{J}(v,\alpha) = \tfrac{1}{2}a_n(v,v) + \Phi^{u_{n-1}}(v,\alpha) - \ell_n(v). \tag{2.5.7}$$

The existence and uniqueness of solutions for the spatial rate problem (2.5.6) relies on techniques from convex minimization and the theory of superposition operators. Once the spatial rate problem has been solved, the displacements u_n are obtained with (2.5.2).

Lemma 2.5.2 (cf. [102, Proposition 4.3])**.** *The rate functional* $\Phi^{u_{n-1}}(\cdot,\alpha)$ *from* (2.4.3) *corresponding to the Dieterich–Ruina model* (2.2.3) *of friction is proper, convex, and lower semi-continuous for any state* $\alpha \in L^2(\Gamma^F)$*.*

Proof. The rate functional $\Phi^{u_{n-1}}(\cdot,\alpha)$ is a superposition operator in the sense of [102, Lemma 4.2]. As $\phi(\,\cdot\,,\alpha)$ is convex, so is $\Phi^{u_{n-1}}(\,\cdot\,,\alpha)$. Moreover, $\Phi^{u_{n-1}}(\,\cdot\,,\alpha)$ is proper, because $\phi(0,\alpha) = 0$. It is lower semi-continuous by [102, Lemma 4.2], since ϕ is continuous and non-negative. □

These properties and the following proposition lead to the desired statement on the existence and uniqueness of solutions for (2.5.6).

Proposition 2.5.3 (cf. [54, Proposition 3.2], [102, Proposition 4.3])**.** *Let* $f \in L^2(\Omega)$*,* $f^N \in L^2(\Gamma^N)$ *and assume that* u_{n-1}*,* $n = 1,\dots,N$*, is sufficiently smooth and does not self-penetrate, so that the contact mapping* $\pi^{u_{n-1}}$ *and thus* $\mathcal{H}_0^{u_{n-1}}$ *are well-defined. Then the spatial rate problem* (2.5.6) *has a unique solution* $\dot{u}_n \in \mathcal{H}_0^{u_{n-1}}$ *for any given state* $\alpha \in L^2(\Gamma^F)$*.*

Proof. The rate functional $\Phi^{u_{n-1}}(\cdot,\alpha)$ is proper, convex, and lower semi-continuous for any state $\alpha \in L^2(\Gamma^F)$ according to the previous Lemma 2.5.2. Moreover, by the assumptions on $\boldsymbol{A}$ and $\boldsymbol{B}$, the bilinear form $(\boldsymbol{A}(x) + \frac{\tau}{2}\boldsymbol{B}(x))(\cdot)\colon(\cdot)$ on the symmetric $d \times d$ matrices is symmetric and uniformly elliptic with respect to $x \in \Omega$. The rest of the proof follows with Korn's inequalities [123] and [50, Lemma 4.1]. □

Therefore, the solution operator $R : L^2(\Gamma^F) \to \mathcal{H}_0^{u_{n-1}}$ of the spatial rate problem (2.5.6)

$$L^2(\Gamma^F) \ni \alpha \mapsto R(\alpha) = \dot{u}_n \in \mathcal{H}_0^{u_{n-1}}, \tag{2.5.8}$$

is well-defined under the above assumptions.

State problem with given rate Discretizing the spatial state problem 2.4.1 with given velocity $\dot{u} \in \mathcal{H}_0^{u_{n-1}}$ in time using the backward Euler scheme and evaluating the deformation-dependent state law with u_{n-1} yields the variational inequality

$$\begin{aligned} \alpha_n \in L^2(\Gamma^F): \quad (\alpha_n, \beta - \alpha_n)_{L^2(\Gamma^F)} + \tau\Psi^{u_{n-1}}(\beta, \dot{u}) - \tau\Psi^{u_{n-1}}(\alpha_n, \dot{u}) \\ \geq (\alpha_{n-1}, \beta - \alpha_n)_{L^2(\Gamma^F)} \quad \forall \beta \in L^2(\Gamma^F) \end{aligned} \tag{2.5.9}$$

where $\alpha_n = \alpha(t_n)$, $n = 1, \ldots, N$, denote the time-discrete, spatial approximations of α. Again, this is equivalent to a convex minimization problem

$$\alpha_n \in L^2(\Gamma^F): \qquad \mathcal{E}(\alpha_n, \dot{u}) \leq \mathcal{E}(\beta, \dot{u}) \qquad \forall \beta \in L^2(\Gamma^F) \tag{2.5.10}$$

with the convex state energy functional $\mathcal{E}(\,\cdot\,, \dot{u})$ given by

$$\mathcal{E}(\beta, \dot{u}) = \tfrac{1}{2}(\beta, \beta)_{L^2(\Gamma^F)} + \tau\Psi^{u_{n-1}}(\beta, \dot{u}) - (\alpha_{n-1}, \beta)_{L^2(\Gamma^F)}$$

Once more, the existence and uniqueness of solutions follows with similar arguments to the ones presented in [102]. Let us begin by recording properties of the state functional $\Psi^{u_{n-1}}$.

Lemma 2.5.4 (cf. [102, Proposition 4.4])**.** *Let* $\log L \in L^\infty(\Gamma^F)$*. The state functional* $\Psi^{u_{n-1}}(\cdot, \dot{u})$ *corresponding to Dieterich's aging* (2.2.5) *or Ruina's slip law* (2.2.6) *is proper, convex, and lower semi-continuous for any velocity* $\dot{u} \in \mathcal{H}_0^{u_{n-1}}$*.*

Proof. For fixed velocity $\dot{u} \in \mathcal{H}_0^{u_{n-1}}$ and thus given rate $V = |[\dot{u}]^{u_{n-1}}| \geq 0$ on Γ^F, the functional $\tau\Psi^{u_{n-1}}(\,\cdot\,, \dot{u})$ is convex due to the convexity of $\psi(\,\cdot\,, V)$. From $\psi_r(0, V) = 0$ and $\psi_d(0, V) = 1$ follows that $\Psi^{u_{n-1}}$ is proper in both cases. To show that $\Psi^{u_{n-1}}$ is lower semi-continuous, let us decompose ψ_d and ψ_r into their linear and nonlinear parts:

$$\begin{aligned} &\psi_d = \psi_{d,1} + \psi_{d,2}, \quad \psi_{d,1} : \alpha \mapsto \tfrac{V}{L}\alpha, && \psi_{d,2} : \alpha \mapsto e^{-\alpha}, \\ &\psi_r = \psi_{r,1} + \psi_{r,2}, \quad \psi_{r,1} : \alpha \mapsto \tfrac{V}{L}\log(\tfrac{V}{L})\alpha, && \psi_{r,2} : \alpha \mapsto \tfrac{1}{2}\tfrac{V}{L}\alpha^2 \end{aligned}$$

Consequently, $\psi_{d,1}$ and $\psi_{r,1}$ multiply their arguments with L^2 functions and their respective contribution to $\Psi^{u_{n-1}}$ is continuous in α. From the non-negativity of $\psi_{d,2}$ and $\psi_{r,2}$ follows the existence of the corresponding integrals and the application of [102, Lemma 4.2] yields the lower semi-continuity of $\Psi^{u_{n-1}}$. □

Proposition 2.5.5 (cf. [54, Proposition 3.3], [102, Proposition 4.4])**.** *For Dieterich's aging law* (2.2.5) *and Ruina's slip law* (2.2.6)*, the spatial state problem* (2.5.10) *has a unique solution* $\alpha_n \in L^2(\Gamma^F)$ *for* $n = 1, \ldots, N$ *and any given velocity* $\dot{u} \in \mathcal{H}_0^{u_{n-1}}$ *with sufficiently smooth* u_{n-1}*.*

Proof. The proof follows from [50, Lemma 4.1]. □

With this statement, the solution operator $S : \mathcal{H}_0^{u_{n-1}} \to L^2(\Gamma^F)$ of the spatial state problem (2.5.10)

$$\mathcal{H}_0^{u_{n-1}} \ni \dot{u} \mapsto S(\dot{u}) = \alpha_n \in L^2(\Gamma^F) \tag{2.5.11}$$

is well-defined.

Coupled spatial problem Combining the spatial rate (2.5.3) and state (2.5.9) problems yields a coupled, time-discrete version of problem 2.4.1.

Problem 2.5.6 (Semi-discretization in time)**.** *Find* $\dot{u}_n \in \mathcal{H}_0^{u_{n-1}}$ *and* $\alpha_n \in L^2(\Gamma^F)$ *satisfying*

$$\begin{aligned} a_n(\dot{u}_n, v - \dot{u}_n) + \Phi^{u_{n-1}}(v, \alpha_n) - \Phi^{u_{n-1}}(\dot{u}_n, \alpha_n) &\geq \ell_n(v - \dot{u}_n), \\ (\alpha_n, \beta - \alpha_n)_{L^2(\Gamma^F)} + \tau\Psi^{u_{n-1}}(\beta, \dot{u}_n) - \tau\Psi^{u_{n-1}}(\alpha_n, \dot{u}_n) &\geq (\alpha_{n-1}, \beta - \alpha_n)_{L^2(\Gamma^F)} \end{aligned}$$

for all $v \in \mathcal{H}_0^{u_{n-1}}$ *and all* $\beta \in L^2(\Gamma^F)$*,* $n = 1, \dots, N$*, with given initial conditions* $u_0, \dot{u}_0 \in \mathcal{H}_0^{u_0}$*,* $\alpha_0 \in L^2(\Gamma^F)$ *and* $\ddot{u}_0$ *obtained from* (2.5.1) *as well as problem* (2.5.5)*.*

Remark 2.5.7. Let us emphasize again, that the contact map $\pi^{u_{n-1}}$ and thus a well-defined $\mathcal{H}_0^{u_{n-1}}$ are available, if the displacement u_{n-1} is sufficiently smooth and does not lead to self-penetration. This is a rather strong assumption, that can be relaxed by enforcing non-penetration in terms of an approximate contact map rather than exactly, see e.g. the next section on the spatial discretization, where round-off errors necessitate a similar construction.

Proving existence and uniqueness of solutions for the time-discrete, coupled problem 2.5.6 is no trivial endeavor and not in the scope of this thesis. For unilateral frictional contact between a deformable body and a rigid foundation, the setting is simpler as nonlinearities arising due to non-penetration and large relative displacements are absent and such results could be shown. In particular, existence and uniqueness of solutions for frictional contact with Dieterich's aging law have been derived based on Banach's fixed point theorem, see [99, Proposition 3.6.], whereas Schauder's fixed point theorem was used to show existence in case of Ruina's slip law [102, Theorem 5.14].

2.6 Spatial discretization

This section is devoted to the spatial discretization of the time-discrete, coupled problem 2.5.6. Let $\mathcal{T}_i$ denote regular, simplicial partitions of polygonal bodies Ω_i with vertices $\mathcal{N}_i^*$, $i = 1, \dots, m$, that resolve the Dirichlet boundaries Γ_i^D. The set of nodes actually carrying degrees of freedom is given by $\mathcal{N}_i = \mathcal{N}_i^* \setminus \overline{\Gamma}_i^D$. For each body Ω_i, the associated d-valued, linear finite element space adhering to the Dirichlet boundary condition is defined as

$$\mathcal{S}_i = \left\{ v \in C(\Omega_i)^d \,:\, v \text{ is linear on all } T \in \mathcal{T}_i \text{ and } v|_{\Gamma_i^D} = 0 \right\}.$$

The combined triangulation $\mathcal{T} = \bigcup_{i=1}^m \mathcal{T}_i$ with nodes $\mathcal{N} = \bigcup_{i=1}^m \mathcal{N}_i$ partitions Ω and induces the product space

$$\mathcal{S} = \mathcal{S}_1 \times \cdots \times \mathcal{S}_m = \operatorname{span}\{\lambda_p e_j \,:\, p \in \mathcal{N},\, j = 1, \dots, d\} \subset \mathcal{H}_0, \tag{2.6.1}$$

where λ_p denotes the scalar nodal basis function corresponding to the node $p \in \mathcal{N}$ and $\{e_1, \dots, e_d\}$ the standard basis in $\mathbb{R}^d$.

2.6.1 Dual mortar discretization of the rate problem

In the context of contact problems, the discretization of non-penetration conditions poses a key challenge. For a long time, *node-to-segment* approaches and its variants were most popular and have experienced a wide variety of application [87]. The idea is to identify nodes of the slave body with opposing segments of the master body at a contact interface—typically by means of a projection. Afterward, non-penetration is enforced for the slave side nodes with respect to the corresponding segments on the master side. Unfortunately, this strategy suffers from instabilities due to artificial jumps in the contact forces during (frictional) sliding [105].

In contrast, the *mortar method* is a *segment-to-segment* approach establishing non-penetration in a weak sense using Lagrange multipliers. Originally, it was devised to couple spectral and finite element methods [15] and applied as a domain decomposition technique for non-matching grids [132]. Therefore, the approach is very versatile with regard to the coupling triangulations and well suited for spatial adaptivity. For our purposes, the triangulations $\mathcal{T}_i$ and $\mathcal{T}_{i+1}$, $i = 1, \dots, m-1$, generally do not match at the common interface $\Gamma^F_{i,i+1}$, i.e. $\mathcal{N}_i \cap \Gamma^F_{i,i+1} \neq \mathcal{N}_{i+1} \cap \Gamma^F_{i,i+1}$. Beyond that, the sets of nodes $\mathcal{N}_i$ are assumed to be pairwise disjoint, i.e. $\mathcal{N}_i \cap \mathcal{N}_i = \varnothing$, $i \neq j$, for notational convenience. The weak non-penetration condition is obtained by multiplying the pointwise constraint with suitable test functions from the mortar space and integrating over the coupling interface of the slave side. Mortar space and test functions can be chosen such that the resulting method possesses enhanced stability properties and error estimates in comparison to the node-to-segment approach [65].
Wohlmuth and Krause were able to prove optimal error bounds by discretizing the weak non-penetration constraints using dual basis functions satisfying a bi-orthogonality property [133]. This strategy ultimately allows an efficient localization of the non-penetration constraints by means of a basis transformation that changes the role of the slave side nodal basis functions to span the space of relative displacements. Moreover, with this discretization, the jump $[\,\cdot\,]$ across Γ^F shows up directly, which is desirable for an efficient algorithmic treatment of the non-penetration condition (2.3.2) and friction law (2.1.12). This approach has been successfully applied to a two-body contact problem with friction [81] and will be the course of action in this exposition as well.

Following [54], the dual mortar discretization of the rate problem with given state will be established using a hierarchical decomposition of the discrete solution space into a subspace with weak zero jump across Γ^F and a subspace containing the relative velocity at Γ^F. Another way of conveying the same discretization strategy is based on algebraic representations similar to [118, Section 3.3]. While the latter has its advantages in demonstrating the implementational details, the former excels at highlighting the structural idea, is mathematically the more elegant approach and fits thematically to the subspace decompositions, that will be encountered in Chapter 3 of this thesis.

First, let us introduce some notation that will facilitate the description of the dual mortar discretization of $\mathcal{H}_0^{u_{n-1}}$ and incorporating non-penetration and tangential friction along the faults Γ^F. The triangulation of Γ^F is considered to be induced

by the top, non-mortar sides Ω_{i+1} of the individual faults $\Gamma^F_{i,i+1}$, $i = 1, \dots, m-1$, according to

$$\mathcal{T}^F = \bigcup_{i=1}^{m-1} \mathcal{T}_i^F, \qquad \mathcal{T}_i^F = \left\{ E = T \cap \Gamma^F_{i,i+1} \,:\, T \in \mathcal{T}_{i+1} \right\},$$

with nodes $\mathcal{N}^F = \bigcup_{i=1}^{m-1} \mathcal{N}_i^F$ and $\mathcal{N}_i^F = \mathcal{N}_{i+1} \cap \Gamma^F_{i,i+1}$, while the corresponding trace spaces read

$$\mathcal{S}^F = (v_1, \dots, v_{m-1}) \subset L^2(\Gamma^F)^d, \qquad v_i \in \mathcal{S}_i^F = \mathcal{S}_{i+1}|_{\Gamma^F_{i,i+1}}$$

and are spanned by the nodal basis $\lambda_p e_j|_{\Gamma^F}$, $p \in \mathcal{N}^F$, $j = 1, \dots, d$.

Following the train of thought from the continuous case in Section 2.3, let us institute with $\widetilde{\Gamma}_T^F \subset \Gamma^F$ and $\widetilde{\Gamma}_B^F \subset \Gamma^F$ approximations of the deformed contact boundaries $\Gamma_T^{F,u_{n-1}}$ and $\Gamma_B^{F,u_{n-1}}$ from the previous time step, respectively. The non-mortar contact boundary $\widetilde{\Gamma}_T^F$ is assumed to be resolved by $\mathcal{T}^F$. Moreover, denote with $\tilde{\pi} : \widetilde{\Gamma}_T^F \to \widetilde{\Gamma}_B^F$ a discrete approximation of the contact mapping $\pi^{u_{n-1}}$. These approximations are necessary, since the triangulations of the deformed bodies $(\mathrm{Id} + u_{n-1,i})(\Omega_i)$ will generally not match across the actual deformed contact boundary $\tilde{\gamma}$

$$\tilde{\gamma} = (\mathrm{Id} + u_{n-1,T})(\widetilde{\Gamma}_T^F)$$

due to a suitable displacement u_{n-1} or discretization errors, that arise from enforcing non-penetration for u_{n-1}. Similar to (2.3.1), the jump of $v \in \mathcal{S}$ across the discrete deformed contact boundary is defined on the top, non-mortar side via

$$\widetilde{[v]} = v_T - v_B \circ \tilde{\pi} \qquad \text{on } \widetilde{\Gamma}_T^F.$$

With the set of non-mortar contact nodes

$$\widetilde{\mathcal{N}}^F = \mathcal{N}^F \cap \overline{\widetilde{\Gamma}_T^F},$$

the pullback of the $L^2(\tilde{\gamma})$ inner product to $\widetilde{\Gamma}_T^F$ given by

$$\langle v,\, w \rangle_{\tilde{\gamma}} = (v \circ (\mathrm{Id} + u_{n-1,T})^{-1}, w \circ (\mathrm{Id} + u_{n-1,T})^{-1})_{L^2(\tilde{\gamma})}$$

and the Kronecker-δ, the dual mortar basis functions φ_q, $q \in \widetilde{\mathcal{N}}^F$, are defined to be piecewise linear on $\mathcal{T}^F$, form a partition of unity, have the same support as $\lambda_q|_{\Gamma^F}$, and satisfy the bi-orthogonality property

$$\langle \lambda_p|_{\Gamma^F},\, \varphi_q \rangle_{\tilde{\gamma}} = \delta_{p,q} \qquad \forall p, q \in \widetilde{\mathcal{N}}^F. \tag{2.6.2}$$

For simplicial grids, the dual mortar basis functions can be constructed elementwise as linear combinations of the nodal basis functions, see e.g. [131], according to

$$\varphi_q|_E = (d\lambda_q - \sum_{\substack{p \in \widetilde{\mathcal{N}}^F \\ p \neq q}} \lambda_p)|_E \qquad \forall E \in \mathcal{T}^F.$$

This construction indicates that dual mortar basis functions are typically discontinuous and thus not contained in $\mathcal{S}^F$.

Based on a weak version of the discrete jump across $\widetilde{\Gamma}_T^F$ with respect to the span of the dual mortar basis functions as test space, the linear projection $\Pi : \mathcal{S} \to \mathcal{S}$, whose components are defined by

$$(\Pi v)_j = \Pi v_j = v_j - \sum_{p \in \widetilde{\mathcal{N}}^F} \langle \widetilde{[v_j]}, \varphi_p \rangle_{\tilde{\gamma}} \, \lambda_p, \qquad j = 1, \dots d,$$

maps to functions, that are weakly continuous across the deformed contact boundary. In an abuse of notation, Π identifies the projection of scalar as well as d-valued functions in the following. Then, the projection Π induces a direct splitting of $\mathcal{S}$

$$\mathcal{S} = \mathcal{V} \oplus \mathcal{W}$$

into its range $\mathcal{V} = \operatorname{im} \Pi$ and kernel $\mathcal{W} = \ker \Pi$. Since it holds $\widetilde{[\lambda_p]} = \lambda_p$ for $p \in \widetilde{\mathcal{N}}^F$, these subspaces are given by

$$\begin{aligned} \mathcal{V} &= \left\{ v \in \mathcal{S} \, : \, \langle \widetilde{[v]}, \varphi_p \rangle_{\tilde{\gamma}} = 0, \, \forall p \in \widetilde{\mathcal{N}}^F \text{ and } j = 1, \dots, d \right\} \\ &= \operatorname{span} \left\{ \mu_p e_j \, : \, \mu_p = \Pi \lambda_p, \, p \in \mathcal{N} \backslash \widetilde{\mathcal{N}}^F \text{ and } j = 1, \dots, d \right\} \end{aligned}$$

and

$$\begin{aligned} \mathcal{W} &= \left\{ v \in \mathcal{S} \, : \, v(p) = 0, \, \forall p \in \mathcal{N} \backslash \widetilde{\mathcal{N}}^F \right\} \\ &= \operatorname{span} \left\{ \lambda_p e_j \, : \, p \in \widetilde{\mathcal{N}}^F \text{ and } j = 1, \dots, d \right\}. \end{aligned}$$

In particular, $\mathcal{V}$ contains all functions in $\mathcal{S}$, that are weakly continuous across the deformed contact boundary in terms of the pullback L^2 inner product $\langle \cdot, \cdot \rangle_{\tilde{\gamma}}$ and the test space spanned by the dual mortar basis functions. The basis functions $\mu_p = \Pi \lambda_p$ spanning $\mathcal{V}$ are the usual nodal basis functions λ_p in the interior of Ω_i, $i = 1, \dots, m$ and on the mortar side of Γ^F, i.e. for all $p \in \mathcal{N} \backslash \widetilde{\mathcal{N}}^F$, while they are extended to the non-mortar side in a weakly continuous way for $p \in \widetilde{\mathcal{N}}^F$.
The space $\mathcal{W}$ is spanned by the usual nodal basis functions λ_p, $p \in \widetilde{\mathcal{N}}^F$, on the non-mortar side and represents the space of (weak) normal and tangential jumps across Γ^F, since the jumps of $v \in \mathcal{V}$ are weakly zero.

The next objective is to split $\mathcal{W}$ locally into its normal and tangential part. For this purpose, the nodal approximation $n_{\mathcal{S}}$ of the normal to the discrete, deformed contact boundary $\tilde{\gamma}$ is introduced as

$$n_{\mathcal{S}} = \sum_{p \in \widetilde{\mathcal{N}}^F} n_p \lambda_p |_{\widetilde{\Gamma}_T^F}, \qquad n_p = \frac{\sum_{E \in \mathcal{T}_p^F} n_E}{\left| \sum_{E \in \mathcal{T}_p^F} n_E \right|},$$

and parametrized over $\widetilde{\Gamma}_T^F$, where $\mathcal{T}_p^F$ denotes the set of simplices $E \in \mathcal{T}_i^F$ with common vertex $p \in \widetilde{\mathcal{N}}^F$, and n_E is an approximation of the normal to the deformed face $(\mathrm{Id} + u_{n-1})_T(E)$ by its average. In addition, $T_p \tilde{\gamma} = (\operatorname{span}\{n_p\})^\perp \subset \mathbb{R}^d$ denotes the approximate tangent space to the deformed contact boundary $\tilde{\gamma}$ with respect to the nodal approximate normal n_p in $p \in \widetilde{\mathcal{N}}^F$.

With this notation, a decomposition of $\mathcal{W}$ into its normal and tangential parts is given by $\mathcal{W} = \mathcal{W}_n \oplus \mathcal{W}_t$ and

$$\mathcal{W}_n = \left\{ \lambda_p x \,:\, p \in \widetilde{\mathcal{N}}^F,\, x \in \operatorname{span}\{n_p\} \right\}, \qquad \mathcal{W}_t = \left\{ \lambda_p x \,:\, p \in \widetilde{\mathcal{N}}^F,\, x \in T_p\tilde{\gamma} \right\}.$$

Remark 2.6.1. In practice, it is convenient to implement the decomposition $\mathcal{S} = \mathcal{V} \oplus \mathcal{W}_n \oplus \mathcal{W}_t$ by means of a basis transformation. Using the set of interior $\mathcal{N}^I$, non-mortar $\widetilde{\mathcal{N}}^F$ and mortar nodes $\widetilde{\mathcal{N}}^M = \mathcal{N} \backslash (\mathcal{N}^I \cup \widetilde{\mathcal{N}}^F)$, let us split the nodal basis $\{\lambda\}$ of $\mathcal{S}$ into corresponding subsets λ^I, λ^F, λ^M. With a similar notation for the bases of $\mathcal{V}$ and $\mathcal{W}$ and their standard algebraic representation as vectors consisting of d-dimensional blocks, the transformed basis $\{\mu^I, \tilde{\lambda}^F, \mu^M\}$ is defined by

$$\begin{pmatrix} \mu^I \\ \tilde{\lambda}^F \\ \mu^M \end{pmatrix} = OB \begin{pmatrix} \lambda^I \\ \lambda^F \\ \lambda^M \end{pmatrix} = \begin{pmatrix} I & 0 & 0 \\ 0 & O^F & 0 \\ 0 & 0 & I \end{pmatrix} \begin{pmatrix} I & 0 & 0 \\ 0 & I & 0 \\ 0 & (D^{-1}M)^T & I \end{pmatrix} \begin{pmatrix} \lambda^I \\ \lambda^F \\ \lambda^M \end{pmatrix},$$

where the block-diagonal matrix O consists of the Householder reflections $O_{pp} = O^F_{pp}$ mapping the first standard basis vector e_1 of $\mathbb{R}^d$ to the averaged domain normal n_p, $p \in \widetilde{\mathcal{N}}^F$, and d-dimensional identity matrices otherwise. Note, that O_{pp} is an orthogonal matrix, i.e. it holds $O^{-1}_{pp} = O^T_{pp}$. The matrix D is given by

$$D_{pq} = \operatorname*{Id}_{d\times d} \langle \lambda_q,\, \varphi_p \rangle_{\tilde{\gamma}}, \qquad p, q \in \widetilde{\mathcal{N}}^F$$

and is diagonal due to the bi-orthogonality relation (2.6.2). The matrix M with entries

$$M_{pq} = \operatorname*{Id}_{d\times d} \langle \lambda_q,\, \varphi_p \rangle_{\tilde{\gamma}}, \qquad p \in \widetilde{\mathcal{N}}^F, q \in \widetilde{\mathcal{N}}^M,$$

is sparse, but involves basis functions from both mortar and non-mortar side. Hence, an efficient implementation of M is not trivial, see e.g. [118] for details.

Remark 2.6.2. This dual mortar approach to non-penetration can be applied to a setting with fault opening, i.e. $[u]^u \cdot n^u \leq 0$, see the literature cited throughout this section.

Remark 2.6.3. A generalization of the dual mortar discretization to body configurations, where multiple, possibly conflicting constraints on non-mortar nodes would occur, has been suggested in the literature, see e.g. [106] for an overview. This issue arises if more than two bodies meet in a single point on the contact boundary at so-called *crosspoints* or if $\overline{\Gamma}^D \cap \overline{\Gamma}^F \neq \varnothing$. The idea is to alter the dual basis in the vicinity of such points ($d = 2$) or lines ($d = 3$). For $d = 2$ and a first-order dual basis, e.g., one would discard the dual basis functions φ_p corresponding to such points $p \in \widetilde{\mathcal{N}}^F$ while neighboring dual basis functions are chosen to be constant on the elements containing p to ensure consistency and preserve its partition of unity property, see [106] for an illustration.

Dual mortar discretization of the solution space In the spirit of [131], the (non-conforming) finite element analog of the solution space $\mathcal{H}_0^{u_{n-1}}$

$$\mathcal{S}_0^{u_{n-1}} = \mathcal{V} \oplus \mathcal{W}_t.$$

incorporates non-penetration by removing the normal jumps. This decomposition motivates the unique splitting of any $v \in \mathcal{S}_0^{u_{n-1}}$

$$v = v_{\mathcal{V}} + v_{\mathcal{W}}, \qquad v \in \mathcal{S}_0^{u_{n-1}} \tag{2.6.3}$$

into contributions

$$v_{\mathcal{V}} = \Pi v = \sum_{\mathcal{N}\setminus\widetilde{\mathcal{N}}^F} v(p)\mu_p \in \mathcal{V}, \qquad v_{\mathcal{W}} = (\mathrm{Id} - \Pi)v = \sum_{p\in\widetilde{\mathcal{N}}^F} [v]_p \, \lambda_p \in \mathcal{W}_t.$$

Here, $[v]_p$ identifies the weak nodal jump of v at $p \in \widetilde{\mathcal{N}}^F$ given by

$$[v]_p = (v - \Pi(v))(p) = (\langle \widetilde{[v_j]}, \varphi_p \rangle_{\tilde{\gamma}})_{j=1}^d \in \mathbb{R}^d.$$

By construction, the weak normal jump $[v]_p \cdot n_p = 0$ vanishes for the nodal vectors $[v]_p$ and all $p \in \widetilde{\mathcal{N}}^F$. Therefore, $v_{\mathcal{W}}$ represents a nodal approximation of the tangential jump of v across $\tilde{\gamma}$ pulled back to $\widetilde{\Gamma}_T^F$.

Fully discretized rate problem with given state Using the finite element approximation $\mathcal{S}_0^{u_{n-1}} \subset \mathcal{H}_0^{u_{n-1}}$, let us discretize the spatial rate problem with given state $\alpha \in L^2(\Gamma^F)$ from (2.5.3) by inserting the splitting (2.6.3). Proceeding as in [99, 102], the friction functional Φ^u from (2.4.3) is diagonalized using a lumping strategy, i.e. the integrand $\phi([v]^u, \alpha)$ is replaced by its nodal interpolation in $\mathcal{S}^F$ leading to the approximate functional $\Phi_{\mathcal{S}} : \mathcal{S}_0^{u_{n-1}} \to \mathbb{R}$,

$$\Phi_{\mathcal{S}}(v, \alpha) = \sum_{p\in\widetilde{\mathcal{N}}^F} \phi_p([v]_p, \alpha), \qquad \phi_p([v]_p, \alpha) = \phi([v]_p, \alpha(p)) \int_{\widetilde{\Gamma}_T^F} \lambda_p \, ds. \tag{2.6.4}$$

This nodal interpolation requires α to be continuous in a neighborhood of each $p \in \widetilde{\mathcal{N}}^F$. Altogether, the mortar discretized rate problem (2.5.3) reads

$$\dot{u}_{n,\mathcal{S}} \in \mathcal{S}_0^{u_{n-1}} : \quad a_n(\dot{u}_{n,\mathcal{S}}, v - \dot{u}_{n,\mathcal{S}}) + \Phi_{\mathcal{S}}(v, \alpha) - \Phi_{\mathcal{S}}(\dot{u}_{n,\mathcal{S}}, \alpha) \geq \ell_{n,\mathcal{S}}(v - \dot{u}_{n,\mathcal{S}}) \tag{2.6.5}$$

for all $v \in \mathcal{S}_0^{u_{n-1}}$ and $n = 1, \ldots, N$ with the bilinear form $a_n(\cdot, \cdot)$ from (2.5.4) and a discrete version $\ell_{n,\mathcal{S}}$ of the linear functional ℓ_n

$$\ell_{n,\mathcal{S}}(v) = \ell(v) + (\rho \ddot{u}_{n-1,\mathcal{S}}, v) + \tfrac{2}{\tau}(\rho \dot{u}_{n-1,\mathcal{S}}, v) - \tfrac{\tau}{2} b(\dot{u}_{n-1,\mathcal{S}}, v) - b(u_{n-1,\mathcal{S}}, v).$$

Here, the data from the previous time step $\ddot{u}_{n-1,\mathcal{S}}$, $\dot{u}_{n-1,\mathcal{S}}$, $u_{n-1,\mathcal{S}}$ is either obtained by finite element approximations $\dot{u}_{0,\mathcal{S}}$, $u_{0,\mathcal{S}} \in \mathcal{S}$ of the initial conditions $\dot{u}_0$, $u_0 \in \mathcal{H}_0^{u_0}$ and a corresponding approximation $\ddot{u}_{0,\mathcal{S}} \in \mathcal{S}$ of the initial acceleration via the auxiliary problem (2.5.5) or determined by discrete analogues of (2.5.1) and (2.5.2).

Since $\mathcal{S}_0^{u_{n-1}}$ is a subspace of $\mathcal{H}_0^{u_{n-1}}$, the existence and uniqueness of discrete, spatial solutions $\dot{u}_{n,\mathcal{S}} \in \mathcal{S}_0^{u_{n-1}}$, $n = 1, \ldots, N$, carries over from the continuous setting in Proposition 2.5.3 by the same arguments and under the same assumptions.

The efficient computation of numerical solutions to the fully discrete rate problem (2.6.5) is a challenging task that will be addressed in Section 2.7.

2.6.2 Piecewise constant discretization of the state problem

Let us turn our attention to the spatial discretization of the state problem (2.5.10) with given rate. Denoting with $\mathcal{C}^F = \{C_p \subset \Gamma^F \,:\, p \in \mathcal{N}^F\}$ a dual partition of the trace grid $\mathcal{T}^F$ of Γ^F, let us consider the subspace $\mathcal{B}^F \subset L^2(\Gamma^F)$ of functions, that are constant on the individual cells $C_p \in \mathcal{C}^F$, $p \in \mathcal{N}^F$. For given rate $\dot{u} \in \mathcal{S}_0^{u_{n-1}}$, a piecewise constant discretization of the state problem (2.5.10) using $\mathcal{B}^F$ yields

$$\begin{aligned} \alpha_{n,\mathcal{B}} \in \mathcal{B}^F : \quad & (\alpha_{n,\mathcal{B}}, \beta - \alpha_{n,\mathcal{B}})_{L^2(\Gamma^F)} + \tau\Psi_{\mathcal{B}}(\beta, \dot{u}) - \tau\Psi_{\mathcal{B}}(\alpha_{n,\mathcal{B}}, \dot{u}) \\ & \qquad \geq (\alpha_{n-1,\mathcal{B}}, \beta - \alpha_{n,\mathcal{B}})_{L^2(\Gamma^F)} \quad \forall \beta \in \mathcal{B}^F, \end{aligned} \tag{2.6.6}$$

where the nodal approximation $\Psi_{\mathcal{B}} : \mathcal{B}^F \to \mathbb{R}$

$$\Psi_{\mathcal{B}}(\beta, \dot{u}) = \sum_{p \in \widetilde{\mathcal{N}}^F} \psi(\beta(p), |\,[\dot{u}]_p\,|)\,|C_p| \tag{2.6.7}$$

of the state functional $\Psi(\cdot, \dot{u})$ from (2.4.5) is obtained by replacing the integrand $\psi(\,\cdot\,, |[\dot{u}]^u|)$ with its nodal interpolation in $\mathcal{S}^F$.
Again, the existence and uniqueness of spatial solutions $\alpha_{n,\mathcal{B}} \in \mathcal{B}^F$, $n = 1, \ldots, N$, transfers directly from the continuous setting, see Proposition 2.5.5.

This variational inequality is equivalent to the convex minimization problem

$$\alpha_{n,\mathcal{B}} \in \mathcal{B}^F : \qquad \mathcal{E}_{\mathcal{B}}(\alpha_{n,\mathcal{B}}, \dot{u}) \leq \mathcal{E}_{\mathcal{B}}(\beta, \dot{u}) \qquad \forall \beta \in \mathcal{B}^F$$

with the discrete, convex state energy functional $\mathcal{E}_{\mathcal{B}}(\,\cdot\,, \dot{u})$ given by

$$\mathcal{E}_{\mathcal{B}}(\beta, \dot{u}) = \tfrac{1}{2}\,(\beta, \beta)_{L^2(\Gamma^F)} - (\alpha_{n-1,\mathcal{B}}, \beta)_{L^2(\Gamma^F)} + \tau\Psi_{\mathcal{B}}(\beta, \dot{u}), \qquad \beta \in \mathcal{B}^F.$$

Note, that the global state energy functional $\mathcal{E}_{\mathcal{B}}(\,\cdot\,, \dot{u})$ fully decouples into nodal contributions. Consequently, the minimizer of $\mathcal{E}_{\mathcal{B}}(\,\cdot\,, \dot{u})$ can be determined by minimizing the local, scalar, convex functionals independently from each other. In general, the associated algebraic problems can be solved with bisection. However, there is an analytic solution in terms of elementary functions in the specific instance of Ruina's slip law (2.2.6):

$$\alpha_{n,\mathcal{B}}(p) = \tfrac{L}{L+\tau V}\left(\alpha_{n-1,\mathcal{B}}(p) - \tfrac{\tau V}{L}\log(\tfrac{V}{L})\right), \qquad p \in \widetilde{\mathcal{N}}^F.$$

For Dieterich's aging law, the analytic solution contains the Lambert W function.

2.6.3 Fully discretized coupled rate-and-state problem

At last, all necessary steps have been taken to state a fully discrete version of the weak coupled rate-and-state problem 2.4.1. Its discretization in time and space is obtained by combining (2.6.5) and (2.6.6) as follows.

Problem 2.6.4 (Discretization in time and space)**.** *Find* $\dot{u}_{n,\mathcal{S}} \in \mathcal{S}_0^{u_{n-1}}$ *and* $\alpha_{n,\mathcal{B}} \in \mathcal{B}^F$ *satisfying*

$$a_n(\dot{u}_{n,\mathcal{S}}, v - \dot{u}_{n,\mathcal{S}}) + \Phi_{\mathcal{S}}(v, \alpha_{n,\mathcal{B}}) - \Phi_{\mathcal{S}}(\dot{u}_{n,\mathcal{S}}, \alpha_{n,\mathcal{B}}) \geq \ell_{n,\mathcal{S}}(v - \dot{u}_{n,\mathcal{S}})$$
$$(\alpha_{n,\mathcal{B}}, \beta - \alpha_{n,\mathcal{B}})_{L^2(\Gamma^F)} + \tau\Psi_{\mathcal{B}}(\beta, \dot{u}_{n,\mathcal{S}}) - \tau\Psi_{\mathcal{B}}(\alpha_{n,\mathcal{B}}, \dot{u}_{n,\mathcal{S}}) \geq (\alpha_{n-1,\mathcal{B}}, \beta - \alpha_{n,\mathcal{B}})_{L^2(\Gamma^F)}$$

for all $v \in \mathcal{S}_0^{u_{n-1}}$ *and* $\beta \in \mathcal{B}^F$, $n = 1, \ldots, N$, *with given initial conditions* $u_{0,\mathcal{S}} \in \mathcal{S}_0^{u_{n-1}}$, $\dot{u}_{0,\mathcal{S}} \in \mathcal{S}_0^{u_{n-1}}$ *and* $\alpha_{0,\mathcal{B}} \in \mathcal{B}^F$.

Proceeding as suggested for the case of unilateral frictional contact [99, 102], this problem is decoupled by means of a fixed point iteration. Similarly to the continuous setting, denote with $R_{\mathcal{S}} : \mathcal{B}^F \to \mathcal{S}_0^{u_{n-1}}$ and $S_{\mathcal{B}} : \mathcal{S}_0^{u_{n-1}} \to \mathcal{B}^F$ the solution operators corresponding to the rate problem with given state (2.6.5) and the state problem with given rate (2.6.6), respectively. Then, the fully discretized coupled problem 2.6.4 is solved iteratively using the fixed point iteration

$$\dot{u}_{n,\mathcal{S}}^{\nu+1} = R_{\mathcal{S}}\left(\omega\alpha_{n,\mathcal{B}}^{\nu+1} + (1-\omega)\alpha_{n,\mathcal{B}}^{\nu}\right), \quad \alpha_{n,\mathcal{B}}^{\nu+1} = S_{\mathcal{B}}\left(\dot{u}_{n,\mathcal{S}}^{\nu}\right), \quad \nu = 0, 1, \ldots \tag{2.6.8}$$

with initial iterate $(\dot{u}_{n,\mathcal{S}}^0, \alpha_{n,\mathcal{B}}^0) = (\dot{u}_{n-1,\mathcal{S}}, \alpha_{n-1,\mathcal{B}})$ and suitable damping parameter $\omega \in (0, 1]$. Note that the cells $C_p \in \mathcal{C}^F$, $p \in \mathcal{N}^F$, contain p in the interior by construction. Thus, the state functions $\alpha \in \mathcal{B}^F$ are constant and hence continuous in a neighborhood of each node $p \in \mathcal{N}^F$ fulfilling the regularity assumptions for nodal interpolation in (2.6.4).

Remark 2.6.5. Showing convergence of the fixed point iteration is a subject of future research. One approach could be to extend a similar proof conducted in case of unilateral rate-and-state contact for a subduction zone [99, 102] to the current layered fault system.

2.7 Truncated Nonsmooth Newton Multigrid algorithm

The last open component for the numerical simulation of the model problem is a highly robust and efficient algebraic solver for the rate problem (2.6.5) with given state $\alpha \in \mathcal{B}^F$. As in the setting with unilateral contact and rate-and-state friction [99, 102], a variant of the Truncated Nonsmooth Newton Multigrid (TNNMG) method will be used. It was originally designed for quadratic obstacle problems [53] and later extended to variational inequalities of second kind with separable nonsmooth nonlinearities [56, 52, 55]. Prior to its inception, monotone multigrid methods (MMG) [75, 133] were the fastest, globally convergent solvers for two body contact problems in the literature. Once the active set is found in the MMG iteration, it reduces to a linear multigrid method and thus features linear multigrid convergence asymptotically. The computational effort per iteration is comparable for both methods, but TNNMG typically reaches the asymptotic phase sooner leading to fewer iterations and faster computation times in practice, see e.g. [55].

Both TNNMG and MMG build on the observation, that the convergence of a simple, globally convergent nonlinear relaxation scheme, e.g. of Gauß-Seidel type, can be accelerated by a suitable Newton-type correction obtained from a linearized problem, that decreases energy efficiently.

An application of TNNMG to the fully discrete rate problem (2.6.5) with given state $\alpha \in \mathcal{B}^F$ is straightforward in many aspects that will be omitted. For details, the interested reader may consult the references mentioned above. Nonetheless, the basic steps will be sketched and important, problem-specific nuances will be highlighted in the following.

Nonlinear smoothing

The variational inequality (2.6.5) with given state $\alpha \in \mathcal{B}^F$ can equivalently be phrased as the minimization problem

$$\dot{u}_{n,\mathcal{S}} \in \mathcal{S}_0^{u_{n-1}} : \qquad \mathcal{J}_{\mathcal{S}}(\dot{u}_{n,\mathcal{S}}) \leq \mathcal{J}_{\mathcal{S}}(v) \qquad \forall v \in \mathcal{S}_0^{u_{n-1}} \tag{2.7.1}$$

with the discrete convex rate energy functional

$$\mathcal{J}_{\mathcal{S}}(v) = \tfrac{1}{2} a_n(v,v) - \ell_{n,\mathcal{S}}(v) + \Phi_{\mathcal{S}}(v,\alpha).$$

Using the splitting (2.6.3) suggested by the decomposition $\mathcal{S}_0^{u_{n-1}} = \mathcal{V} \oplus \mathcal{W}_t$, there is the basis representation

$$v = \sum_{p \in \mathcal{N} \setminus \widetilde{\mathcal{N}}^F} v_p \mu_p + \sum_{p \in \widetilde{\mathcal{N}}^F} v_p \lambda_p \tag{2.7.2}$$

of all $v \in \mathcal{S}_0^{u_{n-1}}$ with coefficients $v_p = v(p)$, $p \in \mathcal{N} \setminus \widetilde{\mathcal{N}}^F$ and $v_p = [v]_p$, $p \in \widetilde{\mathcal{N}}^F$, cf. Remark 2.6.1. In the following, each $v \in \mathcal{S}_0^{u_{n-1}}$ is identified with its unique algebraic representation $(v_p)_{p \in \mathcal{N}}$, $v_p \in \mathbb{R}^d$. In this basis, the discrete nonlinear friction functional

$$\Phi_{\mathcal{S}}(v,\alpha) = \sum_{p \in \widetilde{\mathcal{N}}^F} \phi_p(v_p, \alpha)$$

decouples into separate blocks for the coefficients $v_p \in \mathbb{R}^d$ with respect to the local nonlinearity ϕ_p, $p \in \widetilde{\mathcal{N}}^F$.

The block-separable structure of the convex minimization problem (2.7.1), where blocks correspond to local subspaces at the nodes $p \in \mathcal{N}$, motivates the subspace decomposition

$$\mathcal{S}_0^{u_{n-1}} = \sum_{p \in \mathcal{N}} \mathcal{V}_p, \qquad \mathcal{V}_p = \begin{cases} \{\mu_p x \,:\, x \in \mathbb{R}^d\}, & \text{if } p \in \mathcal{N} \setminus \widetilde{\mathcal{N}}^F \\ \{\lambda_p x \,:\, x \in T_p \tilde{\gamma}\}, & \text{if } p \in \widetilde{\mathcal{N}}^F \end{cases}$$

which induces a nonlinear block Gauß–Seidel method [50]. Enumerating the nodes $\mathcal{N} = \{p_1, \ldots, p_M\}$ in an arbitrary but fixed order, it minimizes $\mathcal{J}_{\mathcal{S}}$ successively in the individual subspaces $\mathcal{V}_{p_i}$ corresponding to the nodes $p_i \in \mathcal{N}$: Starting from an

initial iterate $v^\nu \in \mathcal{S}_0^{u_{n-1}}$ and setting $w_0 = v^\nu$, nodewise successive corrections in the local subspaces $\mathcal{V}_{p_i}$ yield the intermediate iterates

$$w_i = w_{i-1} + \operatorname*{arg\,min}_{\Delta w \in \mathcal{V}_{p_i}} \mathcal{J}_{\mathcal{S}}(w_{i-1} + \Delta w), \qquad i = 1, \dots, M. \tag{2.7.3}$$

Here, the nodewise correction $\Delta w \in \mathcal{V}_p$, $p \in \widetilde{\mathcal{N}}^F$, for given intermediate iterate w can be determined by minimizing the convex, nonsmooth local functional

$$\mathcal{J}_{\mathcal{S},p}(\Delta w) = \tfrac{1}{2} A_{pp} \Delta w \cdot \Delta w - r_p^T \cdot \Delta w + \phi_p(w_p + \Delta w, \alpha), \qquad p \in \widetilde{\mathcal{N}}^F$$

in a suitable subspace of $\mathbb{R}^d$ associated with the local tangent space $\mathcal{V}_p$, where A and b identify the matrix and vector representations of $a_n(\cdot,\cdot)$ and $\ell_{n,\mathcal{S}}(\cdot)$ with respect to (2.7.2) and $r_p = b_p - \sum_{q \in \mathcal{N}} A_{pq} w_q$ denotes the local residual. Eventually, the new iterate is obtained by $\bar{v} = w_M$. This iterative scheme converges globally albeit usually with rapidly deteriorating convergence rates if the system matrix originates from the discretization of a differential operator on increasingly fine grids [56].

First-order dominating model It turns out, that it suffices to determine the local corrections inexactly as long as they generate enough decent towards the unique minimizer of (2.7.1). This notion is captured by the theory of first-order dominating models [56] and has been applied in a setting with local rate-and-state nonlinearities [99]. Most concepts from the latter publication carry over to the present task.

The general idea behind this approach is to approximate the quadratic part of the functional $\mathcal{J}_{\mathcal{S},p}$, $p \in \widetilde{\mathcal{N}}^F$, while the local nonlinearity is evaluated exactly. For this purpose, denote with σ_p the largest eigenvalue of A_{pp} and introduce the model

$$\begin{aligned} \mathcal{I}_p(\Delta w) &= \tfrac{1}{2}\sigma_p \left|\Delta w\right|^2 - r_p^T \cdot \Delta w + \phi_p(w_p + \Delta w, \alpha) \\ &= \tfrac{1}{2}\sigma_p \left|w_p + \Delta w\right|^2 - \hat{r}_p^T \cdot (w_p + \Delta w) + \phi_p(w_p + \Delta w, \alpha) + \text{const.} \end{aligned}$$

where $\hat{r}_p = r_p + \sigma_p w_p$. As the subdifferential $\partial_\omega \phi_p(\omega, \alpha)$ is a one dimensional subspace in direction ω or zero, the unique minimizer of

$$\omega \mapsto \tfrac{1}{2}\sigma_p \left|\omega\right|^2 - \hat{r}_p^T \cdot \omega + \phi_p(\omega, \alpha)$$

is a multiple of $\hat{r}_p$. Thus, determining the minimizer of $\mathcal{I}_p$ comes down to solving a rotationally symmetric (hence one dimensional), scalar convex minimization problem in $\mathcal{V}_p$, which can be achieved with bisection.
For the linear d-dimensional problems in $\mathcal{V}_p$, $p \in \mathcal{N} \setminus \widetilde{\mathcal{N}}^F$, the quadratic part is approximated by the largest eigenvalue as well.

Note, that the model $\mathcal{I}_p$ is first-order accurate, i.e. it holds

$$\mathcal{J}_{\mathcal{S},p}(0) = \mathcal{I}_p(0) \text{ and } \partial \mathcal{J}_{\mathcal{S},p}(0) = \partial \mathcal{I}_p(0),$$

and dominates $\mathcal{J}_{\mathcal{S},p}$ in the sense $\mathcal{J}_{\mathcal{S},p} \leq \mathcal{I}_p$. Moreover, if Δw is a descent direction of $\mathcal{I}_p$, i.e. $\mathcal{I}_p(\Delta w) < \mathcal{I}_p(0)$, then also of $\mathcal{J}_{\mathcal{S},p}$, since it holds

$$\mathcal{J}_{\mathcal{S},p}(\Delta w) \leq \mathcal{I}_p(\Delta w) < \mathcal{I}_p(0) = \mathcal{J}_{\mathcal{S},p}(0).$$

Due to these properties, the first-order dominating model $\mathcal{I}_p$ produces sufficient decent such that an inexact block Gauß-Seidel smoother, that minimizes $\mathcal{I}_p$ instead of $\mathcal{J}_{\mathcal{S},p}$, still converges globally to the solution of problem (2.7.1), see [56].

Remark 2.7.1. When computing the largest eigenvalue σ_p of A_{pp}, $p \in \mathcal{N}$, numerically, one has to be careful not to generate false complex eigenvalues that may arise due to round-off errors. A formulation in $d = 2$ space dimensions for $A_{pp} = (a_{ij})_{i,j=1,2}$, that is robust in this regard, reads

$$\sigma_p = \tfrac{1}{2}(a_{11} + a_{22}) + \sqrt{\tfrac{1}{4}(a_{11} - a_{22})^2 + a_{12}\, a_{21}}.$$

Truncated linear correction

The fundamental idea behind TNNMG methods is to accelerate convergence of nonlinear Gauß–Seidel smoothing (2.7.3) by a suitable correction, that decreases energy efficiently and is essentially determined by a Newton-type search direction δv obtained from a linearized defect problem. Let us suppose that previous nonlinear smoothing yields the smoothed iterate $\bar{v} \in \mathcal{S}_0^{u_{n-1}}$. Then, the ensuing nonsmooth Newton step consists of determining a large subspace $\mathcal{W}(\bar{v}) \subset \mathcal{S}_0^{u_{n-1}}$, such that the functional $\mathcal{J}_{\mathcal{S}}|_{\bar{v}+\mathcal{W}(\bar{v})}$ is twice differentiable in a neighborhood of $\bar{v}$ and subsequently finding δv via

$$\mathcal{J}_{\mathcal{S}}''(\bar{v})|_{\mathcal{W}(\bar{v})\times\mathcal{W}(\bar{v})}\, \delta v = -\mathcal{J}_{\mathcal{S}}'(\bar{v})|_{\mathcal{W}(\bar{v})}, \tag{2.7.4}$$

where $\mathcal{J}_{\mathcal{S}}''(\bar{v})|_{\mathcal{W}(\bar{v})\times\mathcal{W}(\bar{v})}$ denotes the Hessian and $\mathcal{J}_{\mathcal{S}}'(\bar{v})|_{\mathcal{W}(\bar{v})}$ the gradient of $\mathcal{J}_{\mathcal{S}}$ restricted to the subspaces $\mathcal{W}(\bar{v}) \times \mathcal{W}(\bar{v})$ and $\mathcal{W}(\bar{v})$, respectively. These restrictions account for the nonsmoothness of the friction nonlinearity $\Phi_{\mathcal{S}}$.

In general, the locally nonsmooth components of $\Phi_{\mathcal{S}}$ are identified by the set of nodes

$$\mathcal{K}(\bar{v}) = \{p \in \widetilde{\mathcal{N}}^F \,:\, \partial\phi_p(\bar{v}_p, \alpha) \text{ is not single-valued or } \phi_p''(\bar{v}_p, \alpha) > C\}$$

with a large constant C. For the friction law (2.2.1) and its truncation according to (2.1.16), this set is given by $\mathcal{K}(\bar{v}) = \{p \in \widetilde{\mathcal{N}}^F \,:\, \left|[\bar{v}]_p\right| \leq V_{\alpha(p)}\}$. Then, the reduced subspace $\mathcal{W}(\bar{v}) \subset \mathcal{S}_0^{u_{n-1}}$ is chosen as

$$\mathcal{W}(\bar{v}) = \mathcal{V} + \operatorname{span}\{\lambda_p x \,:\, x \in T_p\tilde{\gamma},\, p \in \widetilde{\mathcal{N}}^F \backslash \mathcal{K}(\bar{v})\}.$$

Since the functional $\mathcal{J}_{\mathcal{S}}$ is strongly convex, the coefficient matrix $\mathcal{J}_{\mathcal{S}}''(\bar{v})|_{\mathcal{W}(\bar{v})\times\mathcal{W}(\bar{v})}$ in the linear problem (2.7.4) is symmetric and positive definite on the subspace $\mathcal{W}(\bar{v})$. Therefore, the correction δv can be approximated efficiently by one or few standard linear multigrid steps, that require only slight modifications to incorporate the basis from (2.7.2) and restrictions to $\mathcal{W}(\bar{v})$, see e.g. [55].

The overall method inherits the global convergence of nonlinear Gauß–Seidel smoothing (2.7.3) as long as the correction $\zeta\, \delta v$ does not increase energy with a suitably chosen damping factor $\zeta \in [0, \infty)$, i.e. it holds

$$\mathcal{J}_{\mathcal{S}}(\bar{v} + \zeta\, \delta v) \leq \mathcal{J}_{\mathcal{S}}(\bar{v}). \tag{2.7.5}$$

Remark 2.7.2. By replacing the standard multigrid prolongation operator P with $\tilde{P} = OB^{-1}P$ for the transition from the second finest to the finest level, coarser levels are discretized with respect to the standard basis $\{\lambda\}$. Thus, for all other transitions between levels, the standard multigrid prolongation operators can be used [118]. Note that the inverse of the transformation matrix B can be computed efficiently via

$$B^{-1} = \begin{pmatrix} I & 0 & 0 \\ 0 & I & 0 \\ 0 & -(D^{-1}M)^T & I \end{pmatrix}.$$

Line search

The last building block of the TNNMG iteration is a line search performed in $\mathcal{S}_0^{u_{n-1}}$ in direction δv in order to find an optimal damping factor $\zeta^* \in [0, \infty)$ in (2.7.5) and guarantee monotonicity as well as global convergence of the overall method. In this particular instance, the line search step consists of solving

$$\zeta^* = \operatorname*{argmin}_{\zeta \in [0,\infty)} \mathcal{J}_{\mathcal{S}}(\bar{v} + \zeta\, \delta v) \tag{2.7.6}$$

with bisection to determine ζ^*.

TNNMG iteration

Denoting with P, MG, and ζ the (inexact) solution operators corresponding to nonlinear Gauß–Seidel smoothing (2.7.3), the approximation of suitable Newton-type search directions via the linear problem (2.7.4) and a line search determining an optimal damping factor (2.7.6), one step of the TNNMG iteration applied to a given initial iterate $v^\nu \in \mathcal{S}_0^{u_{n-1}}$ reads:

$$\begin{aligned} \bar{v}_\nu &= P(v^\nu) && \text{(nonlinear smoothing)} \\ \delta v^\nu &= MG\left(\mathcal{J}_{\mathcal{S}}''(\bar{v}_\nu)|_{\mathcal{W}(\bar{v}_\nu)\times\mathcal{W}(\bar{v}_\nu)},\, \mathcal{J}_{\mathcal{S}}'(\bar{v}_\nu)|_{\mathcal{W}(\bar{v}_\nu)}\right) && \text{(linear correction)} \\ v^{\nu+1} &= \bar{v}_\nu + \zeta(\bar{v}_\nu, \delta v^\nu)\, \delta v^\nu && \text{(line search)} \end{aligned} \tag{2.7.7}$$

Global convergence of the TNNMG iteration follows from [56, Corollary 4.5] in conjunction with [56, Theorem 5.6 and Lemma 5.8] incorporating the inexact pre-smoothing operator P, that approximates the local functionals $\mathcal{J}_{\mathcal{S},p}$ by first-order dominating models, cf. [54].

Proposition 2.7.3. *For any initial iterate $v^0 \in \mathcal{S}_0^{u_{n-1}}$, the sequence of iterates $v^\nu \in \mathcal{S}_0^{u_{n-1}}$, $\nu = 1, \ldots$, generated by the TNNMG method* (2.7.7) *converges to the unique solution of the mortar-discretized rate problem* (2.6.5) *with given state $\alpha \in \mathcal{B}^F$.*

An identical proposition holds, if more than one nonlinear pre-smoothing step is used. Since nonlinear post-smoothing can be interpreted as additional pre-smoothing in the following TNNMG step, this statement also applies to TNNMG schemes using one or more post-smoothing steps.

Extension to fault opening The presented TNNMG variant can be extended to a setting that allows fault opening with straightforward modifications, see the respective literature with applications to obstacle problems, e.g. [55, 53, 118]. First, the nonlinear Gauß–Seidel smoother is augmented by an additional projection step enforcing admissibility of the intermediate iterates with respect to the obstacle. For obstacle problems, another advantage of TNNMG as compared to other established monotone multigrid methods, e.g. MMG, is, that coarse defect obstacles do not have to be constructed explicitly, when using a standard multigrid iteration for an inexact solution of the linear defect problem. In particular, the mortar matrix M only needs to be computed on the finest level and any coarse grid corrections are determined in canonical coordinates without obstacles, i.e. the standard transfer operators can be utilized. Thus, it is significantly easier to implement than other nonlinear multigrid methods such as MMG, while at the same time displaying similar or better convergence rates [118]. Since such a correction step does not take obstacles and thus the domain of the functional into account sufficiently, its result δv^ν may violate the non-penetration constraints. Therefore, yet another projection is applied to guarantee admissibility of the coarse correction δv^ν with respect to the obstacle.

A key component of this solution approach is the robust and efficient (inexact) solution of the linear problem (2.7.4). As was noted, this can be achieved, e.g., with a standard multigrid iteration. However, the scaling properties and performance of this linear solver for problems involving multiscale fault geometries, that are typical for geological fault networks, are not clear at this point. Thus, the next chapter focuses on the efficient numerical solution of structurally similar problems, i.e. an elliptic model problem with linear jumps across interfaces, featuring spatially multiscale interface networks with characteristics of geological fault networks.

3 Numerical homogenization of multiscale interface problems

In nature, there is an entire continuum of spatial scales ranging from grains (micro) over rocks (meso) all the way up to tectonic plates (macro) that interacts in geophysical fault networks. Their interplay gives rise to complex dynamics in earth's lithosphere and is the source of earthquakes (see, e.g., [115] and the literature cited therein).

Insights from experiments and geophysical (analogue) modeling suggest that grain sizes in fractured rock [93, 126] as well as fragmentation due to tectonic deformation [116] are distributed in a fractal sense, i.e. grain sizes and interfaces adhere to an exponential law. Sammis et al. [116] proposed a model of fragmentation in tectonic deformation, wherein the breakage of entities due to deformation is caused by the interaction of adjacent blocks of similar size. This assumption results in a Cantor-type geometry [93, 126]. A prototypical geometry used both in the mathematical [61] as well as geoscientific [126] communities is a Cantor set, whose finite-scale approximations are depicted in Figure 3.1.

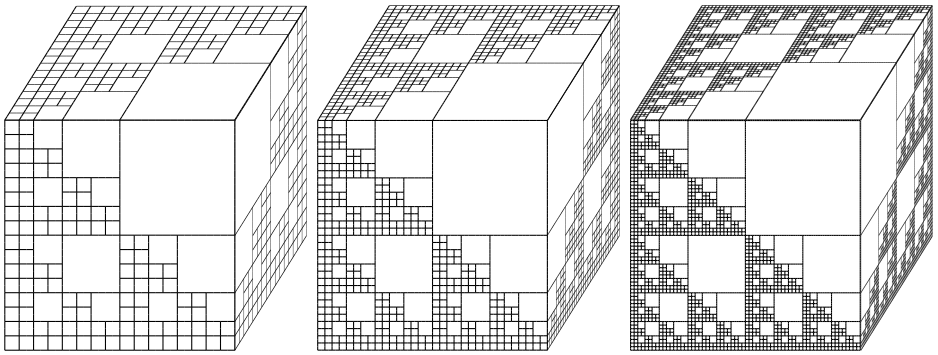

Figure 3.1: Finite-scale, Cantor-type interface networks $\Gamma^{(K)}$ from [126] in $d = 3$ space dimensions with $K = 4, 5, 6$ and increasing resolution from left to right.

As motivated in Section 2.1, mathematical modeling of stress accumulation and release in geological fault networks involves continuum mechanical descriptions of deformations, non-penetration and frictional contact along the faults. Although the considered layered fault system involves multiple spatial scales, it does not exhibit the full range of spatial scales characteristic for multiscale fault networks. This chapter focuses on the spatial multiscale aspects and the challenges presented by the fractal geometry of fault networks. It aims at a thorough and detailed understanding of a class of scalar, elliptic fractal interface problems augmented by linear jumps across interfaces and the construction of robust, efficient and scale-independent algebraic

solvers. Such problems have recently been suggested and analyzed by Heida et al. [61]. Note that they are structurally similar to the linear problems appearing in the correction step of the TNNMG method (2.7.4). Much of the content and ideas presented hereafter has previously appeared in [61] and [78].

Let us consider a simple domain $\Omega \subset \mathbb{R}^d$, $d > 1$, containing individual faults Γ_l that can be ordered from "strong" to "weak", i.e. discontinuities of displacements across Γ_l decrease for increasing l. The intuition is that "more fractured" media exhibit a higher resistance to fragmentation [48, 94]. Then, the level-K interface network $\Gamma^{(K)} = \bigcup_{l=1}^{K} \Gamma_l$ consists of all faults Γ_l up to resolution K. Each level-K interface network $\Gamma^{(K)}$ splits the domain Ω into a finite number of cells representing geological grains, rocks, and plates for example. The completion of piecewise smooth functions in $\Omega \backslash \Gamma^{(K)}$ defines a Hilbert space $\mathcal{H}_K$ with respect to a scalar product involving the broken H^1-seminorm and weighted L^2-norms of jumps across the Γ_l, $1 \leq l \leq K$. The weights of the individual interfaces introduce an exponential scaling of the resistance to jumps across Γ_l. The limit $K \to \infty$ of the level-K interface networks $\Gamma^{(K)}$ is the fractal interface network Γ. In turn, the fractal function space $\mathcal{H}$ on the limiting fractal geometry Γ is given by completion of $\bigcup_{K=1}^{\infty} \mathcal{H}_K$. Then, a class of self-adjoint elliptic variational problems in $\mathcal{H}$ and their level-K approximations on $\mathcal{H}_K$ are considered. Note that the spatial scales are not separable or periodic due to the fractal nature of the geometry. Moreover, the multiscale character of fractal interface problems exceeds the usual lack of smoothness commonly present in multiscale problems, because the solution space $\mathcal{H}$ depends on the fractal geometry which is not accessible by a fixed classical finite element space.

Usually, the field of classical homogenization is a premier candidate for studying computationally feasible, effective mathematical descriptions of multiscale phenomena. Originally developed for elliptic problems with oscillating [2, 3] and random coefficients [68, 137], homogenization theory has become widely popular and applied in an astonishing variety of scenarios including multiscale materials [57, 84], biological materials like lung tissue [6], or polycrystallines [40]. Historically, numerical homogenization mimics paradigms introduced in classical homogenization to derive multiscale discretizations and algebraic solution methods that are robust with respect to the inherent lack of smoothness of multiscale problems. As a global discretization of all scales is computationally unfeasible, the multiscale problem is typically decomposed into a global problem associated with a finite element grid and local auxiliary subproblems. The specific setup of global and local problems characterizes the individual methods. A basic idea, that has been pursued for more than two decades, is to consider multiscale discretizations with approximating ansatz spaces having all relevant fine scale features of a given problem built-in. It gave rise to variational multiscale methods [67], heterogeneous multiscale methods [1, 44], and multiscale finite elements [45]. However, these homogenization strategies usually inherit the necessity of scale separation and periodicity of fine scale behavior from the classical setting. Recall that fractal interface problems possess neither, thus requiring another approach.
With their publication on localized orthogonal decomposition (LOD) [89], Målqvist and Peterseim accomplished a breakthrough in the mathematical understanding of multiscale finite element methods for self-adjoint elliptic problems with oscillating

coefficients. Based on a projection $\Pi : \mathcal{H} \to \mathcal{S}_h$ mapping the solution space $\mathcal{H}$ onto a given finite element space $\mathcal{S}_h \subset \mathcal{H} \subset L^2$ with mesh size parameter h that satisfies stability and approximation properties of the form

$$\|\Pi v\|_{\mathcal{H}} \leq c \|v\|_{\mathcal{H}}, \qquad \|v - \Pi v\|_{L^2} \leq Ch \|v\|_{\mathcal{H}} \qquad \forall v \in \mathcal{H}, \tag{3.0.1}$$

they introduced the space $\mathcal{W}$ as the a-orthogonal complement of the kernel of Π, i.e. the orthogonal complement with respect to the energy scalar product. Interestingly, $\mathcal{W}$ has the same dimension as $\mathcal{S}_h$ and provides approximations with optimal accuracy without requiring any assumptions on scale separation or periodicity. This is the outstanding feature compared to other established methods. In general, the a-orthogonalized nodal basis of $\mathcal{W}$ has global support calling for a localization procedure to obtain a feasible method. The localized basis functions are computed as approximate solutions of local problems posed in a much larger finite element space $\mathcal{S}$ that resolves all fine scale features of the given problem. In the original paper, these local fine scale problems are decoupled and possess a saddlepoint structure, whereas a more recent, computationally more efficient variant [76] employs subspace correction arguments using a simple local smoother on moderately growing patches.

Instead of deriving low dimensional ansatz spaces with built-in fine scale features in the spirit of multiscale discretization methods, one could discretize the solution space $\mathcal{H}$ directly using a large finite element space $\mathcal{S}$ resolving all relevant scales and come up with suitable iterative methods, that converge independently of discretization parameters, e.g. the mesh size of the underlying grid, and of the regularity of the continuous solution. A first major breakthrough was the advent of multigrid methods in the 1970s and 1980s (see the monograph by Hackbusch [58] and the literature cited therein), that combine discretizations on different grids in an iterative scheme and possess optimal complexity, i.e. computational effort scales linearly with the number of unknowns, in contrast to previously state-of-the-art SOR methods [135]. However, classical convergence proofs [19] relied on regularity properties of the continuous solutions seldomly fulfilled in practice. In an effort to eliminate these and other assumptions, e.g. quasi-uniformity of triangulations, in the established multigrid theory, the 1980s also saw the introduction of hierarchical basis [8] and domain decomposition methods [42, 41]. These developments culminated in widely noticed and acclaimed overview contributions by Xu [134] and Yserentant [136] founding the unifying framework of iterative subspace correction. Its central paradigm is to reduce the remaining error by targeting its different frequencies on a set of fully decoupled local subproblems posed in suitably chosen subspaces in each iteration step. Here, projection operators with properties as described in (3.0.1) play an important role in their convergence analysis, see e.g. [79]. Recently, results from classical subspace correction theory have been reinterpreted in a typical multiscale setting with oscillating coefficients by Kornhuber and Yserentant [80].

Both the iterative approach to numerical homogenization based on subspace correction [80] and LOD [89] rely on the existence of suitable projection operators with approximation and stability properties as sketched in (3.0.1) for the construction of the respective local subproblems. A conceptual difference is, that these projections are merely an analytical tool for convergence proofs of the former, while they

actually have to be implemented for the latter. In practice, iterative numerical homogenization is preferable, if the considered problem only has to be solved once or very few times, since LOD requires the solution of local problems with saddlepoint structure and because assembling the algebraic representation of the multiscale basis is computationally rather expensive. The LOD variant is advantageous, if a problem has to be solved for many right hand sides, i.e. the multiscale basis only has to be assembled once and can be reused. A more detailed comparison of the aforementioned approaches is discussed in [77].

The main contribution of this chapter is the explicit construction and analysis of projections $\Pi_{\mathcal{H}_K} : \mathcal{H} \to \mathcal{H}_K$, $\Pi_{\mathcal{S}_k} : \mathcal{H} \to \mathcal{S}_k$ and their composition $\Pi_{k,K} = \Pi_{\mathcal{S}_k} \circ \Pi_{\mathcal{H}_K}$, $K \geq k$, to approximating K-scale spaces $\mathcal{H}_K$ and finite element spaces $\mathcal{S}_k \subset \mathcal{H}_K$, respectively, that all possess the desired properties (3.0.1), relying on local Poincaré inequalities and a trace lemma following standard ideas published by Carstensen [22] and Verfürth [129]. For standard Sobolev and finite element spaces, such projection operators are not only essential in the construction and analysis of multiscale finite element and subspace correction methods as mentioned above, but also in finite element convergence theory and a posteriori error analysis [20, 22, 29, 95, 129]. Compared to the established theory, this endeavor is complicated by the presence of jump terms. Since counterexamples show that local averages cannot be bounded by jumps of the original functions, strong assumptions on the locality of Γ will be necessary.
The projection $\Pi_{\mathcal{H}_K}$ truncates all but the first K scales based on a best-approximation on the individual cells generated by the partition $\Omega \backslash \Gamma^{(K)}$. Its stability and approximation properties follow with general results from functional analysis. On the other hand, $\Pi_{\mathcal{S}_k}$ projects onto finite element spaces relying on Clément-type local averaging. One major advantage is that it can be implemented efficiently. Their composition $\Pi_{k,K}$, e.g., allows to decompose discretization error estimates into a part corresponding to the truncation of all but the first K scales in abstract function spaces and another part associated with the spatial discretization using finite elements. This observation suggests the utilization of $\Pi_{k,K}$ in the context of LOD-type multiscale discretizations such as [89], where the suitability of $\Pi_{\mathcal{S}_k}$ for efficient implementation is an important factor for the actual construction of multiscale bases. If projections with the aforementioned properties are only an analytic tool, e.g. in the convergence proofs of iterative subspace correction methods, one can omit the cell-based detour via $\mathcal{H}_K$ and use $\Pi_{\mathcal{S}_k}$ directly. Altogether, these different variants represent somewhat flexible building blocks that can be adapted to the demands imposed by the numerical approach.

Thereafter, the projection $\Pi_{k,K}$ with $K = k$ is applied in the construction and analysis of a LOD-type multiscale discretization with optimal a priori discretization error estimates in the spirit of [76, 89], see [78]. This approach is not suited for an efficient solution of the linear problem (2.7.4) in the correction step of the TNNMG method, since the underlying rate energy functional generally differs for individual time steps wasting the reusability of the multiscale basis, and is thus to be understood as a brief proof of concept. Finally, mesh- and scale-independent convergence of various subspace correction methods, that feature cell- and patch-based preconditioners, will be shown with $\Pi_{\mathcal{S}_k}$ following [80] and building on arguments going back to Xu [134]

and Yserentant [136]. This chapter is concluded by numerical experiments with increasingly complex fractal interface networks less and less covered by theory, that illustrate the theoretical results obtained for iterative subspace correction methods and the applicability of the approach beyond their limits.

3.1 Multiscale interface problems

Following [61, 78], this section introduces a sequence of faults $(\Gamma_l)_{l\in\mathbb{N}}$, the limiting fractal interface network $\Gamma = \bigcup_{l=1}^{\infty} \Gamma_l$ and the associated fractal function space $\mathcal{H}$ as well as their K-scale approximations $\Gamma^{(K)} \subset \Gamma$ and $\mathcal{H}_K \subset \mathcal{H}$, $K \in \mathbb{N}$. With assumptions on the shape regularity and fractal character of the fractal interface network, fractal interface problems in $\mathcal{H}$ and $\mathcal{H}_K$will be considered. The last objective is to state K-scale approximations in piecewise linear finite element spaces $\mathcal{S}_K \subset \mathcal{H}_K$ containing jumps across the interfaces Γ_l, $1 \leq l \leq K$.

3.1.1 Multiscale interface networks

Let $\Omega \subset \mathbb{R}^d$ be a bounded, convex domain with Lipschitz boundary $\partial\Omega$, that contains a sequence of mutually disjoint interfaces $\Gamma_l \subset \Omega$, $l \in \mathbb{N}$. Each interface Γ_l is assumed to be piecewise affine and possess a finite $(d-1)$-dimensional Hausdorff measure almost everywhere. The fractal interface network Γ and its finite scale approximations $\Gamma^{(K)}$ are given by

$$\Gamma = \bigcup_{l=1}^{\infty} \Gamma_l, \qquad \Gamma^{(K)} = \bigcup_{l=1}^{K} \Gamma_l, \quad K \in \mathbb{N},$$

respectively. Observe that Γ has Lebesgue measure $\mu_d(\Gamma) = 0$ as it is a countable union of interfaces satisfying $\mu_d(\Gamma_k) = 0$. However, its fractal- (and Hausdorff-) dimension may be larger than $d-1$. For each $K \in \mathbb{N}$, the K-scale interface network splits the domain Ω into mutually disjoint, open, simply connected cells $G \in \mathcal{G}^{(K)}$

$$\Omega \backslash \Gamma^{(K)} = \bigcup_{G\in\mathcal{G}^{(K)}} G$$

satisfying $\partial G = \partial\overline{G}$, i.e. the cells do not admit slits. For notational convenience, set $\mathcal{G}^{(0)} = \{\Omega\}$. Moreover, the cells $G \in \mathcal{G}^{(K)}$ are assumed to be star-shaped in the sense that for each $G \in \mathcal{G}^{(K)}$ there is a center $p_G \in G$ and a continuous function $\vartheta_G : S^{d-1} \to \mathbb{R}_{\geq 0}$ on the unit sphere S^{d-1} in $\mathbb{R}^d$, where $\mathbb{R}_{\geq 0} = \{x \in \mathbb{R} \ : \ x \geq 0\}$, such that

$$G = \left\{ p_G + rs \ : \ s \in S^{d-1},\, 0 \leq r < \vartheta_G(s) \right\}. \tag{3.1.1}$$

Denoting with

$$R_G = \max_{s\in S^{d-1}} \vartheta_G(s), \quad r_G = \min_{s\in S^{d-1}} \vartheta_G(s) \tag{3.1.2}$$

the radii of the smallest ball containing G and the largest ball inside G, respectively, we define the shape regularity $\rho_G = \frac{R_G}{r_G} \geq 1$ of G. All cells $G \in \mathcal{G}^{(K)}$ are assumed to be shape regular in the sense that

$$\rho_G \leq \rho \qquad \forall G \in \mathcal{G}^{(K)} \quad \forall K \in \mathbb{N}$$

holds with a constant $\rho \geq 1$.

Next, let us introduce important quantities characterizing the geometry in the upcoming analysis. With the set of invariant cells on level $K \in \mathbb{N}$

$$\mathcal{G}_\infty^{(K)} = \left\{ G \in \mathcal{G}^{(K)} \,:\, G \in \mathcal{G}^{(L)} \,\forall L > K \right\},$$

i.e. cells $G \in \mathcal{G}^{(K)}$, that will not be split by any $\Gamma^{(L)}$, $L > K$, define the maximal size

$$d_K = \max \left\{ 2R_G \,:\, G \in \mathcal{G}^{(K)} \backslash \mathcal{G}_\infty^{(K)} \right\}$$

of cells $G \in \mathcal{G}^{(K)}$ to be divided on higher levels. Assume that the sequence of interfaces $(\Gamma_l)_{l\in\mathbb{N}}$ splits smaller and smaller cells for increasing l, i.e. it holds

$$d_K \to 0 \quad \text{for} \quad K \to \infty. \tag{3.1.3}$$

Let the cardinality of any set M be denoted by $|M| \in \mathbb{N} \cup \{\infty\}$ and the open line segment by

$$(x, y) = \{x + t(y - x) \,:\, t \in (0, 1)\},$$

for any $x, y \in \mathbb{R}^d$. Furthermore, assume that for all fixed $k, l \in \mathbb{N} \cup \{0\}$ with $k < l$, there is a constant $C_{k,l} \geq 0$, such that

$$|(x, y) \cap G \cap \Gamma_l| \leq C_{k,l} \quad \forall G \in \mathcal{G}^{(k)} \tag{3.1.4}$$

holds for almost all $x, y \in \Omega$. Finally, set $C_l = C_{0,l}$ and

$$r_k = \sup_{l>k} \frac{C_{k,l}}{C_{0,l}}, \quad k \in \mathbb{N} \tag{3.1.5}$$

and assume that the interface network $\Gamma^{(K)}$ is self-similar in the sense that

$$r_K C_K \leq C_0 \qquad \forall K \in \mathbb{N} \tag{3.1.6}$$

is bounded by a constant C_0.

To fix ideas and illustrate this notion of multiscale interface networks, consider the following highly localized example adhering to the previous setting.

Example 3.1.1 (Interface network in 2D)**.** In the spirit of [61, 126], let us construct a Cantor-type albeit more local interface network. Consider the unit square $\Omega = (0, 1)^2 \subset \mathbb{R}^2$ with canonical basis $\{e_1, e_2\}$ in $\mathbb{R}^2$ and construct the sequence of interfaces $(\Gamma_k)_{k\in\mathbb{N}}$ inductively as follows. Set

$$\Gamma^{(1)} = \Gamma_1 = \{\tfrac{1}{4}e_1 + (0, e_2)\} \cup \{\tfrac{1}{4}e_2 + (0, e_1)\} \cup \{\tfrac{1}{2}e_1 + (0, \tfrac{1}{4}e_2)\} \cup \{\tfrac{1}{2}e_2 + (0, \tfrac{1}{4}e_1)\}.$$

and, for given $\Gamma^{(k)}$, $k \geq 1$, define

$$\tilde{\Gamma}_{k+1} = \Gamma^{(k)} \cup \{e_1 + \Gamma^{(k)}\} \cup \{e_2 + \Gamma^{(k)}\}$$

as well as $\Gamma_{k+1} = \frac{1}{4}\tilde{\Gamma}_{k+1} \backslash \Gamma^{(k)}$. See Figure 3.3 for an illustration. The resulting limit network Γ is self-similar by construction and an extension to $d = 3$ is straightforward. The associated geometric quantities are given by $d_k = \sqrt{2}\, 4^{-k}$, $C_{k,l} = 2^{l-k+1}$, and $C_k = 2^{k+1}$, $k \geq 1$. Thus, it holds $r_k = 2^{-k}$ and $C_0 = 2$ in (3.1.6).

3.1.2 Fractal function spaces

Ultimately, the goal of this section is to formulate a scalar elliptic model problem on the fractal geometry $\Omega\backslash\Gamma$, whose solution allows for jumps across the fractal interface network Γ. However, the fractal nature of the geometry constitutes a challenging setting for which suitable mathematical notions and a meaningful formalism have to be developed. Natural questions that arise are:

- What is a suitable solution space?
- Do basic notions like weak gradients or jumps across interfaces exist?

To answer these questions and work towards the stated goals, we follow a strategy that is very common in (functional) analysis, the construction of complete metric spaces and Banach spaces in particular. Rather than working with the complete but complicated space, one characterizes it by (equivalence classes of) approximating sequences in a dense subspace. Usually, this subspace is chosen such that it is more accessible with established mathematical tools. Then, concepts developed for approximating sequences carry over to the complete space by density. There is a plethora of instances for this approach including the introduction of $\mathbb{R}$ as the completion of rational numbers or the construction of Sobolev spaces.

For each fixed $K \in \mathbb{N}$, consider the space of piecewise smooth functions

$$\mathcal{C}^1_{K,0} := \left\{ v : \overline{\Omega}\backslash\Gamma^{(K)} \to \mathbb{R} \,:\, v|_G \in C^1(\overline{G}) \quad \forall G \in \mathcal{G}^{(K)} \text{ and } v|_{\partial\Omega} \equiv 0 \right\}.$$

on $\Omega\backslash\Gamma^{(K)}$, that vanish on the boundary $\partial\Omega$. As Γ_l is piecewise affine, $l = 1, \dots, K$, there is a normal ν_ξ to Γ_l at almost all $\xi \in \Gamma_l$. We fix its orientation such that $\nu_\xi \cdot e_m > 0$ with $m = \min\{i = 1, \dots, d \,:\, \nu_\xi \cdot e_i \neq 0\}$ and $\{e_1, \dots, e_d\}$ denoting the canonical basis of $\mathbb{R}^d$. For every $\xi \in \Gamma_l$ for which there is a normal ν_ξ and any $x \neq y \in \mathbb{R}^d$ such that $(y - x) \cdot \nu_\xi \neq 0$, the jump of $v \in \mathcal{C}^1_{K,0}$ across Γ_l at ξ in the direction $y - x$ is defined by

$$[\![v]\!]_{x,y}(\xi) = \lim_{s \downarrow 0} \left(v\left(\xi + s(y - x)\right) - v\left(\xi - s(y - x)\right) \right).$$

Moreover, since $v \in \mathcal{C}^1_{K,0}$ is continuous on both sides of the interface Γ_l, $[\![v]\!]_{x,y}(\xi)$ is equal to the normal jump of $v \in \mathcal{C}^1_{K,0}$ at $\xi \in \Gamma_l$

$$[\![v]\!](\xi) = [\![v]\!]_{\xi - \nu_\xi, \xi + \nu_\xi}(\xi)$$

up to the sign.

For some fixed material constant $\mathfrak{c} > 0$ and the geometrical constants C_l, $l \in \mathbb{N}$, taken from (3.1.4), let us introduce a scalar product on $\mathcal{C}^1_{K,0}$

$$\langle v,\, w \rangle_K = \int_{\Omega\backslash\Gamma^{(K)}} \nabla v \cdot \nabla w \, dx + \sum_{l=1}^{K} (1 + \mathfrak{c})^l \, C_l \int_{\Gamma_l} [\![v]\!]\, [\![w]\!] \; d\Gamma_l, \quad v, w \in \mathcal{C}^1_{K,0}$$

and the associated norm $\|v\|_K = \langle v,\, v \rangle_K^{1/2}$, that scales the jumps across Γ_l with the exponential factor $(1 + \mathfrak{c})^l$, $l \leq K$. Thus, the material constant $\mathfrak{c}$ determines the growth of resistance to jumps with increasing fracturing.

Classical completion of $\mathcal{C}^1_{K,0}$ with respect to $\|\cdot\|_K$ results in a hierarchy of K-scale Hilbert spaces

$$\mathcal{H}_1 \subset \cdots \subset \mathcal{H}_{K-1} \subset \mathcal{H}_K, \qquad K \in \mathbb{N},$$

with scalar products $\langle \cdot,\ \cdot \rangle_K$, dense subspaces $\mathcal{C}^1_{K,0} \subset \mathcal{H}_K$ and isometric embeddings. For fixed $K \in \mathbb{N}$, the Hilbert space $\mathcal{H}_K$ is topologically equivalent to a broken Sobolev space $H^1(\Omega, \mathcal{G}^{(K)})$ supplied with the standard broken Sobolev norm.

Then, a limiting fractal Hilbert space $\mathcal{H}$ with scalar product

$$\langle v,\, w\rangle = \int_{\Omega\backslash\Gamma} \nabla v \cdot \nabla w \, dx + \sum_{l=1}^{\infty} (1+\mathfrak{c})^l \, C_l \int_{\Gamma_l} [\![v]\!]\, [\![w]\!] \; d\Gamma_l, \quad v, w \in \mathcal{H} \tag{3.1.7}$$

and associated norm $\|v\|_{\mathcal{H}} = \langle v,\, v\rangle^{1/2}$ is obtained by completion of $\bigcup_{K\in\mathbb{N}} .\mathcal{H}_K$. For details, the interested reader is referred to [61]. Hereafter, essential properties of the space $\mathcal{H}$, that were derived in the same publication, will be summarized for later use.

Due to the construction of $\mathcal{H}$, the smooth subspaces $(\mathcal{C}^1_{K,0})_{K\in\mathbb{N}}$ and thus the finite-scale spaces $(\mathcal{H}_K)_{K\in\mathbb{N}}$ are dense in $\mathcal{H}$, i.e. for any $v, w \in \mathcal{H}$ there are sequences $(v_K)_{K\in\mathbb{N}}, (w_K)_{K\in\mathbb{N}} \subset (\mathcal{C}^1_{K,0})_{K\in\mathbb{N}}$ satisfying $v_K, w_K \in \mathcal{C}^1_{K,0}$ for all $K \in \mathbb{N}$, such that

$$\|v - v_K\|_{\mathcal{H}} \to 0, \qquad \langle v_K,\, w_K\rangle_K \to \langle v,\, w\rangle \quad \text{for } K \to \infty. \tag{3.1.8}$$

Note that the space $L^2(\Omega\backslash\Gamma)$ implicitly appearing in (3.1.7) is well-defined, since $\Omega\backslash\Gamma$ is Lebesgue measurable according to

$$\Omega\backslash\Gamma = \Omega \cap \big(\textstyle\bigcup_{l=1}^{\infty} \Gamma_l\big)^{\complement} \subset \Omega\backslash\Gamma^{(K)}.$$

Moreover, to really understand (3.1.7), notions of generalized jumps and gradients need to be defined. For this purpose, let us introduce the sequence space $(L^2(\Gamma_l))_{l\in\mathbb{N}}$ equipped with the weighted norm

$$\|z\|^2_{\Gamma} = \sum_{l=1}^{\infty} (1+\mathfrak{c})^l C_l \, \|z_l\|^2_{0,\Gamma_l}, \quad z = (z_l)_{l\in\mathbb{N}} \in (L^2(\Gamma_l))_{l\in\mathbb{N}},$$

where $\|\cdot\|_{0,\Gamma_l}$ denotes the usual norm in $L^2(\Gamma_l)$. Then, for each $v \in \mathcal{H}$ and each sequence $(v_K)_{K\in\mathbb{N}}$ with $v_K \in \mathcal{H}_K$, the limits

$$\nabla v = \lim_{K\to\infty} \nabla v_K \quad \text{in } L^2(\Omega\backslash\Gamma) \quad \text{and} \quad [\![v]\!] = \lim_{K\to\infty} [\![v_K]\!] \quad \text{in } (L^2(\Gamma_K))_{K\in\mathbb{N}}$$

exist and are called weak gradient ∇v and generalized jump $[\![v]\!]$ of v, respectively. Additionally, for all $v \in \mathcal{H}$, there holds a Green's formula

$$\int_{\Omega} v \nabla\cdot\varphi \, dx = -\int_{\Omega\backslash\Gamma} \nabla v \cdot \varphi \, dx + \sum_{l=1}^{\infty} \int_{\Gamma_l} [\![v]\!]\, \varphi \cdot \nu_l \, d\Gamma_l \qquad \forall \varphi \in C^{\infty}_0(\mathbb{R}^d)^d$$

and a global Poincaré-type inequality

$$\|v\|^2_0 \le c \left(|v|^2_{1,\Omega\backslash\Gamma} + \sum_{l=1}^{\infty} (1+\mathfrak{c})^l \, C_l \, \|[\![v]\!]\|^2_{0,\Gamma_l} \right) \tag{3.1.9}$$

where $\|\cdot\|_0^2$ denotes the standard $L^2(\Omega)$ norm, $\|\cdot\|_{0,M}^2$ the standard $L^2(M)$ norm and $|v|_{1,M\setminus\Gamma} = \| \, |\nabla v| \, \|_{0,M\setminus\Gamma}$ for suitable sets $M \subseteq \Omega$; the constant c is bounded in terms of $(1+\frac{1}{\mathfrak{c}})\mathrm{diam}(\Omega)$. Lastly, there is a continuous embedding of the fractal space $\mathcal{H}$ into the Sobolev-Slobodeckij spaces $H^s(\Omega)$ (see, e.g. [121]), i.e. $\mathcal{H} \subset H^s(\Omega)$ with $s \in [0, \frac{1}{2})$. Therefore, the fractal space $\mathcal{H}$ can be identified with a subspace of $\bigcap_{s\in[0,\frac{1}{2})} H^s(\Omega)$, see [61].

3.1.3 Fractal interface problems

Consider the fractal interface problem

$$u \in \mathcal{H}: \qquad a(u,v) = (f,v) \qquad \forall v \in \mathcal{H} \tag{3.1.10}$$

with $f \in L^2(\Omega)$, the standard scalar product $(\,\cdot\,,\,\cdot\,)$ in $L^2(\Omega)$, and the bilinear form

$$a(v,w) = \int_{\Omega\setminus\Gamma} A\nabla v \cdot \nabla w \, dx + \sum_{l=1}^{\infty} (1+\mathfrak{c})^l \, C_l \int_{\Gamma_l} B \, [\![v]\!] \, [\![w]\!] \, d\Gamma_l, \quad v,w \in \mathcal{H} \tag{3.1.11}$$

for given functions $A : \Omega\setminus\Gamma \to \mathbb{R}^{d\times d}$ and $B : \Gamma = \bigcup_{l=1}^{\infty} \Gamma_l \to \mathbb{R}$. Furthermore, assume that $A(x) \in \mathbb{R}^{d\times d}$ is symmetric for all $x \in \Omega\setminus\Gamma$ and satisfies the properties

$$\alpha_0 \, |\xi|^2 \le A(x)\xi \cdot \xi, \quad |A(x)\xi \cdot \eta| \le \alpha_1 \, |\xi| \, |\eta| \quad \forall \xi,\eta \in \mathbb{R}^d \quad \forall x \in \Omega\setminus\Gamma, \tag{3.1.12}$$

where $|\cdot|$ denotes the Euclidean norm, with positive constants $\alpha_0, \alpha_1 \in \mathbb{R}$. The function B is assumed to fulfill

$$0 < \beta_0 \le B(x) \le \beta_1 \qquad \forall x \in \Gamma \tag{3.1.13}$$

with constants $\beta_0, \beta_1 \in \mathbb{R}$. By (3.1.12) and (3.1.13), the bilinear form $a(\cdot,\cdot)$ is symmetric and elliptic in the sense that

$$\mathfrak{a} \, \|v\|_{\mathcal{H}}^2 \le a(v,v), \qquad |a(v,w)| \le \mathfrak{A} \, \|v\|_{\mathcal{H}} \, \|w\|_{\mathcal{H}} \qquad \forall v,w \in \mathcal{H} \tag{3.1.14}$$

holds with $\mathfrak{a} = \min\{\alpha_0, \beta_0\}$ and $\mathfrak{A} = \min\{\alpha_1, \beta_1\}$. Hence, $a(\cdot,\cdot)$ is a scalar product on $\mathcal{H}$ and the associated energy norm $\|\cdot\| = a(\cdot,\cdot)^{1/2}$ is equivalent to $\|\cdot\|_{\mathcal{H}}$.

Due to the continuous embedding (3.1.9) of $\mathcal{H}$ into $L^2(\Omega)$, it holds $(f,\cdot) \in \mathcal{H}^{-1}$, where $\mathcal{H}^{-1}$ denotes the dual space of $\mathcal{H}$, and the Lax-Milgram lemma implies well-posedness of (3.1.10).

Proposition 3.1.2. *The fractal interface problem* (3.1.10) *admits a unique solution* $u \in \mathcal{H}$ *satisfying the stability estimate*

$$\|u\|_{\mathcal{H}} \le \tfrac{1}{\mathfrak{a}} \, c^{\frac{1}{2}} \, \|f\|_0 \tag{3.1.15}$$

with the constant c *from* (3.1.9).

Proof. Using (3.1.14), the Cauchy-Schwarz inequality and the embedding of $\mathcal{H}$ into $L^2(\Omega)$ by (3.1.9) implies

$$\|u\|_{\mathcal{H}}^2 \le \tfrac{1}{\mathfrak{a}} a(u,u) = \tfrac{1}{\mathfrak{a}}(f,u) \le \tfrac{1}{\mathfrak{a}} \, \|f\|_0 \, \|u\|_0 \le \tfrac{1}{\mathfrak{a}} \, c^{\frac{1}{2}} \, \|f\|_0 \, \|u\|_{\mathcal{H}}$$

for the unique solution $u \in \mathcal{H}$ of (3.1.10). □

Remark 3.1.3. In order to model highly heterogeneous media, A may be chosen to oscillate rapidly in space. The numerical methods that will be introduced to approximate the solution are robust with respect to this behavior [76, 80].

3.1.4 Finite scale discretization

Following [78], the fractal space $\mathcal{H}$ is characterized by limiting properties of the finite scale spaces $\mathcal{H}_K$, $K \in \mathbb{N}$, by construction. Thus, it is natural to consider the approximating interface problems

$$u_{\mathcal{H}_K} \in \mathcal{H}_K : \qquad a(u_{\mathcal{H}_K}, v) = \ell(v) \qquad \forall v \in \mathcal{H}_K \tag{3.1.16}$$

on finite scales $K \in \mathbb{N}$. The finite scale bilinear form is given by

$$a(v,w) = a_K(v,w) = \int_{\Omega\setminus\Gamma^{(K)}} A\nabla v \cdot \nabla w \, dx + \sum_{l=1}^{K} (1+\mathfrak{c})^l \, C_l \int_{\Gamma_l} B \, [\![v]\!] \, [\![w]\!] \, d\Gamma_l$$

for $v, w \in \mathcal{H}_K$. Again, the Lax-Milgram lemma implies the well-posedness of (3.1.16) and a straightforward error estimate follows from Céa's lemma.

Proposition 3.1.4. *For each $K \in \mathbb{N}$, the finite scale interface problem* (3.1.16) *admits a unique solution $u_{\mathcal{H}_K} \in \mathcal{H}_K$ satisfying the error estimate*

$$\|u - u_{\mathcal{H}_K}\|_{\mathcal{H}} \leq \tfrac{\mathfrak{A}}{\mathfrak{a}} \inf_{v \in \mathcal{H}_K} \|u - v\|_{\mathcal{H}} \,. \tag{3.1.17}$$

Due to the density of $(\mathcal{H}_K)_{K\in\mathbb{N}}$ in $\mathcal{H}$ by (3.1.8), the above result implies convergence

$$\|u - u_{\mathcal{H}_K}\|_{\mathcal{H}} \to 0 \qquad \text{for } K \to \infty. \tag{3.1.18}$$

Remark 3.1.5. For $A(x) = I$ and cuboid cells $G \in \mathcal{G}^{(K)}$, $K \in \mathbb{N}$, that additionally satisfy quite restrictive conditions on the shape regularity, one can prove exponential error estimates of the form

$$\|u - u_{\mathcal{H}_K}\|_{\mathcal{H}} \leq c \, \|f\|_0 \, \tfrac{1}{\mathfrak{c}} (1+\mathfrak{c})^{-(K-1)}$$

with a constant c depending only on the space dimension d, the Poincaré-type constant in (3.1.9), and shape regularity [61, Theorem 4.2]. The fractal interface network from Example 3.1.1 fulfills these requirements.

Finite elements on finite scales

Let $\mathcal{T}^{(0)}$ be a regular partition of Ω into simplices with maximal diameter $h_0 > 0$ such that the intersection of two different simplices $T, T' \in \mathcal{T}^{(0)}$ is either a common n-simplex for some $n = 0, \ldots, d-1$ or empty. Denote the set of $d-1$ faces of $T \in \mathcal{T}^{(0)}$ by $\mathcal{E}^{(0)}$. The shape regularity $\sigma > 0$, i.e., the maximal ratio of the radii

of the smallest ball containing and largest ball inscribed in $T \in \mathcal{T}^{(0)}$, is preserved under uniform regular refinement [9, 16].

Furthermore, assume that the sequence of partitions resulting from successive uniform regular refinement of $\mathcal{T}^{(0)}$ resolves the interface network in the sense that for each fixed $K \in \mathbb{N}$ there is a partition $\mathcal{T}^{(K)}$, as obtained by a finite number of refinement steps, such that the interfaces Γ_l, $l = 1, \dots, K$, can be represented by faces of simplices $T \in \mathcal{T}^{(K)}$, i.e.

$$\Gamma^{(K)} = \bigcup_{E \in \mathcal{E}_\Gamma^{(K)} \subset \mathcal{E}^{(K)}} E \tag{3.1.19}$$

holds with a suitable subset $\mathcal{E}_\Gamma^{(K)}$ of the set $\mathcal{E}^{(K)}$ of faces of simplices $T \in \mathcal{T}^{(K)}$. In particular, this implies that for all $G \in \mathcal{G}^{(K)}$ the set $\mathcal{T}_G^{(K)} = \{T \in \mathcal{T}^{(K)} : T \subset \overline{G}\}$ is a local partition of G and that the maximal diameter h_K of $T \in \mathcal{T}^{(K)}$ is bounded by the maximal diameter $2d_K$ of $G \in \mathcal{G}^{(K)}$. We additionally assume that $\mathcal{G}^{(K)}$ is not overresolved by $\mathcal{T}^{(K)}$ meaning that there is a uniform bound of d_K by h_K, i.e., that

$$\delta d_K \leq h_K \leq 2d_K, \quad K \in \mathbb{N}, \tag{3.1.20}$$

holds with a constant $\delta > 0$ independent of $K \in \mathbb{N}$.

Next, let us introduce appropriate local and global finite element space. For this purpose, denote with $\mathcal{N}_G^{(K)}$ the set of vertices of $T \in \mathcal{T}_G^{(K)}$ that are not located on the boundary $\partial\Omega$. Consequently, each vertex located on an interface Γ_l with two (or more) adjacent cells $G, G' \in \mathcal{G}^{(K)}$, gives rise to two (or more) different nodes $p \in \mathcal{N}_G^{(K)}$ and $p' \in \mathcal{N}_{G'}^{(K)}$. For each $G \in \mathcal{G}^{(K)}$, define the cell based finite element space $\mathcal{S}_K(G)$ of piecewise affine functions with respect to $\mathcal{T}_G^{(K)}$ that are vanishing on $\partial G \cap \partial\Omega$. The space $\mathcal{S}_K(G)$ is spanned by the standard nodal basis functions $\lambda_p^{(K)}$, $p \in \mathcal{N}_G^{(K)}$. Extending the functions $\lambda_p^{(K)}$, $p \in \mathcal{N}_G^{(K)}$, by zero from $\overline{G}$ to Ω, the global broken finite element space is given by

$$\mathcal{S}_K = \operatorname{span}\left\{\lambda_p^{(K)} : p \in \mathcal{N}^{(K)}\right\}, \qquad \mathcal{N}^{(K)} = \bigcup_{G \in \mathcal{G}^{(K)}} \mathcal{N}_G^{(K)}.$$

Then, the discretization of the K-scale interface problem (3.1.16) with respect to $\mathcal{S}_K$ reads

$$u_{\mathcal{S}_K} \in \mathcal{S}_K : \qquad a_K(u_{\mathcal{S}_K}, v) = \ell(v) \qquad \forall v \in \mathcal{S}_K. \tag{3.1.21}$$

Again, existence and uniqueness of the resulting finite element approximation $u_{\mathcal{S}_K}$ of $u_{\mathcal{H}_K} \in \mathcal{H}_K$ follows from the Lax-Milgram lemma. Convergence is implied by Céa's lemma together with (3.1.18).

Proposition 3.1.6. *The finite element approximations $(u_{\mathcal{S}_K})_{K \in \mathbb{N}}$ converge to the solution u of (3.1.10) in the sense that for each $\varepsilon > 0$ there is a sufficiently large $K \in \mathbb{N}$ such that*

$$\|u_{\mathcal{H}_K} - u_{\mathcal{S}_K}\|_{\mathcal{H}} < \varepsilon.$$

For each fixed $K \in \mathbb{N}$, the expected order of convergence is obtained under suitable regularity assumptions on $u_{\mathcal{H}_K}$.

Proposition 3.1.7. *Let $d \leq 3$, $K \in \mathbb{N}$ and assume that $u_{\mathcal{H}_K}|_G \in H^r(G)$ $\forall G \in \mathcal{G}^{(K)}$ with $r = 2$, if $d = 1, 2$, and $r = 2 + \varepsilon$, $\varepsilon > 0$, if $d = 3$. Then the a priori error estimate*

$$\|u_{\mathcal{H}_K} - u_{\mathcal{S}_K}\|_{\mathcal{H}} \leq c h_K \sum_{G \in \mathcal{G}^{(K)}} \|u_{\mathcal{H}_K}\|_{H^r(G)} \tag{3.1.22}$$

holds with a constant c depending only on the shape regularity σ of $\mathcal{T}^{(K)}$.

Proof. The proof follows from well-known interpolation error estimates [43]. □

If the interface geometry is sufficiently regular such that exponential convergence of $u_{\mathcal{H}_K}$ holds, see Remark 3.1.5, a priori estimates of the discretization error $\|u - u_{\mathcal{S}_K}\|_{\mathcal{H}}$ follow with (3.1.22) via

$$\|u - u_{\mathcal{S}_K}\|_{\mathcal{H}} \leq \|u - u_{\mathcal{H}_K}\|_{\mathcal{H}} + \|u_{\mathcal{H}_K} - u_{\mathcal{S}_K}\|_{\mathcal{H}}\,.$$

In Section 3.3.1, optimal a priori estimates will be obtained directly relying on a multiscale finite element discretization.

3.2 Projections

This section is dedicated to the construction of projection operators $\Pi : \mathcal{H} \to \mathcal{S}_k$ from the fractal function space $\mathcal{H}$ to piecewise linear finite element spaces $\mathcal{S}_k$ with respect to a triangulation $\mathcal{T}^{(k)}$ resolving the level-k interface network $\Gamma^{(k)}$, $k \in \mathbb{N}$, that satisfy stability and approximation properties of the form

$$\|v - \Pi v\|_0^2 \leq \left(1 + \tfrac{1}{\mathfrak{c}}\right) c\, d_K^2\, \|v\|_{\mathcal{H}}^2\,, \qquad \|\Pi v\|_{\mathcal{H}} \leq c'\, \|v\|_{\mathcal{H}} \tag{3.2.1}$$

for all $v \in \mathcal{H}$ with suitable constants $c, c' > 0$. The existence of such operators extends the applicability of well-known approaches to numerical homogenization especially in terms of local orthogonal decomposition and subspace correction to fractal interface problems. Many of the insights presented hereafter have previously appeared in [78].

The construction and analysis of suitable projections $\Pi_{\mathcal{H}_K} : \mathcal{H} \to \mathcal{H}_K$, $\Pi_{\mathcal{S}_k} : \mathcal{H} \to \mathcal{S}_k$ and their composition $\Pi_{k,K} = \Pi_{\mathcal{S}_k} \circ \Pi_{\mathcal{H}_K}$, $K \geq k$, that all possess the desired properties (3.2.1), will be achieved by extending well-known ideas based on local Poincaré inequalities [22, 129]. Following a strategy introduced by Verfürth [129], the latter will be derived relying on estimates on balls and ball segments, whereby the presence of jump terms poses a novel challenge. Another obstacle is the fact that it is not possible to bound jumps of local averages by jumps of the original functions as a counterexample will demonstrate. Therefore, strong assumptions on the locality of the interface network Γ have to be fulfilled for the projections to be stable in the sense of (3.2.1). This construction of quasi projections $\Pi_{k,K}$ is rather flexible and guarantees their usefulness for the development of various multilevel methods and corresponding numerical analysis. Colloquially, the choice of K and k introduces adjustable building blocks, whose relative contributions can be adapted depending

on the numerical algorithm. Whenever the existence of such quasi projections is only an analytic tool and the actual definition unimportant for the implementation, $\Pi_{\mathcal{S}_k}$ or $\Pi_{k,K}$ with $K = k$ could be generic candidates. However, if the goal is to derive discretization error estimates with an approach that requires these operators to be evaluated explicitly, e.g. a setting as presented in [89], concerns like computational complexity arise and impose additional demands on the choice of $\Pi_{k,K}$.

3.2.1 Local Poincaré inequalities

The focus in this section lies on the derivation of a local Poincaré-type inequality for star-shaped sets $\omega \subseteq G \in \mathcal{G}^{(k)} \backslash \mathcal{G}_\infty^{(k)}$. It is imperative to quantify the dependence of the Poincaré constant c_p on various geometric quantities, when applying this result to prove an approximation property of the quasi projection $\Pi_{k,K}$. In $H^1(\Omega)$, there are various known approaches to achieve this task for non-convex, star-shaped sets ω. One idea is to claim the existence of few reference configurations such that every star-shaped set is affine equivalent to one of them and subsequently estimate c_p for each reference configuration. Alternatively, one could construct extension operators from ω to a larger but simple domain, e.g. a ball, and assess the Poincaré constant for the latter [24]. Verfürth introduced a third strategy, that relies on estimates of c_p on balls and ball segments [129]. Verfürth's approach allows for a straightforward extension to the fractal function space $\mathcal{H}$. In this context, the sets ω exhibit a non-empty intersection with Γ_l, $l > k$, in general. Thus, the main challenge will be to handle contributions by jumps across the finer interfaces Γ_l.

Poincaré inequality on balls

As a first step, let us develop a local Poincaré inequality on balls. Let $k \in \mathbb{N}$ and consider star-shaped sets $\omega \subseteq G \in \mathcal{G}^{(k)} \backslash \mathcal{G}_\infty^{(k)}$. The notation

$$B(\omega, R) = \left\{ p_\omega + rs \,:\, s \in S^{d-1}, 0 \leq r < R \right\} \tag{3.2.2}$$

introduces a ball with radius $R > 0$, whose center is given by the one of ω. Moreover,

$$⨍_M v \, dx = \frac{1}{\mu_d(M)} \int_M v \, dx$$

will be used forthwith with suitable sets $M \subset \Omega$. Observe, that deriving a local Poincaré inequality on balls $B = B(\omega, r_\omega)$ according to the ansatz

$$\left\| v - ⨍_B v \, dx \right\|_{0,B}^2 = \int_B \left| ⨍_B v(x) - v(y) \, dx \right|^2 dy \leq \int_B ⨍_B |v(x) - v(y)|^2 \, dx \, dy \tag{3.2.3}$$

for all $v \in \mathcal{H}$ comes down to evaluating the differences $|v(x) - v(y)|^2$. The following lemma is a variant of Lemma 3.5 in [61] and estimates this difference in terms of gradient and jump contributions.

Lemma 3.2.1. *Let $k \in \mathbb{N}\cup\{0\}$, $G \in \mathcal{G}^{(k)}\backslash\mathcal{G}_\infty^{(k)}$ and $K > k$. For almost all $x \neq y \in G$, such that $\left|(x,y)\cap\Gamma^{(K)}\right| < \infty$ and $(x,y) \subset G$, the estimate*

$$|v(x)-v(y)|^2 \leq \left(1+\tfrac{1}{\mathfrak{c}}\right)|x-y|^2\left(\int_0^1 \nabla v\left(x+t(y-x)\right)\,dt\right)^2 + \left(1+\tfrac{1}{\mathfrak{c}}\right)\sum_{l=k+1}^{K}(1+c)^{l-k}\,C_{k,l}\sum_{\xi\in(x,y)\cap\Gamma_l}[\![v]\!]^2(\xi) \qquad \forall v\in\mathcal{C}^1_{K,0}$$

holds, where $\nabla v\left(x+t(y-x)\right)$ is understood to vanish for $x+t(y-x)\in\Gamma^{(K)}$.

Proof. Let $v\in\mathcal{C}^1_{K,0}$. The jumps of v across the sequence of interfaces $(\Gamma_l)_{l\in\mathbb{N}}$ up to level K and average gradient along the line (x,y) give the estimate

$$|v(x)-v(y)|^2 \leq \left(\sum_{l=k+1}^{K}\sum_{\xi\in(x,y)\cap\Gamma_l}[\![v]\!]_{x,y}(\xi) + (y-x)\int_0^1\nabla v\left(x+t(y-x)\right)\,dt\right)^2.$$

Note, that G only contains parts of the interfaces $\Gamma_{k+1},\dots,\Gamma_K$. Using the binomial estimate

$$0\leq(a-b\mathfrak{c})^2 = a^2-2ab\mathfrak{c}+\mathfrak{c}^2b^2 \quad\Rightarrow\quad 2ab\leq\tfrac{1}{\mathfrak{c}}a^2+\mathfrak{c}b^2,$$

where $a,b,\mathfrak{c}\in\mathbb{R}$ and $\mathfrak{c}>0$, let us infer

$$\begin{aligned}
&|v(x)-v(y)|^2\\
&\leq\left(1+\tfrac{1}{c}\right)|x-y|^2\left(\int_0^1\nabla v\left(x+t(y-x)\right)\,dt\right)^2+(1+\mathfrak{c})\left(\sum_{l=k+1}^{K}\sum_{\xi\in(x,y)\cap\Gamma_l}[\![v]\!]_{x,y}(\xi)\right)^2\\
&\leq\left(1+\tfrac{1}{\mathfrak{c}}\right)|x-y|^2\left(\int_0^1\nabla v\left(x+t(y-x)\right)\,dt\right)^2\\
&\quad+(1+\mathfrak{c})\left(1+\tfrac{1}{\mathfrak{c}}\right)\left(\sum_{\xi\in(x,y)\cap\Gamma_{k+1}}[\![v]\!]_{x,y}(\xi)\right)^2+(1+\mathfrak{c})^2\left(\sum_{l=k+2}^{K}\sum_{\xi\in(x,y)\cap\Gamma_l}[\![v]\!]_{x,y}(\xi)\right)^2.
\end{aligned}$$

As $|(x,y)\cap\Gamma_l|\leq C_{k,l}$ holds by definition of $C_{k,l}$ in (3.1.4), the Cauchy-Schwarz inequality in $\mathbb{R}^{|(x,y)\cap\Gamma_l|}$ yields

$$\left(\sum_{\xi\in(x,y)\cap\Gamma_l}[\![v]\!]_{x,y}(\xi)\right)^2\leq C_{k,l}\sum_{\xi\in(x,y)\cap\Gamma_l}[\![v]\!]^2(\xi)$$

and the assertion follows by induction. □

Plugging the statement of the previous lemma into the ansatz in equation (3.2.3) leads to an estimate involving the integration of jump terms, which is addressed by the following lemma (cf. Theorem 3.6 in [61]).

Lemma 3.2.2. *Let $k \in \mathbb{N}$, $\omega \subseteq G \in \mathcal{G}^{(k)} \backslash \mathcal{G}_\infty^{(k)}$ be star-shaped, $B = B(\omega, r_\omega)$ and $K \geq l > k$. It holds*

$$\int_B \int_B \sum_{\xi \in (x,y) \cap \Gamma_l} [\![v]\!]^2(\xi)\, dx\, dy \leq c\, \mu_d(B)\; r_\omega \int_{\Gamma_l \cap B} [\![v]\!]^2\, d\Gamma_l \qquad \forall v \in \mathcal{C}^1_{K,0}$$

with a constant c that only depends on the space dimension d.

Proof. Let $v \in \mathcal{C}^1_{K,0}$ with arbitrary $K \geq l > k$. Let $B(0, 2r_\omega)$ denote the ball centered at zero with radius $2r_\omega$ and set $B_\eta = \{x \in B : x + \eta \in B\}$ for all $\eta \in B(0, 2r_\omega)$. Using the diffeomorphism Ψ defined by

$$\Psi : \{(x, \eta) : \eta \in B(0, 2r_\omega), x \in B_\eta\} \to B \times B, \qquad (x, y) = \Psi(x, \eta) = (x, x + \eta)$$

to transform the integral in the statement of the lemma yields

$$\int_B \int_B \sum_{\xi \in (x,y) \cap \Gamma_l} [\![v]\!]^2(\xi)\, dx\, dy = \int_{B(0,2r_\omega)} \int_{B_\eta} \sum_{\xi \in (x,x+\eta) \cap \Gamma_l} [\![v]\!]^2(\xi)\, dx\, d\eta. \tag{3.2.4}$$

Next, choose $\eta \in B(0, 2r_\omega)$ arbitrary but fixed and consider the integral on B_η. As Γ_l is piecewise affine, it can be represented as a countable union $\Gamma_l = \bigcup_{i \in I} \Gamma_{l,i}$ of its affine components $\Gamma_{l,i}$, $i \in I \subset \mathbb{N}$. For almost all $x \in B_\eta$, the set $(x, x + \eta) \cap \Gamma_l$ is finite and

$$\sum_{\xi \in (x,x+\eta) \cap \Gamma_l} [\![v]\!]^2(\xi) = \sum_{i \in I} \varphi_i(x),$$

where

$$\varphi_i(x) = [\![v]\!]^2(\xi), \quad \text{if } (x, x + \eta) \cap \Gamma_{l,i} = \xi \in \mathbb{R}^d$$

and $\varphi_i(x) = 0$ if $(x, x + \eta) \cap \Gamma_{l,i} = \varnothing$.

Extending φ_i by zero to $\mathbb{R}^d$ and choosing a transformation Φ, that rotates the canonical basis $e_1, \ldots, e_d$ of $\mathbb{R}^d$ such that $\Phi(e_\eta) = e_1$, where $e_\eta = \eta / |\eta|$, leads to

$$\int_{B_\eta} \varphi_i(x)\, dx = \int_{\mathbb{R}^{d-1}} \int_{\mathbb{R}} \varphi_i(x_1, x')\, dx_1\, dx' = \int_{\mathbb{R}^{d-1}} \int_{\mathbb{R}} \varphi_i(\Phi(x_\eta, x'))\, dx_\eta\, dx'. \tag{3.2.5}$$

Introducing the set $U_i = \{x' \in \mathbb{R}^{d-1} : \exists x_\eta \in \mathbb{R} \text{ such that } \Phi(x_\eta, x') \in \Gamma_{l,i} \cap B_\eta\}$, let us note that if U_i is empty or $\Gamma_{l,i}$ is normal to U_i, i.e. U_i is a singleton, then the integral in (3.2.5) vanishes. Otherwise, there is an explicit parameterization $\gamma_i : U_i \to \Gamma_{l,i}$ of $\Gamma_{l,i}$ given by $\gamma_i(x') = \Phi(h_i(x'), x')$, where $h_i : U_i \to \mathbb{R}$ is a suitable smooth function. By definition, φ_i is piecewise constant in η-direction and bounded according to

$$0 \leq \varphi_i(\Phi(x_\eta, x')) \leq [\![v]\!]^2(\gamma_i(x')), \qquad x' \in U_i.$$

Hence, integration over x_η and substitution of these bounds yield

$$\int_{\mathbb{R}^{d-1}} \int_{\mathbb{R}} \varphi_i(\Phi(x_\eta, x'))\, dx_\eta\, dx' \leq \int_{U_i} |\eta|\, [\![v]\!]^2(\gamma_i(x'))\, dx'.$$

As $\Gamma_{l,i}$ is the graph of h_i, its first fundamental form satisfies $g^{\gamma_i}(x') = 1+|\nabla h_i(x')|^2 \geq 1$ and thus

$$\int_{U_i} |\eta| \left[\!\left[v\right]\!\right]^2 (\gamma_i(x'))\, dx' \leq |\eta| \int_{U_i} \left[\!\left[v\right]\!\right]^2 (\gamma_i(x'))\sqrt{g^{\gamma_i}}\, dx' = |\eta| \int_{\Gamma_{l,i}\cap B_\eta} \left[\!\left[v\right]\!\right]^2 \, d\Gamma_{l,i}.$$

For the entirety of Γ_l, summing over $i \in I$ leads to

$$\int_{B_\eta} \sum_{\xi\in(x,x+\eta)\cap\Gamma_l} \left[\!\left[v\right]\!\right]^2 (\xi)\, dx = \sum_{i\in I} \int_{B_\eta} \varphi_i(x)\, dx \leq |\eta| \int_{\Gamma_l\cap B} \left[\!\left[v\right]\!\right]^2 \, d\Gamma_l \tag{3.2.6}$$

and inserting (3.2.6) into (3.2.4) concludes the proof.

□

A local Poincaré inequality on balls follows by collecting the results of this section.

Lemma 3.2.3 (local Poincaré inequality on balls)**.** *Let $k \in \mathbb{N}$, $\omega \subseteq G \in \mathcal{G}^{(k)}\backslash\mathcal{G}_\infty^{(k)}$ be star-shaped and $B = B(\omega, r_\omega)$. It holds*

$$\left\| v - \fint_B v\, dx \right\|_{0,B}^2 \leq \left(1 + \tfrac{1}{\mathfrak{c}}\right) c_B\, r_\omega \left(r_\omega\, |v|_{1,B\backslash\Gamma}^2 + \sum_{l=k+1}^{\infty} (1+\mathfrak{c})^{l-k}\, C_{k,l}\, \|\left[\!\left[v\right]\!\right]\|_{0,\Gamma_l\cap B}^2 \right)$$

for all $v \in \mathcal{H}$ with a constant c_B only depending on the space dimension d.

Proof. As $\bigcup_{K\in\mathbb{N}} \mathcal{C}_{K,0}^1$ is dense in $\mathcal{H}$ and all quantities in the statement of the lemma depend continuously on v, it suffices to show the claim for $v \in \mathcal{C}_{K,0}^1$. Thus, let $v \in \mathcal{C}_{K,0}^1$ with arbitrary $K > k$ and note, that

$$\left\| v - \fint_B v\, dx \right\|_{0,B}^2 = \int_B \left| \fint_B v(x) - v(y)\, dx \right|^2 \, dy \leq \int_B \fint_B |v(x) - v(y)|^2 \, dx\, dy.$$

Recalling Lemma 3.2.1 and using the Cauchy-Schwarz inequality, the difference $|v(x) - v(y)|$ can be estimated in terms of the average gradient and jump contributions along the line segment (x, y) by

$$\begin{aligned} |v(x) - v(y)|^2 \leq \left(1 + \tfrac{1}{\mathfrak{c}}\right) |x-y|^2 \int_0^1 |\nabla v\,(x + t(y-x))|^2 \, dt \\ + \left(1 + \tfrac{1}{\mathfrak{c}}\right) \sum_{l=k+1}^{K} (1+\mathfrak{c})^{l-k}\, C_{k,l} \sum_{\xi\in(x,y)\cap\Gamma_l} \left[\!\left[v\right]\!\right]^2 (\xi). \end{aligned}$$

Following well-known arguments for proving a standard Poincaré inequality on balls for the gradient part (see e.g. Lemma 4.1 in [46]), one understands, that

$$\begin{aligned} &\int_B \fint_B |x-y|^2 \int_0^1 |\nabla v\,(x + t(y-x))|^2 \, dt\, dx\, dy \\ &\leq c_1 \int_B r_\omega \int_{B\backslash\Gamma^{(K)}} |\nabla v(y)|^2\, |x-y|^{1-d} \, dx\, dy \leq c_1\, r_\omega^2\, |v|_{1,B\backslash\Gamma^{(K)}}^2 \end{aligned}$$

holds with a constant $c_1 > 0$ only depending on the space dimension d. Applying Lemma 3.2.2 for the jump terms yields the estimate

$$\int_B \fint_B \sum_{\xi \in (x,y) \cap \Gamma_l} [\![v]\!]^2 (\xi) \, dx \, dy \leq c_2 \, r_\omega \int_{\Gamma_l \cap B} [\![v]\!]^2 \, d\Gamma_l,$$

where c_2 only depends on the space dimension d, concluding the proof. □

Using the same ideas as in the previous proof, one can show a trace analog of the local Poincaré inequality on balls.

Lemma 3.2.4. *Let $k \in \mathbb{N}$, $\omega \subseteq G \in \mathcal{G}^{(k)} \backslash \mathcal{G}_\infty^{(k)}$ be star-shaped, $B = B(\omega, r_\omega)$ and $K \geq l > k$. It holds*

$$\int_{\partial B} \int_B \sum_{\xi \in (x,y) \cap \Gamma_l} [\![v]\!]^2 (\xi) \, dx \, dy \leq c \, \mu_d (B) \int_{\Gamma_l \cap B} [\![v]\!]^2 \, d\Gamma_l \qquad \forall v \in \mathcal{C}_{K,0}^1$$

with a constant c that only depends on the space dimension d.

Proof. Let $v \in \mathcal{C}_{K,0}^1$ with arbitrary $K \geq l > k$. Let $B(0, 2r_\omega)$ denote the ball centered at zero with radius $2r_\omega$ and set $\partial B_x = \{y - x : y \in \partial B\}$ for any $x \in B$. Using Fubini's theorem and the diffeomorphism Ψ defined by

$$\Psi : \{(x, \eta) : x \in B, \eta \in \partial B_x\} \to B \times \partial B, \qquad (x, y) = \Psi(x, \eta) = (x, x + \eta)$$

to transform the integral yields

$$\begin{aligned} &\int_{\partial B} \int_B \sum_{\xi \in (x,y) \cap \Gamma_l} [\![v]\!]^2 (\xi) \, dx \, dy = \int_B \int_{\partial B_x} \sum_{\xi \in (x, x+\eta) \cap \Gamma_l} [\![v]\!]^2 (\xi) \, d\eta \, dx \\ = &\int_B \int_{\partial B(0, 2r_\omega)} \sum_{\xi \in (x, x+\eta) \cap \Gamma_l \cap B} [\![v]\!]^2 (\xi) \, d\eta \, dx = \int_{\partial B(0, 2r_\omega)} \int_B \sum_{\xi \in (x, x+\eta) \cap \Gamma_l \cap B} [\![v]\!]^2 (\xi) \, dx \, d\eta. \end{aligned}$$

Arguing exactly as in the derivation of equation (3.2.5) in the proof of Lemma 3.2.2 leads to

$$\int_B \sum_{\xi \in (x, x+\eta) \cap \Gamma_l \cap B} [\![v]\!]^2 (\xi) \, dx \leq |\eta| \int_{\Gamma_l \cap B} [\![v]\!]^2 \, d\Gamma_l = 2r_\omega \int_{\Gamma_l \cap B} [\![v]\!]^2 \, d\Gamma_l$$

for any $\eta \in \partial B(0, 2r_\omega)$. □

Continuing the train of thought, a trace lemma for balls is derived with the now familiar strategy.

Lemma 3.2.5 (Trace theorem for balls)**.** *Let $k \in \mathbb{N}$, $\omega \subseteq G \in \mathcal{G}^{(k)} \backslash \mathcal{G}_\infty^{(k)}$ be star-shaped, $B = B(\omega, r_\omega)$ and $K > k$. Then*

$$\left\| v - \fint_B v \, dx \right\|_{0,\partial B}^2 \leq \left(1 + \tfrac{1}{\mathfrak{c}}\right) c_{\partial B} \left(r_\omega \, |v|_{1, B \backslash \Gamma}^2 + \sum_{l=k+1}^{\infty} (1 + \mathfrak{c})^{l-k} \, C_{k,l} \, \| [\![v]\!] \|_{0, \Gamma_l \cap B}^2 \right)$$

holds for all $v \in \mathcal{C}_{K,0}^1$ with a constant $c_{\partial B}$ only depending on the space dimension d.

Proof. Let us proceed similarly to the proof of Lemma 3.2.3. Let $v \in \mathcal{C}^1_{K,0}$ with arbitrary $K > k$ and note, that

$$\left\| v - \fint_B v \, dx \right\|^2_{0,\partial B} = \int_{\partial B} \left| \fint_B v(x) - v(y) \, dx \right|^2 dy \leq \int_{\partial B} \fint_B |v(x) - v(y)|^2 \, dx \, dy.$$

Again, the difference $|v(x) - v(y)|$ can be estimated in terms of gradient and jump terms along the line segment (x, y) with Lemma 3.2.1 and the Cauchy-Schwarz inequality. Well-known arguments for the gradient part (see e.g. Lemma 4.1 in [46]) lead to

$$\begin{aligned} &\int_{\partial B} \fint_B |x - y|^2 \int_0^1 |\nabla v \left(x + t(y - x)\right)|^2 \, dt \, dx \, dy \\ &\leq c_1 \int_{\partial B} r_\omega \int_{B \setminus \Gamma^{(K)}} |\nabla v(y)|^2 \, |x - y|^{1-d} \, dx \, dy \leq c_1 \, r_\omega \, |v|^2_{1,B \setminus \Gamma^{(K)}}, \end{aligned}$$

where the constant $c_1 > 0$ only depends on the space dimension d. Applying Lemma 3.2.4 for the jump terms yields the estimate

$$\int_{\partial B} \fint_B \sum_{\xi \in (x,y) \cap \Gamma_l} [\![v]\!]^2 (\xi) \, dx \, dy \leq c_2 \int_{\Gamma_l \cap B} [\![v]\!]^2 \, d\Gamma_l,$$

where c_2 only depends on the space dimension d, concluding the proof. □

Poincaré inequality on star-shaped sets

The next objective is to extend the Poincaré inequality on balls to star-shaped sets $\omega \subseteq G \in \mathcal{G}^{(k)} \setminus \mathcal{G}^{(k)}_\infty$. For this purpose, split

$$\|v\|^2_{0,\omega} = \|v\|^2_{0,B(\omega,r_\omega)} + \|v\|^2_{0,\omega \setminus B(\omega,r_\omega)} \qquad \forall v \in \mathcal{C}^1_{K,0}, K > k$$

into a contribution from the associated ball $B(\omega, r_\omega)$ and the remainder $\omega \setminus B(\omega, r_\omega)$. Strategically, the remainder term will be handled in a similar way as were balls $B(\omega, r_\omega)$ in the previous section. Again, estimating differences $|v(x) - v(y)|$ in terms of gradients and jumps according to Lemma 3.2.1 as well as the integral over jumps in analogy to Lemma 3.2.2 will be essential components. The latter is accomplished by the following lemma.

Lemma 3.2.6. *Let $k \in \mathbb{N}$, $\omega \subseteq G \in \mathcal{G}^{(k)} \setminus \mathcal{G}^{(k)}_\infty$ be star-shaped, $W = \omega \setminus B(\omega, r_\omega)$ and $K \geq l > k$. It holds*

$$\int_W \sum_{\xi \in (p_\omega, y) \cap \Gamma_l \cap W} [\![v]\!]^2 (\xi) \, dy \leq \tfrac{1}{d} \, \rho_\omega^{d-1} \, R_\omega \int_{\Gamma_l \cap W} [\![v]\!]^2 \, d\Gamma_l \qquad \forall v \in \mathcal{C}^1_{K,0}.$$

Proof. Let $v \in \mathcal{C}^1_{K,0}$ with arbitrary $K \geq l > k$ and assume $p_\omega = 0$ without loss of generality. As Γ_l is piecewise affine, it can be represented as a countable union

$\Gamma_l = \bigcup_{i\in I} \Gamma_{l,i}$ of its affine components $\Gamma_{l,i}$, $i \in I \subset \mathbb{N}$. For almost all $y \in W$, the set $(0,y) \cap \Gamma_l \cap W$ is finite and

$$\sum_{(0,y)\cap\Gamma_l\cap W} [\![v]\!]^2(\xi) = \sum_{i\in I} \varphi_i(y),$$

where

$$\varphi_i(y) = [\![v]\!]^2(\xi), \quad \text{if } (0,y)\cap\Gamma_{l,i}\cap W = \xi \in \mathbb{R}^d$$

and $\varphi_i(y) = 0$ if $(0,y)\cap\Gamma_{l,i}\cap W = \varnothing$. Extending φ_i by zero to the ball $B = B(\omega, R_\omega)$, let us consider the integral

$$\int_W \varphi_i(y)\,dy = \int_{B\setminus B(\omega,r_\omega)} \varphi_i(y)\,dy = \int_{S^{d-1}} \int_{r_\omega}^{R_\omega} \varphi_i(\Psi(r,s))\, r^{d-1}\,dr\,ds, \tag{3.2.7}$$

where Ψ denotes the transformation from d-dimensional spherical to Cartesian coordinates.

Introducing the set $S_i = \{s \in S^{d-1} : (0, R_\omega s)\cap\Gamma_{l,i}\cap W \neq \varnothing\}$ of directions that contribute to the integral in (3.2.7), denote with $\partial B_i = \{R_\omega s : s \in S_i\}$ the corresponding segment of ∂B. If ∂B_i is empty or $\Gamma_{l,i}$ is normal to ∂B_i, i.e. ∂B_i is a singleton, then the integral in (3.2.7) vanishes. Otherwise, there is an explicit parameterization $\gamma_i : \partial B_i \to \Gamma_{l,i}$ of $\Gamma_{l,i}$ given by $\gamma_i(s) = \Psi(h_i(s)R_\omega, s)$, where $h_i : \partial B_i \to (0,1)$ is a suitable smooth function. By definition, φ_i is piecewise constant in s-direction and bounded according to

$$0 \le \varphi_i(\Psi(r,s)) \le [\![v]\!]^2(\gamma_i(s)), \qquad s \in S_i.$$

Then, integrating over r and transforming the domain of the integral from S_i to ∂B_i yields

$$\begin{aligned}\int_{S^{d-1}} \int_{r_\omega}^{R_\omega} \varphi_i(\Psi(r,s))\, r^{d-1}\,dr\,ds &\le \tfrac{1}{d} R_\omega \int_{S_i} [\![v]\!]^2(\gamma_i(s))\, R_\omega^{d-1}\,ds \\ &\le \tfrac{1}{d} R_\omega \int_{\partial B_i} [\![v]\!]^2(\gamma_i(s))\,ds.\end{aligned}$$

The first fundamental form g^{γ_i} of $\Gamma_{l,i}$ satisfies

$$\sqrt{g^{\gamma_i}} = h_i(s)^{d-2}\sqrt{h_i(s)^2 + |\nabla h_i(s)|^2 R_\omega^2}$$

and using the shape regularity $\frac{R_\omega}{r_\omega} \le \rho_\omega$ as well as $r_\omega \le h_i(s) R_\omega$ implies

$$1 \le \rho_\omega\, h_i(s) \le \rho_\omega^{d-1} h_i(s)^{d-1} \le \rho_\omega^{d-1} h_i(s)^{d-2}\sqrt{h_i(s)^2 + |\nabla h_i(s)|^2 R_\omega^2} = \rho_\omega^{d-1}\sqrt{g^{\gamma_i}}.$$

Thus, inserting this intermediate estimate results in

$$\int_{\partial B_i} [\![v]\!]^2(\gamma_i(s))\,ds \le \rho_\omega^{d-1} \int_{\partial B_i} [\![v]\!]^2(\gamma_i(s))\sqrt{g^{\gamma_i}}\,ds = \rho_\omega^{d-1} \int_{\Gamma_{l,i}\cap W} [\![v]\!]^2\,d\Gamma_{l,i}.$$

For the entirety of Γ_l, summing over $i \in I$ leads to

$$\int_W \sum_{(0,y)\cap\Gamma_l\cap W} [\![v]\!]^2(\xi)\,dy = \sum_{i\in I} \int_W \varphi_i(y)\,dy \le \tfrac{1}{d}\,\rho_\omega^{d-1} R_\omega \int_{\Gamma_l\cap W} [\![v]\!]^2\,d\Gamma_l. \qquad \square$$

Using this result, let us derive an intermediate estimate in likeness to Lemma 4.1 in [129].

Lemma 3.2.7. *Let $k \in \mathbb{N}$, $\omega \subseteq G \in \mathcal{G}^{(k)} \backslash \mathcal{G}_\infty^{(k)}$ be star-shaped and $K > k$. It holds*

$$\begin{aligned}\|v\|_{0,\omega}^2 \leq \|v\|_{0,B(\omega,r_\omega)}^2 + c\, R_\omega \left(\|v\|_{0,\partial B(\omega,r_\omega)}^2 + \left(1 + \tfrac{1}{\mathfrak{c}}\right) R_\omega \, |v|_{1,\omega\backslash\Gamma^{(K)}}^2 \right) \\ + \tfrac{2}{d} \left(1 + \tfrac{1}{\mathfrak{c}}\right) \rho_\omega^{d-1} R_\omega \sum_{l=k+1}^{K} (1+\mathfrak{c})^{l-k} \, C_{k,l} \, \|[\![v]\!]\|_{0,\Gamma_l \cap (\omega \backslash B(\omega,r_\omega))}^2\end{aligned}$$

for all $v \in \mathcal{C}_{K,0}^1$ with a constant c only depending on the dimension d and the shape regularity ρ_ω.

Proof. Let $v \in \mathcal{C}_{K,0}^1$ with arbitrary $K > k$ and assume $p_\omega = 0$ without loss of generality. Then, split

$$\|v\|_{0,\omega}^2 = \|v\|_{0,B(\omega,r_\omega)}^2 + \|v\|_{0,W}^2 \,,$$

as motivated earlier and set $W = \omega \setminus B(\omega, r_\omega)$ for notational convenience. The essential task is to derive a suitable bound for $\|v\|_{0,W}^2$. For this purpose, let us use spherical coordinates and split the integral into parts I_1 and I_2 as follows:

$$\begin{aligned}\|v\|_{0,W}^2 &= \int_{S^{d-1}} \int_{r_\omega}^{\vartheta_\omega(s)} r^{d-1} \, |v(rs)|^2 \, dr \, ds \\ &= \int_{S^{d-1}} \int_{r_\omega}^{\vartheta_\omega(s)} r^{d-1} \, |v(rs) - v(r_\omega s) + v(r_\omega s)|^2 \, dr \, ds \\ &\leq \underbrace{2 \int_{S^{d-1}} \int_{r_\omega}^{\vartheta_\omega(s)} r^{d-1} \, |v(rs) - v(r_\omega s)|^2 \, dr \, ds}_{=I_1} + \underbrace{2 \int_{S^{d-1}} \int_{r_\omega}^{\vartheta_\omega(s)} r^{d-1} \, |v(r_\omega s)|^2 \, dr \, ds}_{=I_2}\end{aligned}$$

As a first step, consider I_1 and apply Lemma 3.2.1 to obtain

$$\begin{aligned}I_1 \leq \quad & 2 \left(1 + \tfrac{1}{\mathfrak{c}}\right) \int_{S^{d-1}} \int_{r_\omega}^{\vartheta_\omega(s)} r^{d-1} \left(\int_{r_\omega}^{r} \nabla v(zs) \, dz \right)^2 dr \, ds \\ & + 2 \left(1 + \tfrac{1}{\mathfrak{c}}\right) \int_{S^{d-1}} \int_{r_\omega}^{\vartheta_\omega(s)} r^{d-1} \sum_{l=k+1}^{K} (1+\mathfrak{c})^{l-k} \, C_{k,l} \sum_{\xi \in (r_\omega s, rs) \cap \Gamma_l} [\![v]\!]^2 (\xi) \, dr \, ds. \quad (3.2.8)\end{aligned}$$

Moreover, employing the Cauchy-Schwarz inequality and proceeding exactly as in the proof of Lemma 4.1 in [129] for the gradient part yields

$$\begin{aligned}&\int_{S^{d-1}} \int_{r_\omega}^{\vartheta_\omega(s)} r^{d-1} \left(\int_{r_\omega}^{r} \nabla v(zs) \, dz \right)^2 dr \, ds \\ &\leq \int_{S^{d-1}} \left(\int_{r_\omega}^{\vartheta_\omega(s)} z^{d-1} \, |\nabla v(zs)|^2 \, dz \right) \left(\int_{r_\omega}^{\vartheta_\omega(s)} r^{d-1} \int_{r_\omega}^{r} z^{1-d} \, dz \, dr \right) ds.\end{aligned}$$

Using $\vartheta_\omega(s) < R_\omega$, the shape regularity $\rho_\omega = \frac{R_\omega}{r_\omega}$ and a straightforward calculation leads to

$$\int_{r_\omega}^{\vartheta_\omega(s)} \left(r \int_{r_\omega}^{r} z^{-1}\, dz \right) dr = \int_{r_\omega}^{\vartheta_\omega(s)} r\ln(r) - r\ln(r_\omega)\, dr \leq \tfrac{1}{2}\left(\ln(\rho_\omega) - \tfrac{1}{2} + \tfrac{1}{2}\rho_\omega^{-2} \right) R_\omega^2$$

for $d = 2$ and to

$$\begin{aligned} \int_{r_\omega}^{\vartheta_\omega(s)} \left(r^{d-1} \int_{r_\omega}^{r} z^{1-d}\, dz \right) dr &= \int_{r_\omega}^{\vartheta_\omega(s)} \tfrac{r^{d-1}}{d-2} \left(r_\omega^{2-d} - r^{2-d} \right) dr \\ &\leq \tfrac{1}{d-2} \left(\tfrac{\rho_\omega^{d-2}}{d} - \tfrac{1}{2} + \tfrac{d-2}{2d}\rho_\omega^{-2} \right) R_\omega^2 \end{aligned}$$

for $d \geq 3$ and $s \in S^{d-1}$. Thus, there is a constant c' only depending on the space dimension d and shape regularity ρ_ω, such that

$$\begin{aligned} \int_{S^{d-1}} \int_{r_\omega}^{\vartheta_\omega(s)} r^{d-1} \left(\int_{r_\omega}^{r} \nabla v(zs)\, dz \right)^2 dr\, ds &\leq c'\, R_\omega^2\, |v|_{1,W\setminus\Gamma^{(K)}}^2 \\ &\leq c'\, R_\omega^2\, |v|_{1,\omega\setminus\Gamma^{(K)}}^2 . \end{aligned} \tag{3.2.9}$$

Estimating the jump contributions in (3.2.8) with Lemma 3.2.6 gives

$$\begin{aligned} &\int_{S^{d-1}} \int_{r_\omega}^{\vartheta_\omega(s)} r^{d-1} \sum_{\xi \in (r_\omega s, rs) \cap \Gamma_l} [\![v]\!]^2(\xi)\, dr\, ds = \int_W \sum_{\xi \in (0,y) \cap \Gamma_l \cap W} [\![v]\!]^2(\xi)\, dy \\ &\leq \tfrac{1}{d}\, \rho_\omega^{d-1}\, R_\omega \int_{\Gamma_l \cap W} [\![v]\!]^2\, d\Gamma_l = \tfrac{1}{d}\, \rho_\omega^{d-1}\, R_\omega\, \|[\![v]\!]\|_{0,\Gamma_l\cap W}^2 . \end{aligned}$$

and inserting together with (3.2.9) into (3.2.8) results in

$$I_1 \leq 2\left(1 + \tfrac{1}{\mathfrak{c}}\right) \left(c' R_\omega^2\, |v|_{1,W\setminus\Gamma^{(K)}}^2 + \tfrac{1}{d}\, \rho_\omega^{d-1}\, R_\omega \sum_{l=k+1}^{K} (1+\mathfrak{c})^{l-k}\, C_{k,l}\, \|[\![v]\!]\|_{0,\Gamma_l\cap W}^2 \right) .$$

A simple calculation for I_2 using $r_\omega \leq \vartheta_\omega(s) < R_\omega$ and the shape regularity ρ_ω concludes the proof

$$\begin{aligned} I_2 &= 2 \int_{S^{d-1}} \int_{r_\omega}^{\vartheta_\omega(s)} r^{d-1}\, |v(r_\omega s)|^2\, dr\, ds = 2 \int_{S^{d-1}} r_\omega^{d-1}\, |v(r_\omega s)|^2 \int_{r_\omega}^{\vartheta_\omega(s)} \left(\tfrac{r}{r_\omega} \right)^{d-1} dr\, ds \\ &= 2 \int_{S^{d-1}} r_\omega^{d-1}\, |v(r_\omega s)|^2\, \tfrac{r_\omega}{d} \left(\left(\tfrac{\vartheta_\omega(s)}{r_\omega} \right)^d - 1 \right) ds \leq \tfrac{2}{d} \left(\rho_\omega^d - 1 \right) R_\omega\, \|v\|_{0,\partial B(\omega, r_\omega)}^2 . \end{aligned}$$

□

Finally, a local Poincaré inequality on star-shaped sets ensues.

Proposition 3.2.8 (Poincaré inequality on star-shaped sets, cf. [129] Lemma 4.3)**.** *Let $k \in \mathbb{N}$ and $\omega \subseteq G \in \mathcal{G}^{(k)} \setminus \mathcal{G}_\infty^{(k)}$ be star-shaped. It holds*

$$\left\| v - \fint_\omega v\, dx \right\|_{0,\omega}^2 \leq \left(1 + \tfrac{1}{\mathfrak{c}}\right) c_p\, R_\omega \left(R_\omega\, |v|_{1,\omega\setminus\Gamma}^2 + \sum_{l=k+1}^{\infty} (1+\mathfrak{c})^{l-k}\, C_{k,l}\, \|[\![v]\!]\|_{0,\Gamma_l\cap\omega}^2 \right)$$

for all $v \in \mathcal{H}$, where c_p only depends on the dimension d and the shape regularity ρ_ω.

Proof. Again, it suffices to prove the claim for $v \in \mathcal{C}^1_{K,0}$ with arbitrary $K > k$ and subsequently use a density argument, since all quantities depend continuously on v. Observe that $\fint_\omega v\,dx$ minimizes the functional $\|v - \cdot\|^2_{0,\omega}$. Denote $B = B(\omega, r_\omega)$ and apply Lemma 3.2.7 to obtain

$$\begin{aligned}\left\|v - \fint_\omega v\,dx\right\|^2_{0,\omega} &\leq \left\|v - \fint_B v\,dx\right\|^2_{0,\omega} \\ &\leq \left\|v - \fint_B v\,dx\right\|^2_{0,B} + c\,R_\omega \left(\left\|v - \fint_B v\,dx\right\|^2_{0,\partial B} + \left(1 + \tfrac{1}{\mathfrak{c}}\right) R_\omega\,|v|^2_{1,\omega\setminus\Gamma^{(K)}}\right) \\ &\quad + \tfrac{2}{d}\left(1 + \tfrac{1}{\mathfrak{c}}\right)\rho_\omega^{d-1} R_\omega \sum_{l=k+1}^{K} (1+\mathfrak{c})^{l-k}\,C_{k,l}\,\|[\![v]\!]\|^2_{0,\Gamma_l\cap(\omega\setminus B)}\,.\end{aligned}$$

To finish the proof, use $r_\omega < R_\omega$ and apply the Poincaré inequality on balls (Lemma 3.2.3)

$$\left\|v - \fint_B v\,dx\right\|^2_{0,B} \leq \left(1 + \tfrac{1}{\mathfrak{c}}\right) c_B\,R_\omega \left(R_\omega\,|v|^2_{1,B\setminus\Gamma^{(K)}} + \sum_{l=k+1}^{K} (1+\mathfrak{c})^{l-k}\,C_{k,l}\,\|[\![v]\!]\|^2_{0,\Gamma_l\cap B}\right)$$

as well as the trace analogue from Lemma 3.2.5

$$\left\|v - \fint_B v\,dx\right\|^2_{0,\partial B} \leq \left(1 + \tfrac{1}{\mathfrak{c}}\right) c_{\partial B} \left(R_\omega\,|v|^2_{1,B\setminus\Gamma^{(K)}} + \sum_{l=k+1}^{K} (1+\mathfrak{c})^{l-k}\,C_{k,l}\,\|[\![v]\!]\|^2_{0,\Gamma_l\cap B}\right).$$

□

Remark 3.2.9. In Proposition 3.2.8, the explicit dependence of the constant c_p on the space dimension d and shape regularity parameter ρ_ω can be computed similarly to [129].

Additionally, all estimates for star-shaped $\omega \subseteq G \in \mathcal{G}^{(k)}$, $k \in \mathbb{N}$, involving shape regularity parameters can be improved by allowing sphere segments in the definition of star-shaped sets. With this extension, the radius of the largest ball segment contained in ω may be larger, which causes the new shape regularity parameter to be smaller compared to ρ_ω (see Figure 3.2). For ball segments, one would derive a local Poincaré inequality by using Lemma 3.2.7, since they are star-shaped and obtain an extension of Lemma 4.2 in [129]. Then, proving a trace lemma for ball segments with similar arguments will lead to an improved version of Proposition 3.2.8 with a possibly smaller constant c_p.

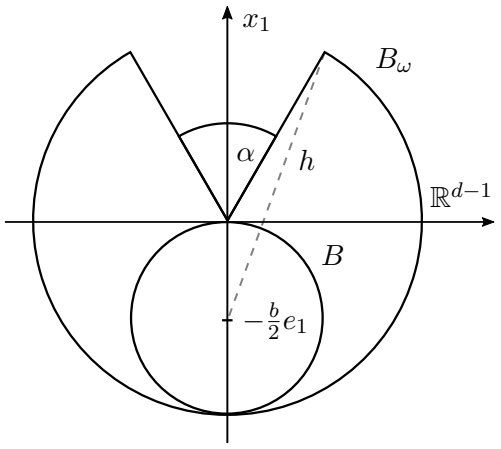

Figure 3.2: Ball segment B_ω and largest contained ball B with radii r_ω and $\frac{1}{2}r_\omega$ respectively, cf. [129].

3.2.2 Trace theorems

Beside the Poincaré-type inequalities from the previous section, another essential tool for deriving suitable stability estimates for the projections $\Pi_{k,K}$ is a trace theorem. Again, Verfürth's approach in [129] guides our efforts. The central idea is to use the triangulation $\mathcal{T}^{(k)}$ resolving the cells $G \in \mathcal{G}^{(k)}$, $k \in \mathbb{N}$, and reduce the problem to showing a trace estimate for the simplices $T \in \mathcal{T}^{(k)}$. The latter is achieved by a typical scaling argument employing an affine transformation $F : \hat{T} \to T$, that is continuously differentiable, bijective, and maps the reference d-simplex $\hat{T}$ with vertices $e_1, \dots, e_d$ and $e_{d+1} = 0$, where $\{e_i : 1 \leq i \leq d\}$ denotes the standard basis in $\mathbb{R}^d$, to a simplex $T \in \mathcal{T}^{(k)}$. The faces of the reference d-simplex $\hat{T}$ are denoted by

$$\hat{E}_i = \{\hat{x} \in \hat{T} : \hat{x}_i = 0\}, \quad 1 \leq i \leq d, \qquad \text{and} \qquad \hat{E}_{d+1} = \left\{\hat{x} \in \hat{T} : \sum_{i=1}^{d} |\hat{x}_i| = 1\right\}.$$

The upcoming lemma provides an estimate for the jump terms in the reference configuration.

Lemma 3.2.10. *Let $k \in \mathbb{N}$, $T \in \mathcal{T}^{(k)}$ with $T \subseteq G \in \mathcal{G}^{(k)} \setminus \mathcal{G}_\infty^{(k)}$, and $E_i \in \mathcal{E}^{(k)}$ a face of T, $1 \leq i \leq d$. Denote with $\hat{T} = F^{-1}(T)$ the reference simplex and with $\hat{E}_i = F^{-1}(E_i)$ the face corresponding to E_i in the reference simplex. It holds*

$$\int_{\hat{E}_i} \sum_{\xi \in (\hat{x}, \hat{x}+e_i) \cap \hat{\Gamma}_l \cap \hat{T}} [\![\hat{v}]\!]^2 (\xi)^2 \, d\hat{x} \leq \int_{\hat{\Gamma}_l \cap \hat{T}} [\![\hat{v}]\!]^2 (\xi) \, d\hat{\Gamma}_l$$

for all $\hat{v} = v \circ F$, $v \in \mathcal{C}^1_{K,0}$ with $K \geq l > k$, where $\hat{\Gamma}_l \cap \hat{T} = F^{-1}(\Gamma_l \cap T)$.

Proof. Let $v \in \mathcal{C}^1_{K,0}$ with arbitrary $K \geq l > k$ and denote $\hat{v} = v \circ F$. As F is an affine transformation, it preserves the dimension of any affine subspace. Therefore, $\hat{\Gamma}_l \cap \hat{T} = F^{-1}(\Gamma_l \cap T)$ is piecewise affine and can be represented as a countable union $\hat{\Gamma}_l \cap \hat{T} = \bigcup_{j \in I} \hat{\Gamma}_{l,j}$ of its affine components $\hat{\Gamma}_{l,j}$, $j \in I \subset \mathbb{N}$. For almost all $\hat{x} \in \hat{E}_i$, the set $(\hat{x}, \hat{x} + e_i) \cap \hat{\Gamma}_l \cap \hat{T}$ is finite and

$$\sum_{\xi \in (\hat{x}, \hat{x}+e_i) \cap \hat{\Gamma}_l \cap \hat{T}} [\![\hat{v}]\!]^2 (\xi) = \sum_{j \in I} \varphi_j(\hat{x}),$$

where

$$\varphi_j(\hat{x}) = [\![\hat{v}]\!]^2 (\xi), \quad \text{if } (\hat{x}, \hat{x} + e_i) \cap \hat{\Gamma}_{l,j} = \xi \in \mathbb{R}^d$$

and $\varphi_j(\hat{x}) = 0$ if $(\hat{x}, \hat{x} + e_i) \cap \hat{\Gamma}_{l,j} = \varnothing$.

Introducing the set $U_j = \{\hat{x} \in \hat{E}_i : \exists \hat{x}_i \in \mathbb{R} \text{ such that } \hat{x} + \hat{x}_i e_i \in \hat{\Gamma}_{l,i}\}$, let us note that if U_j is empty or $\hat{\Gamma}_{l,j}$ is normal to U_j, i.e. U_j is a singleton, then the integral in (3.2.10) vanishes. Otherwise, there is an explicit parameterization $\gamma_j : U_j \to \hat{\Gamma}_{l,j}$ of $\hat{\Gamma}_{l,j}$ given by $\gamma_j(\hat{x}) = \hat{x} + h_j(\hat{x}) e_i$, where $h_j : U_j \to \mathbb{R}$ is a suitable smooth function. As $\hat{\Gamma}_{l,j}$ is the graph of h_j, its first fundamental form satisfies $g^{\gamma_j}(\hat{x}) = 1 + |\nabla h_j(\hat{x})|^2 \geq 1$ and thus

$$\begin{aligned}\int_{\hat{E}_i} \varphi_j(\hat{x})\,d\hat{x} &= \int_{U_j} [\![\hat{v}]\!]^2\,(\gamma_j(\hat{x}))\,d\hat{x} \\ &\leq \int_{U_j} [\![\hat{v}]\!]^2\,(\gamma_j(\hat{x}))\sqrt{g^{\gamma_j}}\,d\hat{x} = \int_{\hat{\Gamma}_{l,j}} [\![\hat{v}]\!]^2\,d\hat{\Gamma}_{l,j}.\end{aligned} \tag{3.2.10}$$

For the entirety of $\hat{\Gamma}_l \cap \hat{T}$, summing over $j \in I$ concludes the proof as per

$$\int_{\hat{E}_i} \sum_{\xi \in (\hat{x},\hat{x}+e_i)\cap\hat{\Gamma}_l\cap\hat{T}} [\![\hat{v}]\!]^2\,(\xi)\,d\hat{x} = \sum_{j\in I}\int_{\hat{E}_i}\varphi_j(\hat{x})\,d\hat{x} \leq \int_{\hat{\Gamma}_l\cap\hat{T}} [\![\hat{v}]\!]^2\,d\hat{\Gamma}_l. \qquad \square$$

Next, the previous lemma will be used to prove a trace lemma in the reference configuration.

Lemma 3.2.11 (cf. [129] Lemma 3.1)**.** *Let $k \in \mathbb{N}$, $T \in \mathcal{T}^{(k)}$ with $T \subseteq G \in \mathcal{G}^{(k)}\backslash\mathcal{G}_\infty^{(k)}$, and $E_i \in \mathcal{E}^{(k)}$ a face of T, $1 \leq i \leq d$. Denote with $\hat{T} = F^{-1}(T)$ the reference simplex and with $\hat{E}_i = F^{-1}(E_i)$ the face corresponding to E_i in the reference simplex. It holds*

$$\|\hat{v}\|^2_{0,\hat{E}_i} \leq \left(1+\tfrac{1}{\mathfrak{c}}\right)\left(\left\|\tfrac{\partial}{\partial\hat{x}_i}\hat{v}\right\|^2_{0,\hat{T}\backslash\hat{\Gamma}^{(K)}} + \sum_{l=k+1}^{K}(1+\mathfrak{c})^{l-k}\,C_{k,l}\,\|[\![\hat{v}]\!]\|^2_{0,\hat{\Gamma}_l\cap\hat{T}}\right)$$

for all $\hat{v} = v \circ F$ satisfying $\hat{v}|_{\hat{E}_{d+1}} = 0$, where $v \in \mathcal{C}^1_{K,0}$ with $K > k$ and denoting $\hat{\Gamma}_l \cap \hat{T} = F^{-1}(\Gamma_l \cap T)$.

Proof. Let $i \in \{1,\dots,d\}$, $\hat{x} \in \hat{E}_i$ and $v \in \mathcal{C}^1_{K,0}$ such that $\hat{v}|_{\hat{E}_{d+1}} = 0$. Furthermore, set $\eta = 1 - \sum_{i=1}^d |\hat{x}_i|$ and note that $\hat{x} + \eta e_i \in \hat{E}_{d+1}$, which implies $\hat{v}(\hat{x}+\eta e_i) = 0$. A derivation similar to the proof of Lemma 3.2.1 results in

$$\begin{aligned}|\hat{v}(\hat{x})|^2 = |\hat{v}(\hat{x}) - \hat{v}(\hat{x}+\eta e_i)|^2 &\leq \left(1+\tfrac{1}{\mathfrak{c}}\right)\int_0^\eta \left|\tfrac{\partial}{\partial\hat{x}_i}\hat{v}\,(\hat{x}+te_i)\right|^2 dt \\ &\quad + \left(1+\tfrac{1}{\mathfrak{c}}\right)\sum_{l=k+1}^{K}(1+\mathfrak{c})^{l-k}\,C_{k,l}\sum_{\xi\in(\hat{x},\hat{x}+\eta e_i)\cap\hat{\Gamma}_l}[\![\hat{v}]\!]^2\,(\xi).\end{aligned}$$

Integrating over $\hat{E}_i$, applying Fubini's theorem to the gradient term to switch the order of integration and using Lemma 3.2.10 to estimate the jump term yields the assertion. $\square$

Moreover, a trace lemma for simplices $T \in \mathcal{T}^{(k)}$, $k \in \mathbb{N}$, follows using the previous trace lemma for the reference configuration and the affine transformation F.

Lemma 3.2.12 (cf. [129] Lemma 3.2)**.** *Let $k \in \mathbb{N}$, $T \in \mathcal{T}^{(k)}$ and $E \in \mathcal{E}^{(k)}$ be a face of the simplex T. It holds*

$$\|v\|^2_{0,E} \leq c\,\left(1+\tfrac{1}{\mathfrak{c}}\right)\left(h_k^{-1}\,\|v\|^2_{0,T} + h_k\,|v|^2_{1,T\backslash\Gamma^{(K)}} + \sum_{l=k+1}^{K}(1+\mathfrak{c})^{l-k}\,C_{k,l}\,\|[\![v]\!]\|^2_{0,\Gamma_l\cap T}\right)$$

for all $v \in \mathcal{C}^1_{K,0}$ with $K > k$ and a constant c depending only on the space dimension d and the shape regularity σ of $\mathcal{T}^{(k)}$.

Proof. Let $v \in \mathcal{C}^1_{K,0}$ with $K > k$, $T \in \mathcal{T}^{(k)}$ and $E \in \mathcal{E}^{(k)}$ be a face of the simplex T. Note that the set of nodal basis functions $\{\lambda^{(k)}\}$ is a partition of unity on E and invoking the triangle inequality leads to

$$\|v\|_{0,E} = \left\| \sum_{p \in \mathcal{N}^{(k)}(E)} \lambda_p^{(k)} v \right\|_{0,E} \leq \sum_{p \in \mathcal{N}^{(k)}(E)} \left\| \lambda_p^{(k)} v \right\|_{0,E}, \tag{3.2.11}$$

where $\mathcal{N}^{(k)}(E) = \mathcal{N}^{(k)} \cap E$ denotes the vertices of E, that are not part of the boundary $\partial\Omega$.

Let $p \in \mathcal{N}^{(k)}(E)$ and consider the affine transformation $F : \hat{T} \to T$ that is continuously differentiable, bijective and maps e_{d+1} onto p. Thus, there is a reference face $\hat{E}_i$, $1 \leq i \leq d$, such that $F(\hat{E}_i) = E$ and $\hat{\lambda}_{d+1} = \lambda_p^{(k)} \circ F$, where $\hat{\lambda}_{d+1}$ is the $(d+1)$-barycentric coordinate of $\hat{T}$. Let us set $\hat{v} = v \circ F$ and apply the standard rule of integral transforms to obtain

$$\begin{aligned} \|v\|^2_{0,E} &= \left(\frac{\mu_{d-1}(E)}{\mu_{d-1}\left(\hat{E}_i\right)} \right) \|\hat{v}\|^2_{0,\hat{E}_i}, \\ \|\hat{v}\|^2_{0,\hat{T}} &= \left(\frac{\mu_d\left(\hat{T}\right)}{\mu_d(T)} \right) \|v\|^2_{0,T} = \left(\frac{\mu_{d-1}\left(\hat{E}_i\right)}{d\,\mu_d(T)} \right) \|v\|^2_{0,T}, \end{aligned} \tag{3.2.12}$$

since $\mu_d\left(\hat{T}\right) = \frac{1}{d!}$ and $\mu_{d-1}\left(\hat{E}_i\right) = \frac{1}{(d-1)!}$. Hence, with Lemma 3.2.11 follows

$$\begin{aligned} &\left\| \lambda_p^{(k)} v \right\|^2_{0,E} = \left(\frac{\mu_{d-1}(E)}{\mu_{d-1}\left(\hat{E}_i\right)} \right) \left\| \hat{\lambda}_{d+1} \hat{v} \right\|^2_{0,\hat{E}_i} \\ &\leq \left(\frac{\mu_{d-1}(E)}{\mu_{d-1}\left(\hat{E}_i\right)} \right) \left(1 + \tfrac{1}{\mathfrak{c}}\right) \left(\left\| \tfrac{\partial}{\partial \hat{x}_i} \left(\hat{\lambda}_{d+1} \hat{v} \right) \right\|^2_{0,\hat{T} \setminus \hat{\Gamma}^{(K)}} + \sum_{l=k+1}^{K} (1+\mathfrak{c})^{l-k} C_{k,l} \left\| \left[\!\left[\hat{\lambda}_{d+1} \hat{v} \right]\!\right] \right\|^2_{0,\hat{\Gamma}_l \cap \hat{T}} \right). \end{aligned}$$

The triangle inequality, the fact that $\frac{\partial}{\partial \hat{x}_i} \hat{\lambda}_{d+1} = -e_i$ and $\left\| \hat{\lambda}_{d+1} \right\|_{\infty,\hat{T}} = 1$ as well as the Cauchy-Schwarz inequality lead to

$$\begin{aligned} \left\| \tfrac{\partial}{\partial \hat{x}_i} \left(\hat{\lambda}_{d+1} \hat{v} \right) \right\|^2_{0,\hat{T} \setminus \hat{\Gamma}^{(K)}} &\leq 2 \left\| \hat{v} \tfrac{\partial}{\partial \hat{x}_i} \hat{\lambda}_{d+1} \right\|^2_{0,\hat{T}} + 2 \left\| \hat{\lambda}_{d+1} \tfrac{\partial}{\partial \hat{x}_i} \hat{v} \right\|^2_{0,\hat{T} \setminus \hat{\Gamma}^{(K)}} \\ &\leq 2 \|\hat{v}\|^2_{0,\hat{T}} + 2 \left\| \tfrac{\partial}{\partial \hat{x}_i} \hat{v} \right\|^2_{0,\hat{T} \setminus \hat{\Gamma}^{(K)}}. \end{aligned} \tag{3.2.13}$$

In order to transform $\left\| \frac{\partial}{\partial \hat{x}_i} \hat{v} \right\|_{0,\hat{T} \setminus \hat{\Gamma}^{(K)}}$ back to the original simplex T, apply the chain rule to obtain

$$\tfrac{\partial}{\partial \hat{x}_i} \hat{v}\left(\hat{x}\right) = \tfrac{\partial}{\partial \hat{x}_i} v\left(F(\hat{x})\right) = \sum_{j=1}^{d} \tfrac{\partial v}{\partial x_j}\left(F\left(\hat{x}\right)\right) \tfrac{\partial F_j}{\partial \hat{x}_i}\left(\hat{x}\right) = \nabla v\left(F\left(\hat{x}\right)\right) \cdot DF\left(\hat{x}\right) \cdot e_i,$$

where DF denotes the Jacobian of F, and derive the estimate

$$\begin{aligned} &\left\| \tfrac{\partial}{\partial \hat{x}_i} \hat{v} \right\|^2_{0,\hat{T} \setminus \hat{\Gamma}^{(K)}} = \left(\frac{\mu_{d-1}\left(\hat{E}_i\right)}{d\,\mu_d(T)} \right) \|\nabla v \cdot DF \cdot e_i\|^2_{0,T \setminus \Gamma^{(K)}} \\ \leq &\left(\frac{\mu_{d-1}\left(\hat{E}_i\right)}{d\,\mu_d(T)} \right) |F(e_i) - p|^2 \, |v|^2_{1,T \setminus \Gamma^{(K)}} \leq \left(\frac{\mu_{d-1}\left(\hat{E}_i\right)}{d\,\mu_d(T)} \right) h_k^2 \, |v|^2_{1,T \setminus \Gamma^{(K)}}. \end{aligned} \tag{3.2.14}$$

Inserting (3.2.12) and (3.2.14) into (3.2.13) yields

$$\left\| \frac{\partial}{\partial \hat{x}_i} \left(\hat{\lambda}_{d+1} \hat{v} \right) \right\|^2_{0,\hat{T}\setminus\hat{\Gamma}^{(K)}} \leq \frac{2}{d} \left(\frac{\mu_{d-1}\left(\hat{E}_i\right)}{\mu_d(T)} \right) \left(\|v\|^2_{0,T} + h_k^2 \, |v|^2_{1,T\setminus\Gamma^{(K)}} \right)$$

and together with

$$\left\| \left[\!\left[\hat{\lambda}_{d+1} \hat{v} \right]\!\right] \right\|^2_{0,\hat{\Gamma}_l\cap\hat{T}} \leq \left\| \left[\!\left[\hat{v} \right]\!\right] \right\|^2_{0,\hat{\Gamma}_l\cap\hat{T}} \leq \left(\frac{\mu_{d-1}(E)}{\mu_{d-1}\left(\hat{E}_i\right)} \right) \left\| \left[\!\left[v \right]\!\right] \right\|^2_{0,\Gamma_l\cap T}$$

using again (3.2.12) follows the estimate

$$\left\| \lambda_p^{(k)} v \right\|^2_{0,E} \leq c \left(1 + \tfrac{1}{\mathfrak{c}} \right) \left(h_k^{-1} \|v\|^2_{0,T} + h_k \, |v|^2_{1,T\setminus\Gamma^{(K)}} + \sum_{l=k+1}^{K} (1+\mathfrak{c})^{l-k} \, C_{k,l} \left\| \left[\!\left[v \right]\!\right] \right\|^2_{0,\Gamma_l\cap T} \right)$$

with a constant c only depending on the space dimension d and the shape regularity σ of $\mathcal{T}^{(k)}$. Plugging this into (3.2.11) concludes the proof. □

As the triangulation $\mathcal{T}^{(k)}$, $k \in \mathbb{N}$, resolves the cells $G \in \mathcal{G}^{(k)}\setminus\mathcal{G}^{(k)}_\infty$ and interfaces Γ_l, $l < k$, any $\Gamma_l \cap \partial G$ can be represented by a set of edges. Then, applying the previous trace lemma leads to an estimate controlling the jump across Γ_l on the side of G.

Lemma 3.2.13. *Let $k \in \mathbb{N}$, $\omega \subseteq G \in \mathcal{G}^{(k)}\setminus\mathcal{G}^{(k)}_\infty$ a patch that is locally partitioned by $\mathcal{T}^{(k)}$, i.e. there is a set $\mathcal{T}^{(k)}_\omega \subseteq \mathcal{T}^{(k)}$ such that $\omega = \bigcup_{T\in\mathcal{T}^{(k)}_\omega} T$, and $1 \leq l \leq k$. It holds*

$$\|v\|^2_{0,\Gamma_l\cap\partial\omega} \leq c \left(1 + \tfrac{1}{\mathfrak{c}} \right) \left(h_k^{-1} \|v\|^2_{0,\omega} + h_k \, |v|^2_{1,\omega\setminus\Gamma^{(K)}} + \sum_{s=k+1}^{K} (1+\mathfrak{c})^{s-k} \, C_{k,s} \left\| \left[\!\left[v \right]\!\right] \right\|^2_{0,\Gamma_s\cap\omega} \right)$$

for all $v \in \mathcal{C}^1_{K,0}$ with $K > k$ and a constant c that depends only on the space dimension d, the shape regularity σ of $\mathcal{T}^{(k)}$.

Proof. Let $v \in \mathcal{C}^1_{K,0}$, $K > k$, and denote by $\mathcal{E}^{(k)}_\omega \subset \mathcal{E}^{(k)}$ the set of faces of simplices $T \in \mathcal{T}^{(k)}_\omega$. Then, there is a subset of faces $\mathcal{E}^{(k)}_{\partial\omega} \subset \mathcal{E}^{(k)}_\omega$ that resolves the cell boundary, i.e.

$$\partial\omega = \bigcup_{E\in\mathcal{E}^{(k)}_{\partial\omega}} E.$$

For each face $E \in \mathcal{E}^{(k)}_{\partial\omega}$, there is a simplex $T_E \subset \mathcal{T}^{(k)}_\omega$ such that E is a face of T_E. Note that a single simplex $T \in \mathcal{T}^{(k)}_\omega$ may contribute at most all of its $d+1$ faces to $\mathcal{E}^{(k)}_{\partial\omega}$. With the previous trace lemma for simplices (Lemma 3.2.12), it follows

$$\begin{aligned}
\|v\|^2_{0,\Gamma_l\cap\partial\omega} &= \sum_{E\in\mathcal{E}^{(k)}_{\partial\omega}} \|v\|^2_{0,E} \\
&\leq c' \left(1 + \tfrac{1}{\mathfrak{c}} \right) \sum_{E\in\mathcal{E}^{(k)}_{\partial\omega}} \left(h_k^{-1} \|v\|^2_{0,T_E} + h_k \, |v|^2_{1,T_E\setminus\Gamma^{(K)}} + \sum_{s=k+1}^{K} (1+\mathfrak{c})^{s-k} \, C_{k,s} \left\| \left[\!\left[v \right]\!\right] \right\|^2_{0,\Gamma_s\cap T_E} \right) \\
&\leq c \left(1 + \tfrac{1}{\mathfrak{c}} \right) \sum_{T\in\mathcal{T}^{(k)}_\omega} \left(h_k^{-1} \|v\|^2_{0,T} + h_k \, |v|^2_{1,T\setminus\Gamma^{(K)}} + \sum_{s=k+1}^{K} (1+\mathfrak{c})^{s-k} \, C_{k,s} \left\| \left[\!\left[v \right]\!\right] \right\|^2_{0,\Gamma_s\cap T} \right) \\
&\leq c \left(1 + \tfrac{1}{\mathfrak{c}} \right) \left(h_k^{-1} \|v\|^2_{0,\omega} + h_k \, |v|^2_{1,\omega\setminus\Gamma^{(K)}} + \sum_{s=k+1}^{K} (1+\mathfrak{c})^{s-k} \, C_{k,s} \left\| \left[\!\left[v \right]\!\right] \right\|^2_{0,\Gamma_s\cap\omega} \right)
\end{aligned}$$

with a constant c that only depends on the space dimension d and the shape regularity σ of $\mathcal{T}^{(k)}$. □

Recall that the triangulation $\mathcal{T}_G^{(k)} \subset \mathcal{T}^{(k)}$ is a local partition of $G \in \mathcal{G}^{(k)} \backslash \mathcal{G}_\infty^{(k)}$, $k \in \mathbb{N}$. Thus, setting $\omega = G$ in the previous lemma yields a cell-based version, see [78].

Corollary 3.2.14. *Let $k \in \mathbb{N}$, $G \in \mathcal{G}^{(k)} \backslash \mathcal{G}_\infty^{(k)}$, and $1 \leq l \leq k$. It holds*

$$\|v\|_{0,\Gamma_l \cap \partial G}^2 \leq c \left(1 + \tfrac{1}{\mathfrak{c}}\right) \left(d_k^{-1} \|v\|_{0,G}^2 + d_k \, |v|_{1,G \backslash \Gamma^{(K)}}^2 + \sum_{s=k+1}^{K} (1+\mathfrak{c})^{s-k} \, C_{k,s} \, \|[\![v]\!]\|_{0,\Gamma_s \cap G}^2 \right)$$

for all $v \in \mathcal{C}_{K,0}^1$ with $K > k$ and a constant c that depends only on the space dimension d, the shape regularity σ of $\mathcal{T}^{(k)}$ and the constant δ in (3.1.20).

3.2.3 Projections to $\mathcal{H}_K$

This section is devoted to the construction of a projection $\Pi_{\mathcal{H}_K} : \mathcal{H} \to \mathcal{H}_K$ from the fractal space $\mathcal{H}$ to a finite scale approximation $\mathcal{H}_K$, $K \in \mathbb{N}$, that satisfies approximation and stability properties of the form

$$\|v - \Pi_{\mathcal{H}_K} v\|_0^2 \leq \left(1 + \tfrac{1}{\mathfrak{c}}\right) c \, d_K^2 \, \|v\|_{\mathcal{H}}^2 , \qquad \|\Pi_{\mathcal{H}_K} v\|_{\mathcal{H}} \leq c' \, \|v\|_{\mathcal{H}}$$

for all $v \in \mathcal{H}$ with suitable constants $c, c' > 0$.

To motivate the approach presented hereafter, observe that $v \in \mathcal{H}_K$ consists of cell-based, local contributions $v|_G \in H^1(G)$, $G \in \mathcal{G}^{(K)}$. Colloquially, the projection $\Pi_{\mathcal{H}_K}$ has to approximate $v|_G$, $v \in \mathcal{H}$, on the cells $G \in \mathcal{G}^{(K)} \backslash \mathcal{G}_\infty^{(K)}$ by a function $\Pi_{\mathcal{H}_K} v|_G \in H^1(G)$ and thus remove all jumps across $\Gamma \cap G$ in a suitable fashion. Constructing the projection $\Pi_{\mathcal{H}_K}$ such that it preserves the mean value of v, i.e. $⨍_G v \, dx = ⨍_G \Pi_{\mathcal{H}_K} v \, dx$, guarantees that $v - \Pi_{\mathcal{H}_K} v$ has mean value zero and facilitates the straightforward application of previously derived Poincaré inequalities in the derivation of the desired approximation and stability properties.

Observe that $|||\cdot|||_G^2 = (⨍_G \cdot \, dx)^2 + |\cdot|_{1,G}^2$ is a norm on $H^1(G)$, which is equivalent to the standard H^1-norm. The best approximation of $v|_G$ with respect to $|||\cdot|||_G$ in the affine space $⨍_G v \, dx + \mathcal{W}$, where $\mathcal{W} = \{w \in H^1(G) : ⨍_G w \, dx = 0\}$, will turn out to be a good choice.

Definition 3.2.15. For every $K \in \mathbb{N}$, define the linear projection $\Pi_{\mathcal{H}_K} : \mathcal{H} \to \mathcal{H}_K$ by setting

$$(\Pi_{\mathcal{H}_K} v)|_G = \begin{cases} \operatorname*{arg\,min}_{v_K \in H^1(G)} \{ |v - v_K|_{1,G \backslash \Gamma} : ⨍_G v - v_K \, dx = 0 \}, & G \in \mathcal{G}^{(K)} \backslash \mathcal{G}_\infty^{(K)} \\ v|_G, & G \in \mathcal{G}_\infty^{(K)} \end{cases}$$

for all $G \in \mathcal{G}^{(K)}$ and $v \in \mathcal{H}$.

This operator is indeed a linear projection and well-defined. For $G \in \mathcal{G}^{(K)} \setminus \mathcal{G}_\infty^{(K)}$, the set of feasible functions from $H^1(G)$ with appropriate mean value—the affine space $⨍_G v\,dx + \mathcal{W}$—is closed and convex. Therefore, the quadratic optimization problem associated with the cell $G \in \mathcal{G}^{(K)} \setminus \mathcal{G}_\infty^{(K)}$ consists of minimizing a strictly convex functional over a closed and convex set, thus admitting a unique solution. Its critical point, the local contribution $v_K \in H^1(G)$, and hence unique global minimizer satisfies

$$\int_{G\setminus\Gamma} \nabla v \cdot \nabla w\,dx = \int_{G\setminus\Gamma} \nabla v_K \cdot \nabla w\,dx \qquad \forall w \in \mathcal{W}. \tag{3.2.15}$$

Example 3.2.16 (1D best approximation)**.** Consider $\Pi_{\mathcal{H}_K}$ for a 1D domain $\Omega \subset \mathbb{R}$ on the cell $G \in \mathcal{G}^{(K)} \setminus \mathcal{G}_\infty^{(K)}$. The cell (interval) G is partitioned into subintervals $I_1, \dots, I_m$ by the finer level interface networks Γ_l, $l > K$. On these subintervals, $v|_{I_i}$ is piecewise in $H^1(I_i)$, $1 \le i \le m$. Colloquially, $\Pi_{\mathcal{H}_K} v|_G$ can be constructed from the $v|_{I_i}$ by shifting the individual functions, i.e. adding a specific constant, such that $\Pi_{\mathcal{H}_K} v|_G$ is continuous across finer interfaces Γ_l, $l > K$, and $\int_G \Pi_{\mathcal{H}_K} v\,dx = \int_G v\,dx$ holds. In higher space dimensions, the strategy of gluing piecewise $H^1(I_i)$ functions at the interior jumps of $v|_G$, $v \in \mathcal{H}$, to obtain a $H^1(G)$ function for the entirety of G does not work in general.

Lemma 3.2.17 (local stability property)**.** *Let $K \in \mathbb{N}$ and $G \in \mathcal{G}^{(K)} \setminus \mathcal{G}_\infty^{(K)}$. The linear projection $\Pi_{\mathcal{H}_K}$ satisfies*

$$|\Pi_{\mathcal{H}_K} v|_{1,G} \le |v|_{1,G\setminus\Gamma} \qquad \forall v \in \mathcal{H}.$$

Proof. Let $v \in \mathcal{H}$, denote $v_K = \Pi_{\mathcal{H}_K} v|_G$ and use equation (3.2.15) as well as the Cauchy-Schwarz inequality to obtain

$$|v_K|_{1,G}^2 = \int_{G\setminus\Gamma} \nabla v \cdot \nabla v_K\,dx \le |v|_{1,G\setminus\Gamma}\,|v_K|_{1,G}\,. \qquad \square$$

Approximation property

The following global approximation lemma is a consequence of the local Poincaré inequality for star-shaped domains (Proposition 3.2.8).

Lemma 3.2.18. *Let $K \in \mathbb{N}$. The linear projection $\Pi_{\mathcal{H}_K}$ satisfies*

$$\|v - \Pi_{\mathcal{H}_K} v\|_0^2 \le \left(1 + \tfrac{1}{\mathfrak{c}}\right) c_K\, d_K \left(d_K\, |v|_{1,\Omega\setminus\Gamma}^2 + \sum_{l=K+1}^{\infty} (1+\mathfrak{c})^{l-K}\, C_{K,l}\, \|[\![v]\!]\|_{0,\Gamma_l}^2 \right)$$

for all $v \in \mathcal{H}$ with a constant $c_K > 0$ that only depends on the dimension d and the shape regularity parameter ρ_K.

Proof. Let $v \in \mathcal{H}$ and note that

$$\|v - \Pi_{\mathcal{H}_K} v\|_0^2 = \sum_{G\in\mathcal{G}^{(K)}} \|v - \Pi_{\mathcal{H}_K} v\|_{0,G}^2 = \sum_{G\in\mathcal{G}^{(K)}\setminus\mathcal{G}_\infty^{(K)}} \|v - \Pi_{\mathcal{H}_K} v\|_{0,G}^2\,, \tag{3.2.16}$$

since $\Pi_{\mathcal{H}_K}$ is the identity on cells $G \in \mathcal{G}_\infty^{(K)}$. Henceforth, consider the cells $G \in \mathcal{G}^{(K)} \setminus \mathcal{G}_\infty^{(K)}$ and observe that $⨍_G v - \Pi_{\mathcal{H}_K} v \, dx = 0$, i.e. $v - \Pi_{\mathcal{H}_K} v$ has mean value zero on G, by definition of $\Pi_{\mathcal{H}_K}$ in 3.2.15. Moreover, $\Pi_{\mathcal{H}_K} v|_G$ does not jump across Γ_l, $l > K$. Thus, applying the local Poincaré inequality for star-shaped sets (Proposition 3.2.8) on the cells $G \in \mathcal{G}^{(K)} \setminus \mathcal{G}_\infty^{(K)}$ yields

$$\begin{aligned} &\|v - \Pi_{\mathcal{H}_K} v\|_{0,G}^2 \\ &\leq \left(1 + \tfrac{1}{\mathfrak{c}}\right) c_G \, d_K \left(d_K \, |v - \Pi_{\mathcal{H}_K} v|_{1,G\setminus\Gamma}^2 + \sum_{l=K+1}^{\infty} (1+c)^{l-K} \, C_{K,l} \, \|[\![v]\!]\|_{0,\Gamma_l \cap G}^2 \right) \end{aligned}$$

with a constant c_G that only depends on the space dimension d and shape regularity ρ_G. Using the triangle inequality and local stability given by Lemma 3.2.17 results in

$$|v - \Pi_{\mathcal{H}_K} v|_{1,G\setminus\Gamma} \leq 2 \, |v|_{1,G\setminus\Gamma}$$

and the local approximation estimate

$$\|v - \Pi_{\mathcal{H}_K} v\|_{0,G}^2 \leq \left(1 + \tfrac{1}{\mathfrak{c}}\right) c_G \, d_K \left(d_K \, |v|_{1,G\setminus\Gamma}^2 + \sum_{l=K+1}^{\infty} (1+\mathfrak{c})^{l-K} \, C_{K,l} \, \|[\![v]\!]\|_{0,\Gamma_l \cap G}^2 \right).$$

Finally, insertion into (3.2.16) concludes the proof. □

Remark 3.2.19. Let $K \in \mathbb{N}$ and $G \in \mathcal{G}^{(K)} \setminus \mathcal{G}_\infty^{(K)}$. Following the previous proof, it becomes evident that there is a local variant of the global approximation lemma establishing

$$\|v - \Pi_{\mathcal{H}_K} v\|_{0,G}^2 \leq \left(1 + \tfrac{1}{\mathfrak{c}}\right) c_G \, d_K \left(d_K \, |v|_{1,G\setminus\Gamma}^2 + \sum_{l=K+1}^{\infty} (1+\mathfrak{c})^{l-K} \, C_{K,l} \, \|[\![v]\!]\|_{0,\Gamma_l \cap G}^2 \right)$$

for all $v \in \mathcal{H}$ with a constant $c_G > 0$ that only depends on the dimension d and the shape regularity parameter ρ_G.

With additional assumptions on the geometry of the interface network Γ, we infer an approximation property for the projections $\Pi_{\mathcal{H}_K}$, $K \in \mathbb{N}$.

Corollary 3.2.20 (approximation property)**.** *Let $K \in \mathbb{N}$ and assume that the condition*

$$r_K \, (1+\mathfrak{c})^{-K} \leq d_K \tag{3.2.17}$$

on the geometry of the interface network Γ is fulfilled. Then the linear projection $\Pi_{\mathcal{H}_K}$ has the approximation property

$$\|v - \Pi_{\mathcal{H}_K} v\|_0^2 \leq \left(1 + \tfrac{1}{\mathfrak{c}}\right) c_K \, d_K^2 \, \|v\|_{\mathcal{H}}^2 \qquad \forall v \in \mathcal{H}$$

with a constant $c_K > 0$ that only depends on the dimension d and the shape regularity ρ_K.

Proof. Let $v \in \mathcal{H}$. By the definition of r_K in (3.1.5) and condition (3.2.17), it holds

$$(1+\mathfrak{c})^{-K} C_{K,l} \leq r_K (1+\mathfrak{c})^{-K} C_l \leq d_K C_l \tag{3.2.18}$$

and applying the global approximation Lemma 3.2.18 leads to the estimate

$$\begin{aligned}\|v - \Pi_{\mathcal{H}_K} v\|_0^2 &\leq \left(1+\tfrac{1}{\mathfrak{c}}\right) c_K d_K^2 \left(|v|_{1,\Omega\setminus\Gamma}^2 + \sum_{l=K+1}^{\infty} (1+\mathfrak{c})^l C_l \, \|[\![v]\!]\|_{0,\Gamma_l}^2 \right) \\ &\leq \left(1+\tfrac{1}{\mathfrak{c}}\right) c_K d_K^2 \, \|v\|_{\mathcal{H}}^2\end{aligned}$$

with a constant c_K only depending on the dimension d and the shape regularity ρ_K. □

Stability

For each fixed $K \in \mathbb{N}$, the boundedness of $\Pi_{\mathcal{H}_K}$

$$\|\Pi_{\mathcal{H}_K} v\|_{\mathcal{H}} \leq \kappa_K \|v\|_{\mathcal{H}} \qquad \forall v \in \mathcal{H}$$

with a constant $\kappa_K > 0$ is a consequence of the closed graph theorem and can be derived with general results from functional analysis. In preparation for this proof, let us show the following well-known statement.

Lemma 3.2.21. *Let $P : \mathcal{X} \to \mathcal{X}$ be a linear projection on a Banach space $\mathcal{X}$. If* $\ker P$ *and* $\operatorname{im} P$ *are closed, then P is continuous.*

Proof. Let $(v_n)_{n\in\mathbb{N}}$ be a sequence in $\mathcal{X}$, such that $v_n \to v \in \mathcal{X}$ and $Pv_n \to v_K$. Thus, $v_n - Pv_n \in \ker P$, since

$$P(v_n - Pv_n) = Pv_n - Pv_n = 0$$

and $v_n - Pv_n \to v - v_K$. As $\ker P$ and $\operatorname{im} P$ are closed by assumption, it holds

$$v - v_K \in \ker P \text{ and } v_K \in \operatorname{im} P.$$

This leads to $0 = P(v - v_K) = Pv - Pv_K$ and ultimately $Pv = Pv_K = v_K$, since $Pw = w$ for all $w \in \operatorname{im} P$. Altogether, the graph of P is closed as $Pv_n \to v_K = Pv$. Applying the closed graph theorem yields the statement of the lemma. □

Lemma 3.2.22. *Let $K \in \mathbb{N}$. The linear projection $\Pi_{\mathcal{H}_K}$ is continuous with respect to the $\|\cdot\|_{\mathcal{H}}$-norm and thus bounded.*

Proof. Note, that $\operatorname{im} \Pi_{\mathcal{H}_K} = \mathcal{H}_K$ is a complete subspace of $\mathcal{H}$ and thus closed. Let us show that the kernel $\ker \Pi_{\mathcal{H}_K} \subset \mathcal{H}$ is closed and subsequently apply the previous lemma.
Let $(v_n)_{n\in\mathbb{N}}$ be a sequence in $\ker \Pi_{\mathcal{H}_K}$ converging to $v \in \mathcal{H}$. For all $G \in \mathcal{G}_\infty^{(K)}$ and $n \in \mathbb{N}$, it holds $(\Pi_{\mathcal{H}_K} v_n)|_G \equiv 0$ and hence $(\Pi_{\mathcal{H}_K} v)|_G \equiv 0$.

For all $G \in \mathcal{G}^{(K)} \backslash \mathcal{G}_\infty^{(K)}$ and $n \in \mathbb{N}$, it holds $\int_G v_n \, dx = 0$ and inserting into (3.2.15) yields

$$\int_{G\backslash\Gamma} \nabla v_n \cdot \nabla w \, dx = 0 \qquad \forall w \in \mathcal{W}.$$

Therefore, as $n \to \infty$, we conclude $\int_G v \, dx = 0$ and

$$\int_{G\backslash\Gamma} \nabla v \cdot \nabla w \, dx = 0 \qquad \forall w \in \mathcal{W}$$

by continuous embedding $\mathcal{H} \subset L^2(\Omega) \subset L^1(\Omega)$. The optimization problem associated with $\Pi_{\mathcal{H}_K} v|_G$ on $G \in \mathcal{G}^{(K)} \backslash \mathcal{G}_\infty^{(K)}$ admits a unique solution $v_K \in H^1(G)$ (see Definition 3.2.15 f.) satisfying

$$\int_{G\backslash\Gamma} \nabla v_K \cdot \nabla w \, dx = \int_{G\backslash\Gamma} \nabla v \cdot \nabla w \, dx = 0 \qquad \forall w \in \mathcal{W}.$$

Thus, $\Pi_{\mathcal{H}_K} v|_G = v_K \equiv 0$ for any $G \in \mathcal{G}^{(K)} \backslash \mathcal{G}_\infty^{(K)}$ and $v \in \ker \Pi_{\mathcal{H}_K}$. □

Although the previous arguments establish the boundedness of $\Pi_{\mathcal{H}_K}$ and therefore the existence of a constant κ_K, its dependence on $K \in \mathbb{N}$ remains to be investigated. The upcoming considerations aim at assessing this dependence and identifying sufficient conditions for the uniform stability of $\Pi_{\mathcal{H}_K}$.

As a first step, we provide a bound for the jump contributions to $\|\Pi_{\mathcal{H}_K} v\|_{\mathcal{H}}$ in terms of $\|v\|_{\mathcal{H}}$.

Lemma 3.2.23. *Let $K \in \mathbb{N}$ and assume that conditions* (3.1.20) *and* (3.2.17) *are fulfilled. Then it holds*

$$\sum_{l=1}^{K} (1+\mathfrak{c})^l C_l \, \|[\![v - \Pi_{\mathcal{H}_K} v]\!]\|_{0,\Gamma_l}^2 \leq c \left(1 + \tfrac{1}{\mathfrak{c}}\right)^2 d_K \left(\sum_{l=1}^{K} (1+\mathfrak{c})^l C_l \right) \|v\|_{\mathcal{H}}^2$$

for all $v \in \mathcal{C}_{L,0}^1$ with $L > K$ and a constant c only depending on the space dimension d, shape regularity ρ_K, shape regularity σ_G of $\mathcal{T}^{(K)}$ and the constant δ in (3.1.20).

Proof. Let $K \in \mathbb{N}$, $v \in \mathcal{C}_{L,0}^1$ with $L > K$ and consider that

$$\begin{aligned} \|[\![v - \Pi_{\mathcal{H}_K} v]\!]\|_{0,\Gamma_l}^2 &= \sum_{\substack{G,G' \in \mathcal{G}^{(K)} \\ G \neq G'}} \int_{\Gamma_l \cap \partial G \cap \partial G'} \left((v - \Pi_{\mathcal{H}_K} v)|_G - (v - \Pi_{\mathcal{H}_K} v)|_{G'} \right)^2 d\Gamma_l \\ &\leq 4 \sum_{G \in \mathcal{G}^{(K)}} \|v - \Pi_{\mathcal{H}_K} v\|_{0,\Gamma_l \cap \partial G}^2 \end{aligned} \tag{3.2.19}$$

holds for $l \leq K$. As $\Pi_{\mathcal{H}_K} v$ does not jump across Γ_s, $s > K$, applying trace Corollary 3.2.14 and using the local stability of $\Pi_{\mathcal{H}_K}$ (Lemma 3.2.17) leads to

$$\begin{aligned} \|v - \Pi_{\mathcal{H}_K} v\|_{0,\Gamma_l \cap \partial G}^2 \leq c' \left(1 + \tfrac{1}{\mathfrak{c}}\right) \Bigg(& d_K^{-1} \|v - \Pi_{\mathcal{H}_K} v\|_{0,G}^2 \\ & + 4 d_K \, |v|_{1,G\backslash\Gamma^{(L)}}^2 + \sum_{s=K+1}^{L} (1+\mathfrak{c})^{s-K} C_{K,s} \, \|[\![v]\!]\|_{0,\Gamma_s \cap G}^2 \Bigg) \end{aligned}$$

with a constant c' only depending on the space dimension d, the shape regularity σ of $\mathcal{T}^{(k)}$ and the constant δ in (3.1.20). Furthermore, the local approximation estimate from Remark 3.2.19 states

$$\|v - \Pi_{\mathcal{H}_K} v\|_{0,G}^2 \leq \left(1 + \tfrac{1}{\mathfrak{c}}\right) c_G \, d_K \left(d_K \, |v|_{1,G\setminus\Gamma^{(L)}}^2 + \sum_{s=K+1}^{L} (1+\mathfrak{c})^{s-K} \, C_{K,s} \, \|[\![v]\!]\|_{0,\Gamma_s\cap G}^2 \right)$$

with a constant c_G depending only on the space dimension d and the shape regularity parameter ρ_G. Thus, inserting the local approximation estimate and using equation (3.2.18), which is a consequence of condition (3.2.17), yields

$$\begin{aligned} &\|v - \Pi_{\mathcal{H}_K} v\|_{0,\Gamma_l\cap\partial G}^2 \\ &\leq c \left(1 + \tfrac{1}{\mathfrak{c}}\right)^2 d_K \left(|v|_{1,G\setminus\Gamma^{(L)}}^2 + \sum_{s=K+1}^{L} (1+\mathfrak{c})^{s} \, C_s \, \|[\![v]\!]\|_{0,\Gamma_s\cap G}^2 \right) \end{aligned} \tag{3.2.20}$$

with a constant c depending only on the space dimension d, the shape regularity parameter ρ_G, the shape regularity σ of $\mathcal{T}^{(k)}$ and the constant δ in (3.1.20). Plugging (3.2.20) into (3.2.19) and summing over $G \in \mathcal{G}^{(K)}$ results in the assertion. □

Next, a stability result for the projections $\Pi_{\mathcal{H}_K}$, $K \in \mathbb{N}$, will be proved.

Proposition 3.2.24. *Assume that* (3.1.20) *and condition* (3.2.17) *are fulfilled. Then the projection* $\Pi_{\mathcal{H}_K}$, $K \in \mathbb{N}$, *is stable in the sense that*

$$\|\Pi_{\mathcal{H}_K} v\|_{\mathcal{H}}^2 \leq c \left(1 + \tfrac{1}{\mathfrak{c}}\right)^3 d_K \left(\sum_{l=1}^{K} (1+\mathfrak{c})^l C_l \right) \|v\|_{\mathcal{H}}^2 \qquad \forall v \in \mathcal{H}$$

holds with a constant c *that only depends on the space dimension* d, *shape regularity* ρ_K, *shape regularity* σ_G *of* $\mathcal{T}^{(K)}$ *and the constant* δ *in* (3.1.20).

Proof. As $\bigcup_{L\in\mathbb{N}} \mathcal{C}_{L,0}^1$ is dense in $\mathcal{H}$ and $\Pi_{\mathcal{H}_K}$ is continuous for each fixed $K \in \mathbb{N}$ by Lemma 3.2.22, it is sufficient to prove the assertion for any $v \in \mathcal{C}_{L,0}^1$ with arbitrary $L \geq K$. To that end, it suffices to show a corresponding bound for $\|I - \Pi_{\mathcal{H}_K}\|_{\mathcal{H}}$, since

$$\|\Pi_{\mathcal{H}_K} v\|_{\mathcal{H}} \leq \|v - \Pi_{\mathcal{H}_K} v\|_{\mathcal{H}} + \|v\|_{\mathcal{H}} \,.$$

Now, apply the triangle inequality as well as the stability of $\Pi_{\mathcal{H}_K}$ with respect to $|\cdot|_{1,\Omega\setminus\Gamma}$ implied by Lemma 3.2.17 and use that, by construction, $\Pi_{\mathcal{H}_K} v$ does not jump across Γ_l, $l > K$, to obtain

$$\begin{aligned} \|v - \Pi_{\mathcal{H}_K} v\|_{\mathcal{H}}^2 &= |v - \Pi_{\mathcal{H}_K} v|_{1,\Omega\setminus\Gamma}^2 + \left(1 + \tfrac{1}{\mathfrak{c}}\right) \sum_{l=1}^{L} (1+\mathfrak{c})^l \, C_l \, \|[\![v - \Pi_{\mathcal{H}_K} v]\!]\|_{0,\Gamma_l}^2 \\ &\leq 4 \, \|v\|_{\mathcal{H}}^2 + \left(1 + \tfrac{1}{\mathfrak{c}}\right) \sum_{l=1}^{K} (1+\mathfrak{c})^l \, C_l \, \|[\![v - \Pi_{\mathcal{H}_K} v]\!]\|_{0,\Gamma_l}^2 \,. \end{aligned}$$

Estimating the remaining jump contributions with Lemma 3.2.23 concludes the proof. □

Finally, uniform stability of $\Pi_{\mathcal{H}_K}$ is obtained, if d_K balances out the exponential factors in the statement of Proposition 3.2.24.

Corollary 3.2.25. *Assume that* (3.1.20) *and condition* (3.2.17) *are satisfied and additionally*

$$d_K \left(\sum_{l=1}^{K} (1+\mathfrak{c})^l C_l \right) \leq c_0, \qquad K \in \mathbb{N}, \tag{3.2.21}$$

holds with a constant c_0 independent of K. Then the projections $\Pi_{\mathcal{H}_K}$, $K \in \mathbb{N}$, are uniformly stable, i.e.,

$$\|\Pi_{\mathcal{H}_K} v\|_{\mathcal{H}} \leq c \, \|v\|_{\mathcal{H}} \qquad \forall v \in \mathcal{H}$$

holds for each $K \in \mathbb{N}$ with a constant c depending only on the space dimension d, shape regularity ρ of $\mathcal{G}^{(k)}K$, shape regularity σ of $\mathcal{T}^{(K)}$, the constant δ in (3.1.20)*, the constant c_0 in* (3.2.21)*, and the material constant $\mathfrak{c}$.*

Remark 3.2.26. In the spirit of Occam's razor, one strives for a version of the previous corollary that is sufficiently general while relying on as few and nonrestrictive assumptions as possible. Pursuing this ideal, one would like to get rid of the condition stated in (3.2.21) by using an estimate of the form

$$\|[\![v - \Pi_{\mathcal{H}_K} v]\!]\|_{0,\Gamma_l} \overset{?}{\leq} c_l \, \|[\![v]\!]\|_{0,\Gamma_l},$$

where $c_l > 0$ is an appropriate constant, instead of Lemma 3.2.23. This way, contributions involving the $|\cdot|_1$- or $\|\cdot\|_0$-norms need not scale suitably with the factors $(1+c)^l C_l$ in the proof of Proposition 3.2.24.
However, finding such an estimate is impossible as the following counter-example suggests. Recall the 1D setting from Example 3.2.16. In particular, suppose that $G = (0,1) \subset \mathbb{R}$ is partitioned into $I_1 = (0, x_1)$, $I_2 = (x_1, x_2)$ and $I_3 = (x_2, 1)$ with $x_1 < x_2$. Consider a piecewise constant $v|_G$, $v \in \mathcal{H}$, namely $v|_{I_1} := 0$, $v|_{I_2} := z \neq 0$ and $v|_{I_3} := 0$. Then $\Pi_{\mathcal{H}_K} v|_G = (x_2 - x_1) z \neq 0$ and

$$0 < \|v - \Pi_{\mathcal{H}_K} v\|_{0,\partial G} \not\leq c_l \, \|v\|_{0,\partial G} = 0.$$

Extending this construction to higher space dimensions is straightforward.

Thus, condition (3.2.21) is a consequence of the fact that the jump contributions of $\|\Pi_{\mathcal{H}_K} v\|_{\mathcal{H}}$ cannot be bounded by the jump contributions of $\|v\|_{\mathcal{H}}$ alone. It relates the geometry of the interface network represented by d_K and C_l with the material constant $\mathfrak{c}$ and implies highly localized $\Gamma^{(K)}$ for feasible $\mathfrak{c} > 0$, e.g., the network described in Example 3.1.1. The condition is quite restrictive and actually excludes regular Cantor networks such as [61, 126]. For given interface geometry, (3.2.21) leads to an upper bound for $\mathfrak{c}$, while (3.2.17) establishes a lower bound.

Example 3.2.27. Recall the Cantor-type interface network introduced in Example 3.1.1. In this specific instance, the geometric condition given by (3.2.17) is satisfied,

if $\mathfrak{c} \geq 1$. Moreover, condition (3.2.21) is fulfilled, if there is a constant c_0 independent of K such that

$$d_K \sum_{l=1}^{K} (1+\mathfrak{c})^l C_l = \sqrt{2}\, 4^{-K} \left(2^K (1+\mathfrak{c})^K - 1\right) \tfrac{2+2\mathfrak{c}}{1+2\mathfrak{c}} \leq c_0$$

holds. This is the case for all $\mathfrak{c} \leq 1$. In conjunction, $\mathfrak{c} = 1$ is the only possible parameter choice to adhere to both conditions.

3.2.4 Projections to finite element spaces $\mathcal{S}_K$

The next objective is to introduce projections $\Pi_{\mathcal{S}_K} : \mathcal{H} \longrightarrow \mathcal{S}_K$, $K \in \mathbb{N}$, that approximate functions from the fractal space $\mathcal{H}$ by suitable candidates from a finite element space $\mathcal{S}_K$. As nodal interpolation loses its approximation properties in higher space dimensions, the coefficients of the FE basis functions are determined by Clément-type local averaging. This Clément-type operator is chosen such that it smoothes jumps across the interfaces $(\Gamma_l)_{k<l\leq K}$, is computationally feasible and fulfills approximation and stability properties of the form

$$\|v - \Pi_{\mathcal{S}_K} v\|_0^2 \leq \left(1 + \tfrac{1}{\mathfrak{c}}\right) c\, h_K^2 \, \|v\|_{\mathcal{H}}^2 , \qquad \|\Pi_{\mathcal{S}_K} v\|_{\mathcal{H}} \leq c' \, \|v\|_{\mathcal{H}}$$

for all $v \in \mathcal{H}$ with suitable constants $c, c' > 0$.

Definition 3.2.28. For any $K \in \mathbb{N}$, the Clément-type projection $\Pi_{\mathcal{S}_K} : \mathcal{H} \to \mathcal{S}_K$ is defined by setting

$$\Pi_{\mathcal{S}_K} v = \sum_{p \in \mathcal{N}^{(K)}} \left(\Pi_{\omega_p} v\right) \lambda_p^{(K)}, \tag{3.2.22}$$

where $\omega_p = \operatorname{supp} \lambda_p^{(K)}$, $p \in \mathcal{N}^{(K)}$, denotes the support of the corresponding nodal basis function and $\Pi_{\omega_p} : \mathcal{H} \to \mathbb{R}$ satisfies the properties

(P1) Π_{ω_p} is linear, i.e., it holds $\Pi_{\omega_p}(v+w) = \Pi_{\omega_p} v + \Pi_{\omega_p} w$ for all $v, w \in \mathcal{H}$.

(P2) Π_{ω_p} is the identity on constant functions, i.e. $\Pi_{\omega_p} v = v$ for all $v \in \mathcal{P}_0(G)$, $\omega_p \subset G \in \mathcal{G}^{(K)}$.

(P3) Π_{ω_p} satisfies a uniform stability estimate of the form

$$\left\| \Pi_{\omega_p} v \right\|_{0,\omega_p} \leq c \, \|v\|_{0,\omega_p} \quad \forall v \in \mathcal{H}$$

for all patches ω_p, $p \in \mathcal{N}^{(K)}$, where the constant c only depends on the space dimension d and shape regularity σ of $\mathcal{T}^{(K)}$.

There are a plethora of local operators Π_{ω_p} satisfying (P1)-(P3) that are known from standard finite element theory. Some examples include the original Clément operator or the Oswald projection (see e.g. [21, 98]). However, the L^2-stability required by (P3) is not a standard property of all such operators in the literature, e.g., it does not hold for the Scott-Zhang quasi-interpolation [120]. To fix ideas, consider the following example.

Example 3.2.29 (Weighted Clément quasi-projection)**.** Let $\omega_p = \operatorname{supp} \lambda_p^{(K)}$, $p \in \mathcal{N}^{(K)}$, and consider the operator $\Pi_{\omega_p} : \mathcal{H} \to \mathbb{R}$ given by

$$\Pi_{\omega_p} v = \frac{\int_{\omega_p} \lambda_p^{(K)} \, v \, dx}{\int_{\omega_p} \lambda_p^{(K)} \, dx}. \tag{3.2.23}$$

The weighted Clément quasi-projection is a projection onto $\mathbb{R}$ with respect to the weighted $L^2(\omega_p)$ inner product $(u, v) = \int_{\omega_p} \lambda_p^{(K)} \, u \, v \, dx$. For a detailed discussion of this operator, see e.g. [23] and [22].
Showing (P1)-(P2) is straightforward and property (P3) follows with the Cauchy-Schwarz inequality (see e.g. [25]). It holds

$$\left\| \Pi_{\omega_p} v \right\|_{0,\omega_p} \leq \mu_d(\omega_p)^{\frac{1}{2}} \left| \int_{\omega_p} \lambda_p^{(K)} \, dx \right|^{-1} \left\| \lambda_p^{(K)} \right\|_{0,\omega_p} \|v\|_{0,\omega_p} \leq c \, \|v\|_{0,\omega_p},$$

for all $v \in L^2(\Omega)$ with a constant $c = \max_{p \in \mathcal{N}^{(K)}} \mu_d(\omega_p)^{\frac{1}{2}} \left| \int_{\omega_p} \lambda_p^{(K)} \, dx \right|^{-1} \left\| \lambda_p^{(K)} \right\|_{0,\omega_p}$ that is independent of the patch size, since the second term is bounded by $\mu_d(\omega_p)^{-1}$ according to the mean value theorem and the third by $\mu_d(\omega_p)^{1/2}$.

Approximation property

Expanding general arguments presented in [22, Lemma 2.5], a local approximation estimate on the patches ω_p, $p \in \mathcal{N}^{(K)}$, can be shown.

Lemma 3.2.30. *Let $K \in \mathbb{N}$, $p \in \mathcal{N}^{(K)}$ and consider the patch $\omega = \operatorname{supp} \lambda_p^{(K)}$. Then it holds*

$$\|v - \Pi_\omega v\|_{0,\omega}^2 \leq \left(1 + \tfrac{1}{\mathfrak{c}}\right) c \, h_K \left(h_K \, |v|_{1,\omega \setminus \Gamma}^2 + \sum_{l=K+1}^{\infty} (1 + \mathfrak{c})^{l-K} \, C_{K,l} \, \|[\![v]\!]\|_{0,\Gamma_l \cap \omega}^2 \right)$$

for all $v \in \mathcal{H}$ with a constant c that only depends on the space dimension d and shape regularity σ of $\mathcal{T}^{(K)}$.

Proof. Let $v \in \mathcal{H}$ and observe that

$$\left\| \Pi_\omega v - \fint_\omega v \, dx \right\|_{0,\omega}^2 = \left\| \Pi_\omega \left(v - \fint_\omega v \, dx \right) \right\|_{0,\omega}^2 \leq c \left\| v - \fint_\omega v \, dx \right\|_{0,\omega}^2$$

holds with a constant c that only depends on the space dimension d and shape regularity σ of $\mathcal{T}^{(K)}$ due to properties (P1)-(P3) of Π_ω. Then, using the triangle inequality yields

$$\|v - \Pi_\omega v\|_{0,\omega}^2 \leq 2 \left\| v - \fint_\omega v \, dx \right\|_{0,\omega}^2 + 2 \left\| \Pi_\omega v - \fint_\omega v \, dx \right\|_{0,\omega}^2 \leq (2 + 2c) \left\| v - \fint_\omega v \, dx \right\|_{0,\omega}^2.$$

Since $\omega \subseteq G \in \mathcal{G}^{(K)} \setminus \mathcal{G}_\infty^{(K)}$ is star-shaped, applying the Poincaré inequality for star-shaped sets (Proposition 3.2.8) leads to the assertion. □

Next up is a similar estimate on patches $\omega \subseteq G \in \mathcal{G}^{(k)} \setminus \mathcal{G}_\infty^{(k)}$, $k \leq K$, that are locally partitioned by $\mathcal{T}_\omega^{(k)} \subseteq \mathcal{T}^{(k)}$. By assumption, $\mathcal{T}^{(K)}$ is a refinement of $\mathcal{T}^{(k)}$. Thus, there is a set of simplices $\mathcal{T}_\omega^{(K)} = \{T \in \mathcal{T}^{(K)} : T \cap \omega \neq \varnothing\} \subseteq \mathcal{T}^{(K)}$ that is a triangulation of ω. Denote with $\mathcal{N}_\omega^{(K)} = \{p \in \mathcal{N}^{(K)} : \mu_d\left(\operatorname{supp} \lambda_p^{(K)} \cap \omega\right) > 0\}$ the set of vertices, whose associated nodal basis functions $\{\lambda_p^{(K)}|_\omega\}$ form a partition of unity on ω, i.e.

$$\sum_{p \in \mathcal{N}_\omega^{(K)}} \lambda_p^{(K)}|_\omega = 1 \tag{3.2.24}$$

in ω. Moreover, denote with $\nu_p = \operatorname{supp} \lambda_p^{(K)}|_\omega$ the support patch corresponding to $p \in \mathcal{N}_\omega^{(K)}$.

Proposition 3.2.31. *Let $K \in \mathbb{N}$ and $\omega \subseteq G \in \mathcal{G}^{(k)} \setminus \mathcal{G}_\infty^{(k)}$, $k \leq K$, a patch that is locally partitioned by $\mathcal{T}_\omega^{(k)} \subseteq \mathcal{T}^{(k)}$. Then the projection $\Pi_{\mathcal{S}_K} : \mathcal{H} \to \mathcal{S}_K$ satisfies*

$$\|v - \Pi_{\mathcal{S}_K} v\|_{0,\omega}^2 \leq \left(1 + \tfrac{1}{\mathfrak{c}}\right) c\, h_K \left(h_K \, |v|_{1,\omega\setminus\Gamma}^2 + \sum_{l=K+1}^{\infty} (1+\mathfrak{c})^{l-K} \, C_{K,l} \, \|[\![v]\!]\|_{0,\Gamma_l \cap \omega}^2 \right)$$

for all $v \in \mathcal{H}$ with a constant c that only depends on the space dimension d and shape regularity σ of $\mathcal{T}^{(K)}$.

Proof. Let $v \in \mathcal{H}$. Thus, it follows with (3.2.24) and Hölder's inequality in ℓ^1

$$\begin{aligned}
\|v - \Pi_{\mathcal{S}_K} v\|_{0,\omega}^2 &= \left\| \sum_{p \in \mathcal{N}_\omega^{(K)}} \left(v - \Pi_{\nu_p} v\right) \lambda_p^{(K)} \right\|_{0,\omega}^2 \\
&\leq \int_\omega \left(\sum_{p \in \mathcal{N}_\omega^{(K)}} \left| v - \Pi_{\nu_p} v \right|^2 \lambda_p^{(K)} \right) \left(\sum_{p \in \mathcal{N}_\omega^{(K)}} \lambda_p^{(K)} \right) dx.
\end{aligned}$$

Using (3.2.24) and applying the local approximation estimate from Lemma 3.2.30 yields

$$\begin{aligned}
&\|v - \Pi_{\mathcal{S}_K} v\|_{0,\omega}^2 \\
&\leq \sum_{p \in \mathcal{N}_\omega^{(K)}} \int_\omega \left| v - \Pi_{\nu_p} v \right|^2 \lambda_p^{(K)} \, dx \leq \sum_{p \in \mathcal{N}_\omega^{(K)}} \left\| v - \Pi_{\nu_p} v \right\|_{0,\omega}^2 \\
&\leq \sum_{p \in \mathcal{N}_\omega^{(K)}} \left(1 + \tfrac{1}{\mathfrak{c}}\right) c\, h_K \left(h_K \, |v|_{1,\nu_p\setminus\Gamma}^2 + \sum_{l=K+1}^{\infty} (1+\mathfrak{c})^{l-K} \, C_{K,l} \, \|[\![v]\!]\|_{0,\Gamma_l \cap \nu_p}^2 \right) \\
&\leq \left(1 + \tfrac{1}{\mathfrak{c}}\right) (d+1)\, c\, h_K \left(h_K \, |v|_{1,\omega\setminus\Gamma}^2 + \sum_{l=K+1}^{\infty} (1+\mathfrak{c})^{l-K} \, C_{K,l} \, \|[\![v]\!]\|_{0,\Gamma_l \cap \omega}^2 \right)
\end{aligned}$$

with a constant c depending only on the space dimension d and shape regularity σ of $\mathcal{T}^{(K)}$, as any part of ω is covered by at most $d+1$ patches ν_p, $p \in \mathcal{N}_\omega^{(K)}$. □

As was the case for the projection $\Pi_{\mathcal{H}_K}$, additional assumptions on the geometry imply a similar approximation property.

Corollary 3.2.32 (approximation property)**.** *Let $K \in \mathbb{N}$ and $\omega \subseteq G \in \mathcal{G}^{(k)} \backslash \mathcal{G}_\infty^{(k)}$, $k \leq K$, a patch that is locally partitioned by $\mathcal{T}_\omega^{(k)} \subseteq \mathcal{T}^{(k)}$. Assume that condition* (3.2.17) *is fulfilled. Then the projection $\Pi_{\mathcal{S}_K} : \mathcal{H} \to \mathcal{S}_K$ satisfies*

$$\|v - \Pi_{\mathcal{S}_K} v\|_{0,\omega}^2 \leq \left(1 + \tfrac{1}{\mathfrak{c}}\right) c\, h_K^2 \left(|v|_{1,\omega\backslash\Gamma}^2 + \sum_{l=K+1}^{\infty} (1+\mathfrak{c})^l\, C_l\, \|[\![v]\!]\|_{0,\Gamma_l\cap\omega}^2 \right)$$

for all $v \in \mathcal{H}$ with a constant c that only depends on the space dimension d, shape regularity σ of $\mathcal{T}^{(K)}$ and the constant δ in (3.1.20)*.*

A global version is obtained by setting $\omega = \Omega$ and following the proof of Proposition 3.2.31.

Corollary 3.2.33 (global approximation property)**.** *Let $K \in \mathbb{N}$ and assume that condition* (3.2.17) *is fulfilled. Then the projection $\Pi_{\mathcal{S}_K} : \mathcal{H} \to \mathcal{S}_K$ satisfies*

$$\|v - \Pi_{\mathcal{S}_K} v\|_0^2 \leq \left(1 + \tfrac{1}{\mathfrak{c}}\right) c\, h_K^2\, \|v\|_{\mathcal{H}}^2$$

for all $v \in \mathcal{H}$ with a constant c that only depends on the space dimension d, shape regularity σ of $\mathcal{T}^{(K)}$ and the constant δ in (3.1.20)*.*

Stability

Proving the desired stability property involves essentially the same arguments as for the projection $\Pi_{\mathcal{H}_K}$. Let us start with a first auxiliary result bounding the local gradient contributions to $\|\Pi_{\mathcal{S}_K} v\|_{\mathcal{H}}$ in terms of $\|v\|_{\mathcal{H}}$.

Lemma 3.2.34. *Let $K \in \mathbb{N}$ and $\omega \subseteq G \in \mathcal{G}^{(k)} \backslash \mathcal{G}_\infty^{(k)}$, $k \leq K$, a patch that is locally partitioned by $\mathcal{T}_\omega^{(k)} \subseteq \mathcal{T}^{(k)}$. Assume that condition* (3.2.17) *is fulfilled. Then the projection $\Pi_{\mathcal{S}_K} : \mathcal{H} \to \mathcal{S}_K$ satisfies*

$$|\Pi_{\mathcal{S}_K} v|_{1,\omega\backslash\Gamma}^2 \leq \left(1 + \tfrac{1}{\mathfrak{c}}\right) c \left(|v|_{1,\omega\backslash\Gamma}^2 + \sum_{l=K+1}^{\infty} (1+\mathfrak{c})^l\, C_l\, \|[\![v]\!]\|_{0,\Gamma_l\cap\omega}^2 \right) \qquad \forall v \in \mathcal{H}$$

with a constant c only depending on the space dimension d, shape regularity σ of $\mathcal{T}^{(K)}$ and the constant δ in (3.1.20)*.*

Proof. Let $v \in \mathcal{H}$. Since $\{\lambda_p^{(K)}|_\omega : p \in \mathcal{N}_\omega^{(K)}\}$ is a partition of unity on ω (see (3.2.24)), it holds $\sum_{p\in\mathcal{N}_\omega^{(K)}} \nabla\lambda_p^{(K)}|_\omega = 0$ almost everywhere in ω. Thus, using Hölder's inequality in ℓ^1 leads to the estimate

$$\begin{aligned} |\Pi_{\mathcal{S}_K} v|_{1,\omega\backslash\Gamma}^2 &= \left| \sum_{p\in\mathcal{N}_\omega^{(K)}} \left(v - \Pi_{\nu_p} v\right) \nabla\lambda_p^{(K)} \right|_{1,\omega\backslash\Gamma}^2 \\ &\leq \int_{\omega\backslash\Gamma} \left(\sum_{p\in\mathcal{N}_\omega^{(K)}} h_K^{-2} \left| \left(I - \Pi_{\nu_p}\right) v|_{\nu_p} \right|^2 \right) \left(\sum_{p\in\mathcal{N}_\omega^{(K)}} \left|\nabla\lambda_p^{(K)}\right|^2 h_K^2 \right) dx. \end{aligned}$$

Due to the construction of the triangulation $\mathcal{T}^{(K)}$ in Section 3.1.4, the second sum is bounded by a constant c' that only depends on its shape regularity σ. Then, applying the local approximation property from Corollary 3.2.32 yields

$$\begin{aligned}|\Pi_{\mathcal{S}_K} v|^2_{1,\omega\setminus\Gamma} &\leq c' \sum_{p\in\mathcal{N}_\omega^{(K)}} h_K^{-2} \left\|v - \Pi_{\nu_p} v\right\|^2_{0,\nu_p} \\ &\leq \left(1+\tfrac{1}{\mathfrak{c}}\right) c \sum_{p\in\mathcal{N}_\omega^{(K)}} \left(|v|^2_{1,\nu_p\setminus\Gamma} + \sum_{l=K+1}^{\infty} (1+\mathfrak{c})^l\, C_l \left\|[\![v]\!]\right\|^2_{0,\Gamma_l\cap\nu_p}\right)\end{aligned}$$

with a constant c depending only on the space dimension d, the shape regularity σ of $\mathcal{T}^{(K)}$ and the constant δ in (3.1.20). Finally, any part of ω is covered at most $d+1$ times by local patches $\nu_p \in \Omega_\omega^{(K)}$ resulting in the assertion. □

The next step is to bound the jump contributions to $\|\Pi_{\mathcal{S}_K} v\|_{\mathcal{H}}$ in terms of $\|v\|_{\mathcal{H}}$.

Lemma 3.2.35. *Let $K \in \mathbb{N}$ and $\omega \subseteq G \in \mathcal{G}^{(k)}\setminus\mathcal{G}_\infty^{(k)}$, $k \leq K$, a patch that is locally partitioned by $\mathcal{T}_\omega^{(k)} \subseteq \mathcal{T}^{(k)}$. Assume that conditions* (3.1.20) *and* (3.2.17) *are fulfilled. Then the projection $\Pi_{\mathcal{S}_K} : \mathcal{H} \to \mathcal{S}_K$ satisfies*

$$\begin{aligned}&\sum_{l=k+1}^{K} (1+\mathfrak{c})^l C_l \int_{\Gamma_l\cap\omega} [\![v - \Pi_{\mathcal{S}_K} v]\!]^2 \, d\Gamma_l \\ \leq\, & c\left(1+\tfrac{1}{\mathfrak{c}}\right)^2 h_K \left(\sum_{l=k+1}^{K} (1+\mathfrak{c})^l C_l\right)\left(|v|^2_{1,\omega\setminus\Gamma^{(L)}} + \sum_{s=K+1}^{L} (1+\mathfrak{c})^s\, C_s \left\|[\![v]\!]\right\|^2_{0,\Gamma_s\cap\omega}\right)\end{aligned}$$

for all $v \in \mathcal{C}^1_{L,0}$, $L > K$, with a constant c only depending on the space dimension d, shape regularity σ of $\mathcal{T}^{(K)}$ and the constant δ in (3.1.20).

Proof. Let $v \in \mathcal{C}^1_{L,0}$, $L > K$. By assumption, the triangulation $\mathcal{T}^{(K)}$ is a regular refinement of $\mathcal{T}^{(k)}$. Thus, the interface network $\Gamma^{(K)}$ splits ω into subcells $G_\omega = G\cap\omega$, $G \in \mathcal{G}^{(K)}$, that are locally partitioned by $\mathcal{T}^{(K)}_{G_\omega} \subseteq \mathcal{T}^{(K)}$. Note that $\Pi_{\mathcal{S}_K} v$ does not contain any jumps inside the G_ω, since it does not jump across Γ_s, $s > K$. The rest of the proof is similar to the one of Lemma 3.2.23. It holds

$$\begin{aligned}\left\|[\![v - \Pi_{\mathcal{S}_K} v]\!]\right\|^2_{0,\Gamma_l\cap\omega} &= \sum_{\substack{G,G'\in\mathcal{G}^{(K)}\\ G\neq G'}} \int_{\Gamma_l\cap\partial G_\omega\cap\partial G'_\omega} \left((v-\Pi_{\mathcal{S}_K} v)|_{G_\omega} - (v-\Pi_{\mathcal{S}_K} v)|_{G'_\omega}\right)^2 d\Gamma_l \\ &\leq 4 \sum_{G\in\mathcal{G}^{(K)}} \|v - \Pi_{\mathcal{S}_K} v\|^2_{0,\Gamma_l\cap\partial G_\omega} \qquad (3.2.25)\end{aligned}$$

for $k \leq l \leq K$ and applying trace Lemma 3.2.13 as well as (3.2.18), which is a consequence of condition (3.2.17), leads to

$$\begin{aligned}\|v - \Pi_{\mathcal{S}_K} v\|^2_{0,\Gamma_l\cap\partial G_\omega} \leq\, & c\left(1+\tfrac{1}{\mathfrak{c}}\right)\Big(h_K^{-1}\|v - \Pi_{\mathcal{S}_K} v\|^2_{0,G_\omega} + h_K\,|v - \Pi_{\mathcal{S}_K} v|^2_{1,G_\omega\setminus\Gamma^{(L)}} \\ &+ h_K \sum_{s=K+1}^{L} (1+\mathfrak{c})^s\, C_s \left\|[\![v]\!]\right\|^2_{0,\Gamma_s\cap G_\omega}\Big) \qquad (3.2.26)\end{aligned}$$

with a constant c only depending on the space dimension d, the shape regularity σ of $\mathcal{T}^{(K)}$ and the constant δ in (3.1.20). With the local stability of $\Pi_{\mathcal{S}_K}$ (Lemma 3.2.34) follows

$$\begin{aligned}|v - \Pi_{\mathcal{S}_K} v|^2_{1,G_\omega\setminus\Gamma^{(L)}} &\leq 2\,|v|^2_{1,G_\omega\setminus\Gamma^{(L)}} + 2\,|\Pi_{\mathcal{S}_K} v|^2_{1,G_\omega\setminus\Gamma^{(L)}} \\ &\leq \left(1+\tfrac{1}{\mathfrak{c}}\right) c \left(|v|^2_{1,G_\omega\setminus\Gamma^{(L)}} + \sum_{s=K+1}^{L} (1+\mathfrak{c})^s\, C_s\, \|[\![v]\!]\|^2_{0,\Gamma_s\cap G_\omega} \right),\end{aligned}$$

where the constant c has the same dependencies as in (3.2.26). Inserting this estimate and the local approximation property (Corollary 3.2.32) into (3.2.20) yields

$$\begin{aligned}&\|v - \Pi_{\mathcal{S}_K} v\|^2_{0,\Gamma_l\cap\partial G_\omega} \\ &\leq c\,\left(1+\tfrac{1}{\mathfrak{c}}\right)^2 h_K \left(|v|^2_{1,G_\omega\setminus\Gamma^{(L)}} + \sum_{s=K+1}^{L} (1+\mathfrak{c})^s\, C_s\, \|[\![v]\!]\|^2_{0,\Gamma_s\cap G_\omega} \right),\end{aligned} \tag{3.2.27}$$

where the constant c has the same dependencies as in (3.2.26). Plugging (3.2.27) into (3.2.25) and summing over $G \in \mathcal{G}^{(K)}$ concludes the proof. □

Remark 3.2.36. Assuming that conditions (3.1.20) and (3.2.17) are fulfilled, arguments similar to the derivation of equation (3.2.27) imply that for $K \in \mathbb{N}$ and $\omega \subseteq G \in \mathcal{G}^{(k)}\setminus\mathcal{G}^{(k)}_\infty$, $k \leq K$, a patch that is locally partitioned by $\mathcal{T}^{(k)}_\omega \subseteq \mathcal{T}^{(k)}$, the projection $\Pi_{\mathcal{S}_K} : \mathcal{H} \to \mathcal{S}_K$ satisfies

$$\|v - \Pi_{\mathcal{S}_K} v\|^2_{0,\Gamma_l\cap\partial\omega} \leq c\,\left(1+\tfrac{1}{\mathfrak{c}}\right)^2 h_K \left(|v|^2_{1,\omega\setminus\Gamma^{(L)}} + \sum_{s=K+1}^{L} (1+\mathfrak{c})^s\, C_s\, \|[\![v]\!]\|^2_{0,\Gamma_s\cap\omega} \right),$$

for interfaces Γ_l, $l \leq k$, for all $v \in \mathcal{C}^1_{L,0}$, $L > K$, with a constant c only depending on the space dimension d, shape regularity σ of $\mathcal{T}^{(K)}$ and the constant δ in (3.1.20).

Combining the previous findings leads to a global stability result.

Proposition 3.2.37. *Let $K \in \mathbb{N}$ and assume that* (3.1.20) *and condition* (3.2.17) *are fulfilled. Then the projection $\Pi_{\mathcal{S}_K}$ is stable in the sense that*

$$\|\Pi_{\mathcal{S}_K} v\|^2_{\mathcal{H}} \leq c\left(1+\tfrac{1}{\mathfrak{c}}\right)^3 \left(4 + h_K \left(\sum_{l=1}^{K} (1+\mathfrak{c})^l C_l\right)\right) \|v\|^2_{\mathcal{H}} \qquad \forall v \in \mathcal{H}$$

holds with a constant c that only depends on the space dimension d, shape regularity ρ_K, shape regularity σ of $\mathcal{T}^{(K)}$ and the constant δ in (3.1.20).

Proof. By a density argument, it is sufficient to prove the assertion for any $v \in \mathcal{C}^1_{L,0}$ with arbitrary $L \geq K$. To that end, we derive a corresponding bound for $\|I - \Pi_{\mathcal{S}_K}\|_{\mathcal{H}}$, since

$$\|\Pi_{\mathcal{S}_K} v\|_{\mathcal{H}} \leq \|v - \Pi_{\mathcal{S}_K} v\|_{\mathcal{H}} + \|v\|_{\mathcal{H}}\,.$$

Now, apply the triangle inequality as well as the stability of $\Pi_{\mathcal{S}_K}$ with respect to $|\cdot|_{1,\Omega\setminus\Gamma^{(L)}}$ implied by Lemma 3.2.34 and use that, by construction, $\Pi_{\mathcal{S}_K} v$ does not jump across Γ_l, $l > K$, to obtain

$$\begin{aligned}\|v - \Pi_{\mathcal{S}_K} v\|_{\mathcal{H}}^2 &= |v - \Pi_{\mathcal{S}_K} v|_{1,\Omega\setminus\Gamma^{(L)}}^2 + \left(1 + \tfrac{1}{\mathfrak{c}}\right) \sum_{l=1}^{L} (1+\mathfrak{c})^l \, C_l \, \|[\![v - \Pi_{\mathcal{S}_K} v]\!]\|_{0,\Gamma_l}^2 \\ &\leq 4\, c \left(1 + \tfrac{1}{\mathfrak{c}}\right) \|v\|_{\mathcal{H}}^2 + \left(1 + \tfrac{1}{\mathfrak{c}}\right) \sum_{l=1}^{K} (1+\mathfrak{c})^l \, C_l \, \|[\![v - \Pi_{\mathcal{S}_K} v]\!]\|_{0,\Gamma_l}^2\end{aligned}$$

with a constant c only depending on the space dimension d, shape regularity σ of $\mathcal{T}^{(K)}$ and the constant δ in (3.1.20). Estimating the remaining jump contributions with Lemma 3.2.23 concludes the proof. □

Finally, uniform stability of $\Pi_{\mathcal{S}_K}$ is obtained, if h_K balances out the exponential factors in the statement of Proposition 3.2.37.

Corollary 3.2.38. *Assume that* (3.1.20) *and conditions* (3.2.17) *and* (3.2.21) *are satisfied. Then the projections* $\Pi_{\mathcal{S}_K}$, $K \in \mathbb{N}$, *are uniformly stable, i.e.,*

$$\|\Pi_{\mathcal{S}_K} v\|_{\mathcal{H}} \leq c \, \|v\|_{\mathcal{H}} \qquad \forall v \in \mathcal{H}$$

holds with a constant c depending only on the space dimension d, shape regularity ρ of $\mathcal{G}^{(k)}K$, shape regularity σ of $\mathcal{T}^{(K)}$, the constant δ in (3.1.20)*, the constant c_0 in* (3.2.21)*, and the material constant $\mathfrak{c}$.*

By composing the previously established projections $\Pi_{\mathcal{H}_K}$ and $\Pi_{\mathcal{S}_k}$, a projection

$$\Pi_{k,K} : \mathcal{H} \to \mathcal{S}_k$$

is obtained, that exhibits similar approximation and stability properties. For $K = k$, this construction of $\Pi_{k,k}$ coincides with the projection Π_k presented in [78].

Definition 3.2.39. For every $k, K \in \mathbb{N}$ with $K \geq k$, define the quasi projection

$$\Pi_{k,K} = \Pi_{\mathcal{S}_k} \circ \Pi_{\mathcal{H}_K} : \mathcal{H} \to \mathcal{S}_k.$$

The operator $\Pi_{k,K}$ inherits the approximation property from the (quasi) projections $\Pi_{\mathcal{S}_k}$ and $\Pi_{\mathcal{H}_K}$.

Theorem 3.2.40. *Let $k, K \in \mathbb{N}$ with $K \geq k$ and assume that the conditions* (3.1.20)*,* (3.2.17)*,* (3.2.21) *hold. Then the quasi projection $\Pi_{k,K} : \mathcal{H} \to \mathcal{S}_k$ possesses the approximation property*

$$\|v - \Pi_{k,K} v\|_0 \leq c h_k \, \|v\|_{\mathcal{H}} \qquad v \in \mathcal{H}$$

with a constant c that only depends on the space dimension d, shape regularity ρ_K of $\mathcal{G}^{(K)}$, shape regularity σ_k of $\mathcal{T}^{(k)}$, the constant δ in (3.1.20) *and the constant c_0 in* (3.2.21)*.*

Proof. With the triangle inequality, the stability of $\Pi_{\mathcal{S}_k}$ from Corollary 3.2.38 as well as the approximation properties from Corollary 3.2.20 and 3.2.32, the assertion follows via

$$\|v - \Pi_{k,K} v\|_0 \leq \|v - \Pi_{\mathcal{S}_k} v\|_0 + \|\Pi_{\mathcal{S}_k} (v - \Pi_{\mathcal{H}_K} v)\|_0 \leq c h_k \|v\|_{\mathcal{H}} . \qquad \square$$

The uniform stability of $\Pi_{k,K}$ follows directly from the uniform stability of $\Pi_{\mathcal{H}_K}$ and $\Pi_{\mathcal{S}_k}$ (see Corollary 3.2.25 and 3.2.38).

Theorem 3.2.41. *Let $k, K \in \mathbb{N}$ with $K \geq k$ and assume that the conditions* (3.1.20), (3.2.17), (3.2.21) *hold. Then the quasi projection $\Pi_{k,K} : \mathcal{H} \to \mathcal{S}_k$ is uniformly stable, i.e. it holds*

$$\|\Pi_{k,K} v\|_{\mathcal{H}} \leq c \|v\|_{\mathcal{H}} \qquad v \in \mathcal{H}$$

with a constant c that only depends on the space dimension d, shape regularity ρ_K of $\mathcal{G}^{(K)}$, shape regularity σ_k of $\mathcal{T}^{(k)}$, the constant δ in (3.1.20) *and the constant c_0 in* (3.2.21).

This construction of quasi projections $\Pi_{k,K}$ is rather flexible and guarantees their usefulness for the development of various multilevel methods and corresponding numerical analysis. Colloquially, the choice of K and k introduces adjustable building blocks, whose relative contributions can be adapted depending on the numerical algorithm and desired statements one wants to prove. Next, the previous findings will be applied to iterative subspace correction methods and a multiscale finite element method based on localized orthogonal decomposition, respectively.

3.3 Numerical homogenization

Now that the existence of projection operators with suitable stability and approximation properties has been established in the context of fractal interface networks, let us turn our attention to the construction of fast and efficient numerical methods for problem (3.1.10).

First, a LOD-type approach by Målqvist and Peterseim [89] will be considered. Note that the broader class of multiscale finite element methods is not suited for the efficient solution of spatial problems arising from the time-discretization of contact problems with friction as described in Chapter 2. A key benefit of these methods is that the computationally expensive part, i.e. assembling the multiscale finite element basis and corresponding stiffness matrix, can be treated in an offline stage and reused for different right hand sides. Unfortunately, the system matrix of the truncated linear correction problem (2.7.4) generally differs for individual time steps, which wastes the reusability and makes iterative subspace correction methods the superior choice. Nonetheless, a simple application of LOD with cell-based localization by subspace correction, cf. [78], will be presented as a proof of concept. The corresponding multiscale discretization provides optimal a priori discretization error estimates. Extensions to patch-based localization in the spirit of [89] and computationally more efficient approaches analogous to [76] are possible, but will not be examined.

Thereafter, various subspace correction methods arising from cell- and patch-based subspace decompositions as well as parallel and sequential preconditioning will be introduced using ideas from [80]. Then, well-known results from subspace correction theory [134, 136] yield convergence rates that are independent from mesh size and scale parameters. Finally, the different subspace correction schemes and theoretical findings will be assessed in a series of numerical experiments with a highly localized fractal interface geometry. In further experiments with fractal interface geometries less and less covered by theory, the potential of the approach beyond the rigorous results will be demonstrated.

3.3.1 Multiscale finite element discretization

Following the delineation in [78], let us fix $k \in \mathbb{N}$ and construct a multiscale finite element space with the same dimension as $\mathcal{S}_k$, whose discretization error is of order h_k, based on the cells $G \in \mathcal{G}^{(k)}$.

Using the projection $\Pi_k : \mathcal{H} \to \mathcal{S}_k$ given by

$$\Pi_k = \Pi_{\mathcal{S}_k} \circ \Pi_{\mathcal{H}_k}, \tag{3.3.1}$$

cf. Definition 3.2.39 with the choice $K = k$, a suitable multiscale basis can be derived by applying local orthogonal decomposition [89] with localization by subspace decomposition [76].

Let $\mathcal{V}_k = \ker \Pi_k \subset \mathcal{H}$ denote the kernel of Π_k, i.e. the high-frequency features of $\mathcal{H}$ not represented by the projection Π_k, and $\mathcal{C} : \mathcal{H} \to \mathcal{V}_k$ the orthogonal projection of $\mathcal{H}$ onto $\mathcal{V}_k$ with respect to the scalar product $a(\cdot, \cdot)$ in $\mathcal{H}$. Then, the orthogonal complement $\mathcal{W}_k$ of $\ker \Pi_k$ in $\mathcal{H}$, i.e. $\mathcal{H} = \mathcal{W}_k \oplus \mathcal{V}_k$, is a multiscale finite element space

$$\mathcal{W}_k = \{v - \mathcal{C}v \,:\, v \in \mathcal{H}\} = \{v - \mathcal{C}v \,:\, v \in \mathcal{S}_k\} = \operatorname{span}\{(I - \mathcal{C})\lambda_p^{(k)} \,:\, p \in \mathcal{N}^{(k)}\}$$

and isomorphic to $\mathcal{S}_k$. Since $\dim \mathcal{W}_k = \dim \mathcal{S}_k$, it is viewed as a modified coarse space that is enriched with fine scale information.

Proceeding similarly to the error analysis first presented in Peterseim [97], Målqvist and Peterseim [89] and later also [76], the multiscale discretization

$$u_k \in \mathcal{W}_k : \qquad a(u_k, v) = (f, v) \qquad \forall v \in \mathcal{W}_k. \tag{3.3.2}$$

satisfies the following a priori discretization error estimate.

Lemma 3.3.1. *The discrete problem* (3.3.2) *possesses a unique solution* $u_k \in \mathcal{W}_k$ *given by*

$$u_k = (I - \mathcal{C})\Pi_k u, \tag{3.3.3}$$

where $u \in \mathcal{H}$ *denotes the unique solution of the fractal interface problem* (3.1.10)*. The discretization error has the representation* $u - u_k = \mathcal{C}u$ *and the error estimate*

$$\|u - u_k\|_{\mathcal{H}} \leq c h_k \|f\|_0$$

holds with c *depending only on the constants appearing in Theorem 3.2.40.*

Proof. The functions in $\mathcal{W}_k$ are a-orthogonal to the functions in the range of $\mathcal{C}$, hence

$$a(u - u_k, v) = 0 \quad \forall v \in \mathcal{W}_k$$

holds and u_k given by (3.3.3) is the unique solution of the discrete problem (3.3.2). Note that $\Pi_k(u - \Pi_k u) = 0$ holds and thus $u - \Pi_k u \in \ker \Pi_k$. Therefore, the error $u - u_k$ can be written as

$$u - u_k = u - (I - \mathcal{C})\Pi_k u = (I - \mathcal{C})(u - \Pi_k u) + \mathcal{C}u = \mathcal{C}u$$

and with the identity

$$\|\mathcal{C}u\|_{\mathcal{H}}^2 = a(u, \mathcal{C}u - \Pi_k \mathcal{C}u) = (f, \mathcal{C}u - \Pi_k \mathcal{C}u)$$

as well as the Cauchy-Schwarz inequality follows the estimate

$$\|\mathcal{C}u\|_{\mathcal{H}}^2 \leq \|f\|_0 \|\mathcal{C}u - \Pi_k \mathcal{C}u\|_0 \leq c h_k \|f\|_0 \|\mathcal{C}u\|_{\mathcal{H}},$$

where the second inequality is obtained using the approximation theorem 3.2.40 of Π_k. □

Although this multiscale space possesses the desired properties, it is computationally unfeasible, unfortunately. As is typical for this kind of construction, the multiscale basis functions $(I - \mathcal{C})\lambda_p^{(k)}$, $p \in \mathcal{N}^{(k)}$, of $\mathcal{W}_k$ have global support. This leads to a dense stiffness matrix, which is detrimental to the construction of fast and efficient solvers. To remedy this shortcoming, let us consider the following strategy of localization. The local approximations $\mathcal{C}_\nu : \mathcal{H} \to \mathcal{H}$, $\nu \in \mathbb{N}$, of $\mathcal{C}$ induce the approximate subspaces

$$\mathcal{W}_k^{(\nu)} = \operatorname{span}\{(I - \mathcal{C}_\nu)\lambda_p^{(k)} \,:\, p \in \mathcal{N}^{(k)}\}$$

and corresponding Galerkin discretizations

$$u_k^{(\nu)} \in \mathcal{W}_k^{(\nu)} : \qquad a(u_k^{(\nu)}, v) = (f, v) \qquad \forall v \in \mathcal{W}_k^{(\nu)}. \tag{3.3.4}$$

Provided that the sequence of approximations converges, there holds a discretization error estimate as derived in [76].

Theorem 3.3.2. *Assume that the approximations $\mathcal{C}_\nu : \mathcal{H} \to \mathcal{H}$, $\nu \in \mathbb{N}$, of $\mathcal{C}$ are convergent in the sense that*

$$\|\mathcal{C}v - \mathcal{C}_\nu v\|_a \leq q \|\mathcal{C}v\|_a, \qquad \nu \in \mathbb{N}, \tag{3.3.5}$$

holds for all $v \in \mathcal{H}$ with some convergence rate $q < 1$. Then, it holds the discretization error estimate

$$\left\|u - u_k^{(\nu)}\right\|_{\mathcal{H}} \leq (1 + q^\nu) \tfrac{\mathfrak{A}}{\mathfrak{a}} \|u - u_k\|_{\mathcal{H}} + q^\nu \tfrac{\mathfrak{A}}{\mathfrak{a}} \|u - \Pi_k u\|_{\mathcal{H}}, \qquad \nu \in \mathbb{N}. \tag{3.3.6}$$

Proof. Using $(I - \mathcal{C}_\nu)\Pi_k u \in \mathcal{W}_k^{(\nu)}$ and the representation $u_k = (I - \mathcal{C})\Pi_k u$ from (3.3.3) yields

$$\left\|u - u_k^{(\nu)}\right\|_a \leq \|u - (I - \mathcal{C}_\nu)\,\Pi_k u\|_a = \|(u - u_k) - (\mathcal{C}\Pi_k u - \mathcal{C}_\nu \Pi_k u)\|_a\,.$$

Next, the convergence of the approximations $\mathcal{C}_\nu$ by (3.3.5) together with (3.3.3) provides

$$\|\mathcal{C}\Pi_k u - \mathcal{C}_\nu \Pi_k u\|_a \leq q^\nu \|\mathcal{C}\Pi_k u\|_a \leq q^\nu(\|u - u_k\|_a + \|u - \Pi_k u\|_a),$$

which leads to the assertion with the triangle inequality and the norm equivalence (3.1.14). □

Cell-based subspace correction

All that remains to be done is to construct convergent local approximations $\mathcal{C}_\nu : \mathcal{H} \to \mathcal{H}$, $\nu \in \mathbb{N}$, by local subspace correction. The cell-based construction of $\Pi_{\mathcal{H}_k}$ via Definition 3.2.15 and locality of $\Pi_{\mathcal{S}_k}$ by Definition 3.2.28 motivate splitting

$$\mathcal{V}_k = \sum_{G \in \mathcal{G}^{(k)}} \mathcal{V}_G \tag{3.3.7}$$

into the subspaces

$$\mathcal{V}_G = \{(I - \Pi_k)v|_G \,:\, v \in \mathcal{H}\} \subset \mathcal{V}_k, \qquad G \in \mathcal{G}^{(k)}, \tag{3.3.8}$$

where the restriction to cells $v|_G$ is defined by $v|_G(x) = v(x)$ for $x \in G$ and $v|_G(x) = 0$ otherwise. Due to the trace Lemma 3.2.14 and the continuous embedding of $\mathcal{H}$ into $L^2(\Omega)$, the linear map $\mathcal{H} \ni v \to v|_G \in \mathcal{H}$ is uniformly bounded in $\mathcal{H}$ for all $G \in \mathcal{G}^{(k)}$ and fixed $k \in \mathbb{N}$.

Moreover, the subspaces $\mathcal{V}_G$ are closed. To prove this statement, note that convergence of a sequence $(v_i)_{i\in\mathbb{N}} \subset \mathcal{V}_G \subset \mathcal{V}_k$ to some $v \in \mathcal{H}$ implies $v \in \mathcal{V}_k$, i.e. $\Pi_k v = 0$, as $\mathcal{V}_k$ is closed. Then, $v = v|_G$, as $\operatorname{supp} v_i \subset G$ for all $i \in \mathbb{N}$, leads to $v = (I - \Pi_k)v|_G \in \mathcal{V}_G$. The following lemma institutes stability and boundedness of the cell-based splitting and is the central result of this section.

Lemma 3.3.3. *The splitting* (3.3.7) *is stable in the sense that for each $v \in \mathcal{V}_k$ there is a decomposition $(v_G)_{G\in\mathcal{G}^{(k)}}$ of v with $v_G \in \mathcal{V}_G$, $G \in \mathcal{G}^{(k)}$, such that*

$$\sum_{G \in \mathcal{G}^{(k)}} \|v_G\|_a^2 \leq K_1 \|v\|_a^2 \tag{3.3.9}$$

holds with a constant K_1 depending only on the constants appearing in Theorems 3.2.40, 3.2.41, the geometric constant C_0 in (3.1.6) *and the ellipticity constants $\mathfrak{a}$, $\mathfrak{A}$ from* (3.1.14).

Assume that the number of neighboring cells of G in $\mathcal{G}^{(k)}$ is uniformly bounded by $c_N \in \mathbb{R}$ for all $k \in \mathbb{N}$ and $G \in \mathcal{G}^{(k)}$. Then the splitting (3.3.7) *is bounded in the*

sense that for each $v \in \mathcal{V}_k$ all decompositions $(v_G)_{G\in\mathcal{G}^{(k)}}$ of v with $v_G \in \mathcal{V}_G$, $G \in \mathcal{G}^{(k)}$, satisfy

$$\|v\|_a^2 \leq K_2 \sum_{G\in\mathcal{G}^{(k)}} \|v_G\|_a^2 \tag{3.3.10}$$

with a constant K_2 depending only on c_N.

Proof. Note that the overlap of the subspaces $\mathcal{V}_G$, $G \in \mathcal{G}^{(k)}$, is $\Gamma^{(k)}$. Thus, the claimed boundedness in (3.3.10) with a constant K_2 depending only on c_N follows immediately with the Cauchy-Schwarz inequality.

By density and continuity arguments, it is sufficient to show (3.3.9) for $v \in \mathcal{V}_k \cap \mathcal{H}_K$. Let us consider the splitting of v into its local components

$$v_G = (I - \Pi_k)v|_G \in \mathcal{V}_G, \qquad G \in \mathcal{G}^{(k)}.$$

Due to the locality of the construction of Π_k, it holds $((I - \Pi_K)v)\,|_G = (I-\Pi_K)(v|_G)$, which implies

$$\begin{aligned}\|v_G\|_{\mathcal{H}}^2 = |v - \Pi_k v|_{1,G\setminus\Gamma^{(K)}}^2 + \sum_{l=1}^{k}(1+\mathfrak{c})^l C_l \,\|v - \Pi_k v\|_{0,\Gamma_l\cap\partial G}^2 \\ + \sum_{l=k+1}^{K} (1+\mathfrak{c})^l C_l \,\|[\![v]\!]\|_{0,\Gamma_l\cap G}^2 \,.\end{aligned} \tag{3.3.11}$$

The individual terms on the right hand side can be estimated as follows. Lemma 3.2.34 implies the local boundedness of $\Pi_{\mathcal{S}_k}$

$$|\Pi_{\mathcal{S}_k} w|_{1,G}^2 \leq (1 + \tfrac{1}{\mathfrak{c}})\, c\, |w|_{1,G}^2 \qquad \forall w \in \mathcal{H}_k,$$

since $w \in \mathcal{H}_k$ does not jump on levels finer than k. Then, the Cauchy-Schwarz inequality and Lemma 3.2.17 lead to

$$|v - \Pi_k v|_{1,G\setminus\Gamma^{(K)}}^2 \leq C\, |v|_{1,G\setminus\Gamma^{(K)}}^2 \tag{3.3.12}$$

with a constant C depending only on the space dimension d, shape regularity σ of $\mathcal{T}^{(k)}$ and the constant δ appearing in (3.1.20). Using the trace Lemma 3.2.14 in conjunction with local boundedness (3.3.12), as well as the geometric conditions (3.1.6), (3.2.17) and (3.2.21), the second term is estimated according to

$$\begin{aligned}&\sum_{l=1}^{k}(1+\mathfrak{c})^l C_l \,\|v - \Pi_k v\|_{0,\Gamma_l\cap\partial G}^2 \\ &\leq C\Big((1+\mathfrak{c})^k C_k d_k^{-1} \,\|v - \Pi_k v\|_{0,G}^2 + (1+\mathfrak{c})^k C_k d_k \,|v|_{1,G\setminus\Gamma^{(K)}}^2 \\ &\qquad + \sum_{l=k+1}^{K} (1+\mathfrak{c})^l C_{k,l} C_k \,\|[\![v]\!]\|_{0,\Gamma_l\cap G}^2 \Big) \\ &\leq C' \left(d_k^{-2} \,\|v - \Pi_k v\|_{0,G}^2 + |v|_{1,G\setminus\Gamma^{(K)}}^2 + \sum_{l=k+1}^{K} (1+\mathfrak{c})^l C_l \,\|[\![v]\!]\|_{0,\Gamma_l\cap G}^2 \right)\end{aligned}$$

with C' additionally depending on the material constant $\mathfrak{c}$, the constant δ in (3.1.20) and the constants appearing in (3.1.6) and (3.2.21). After inserting the previous findings into (3.3.11), summing over G and estimating d_k by h_k via (3.1.20) yield

$$\sum_{G\in\mathcal{G}^{(k)}} \|v_G\|_{\mathcal{H}}^2 \leq C'' \left(h_k^{-2} \|v - \Pi_k v\|_0^2 + \|v\|_{\mathcal{H}}^2 \right).$$

Finally, the approximation property stated in Proposition 3.2.40 and norm equivalence (3.1.14) give rise to the assertion. □

With the previous lemma, it is straightforward to construct local approximations $\mathcal{C}_\nu$ based on the preconditioner

$$T = \sum_{G\in\mathcal{G}^{(k)}} P_G$$

with a-orthogonal Ritz projections $P_G : \mathcal{H} \to \mathcal{V}_G$, $G \in \mathcal{G}^{(k)}$, given by

$$P_G w \in \mathcal{V}_G : \qquad a(P_G w, v) = a(w, v) \qquad \forall v \in \mathcal{V}_G \tag{3.3.13}$$

for $w \in \mathcal{H}$. Now, Lemma 3.3.3 and a proof similar to [80, Lemma 3.1] show

$$1/K_1 a(v, v) \leq a(Tv, v) \leq K_2 a(v, v) \qquad \forall v \in \mathcal{V}_k$$

or, equivalently, the bound $\kappa \leq K_1 K_2$ of the condition number $\kappa = \|T\|_a \|T^{-1}\|_a$ of T restricted to $\mathcal{V}_k$, see [80, Theorem 3.2].

The local approximations $\mathcal{C}_\nu$ of $\mathcal{C}$ are defined by a basic damped Richardson iteration

$$\mathcal{C}_{\nu+1} = \mathcal{C}_\nu + \omega T(I - \mathcal{C}_\nu), \qquad \mathcal{C}_0 = 0, \tag{3.3.14}$$

with a suitable damping parameter ω. It holds $\mathcal{C}_\nu v \in \mathcal{V}_k$, $\nu \in \mathbb{N}$, for any $v \in \mathcal{H}$ and convergence of the Richardson iteration (3.3.14) is established by elementary arguments, see e.g. [33, Chapter 8].

Theorem 3.3.4. *Assume that the number of neighboring cells of G from $\mathcal{G}^{(k)}$ is uniformly bounded by $c_N \in \mathbb{R}$ for all $k \in \mathbb{N}$ and $G \in \mathcal{G}^{(k)}$. Then the approximations $\mathcal{C}_\nu$, $\nu \in \mathbb{N}$, of $\mathcal{C}$ defined in* (3.3.14) *are convergent for $\omega < 2/K_2$ in the sense of* (3.3.5)*. Choosing the damping factor $\omega = 1/K_2$ yields convergence with $q = 1 - 1/(K_1 K_2)$. The constants K_1, K_2 depend only on constants appearing in Theorems 3.2.40, 3.2.41, the geometric constant C_0 in* (3.1.6)*, c_N, and the ellipticity constants $\mathfrak{a}$, $\mathfrak{A}$ from* (3.1.14)*.*

Naturally, better convergence rates can be achieved with more elaborate iterative schemes [76]. Starting with (3.3.6) and using Lemma 3.3.1 yields the sought discretization error estimate

$$\left\| u - u_k^{(\nu)} \right\|_{\mathcal{H}} = \mathcal{O}(h_k)$$

once $\nu \in \mathbb{N}$ is large enough such that the stopping criterion $q^\nu \frac{\mathfrak{A}}{\mathfrak{a}} \|u - \Pi_k u\|_{\mathcal{H}} = \mathcal{O}(h_k)$ is fulfilled.

Initially, the support of the first iterate $(I-\mathcal{C}_1)\lambda_p^{(k)} = (I-\omega T)\lambda_p^{(k)}$ is either contained in $\overline{G}$, if p is an inner node in G, or contained in the neighboring cells $\overline{G} \cup \overline{G'}$, if $p \in \overline{G} \cap \Gamma_k \cap \overline{G'}$ is an interface node. Using the same reasoning inductively, one understands that the support of the approximate multiscale basis functions $(I-\mathcal{C}_\nu)\lambda_p^{(k)} = (I-\omega T)^\nu \lambda_p^{(k)}$, $p \in \mathcal{N}^{(k)}$, grows at most by one layer of cells in each iteration step. Consequently, the support of the multiscale basis functions depends logarithmically on the desired accuracy of order h_k.

Discretization

Constructing the multiscale basis of $\mathcal{W}_k^{(\nu)}$ comes down to solving the local problems (3.3.13) in infinite dimensional function spaces $\mathcal{V}_G$, $G \in \mathcal{G}^{(k)}$. A computationally feasible multiscale finite element discretization is obtained by replacing $\mathcal{H}$ with a large finite element space $\mathcal{S} \subset \mathcal{H}$ associated with a strong refinement $\mathcal{T}$ of $\mathcal{T}^{(k)}$ that resolves the necessary fine scale features of the multiscale interface problem to provide the desired accuracy of order h_k. Substituting $\mathcal{H}$ and the subspaces with their discrete counterparts and proceeding literally as above gives rise to discrete variants of the discretization error estimates in Lemma 3.3.1 and Theorem 3.3.2 as well as the convergence result in Theorem 3.3.4. In the discrete setting, the damped Richardson iteration (3.3.14) manifests as a damped block Jacobi iteration, whose blocks are given by the cells $G \in \mathcal{G}^{(k)}$.

3.3.2 Iterative subspace correction

Next, let us consider the construction and convergence analysis of subspace correction methods for the fractal interface problem (3.1.10) and computationally feasible, discrete versions for K-scale finite element approximations (3.1.21). Building on the train of thought from [78] and the previous section, a cell-based, multilevel subspace decomposition will be introduced. Thereafter, we will focus on a subspace decomposition in function space based on a spatial hierarchy of local patches in the spirit of [80]. These decompositions induce preconditioners that accelerate the convergence of a global conjugate gradient (cg) iteration. The convergence of the method follows from notions established in subspace correction theory [134, 136] with convergence rates that are independent of the mesh size h_K and scales $K \in \mathbb{N}$.

Cell-based subspace decomposition

Fixing a coarse and fine level $k < K \in \mathbb{N}$, let us begin by introducing the cell-based multilevel splitting

$$\mathcal{H} = \mathcal{V}^{(k)} + \sum_{l=k+1}^{K} \sum_{G \in \mathcal{G}^{(l)}} \mathcal{V}_G^{(l)} \tag{3.3.15}$$

with

$$\mathcal{V}^{(k)} = \mathcal{S}_k, \qquad \mathcal{V}_G^{(l)} = \{v|_G : v \in \mathcal{H}\}, \quad G \in \mathcal{G}^{(l)}, \quad k < l \leq K.$$

Using the projections $\Pi_l = \Pi_{\mathcal{S}_l} \circ \Pi_{\mathcal{H}_l}$, $k \leq l < K$, from the previous section, each $v \in \mathcal{H}$ can be decomposed into its local components inductively. For this purpose, set $v^{(k)} = \Pi_k v \in \mathcal{S}_k$,

$$\begin{aligned} v_G^{(l)} &= (\Pi_l v - \Pi_{l-1} v)|_G \in \mathcal{V}_G^{(l)}, \quad G \in \mathcal{G}^{(l)} \quad k < l < K, \\ v_G^{(K)} &= (v - \Pi_{K-1} v)|_G \in \mathcal{V}_G^{(K)}, \quad G \in \mathcal{G}^{(K)} \end{aligned} \tag{3.3.16}$$

for all $v \in \mathcal{H}$. By construction, it holds

$$v^{(k)} + \sum_{l=k+1}^{K} \sum_{G \in \mathcal{G}^{(l)}} v_G^{(l)} = \Pi_k v + \sum_{l=k+1}^{K-1} (\Pi_l v - \Pi_{l-1} v) + v - \Pi_{K-1} v = v$$

for all $v \in \mathcal{H}$. With the existence of this splitting up to level $K \in \mathbb{N}$, a suitable splitting up to level $K+1$ can be obtained by using

$$\sum_{G \in \mathcal{G}^{(K)}} v_G^{(K)} = v - \Pi_{K-1} v = \sum_{G \in \mathcal{G}^{(K)}} (\Pi_K v - \Pi_{K-1} v)|_G + \sum_{G \in \mathcal{G}^{(K+1)}} (v - \Pi_K v)|_G \,.$$

Using stability and approximation properties of $\Pi_l : \mathcal{H} \to \mathcal{S}_l$ and arguing similarly to the proof of Lemma 3.3.3 leads to the stability and boundedness of the cell-based splitting (3.3.15) with corresponding constants K_1 and K_2.

Lemma 3.3.5 (stability)**.** *The splitting* (3.3.15) *is stable in the sense that for each $v \in \mathcal{H}$ there is a decomposition of v given by* (3.3.16)*, such that*

$$\left\| v^{(k)} \right\|_a^2 + \sum_{l=k+1}^{K} \sum_{G \in \mathcal{G}^{(l)}} \left\| v_G^{(l)} \right\|_a^2 \leq K_1 \|v\|_a^2$$

holds with a constant K_1 only depending on the number of levels $K - k + 1$, the constants appearing in Theorems 3.2.40, 3.2.41, the geometric constant C_0 in (3.1.6) *and the ellipticity constants $\mathfrak{a}$, $\mathfrak{A}$ from* (3.1.14)*.*

Lemma 3.3.6 (boundedness)**.** *Assume that the number of neighboring cells of G in $\mathcal{G}^{(l)}$ is uniformly bounded by $c_N \in \mathbb{R}$ for all $l \in \mathbb{N}$ and $G \in \mathcal{G}^{(l)}$. Then, the splitting* (3.3.18) *is bounded such that for each $v \in \mathcal{H}$ all decompositions $v^{(k)} \in \mathcal{V}^{(k)}$ and $v_G^{(l)} \in \mathcal{V}_G^{(l)}$, $k < l \leq K$, satisfy*

$$\|v\|_a^2 \leq K_2 \left(\left\| v^{(k)} \right\|_a^2 + \sum_{l=k+1}^{K} \sum_{G \in \mathcal{G}^{(l)}} \left\| v_G^{(l)} \right\|_a^2 \right)$$

with a constant K_2 only depending on c_N.

It will be convenient to introduce a numbering $\{G_1, \ldots, G_m\}$ of the cells $G_i \in \mathcal{V}_{G_i}^{(l)}$, $k < l \leq K$ to describe a sequential subspace correction method induced by the splitting (3.3.15). Therefor, the first $i_K = \left|\mathcal{G}^{(K)}\right|$ cells consist of the level-K splitting $\{G_1, \ldots, G_{i_K}\} = \mathcal{G}^{(K)}$, the next $i_{K-1} = \left|\mathcal{G}^{(K-1)}\right|$ cells consist of the level-$(K-1)$ splitting $\{G_{i_K+1}, \ldots, G_{i_K+i_{K-1}}\} = \mathcal{G}^{(K-1)}$ and so on. Denote the corresponding subspaces $\mathcal{V}_i = \mathcal{V}_{G_i}$ and $\mathcal{V}_0 = \mathcal{V}^{(k)}$. Using this notation, the following Cauchy-Schwarz-type inequality holds for the splitting (3.3.18), which is a crucial property for convergence proofs of sequentially preconditioned iterative schemes.

Lemma 3.3.7 (Cauchy-Schwarz type inequality, cf. [78])**.** *Assume that the number of neighboring cells of G in $\mathcal{G}^{(l)}$ is uniformly bounded by $c_N \in \mathbb{R}$ for all $l \in \mathbb{N}$ and $G \in \mathcal{G}^{(l)}$. Then the Cauchy-Schwarz type inequality*

$$\sum_{i,j=0}^{m} a(v_i, w_j) \leq K_3 \left(K - k + 1\right) \left(\sum_{i=0}^{m} a(v_i, v_i)\right)^{1/2} \left(\sum_{j=0}^{m} a(w_j, w_j)\right)^{1/2}$$

holds for all $v_i \in \mathcal{V}_i$, $w_j \in \mathcal{V}_j$, $i, j = 0, \ldots, m$, with a constant K_3 depending only on c_N.

Proof. Fixing $G \in \mathcal{G}^{(s)}$, $k < s \leq K$, let us introduce the local scalar product

$$a_G(v, w) = \int_{G \setminus \Gamma} A \nabla v \cdot \nabla w \, dx + \tfrac{1}{2} \sum_{l=1}^{s} \left(1 + \mathfrak{c}\right)^l C_l \int_{\Gamma_l \cap G} B \, [\![v]\!] \, [\![w]\!] \, d\Gamma_l \\ + \sum_{l=s+1}^{\infty} \left(1 + \mathfrak{c}\right)^l C_l \int_{\Gamma_l \cap G} B \, [\![v]\!] \, [\![w]\!] \, d\Gamma_l \quad v, w \in \mathcal{H}$$

satisfying

$$\sum_{G \in \mathcal{G}^{(s)}} a_G(v, w) = a(v, w), \qquad v, w \in \mathcal{H}. \tag{3.3.17}$$

Since the common support of $v_i \in \mathcal{V}_i$ and $w_j \in \mathcal{V}_j$ is contained in $\overline{G_i} \cap \overline{G_j}$, $i, j = 1, \ldots, m$, the Cauchy-Schwarz inequality and Gershgorin's theorem lead to

$$\sum_{i,j=0}^{m} a_G(v_i, w_j) \leq \left(c_N + 1\right) \left(\sum_{i=0}^{m} a_G(v_i, v_i)\right)^{1/2} \left(\sum_{j=0}^{m} a_G(w_j, w_j)\right)^{1/2}.$$

Finally, summing over $G \in \mathcal{G}^{(l)}$, $k < lK$ and applying the Cauchy-Schwarz inequality in $\mathbb{R}^{m+1}$ together with (3.3.17) lead to the assertion. □

Patch-based subspace decomposition

Fixing a coarse and fine level $k < K \in \mathbb{N}$, let us consider the multilevel splitting

$$\mathcal{H} = \mathcal{V}^{(k)} + \sum_{l=k+1}^{K} \sum_{p \in \mathcal{N}^{(l)}} \mathcal{V}_p^{(l)} \tag{3.3.18}$$

with $\mathcal{V}^{(k)} = \mathcal{S}_k$ and

$$\begin{aligned} \mathcal{V}_p^{(l)} &= \{\lambda_p^{(l)} v \,:\, v \in \mathcal{S}_l\}, && p \in \mathcal{N}^{(l)}, \quad k < l < K \\ \mathcal{V}_p^{(K)} &= \{\lambda_p^{(K)} v \,:\, v \in \mathcal{H}\}, && p \in \mathcal{N}^{(K)}, \end{aligned}$$

where $\omega_p = \operatorname{supp} \lambda_p^{(l)}$, $p \in \mathcal{N}^{(l)}$, $k < l \leq K$, is the support patch of the respective nodal basis function. All $v_p \in \mathcal{V}_p^{(l)}$, $k < l \leq K$, satisfy $v_p|_{\partial \omega_p \setminus \Gamma^{(l)}} = 0$. In particular,

if p is not a vertex of an edge resolving the interface network $\Gamma^{(l)}$, it holds $v_p|_{\partial\omega_p} = 0$. Due to the locality of the spaces $\mathcal{V}_p^{(l)}$, $k < l \leq K$, we have

$$\|v_p\|_{\mathcal{H}}^2 = |v_p|_{1,\omega_p\setminus\Gamma}^2 + \sum_{s=1}^{l}(1+\mathfrak{c})^s C_s \|v_p\|_{0,\Gamma_s\cap\partial\omega_p}^2 + \sum_{s=l+1}^{\infty}(1+\mathfrak{c})^s C_s \|[\![v_p]\!]\|_{0,\Gamma_s\cap\omega_p}^2 \quad (3.3.19)$$

for all $v_p \in \mathcal{V}_p^{(l)}$.

Next, the aforementioned splitting will be constructed inductively using the projections $\Pi_{\mathcal{S}_l}$, $k \leq l < K$, from the previous section. For this purpose, let us set

$$v^{(k)} = \Pi_{\mathcal{S}_k} v, \quad v_p^{(l)} = \lambda_p^{(l)} \left(\Pi_{\mathcal{S}_l} v - \Pi_{\mathcal{S}_{l-1}} v\right), \quad v_p^{(K)} = \lambda_p^{(K)} \left(v - \Pi_{\mathcal{S}_{K-1}} v\right) \quad (3.3.20)$$

with $k < l < K$ for all $v \in \mathcal{H}$. As the nodal basis $\{\lambda_p^{(l)}\}$ is a partition of unity, it holds

$$v^{(k)} + \sum_{l=k+1}^{K} \sum_{p\in\mathcal{N}^{(l)}} v_p^{(l)} = \Pi_{\mathcal{S}_k} v + \sum_{l=k+1}^{K-1} \left(\Pi_{\mathcal{S}_l} v - \Pi_{\mathcal{S}_{l-1}} v\right) + v - \Pi_{\mathcal{S}_{K-1}} v = v$$

for all $v \in \mathcal{H}$. With the existence of this splitting up to level $K \in \mathbb{N}$, a suitable splitting up to level $K+1$ can be constructed using

$$\sum_{p\in\mathcal{N}^{(K)}} v_p^{(K)} = v - \Pi_{\mathcal{S}_{K-1}} v = \sum_{p\in\mathcal{N}^{(K)}} \lambda_p^{(K)} \left(\Pi_{\mathcal{S}_K} v - \Pi_{\mathcal{S}_{K-1}} v\right) + \sum_{p\in\mathcal{N}^{(K+1)}} \lambda_p^{(K+1)} \left(v - \Pi_{\mathcal{S}_K} v\right).$$

The following lemma establishes an important intermediate statement for proving the stability and boundedness of the splitting (3.3.18). It is an extension of well-known arguments presented, e.g., in [80, Lemma 4.3].

Lemma 3.3.8. *Let $1 < k \in \mathbb{N}$, $l = k-1, k$, and assume that conditions* (3.2.17) *and* (3.2.21) *are satisfied. Moreover, let the refinement factor*

$$\frac{h_K}{h_{K+1}} \leq c_r \qquad \forall K \in \mathbb{N} \quad (3.3.21)$$

be uniformly bounded by the constant c_r. It holds

$$\sum_{p\in\mathcal{N}^{(k)}} \left\|\lambda_p^{(k)} \left(v - \Pi_{\mathcal{S}_l} v\right)\right\|_{\mathcal{H}}^2 \leq c \|v\|_{\mathcal{H}}^2$$

for all $v \in \mathcal{H}$ with a constant c only depending on the space dimension d, shape regularity σ of $\mathcal{T}^{(k)}$ and $\mathcal{T}^{(l)}$ as well as the constant δ in (3.1.20) *and c_r.*

Proof. By a density argument, it suffices to show the claim for any $v \in \mathcal{C}_{L,0}^1$ with arbitrary $L > k$. Fix $p \in \mathcal{N}^{(k)}$ and denote $w = v - \Pi_{\mathcal{S}_l} v$. Using the locality of $\lambda_p^{(k)} w$ from (3.3.19) yields

$$\begin{aligned}\left\|\lambda_p^{(k)} w\right\|_{\mathcal{H}}^2 = \left|\lambda_p^{(k)} w\right|_{1,\Omega\setminus\Gamma^{(L)}}^2 &+ \sum_{s=1}^{k}(1+\mathfrak{c})^s C_s \left\|\lambda_p^{(k)} w\right\|_{0,\Gamma_s\cap\partial\omega_p}^2 \\ &+ \sum_{s=k+1}^{L} (1+\mathfrak{c})^s C_s \left\|\left[\!\left[\lambda_p^{(k)} w\right]\!\right]\right\|_{0,\Gamma_s\cap\omega_p}^2. \end{aligned} \quad (3.3.22)$$

Moreover, it holds $\nabla(\lambda_p^{(k)} w) = w\nabla\lambda_p^{(k)} + \lambda_p^{(k)}\nabla w$ in a weak sense, ${\lambda_p^{(k)}}^2 \leq \lambda_p^{(k)}$ and thus

$$\begin{aligned}\left|\lambda_p^{(k)} w\right|^2_{1,\Omega\setminus\Gamma^{(L)}} &\leq 2\int_{\Omega\setminus\Gamma^{(L)}} \left(w\nabla\lambda_p^{(k)}\right)^2 dx + 2\int_{\Omega\setminus\Gamma^{(L)}} \left(\lambda_p^{(k)}\nabla w\right)^2 dx \\ &\leq 2\int_{\Omega\setminus\Gamma^{(L)}} w^2 \left|\nabla\lambda_p^{(k)}\right|^2 dx + 2\int_{\Omega\setminus\Gamma^{(L)}} \lambda_p^{(k)} \left|\nabla w\right|^2 dx.\end{aligned}$$

Due to the construction of the triangulation $\mathcal{T}^{(k)}$ in section 3.1.4, the sum

$$\sum_{p\in\mathcal{N}^{(k)}} \left|\nabla\lambda_p^{(k)}\right|^2 h_k^2 \leq c'$$

is bounded by a constant c' that only depends on the shape regularity σ of $\mathcal{T}^{(k)}$. Thus, summing over $p \in \mathcal{N}^{(k)}$, using that $\{\lambda_p^{(k)}\}$ is a partition of unity and applying the global approximation property (Corollary 3.2.33) of $\Pi_{\mathcal{S}_l}$ as well as the implied, global version of Lemma 3.2.34 results in

$$\sum_{p\in\mathcal{N}^{(k)}} \left|\lambda_p^{(k)} w\right|^2_{1,\Omega\setminus\Gamma^{(L)}} \leq 2c'\, h_k^{-2} \left\|w\right\|_0^2 + 2\left|w\right|^2_{1,\Omega\setminus\Gamma^{(L)}} \leq \left(1+\tfrac{1}{\mathfrak{c}}\right) c \left\|v\right\|^2_{\mathcal{H}}, \tag{3.3.23}$$

with a constant c only depending on the space dimension d, shape regularity σ of $\mathcal{T}^{(k)}$ and $\mathcal{T}^{(l)}$ as well as the constant δ in (3.1.20) and the refinement factor c_r in (3.3.21).
The boundary terms in (3.3.22) vanish for $p \notin \Gamma_s$ and can otherwise be estimated by Remark 3.2.36 as per

$$\begin{aligned}&\left\|\lambda_p^{(k)} w\right\|^2_{0,\Gamma_s\cap\partial\omega_p} \\ &\leq \left\|w\right\|^2_{0,\Gamma_s\cap\partial\omega_p} \leq c\left(1+\tfrac{1}{\mathfrak{c}}\right)^2 h_l \left(\left|v\right|^2_{1,\omega_p\setminus\Gamma^{(L)}} + \sum_{t=l+1}^{L} (1+\mathfrak{c})^t\, C_t \left\|[\![v]\!]\right\|^2_{0,\Gamma_t\cap\omega_p}\right)\end{aligned} \tag{3.3.24}$$

for interfaces Γ_s, $s \leq k$, with a constant c only depending on the space dimension d, shape regularity σ of $\mathcal{T}^{(k)}$ and the constant δ in (3.1.20). Inserting assumptions (3.2.21) and (3.1.20) yields

$$\sum_{s=1}^{k} (1+\mathfrak{c})^s C_s \left\|\lambda_p^{(k)} w\right\|^2_{0,\Gamma_s\cap\partial\omega_p} \leq c\left(1+\tfrac{1}{\mathfrak{c}}\right)^2 \left(\left|v\right|^2_{1,\omega_p\setminus\Gamma^{(L)}} + \sum_{t=l+1}^{L} (1+\mathfrak{c})^t\, C_t \left\|[\![v]\!]\right\|^2_{0,\Gamma_t\cap\omega_p}\right),$$

where the constant c now additionally depends on the refinement factor c_r from (3.3.21).
Any simplex $T \in \mathcal{T}^{(k)}$ is covered by at most $d+1$ patches ω_p, $p \in \mathcal{N}^{(k)}$. Thus, summing (3.3.22) over $p \in \mathcal{N}^{(k)}$, inserting (3.3.23) and (3.3.24) as well as using that $\Pi_{\mathcal{S}_l}$ does not jump in ω_p, which implies $\left\|[\![\lambda_p^{(k)} w]\!]\right\|_{0,\Gamma_s\cap\omega_p} \leq \left\|[\![v]\!]\right\|_{0,\Gamma_s\cap\omega_p}$, results in the desired statement. □

As a consequence of the approximation and stability properties of $\Pi_{\mathcal{S}_l}$, $k \leq l < K$, the patch-based splitting (3.3.18) possesses stability, boundedness properties and satisfies a Cauchy-Schwarz-type inequality.

Lemma 3.3.9 (stability)**.** *Let $k < K \in \mathbb{N}$ and assume that conditions* (3.2.17) *and* (3.2.21) *are satisfied. The splitting* (3.3.18) *is stable in the sense that for each $v \in \mathcal{H}$ there is a decomposition given by* (3.3.20)*, such that*

$$\left\|v^{(k)}\right\|_a^2 + \sum_{l=k+1}^{K} \sum_{p\in\mathcal{N}^{(l)}} \left\|v_p^{(l)}\right\|_a^2 \leq K_1 \|v\|_a^2$$

holds with a constant K_1 only depending on the number of levels $K-k+1$, the constants appearing in Lemma 3.3.8, Corollary 3.2.38, and the ellipticity constants $\mathfrak{a}$, $\mathfrak{A}$ from (3.1.14)*.*

Proof. Let $v \in \mathcal{H}$ and consider the decomposition (3.3.20). Its stability is a consequence of the stability of $\Pi_{\mathcal{S}_l}$, $k \leq l < K$, in Corollary 3.2.38 and Lemma 3.3.8, since

$$\begin{aligned}
\sum_{p\in\mathcal{N}^{(l)}} \left\|v_p^{(l)}\right\|_{\mathcal{H}}^2 &\leq \sum_{p\in\mathcal{N}^{(l)}} 2\left\|\lambda_p^{(l)}\left(v-\Pi_l v\right)\right\|_{\mathcal{H}}^2 + 2\left\|\lambda_p^{(l-1)}\left(v-\Pi_{l-1}v\right)\right\|_{\mathcal{H}}^2, \quad k<l<K\\
\sum_{p\in\mathcal{N}^{(K)}} \left\|v_p^{(K)}\right\|_{\mathcal{H}}^2 &= \sum_{p\in\mathcal{N}^{(K)}} \left\|\lambda_p^{(K)}\left(v-\Pi_{K-1}v\right)\right\|_{\mathcal{H}}^2.
\end{aligned}$$

The norm equivalence in (3.1.14) concludes the proof. □

Lemma 3.3.10 (boundedness)**.** *The splitting* (3.3.18) *is bounded such that for each $v \in \mathcal{H}$ all decompositions $v^{(k)} \in \mathcal{V}^{(k)}$ and $v_p^{(l)} \in \mathcal{V}_p^{(l)}$, $k < l \leq K$, satisfy*

$$\|v\|_a^2 \leq K_2 \left(\left\|v^{(k)}\right\|_a^2 + \sum_{l=k+1}^{K} \sum_{p\in\mathcal{N}^{(l)}} \left\|v_p^{(l)}\right\|_a^2\right)$$

with a constant K_2 only depending on the space dimension d.

Proof. A standard covering argument yields the boundedness of the splitting. By induction, any simplex $T \in \mathcal{T}^{(K)}$ is contained in at most $K_2 = 1 + (d+1)(K-k)$ patches. Using the triangle and Cauchy-Schwarz inequalities in $\mathbb{R}^{1+(d+1)K}$ leads to the assertion according to

$$\|v\|_a^2 \leq \left(\left\|v^{(k)}\right\|_a + \sum_{l=k+1}^{K} \sum_{p\in\mathcal{N}^{(l)}} \left\|v_p^{(l)}\right\|_a\right)^2 \leq K_2 \left(\left\|v^{(k)}\right\|_a^2 + \sum_{l=k+1}^{K} \sum_{p\in\mathcal{N}^{(l)}} \left\|v_p^{(l)}\right\|_a^2\right). \quad \square$$

To describe a sequential subspace correction method induced by the splitting (3.3.20), let us introduce a numbering $\{p_1, \ldots, p_m\}$ of the nodes $p \in \mathcal{N}^{(l)}$, $k \leq l \leq K$, such that the first $i_K = \left|\mathcal{N}^{(K)}\right|$ nodes consist of the level-K nodes in some fixed order, the next $i_{K-1} = \left|\mathcal{N}^{(K-1)}\right|$ nodes consist of the level-$(K-1)$ nodes in some fixed order and so on. Denote the corresponding subspaces $\mathcal{V}_i = \mathcal{V}_{p_i}$ and Ritz projections $P_i = P_{\mathcal{V}_i}$, $i = 1, \ldots, m$.

Lemma 3.3.11 (Cauchy-Schwarz type inequality)**.** *The Cauchy-Schwarz type inequality*

$$\sum_{i,j=0}^{m} a(v_i, w_j) \leq K_3 \left(\sum_{i=0}^{m} a(v_i, v_i) \right)^{1/2} \left(\sum_{j=0}^{m} a(w_j, w_j) \right)^{1/2}$$

holds for all $v_i \in \mathcal{V}_i$ and $w_j \in \mathcal{V}_j$ with $i, j = 0, \ldots, m$, with a constant K_3 depending only on the space dimension d.

Proof. Any simplex $T \in \mathcal{T}^{(K)}$ is contained in at most K_2 patches (see previous proof). Then, using the Cauchy-Schwarz inequality as in the proof of [80, Lemma 5.1] leads to the assertion. □

Parallel subspace correction

Utilizing the cell- and patch-based subspace decompositions, let us approximate the solution u of the multiscale interface problem (3.1.10) employing a basic iteration in function space as in [80]. Its convergence is a consequence of well-known results from subspace correction theory [134, 136] and later extensions to an infinite dimensional solution space [80], whose applicability relies on the stability and boundedness of the respective splitting.

The splittings (3.3.18) and (3.3.15) provide a preconditioner of the form

$$T = P_0 + \cdots + P_m \tag{3.3.25}$$

with a-orthogonal Ritz projections $P_i : \mathcal{H} \to \mathcal{V}_i$

$$a(P_i v, v_i) = a(v, v_i) \qquad \forall v_i \in \mathcal{V}_i,$$

whose numbering corresponds to the one of the respective subspaces. Evaluating the operator T comes down to solving a global problem associated with $\mathcal{V}_0$ and continuous local problems in $\mathcal{V}_i$. Since all of these subproblems take the same input, they can be processed in *parallel*.
Similar to basic findings from subspace correction theory in finite dimensions [134, 136], stability and boundedness of the splittings imply the following spectral equivalence, see [80, Lemma 3.1].

Lemma 3.3.12. *The operator $T : \mathcal{H} \to \mathcal{H}$ from* (3.3.25)*, that is induced by the splitting* (3.3.15) *or* (3.3.18)*, is symmetric with respect to the inner product $a(\cdot, \cdot)$ in $\mathcal{H}$. Under the assumptions of Lemma 3.3.5 and Lemma 3.3.6 or Lemma 3.3.9 and Lemma 3.3.10, it holds*

$$1/K_1 \, a(v, v) \leq a(Tv, v) \leq K_2 \, a(v, v)$$

for all $v \in \mathcal{H}$ with their respective positive constants K_1 and K_2.

Then, the Riesz representation theorem leads to an estimate of the condition number κ of the preconditioner T, i.e. the ratio of smallest upper to largest lower bound of its spectrum, in terms of the constants K_1 and K_2, see [80, Theorem 3.2].

Theorem 3.3.13. *The spectrum of the operator $T : \mathcal{H} \to \mathcal{H}$ from* (3.3.25)*, that is induced by the splitting* (3.3.15) *or* (3.3.18)*, is a subset of the interval $[1/K_1, K_2]$ with constants K_1 and K_2 from Lemma 3.3.12 under the assumptions stated therein. Thus, the condition number κ of T satisfies the estimate*

$$\kappa \leq K_1 K_2. \tag{3.3.26}$$

After fixing a starting value $w^{(0)} = u^{(0)}$, the solution u of the multiscale interface problem is approximated by the iteration

$$w^{(l)} = \sum_{\nu=0}^{l} \alpha_{l\nu} u^{(\nu)}, \quad \sum_{\nu=0}^{l} \alpha_{l\nu} = 1, \tag{3.3.27}$$

with iterates $w^{(l)}$, that consist of weighted averages of the basic iterates

$$u^{(\nu+1)} = u^{(\nu)} + T\left(u - u^{(\nu)}\right). \tag{3.3.28}$$

In order to obtain a general error estimate of this method, let us consider the difference of the exact solution u and the iterates $w^{(l)}$ generated by (3.3.27). By induction, the basic iterates can be reformulated as

$$u^{(\nu)} = u - (I - T)^{\nu}\left(u - u^{(0)}\right)$$

and thus it holds

$$u - w^{(l)} = u - u\sum_{\nu=0}^{l} \alpha_{l\nu} + \sum_{\nu=0}^{l} \alpha_{l\nu}(I - T)^{\nu}\left(u - u^{(0)}\right) = \sum_{\nu=0}^{l} \alpha_{l\nu}(I - T)^{\nu}\left(u - u^{(0)}\right).$$

Using the spectral mapping theorem from the appendix in [80], the spectrum of the operator polynomial

$$p(T) = \sum_{\nu=0}^{l} \alpha_{l\nu}(I - T)^{\nu}$$

is given in terms of the spectrum $\sigma(T)$ of T, in particular by $p(\lambda)$ with $\lambda \in \sigma(T)$. Since $p(T)$ is a bounded, symmetric, linear operator, its norm corresponds to its spectral radius, which ultimately entails an error estimate with respect to the condition number κ of T. Different choices of weights $\alpha_{l\nu}$ lead to distinct iterative methods. The minimal value of the spectral radius of $p(T)$ is attained for suitable Chebyshev polynomials. Hence, choosing the weights $\alpha_{l\nu}$ accordingly, which is implemented by the conjugate gradient (cg) method, yields minimal and therefore optimal convergence rates [33, Chapter 8].

Theorem 3.3.14 (cf. [80, Theorem 3.4])**.** *The iteration* (3.3.27) *with optimally chosen weights $\alpha_{l\nu}$ admits the error estimate*

$$\left\|u - w^{(l)}\right\|_a \leq \tfrac{2q^l}{1+q^{2l}} \left\|u - u^{(0)}\right\|_a$$

for any fixed initial iterate $u^{(0)} \in \mathcal{H}$ with convergence rate

$$q = \tfrac{\sqrt{\kappa}-1}{\sqrt{\kappa}+1},$$

where $\kappa \leq K_1 K_2$ denotes the condition number of the operator T from (3.3.25)*.*

In particular, this theorem implies that given a current iterate $u^{(0)}$, the number of conjugate gradient iterations $l \sim \ln(1/\varepsilon)$ required to reduce the norm of the approximation error by a factor ε, i.e. it holds

$$\left\|u - w^{(l)}\right\|_a \leq \varepsilon \left\|u - u^{(0)}\right\|_a,$$

is proportional to the logarithm of the required accuracy. See [33, Corollary 8.18] for a more thorough investigation of the required number of iterations. Moreover, since the constants K_1 and K_2 given by Lemma 3.3.5 and Lemma 3.3.6 or Lemma 3.3.9 and Lemma 3.3.10, respectively, are independent of the mesh size and scale parameters for the cell- or patch-based splittings, so is the convergence rate q of the preconditioned cg iteration.

Sequential subspace correction

Recall that the basic parallel scheme (3.3.28) computes corrections in the subspaces $\mathcal{V}_i$, $0 \leq i \leq m$, for the same initial iterate $u^{(\nu)}$. Another approach are Gauß-Seidel type methods, where corrections in the subspaces $\mathcal{V}_i$ are processed *sequentially* in an arbitrary but fixed order and previous, intermediate ones are taken into account. In particular, this idea leads to an iteration, where, given an arbitrary initial iterate $u^{(0)} \in \mathcal{H}$, one step of the basic scheme consists of computing intermediate corrections

$$u^{(\nu,0)} = u^{(\nu)}, \qquad u^{(\nu,i+1)} = u^{(\nu,i)} + P_i(u - u^{(\nu,i)}), \qquad i = 0, \ldots, m \tag{3.3.29}$$

and setting the new iterate $u^{(\nu+1)} = u^{(\nu,m+1)}$. In practice, Gauß-Seidel type methods typically converge faster than similar parallel versions – at the cost of parallelizability.

If the subspaces $\mathcal{V}_i$, $0 \leq i \leq m$, are traversed in a symmetric fashion, e.g., as determined by the symmetric error propagation operator E

$$E = (I - P_m) \cdots (I - P_1)(I - P_0)(I - P_1) \cdots (I - P_m), \tag{3.3.30}$$

its convergence can be accelerated with the cg iteration as in the previous section. In the spirit of [134, 136], let us derive a basic convergence result using the stability of the subspace decomposition and a Cauchy-Schwarz type inequality for the respective splittings. Its proof is similar to the one of [80, Theorem 5.2].

Theorem 3.3.15. *The linear, Gauß-Seidel type iteration corresponding to the error propagation operator E converges with respect to the energy norm and satisfies the error estimate*

$$\left\|u - u^{(\nu+1)}\right\|_a \leq \left(1 - \tfrac{1}{K_1 K_3^2}\right) \left\|u - u^{(\nu)}\right\|_a$$

for any initial iterate $u^{(0)} \in \mathcal{H}$ with K_1, K_3 depending only on the constants appearing in Lemma 3.3.5 and Lemma 3.3.7 for the cell-based splitting (3.3.16) *or Lemma 3.3.9 and Lemma 3.3.11 for the patch-based splitting* (3.3.20)*.*

Proof. Let $v \in \mathcal{H}$ and $v = v_0 + \cdots v_m$ a stable decomposition given by (3.3.16) or (3.3.20). Denote $E_{-1} = I$, $E_m = E$ and define the intermediate error propagation

operators E_j, $0 \leq j \leq m$, recursively by $E_j = (I - P_j)E_{j-1}(I - P_j)$. Then, it holds $I - E_0 = P_0 = P_0E_{-1} + E_{-1}P_0 - P_0E_{-1}P_0$ and

$$\begin{aligned}\sum_{i=0}^{j} P_iE_{i-1} + E_{i-1}P_i - P_iE_{i-1}P_i &= I - E_{j-1} + P_jE_{j-1} + E_{j-1}P_j - P_jE_{j-1}P_j \\ &= I - (I - P_j)E_{j-1}(I - P_j) = I - E_j \qquad (3.3.31)\end{aligned}$$

for $j \leq m$ by induction. Note that E_j maps into the a-orthogonal complement of V_j, i.e. $a(E_jv, v_j) = 0$, which implies

$$\|v\|_a^2 = \sum_{j=0}^{m} a((I - E_j)v, v_j) = \sum_{j=0}^{m}\sum_{i=0}^{j} a((P_iE_{i-1} + E_{i-1}P_i - P_iE_{i-1}P_i)v, v_j)$$

together with the previous identity (3.3.31). Applying the Cauchy-Schwarz type inequality in Lemma 3.3.7 for the cell-based splitting or the one in Lemma 3.3.11 for the patch-based splitting leads to the estimate

$$\|v\|_a^2 \leq K_3 \left(\sum_{i=0}^{m} \|(P_iE_{i-1} + E_{i-1}P_i - P_iE_{i-1}P_i)v\|_a^2\right)^{1/2} \left(\sum_{j=0}^{m} \|v_j\|_a^2\right)^{1/2}$$

with the respective constants K_3. Then, squaring the previous estimate and using the stability of the given decomposition of v by Lemma 3.3.5 or Lemma 3.3.9 yields

$$\|v\|_a^2 \leq K_1K_3^2 \sum_{i=0}^{m} \|(P_iE_{i-1} + E_{i-1}P_i - P_iE_{i-1}P_i)v\|_a^2 .$$

The summands can be expressed as differences according to

$$\|(P_iE_{i-1} + E_{i-1}P_i - P_iE_{i-1}P_i)v\|_a^2 = \|E_{i-1}v\|_a^2 - \|E_iv\|_a^2 ,$$

see (3.3.31), and all but the first and last terms cancel in the telescoping sum, i.e. it holds

$$\|v\|_a^2 \leq K_1K_3^2 \left(\|v\|_a^2 - \|Ev\|_a^2\right). \qquad \square$$

Discrete versions

Performing the iterations (3.3.28) and (3.3.29) in function space requires evaluating the Ritz projections to infinite dimensional subspaces $\mathcal{V}_i$ corresponding to the finest level of the subspace decomposition and is thus computationally unfeasible. Recall that the approximation of $\mathcal{H}$ by $\mathcal{H}_K$, which effectively truncates all contributions from interfaces Γ_L, $L > K$, finer than K, converges for $K \to \infty$, see (3.1.18). For the fractal interface network from Example 3.1.1, there are even exponential error estimates, see Remark 3.1.5. Subsequently, the finite element discretization (3.1.21) is obtained by approximating $\mathcal{H}_K$ with the finite element space $\mathcal{S}_K$. Essentially, the previous construction of iterative solvers and their convergence theory translate directly to the discrete setting by replacing the infinite dimensional solution space $\mathcal{H}$ with $\mathcal{S}_K$.

However, there is one subtlety that requires special attention. The construction of the patch-based decomposition (3.3.20) that is stable in the sense of Lemma 3.3.9 needs adaptation, since the product $\lambda_p^{(l)} v$, $v \in \mathcal{S}_l$ and $k < l \leq K$, is piecewise of degree ≤ 2 and therefore no longer contained in $\mathcal{S}_l$, i.e. $\mathcal{V}_p^{(l)} \not\subset \mathcal{S}_K$. As a remedy, let us employ the nodal interpolation operator $\mathcal{I}_l : \mathcal{C}^1_{l,0} \to \mathcal{S}_l$, $k < l \leq K$, that interpolates at the nodes $p \in \mathcal{N}^{(l)}$ and is the identity for functions in $\mathcal{S}_l$. Interpolating the individual contributions of the splitting (3.3.20) guarantees $\mathcal{I}_l(\lambda_p^{(l)} v) \in \mathcal{S}_l$ for all $v \in \mathcal{S}_l$, see [80] for similar arguments in a 2-level setting. Thus, a suitable discrete variant of the former decomposition reads

$$\begin{aligned} \tilde{v}^{(k)} &= \Pi_{\mathcal{S}_k} v, \\ \tilde{v}_p^{(l)} &= \mathcal{I}_l \left(\lambda_p^{(l)} \left(\Pi_{\mathcal{S}_l} v - \Pi_{\mathcal{S}_{l-1}} v \right) \right), \\ \tilde{v}_p^{(K)} &= \mathcal{I}_K \left(\lambda_p^{(K)} \left(v - \Pi_{\mathcal{S}_{K-1}} v \right) \right) \end{aligned} \tag{3.3.32}$$

for all $v \in \mathcal{S}_K$. Note that it holds $\tilde{v}^{(k)} \in \mathcal{S}_k$ and $\tilde{v}_p^{(l)} \in \mathcal{S}_l$, $k < l \leq K$. Provided that an estimate of the form

$$\left\| \mathcal{I}_l(\lambda_p^{(l)}(\Pi_{\mathcal{S}_l} v - \Pi_{\mathcal{S}_{l-1}} v)) \right\|_{\mathcal{H}} \leq c_{\mathcal{I}} \left\| \lambda_p^{(l)}(\Pi_{\mathcal{S}_l} v - \Pi_{\mathcal{S}_{l-1}} v)) \right\|_{\mathcal{H}} \qquad k < l \leq K \tag{3.3.33}$$

holds for all $v \in \mathcal{S}_K$ with a suitable constant $c_{\mathcal{I}}$, a stability property similar to Lemma 3.3.9 carries over from the stability of the decomposition (3.3.20).

Lemma 3.3.16. *Let $k < K \in \mathbb{N}$ and assume that conditions* (3.2.17) *and* (3.2.21) *are satisfied. The discrete splitting of $\mathcal{S}_K$ is stable in the sense that for each $v \in \mathcal{S}_K$ there is a decomposition given by* (3.3.32)*, such that*

$$\left\| \tilde{v}^{(k)} \right\|_a^2 + \sum_{l=k+1}^{K} \sum_{p \in \mathcal{N}^{(l)}} \left\| \tilde{v}_p^{(l)} \right\|_a^2 \leq K_1 \left\| v \right\|_a^2$$

holds with a constant K_1 only depending on the number of levels $K - k + 1$, the constants appearing in Lemma 3.3.8, Corollary 3.2.38, the ellipticity constants $\mathfrak{a}$, $\mathfrak{A}$ from (3.1.14) *and $c_{\mathcal{I}}$.*

To prove (3.3.33), observe that $v \in \mathcal{S}_l$ is continuous on the simplices $T \in \mathcal{T}^{(l)}$ and that the nodal interpolation operator possesses the following standard approximation and stability properties

$$\left\| v - \mathcal{I}_l v \right\|_{0,T} \leq c h_l \left| v \right|_{1,T}, \quad \left| \mathcal{I}_l v \right|_{1,T} \leq c \left| v \right|_{1,T} \quad \forall v \in C^0(T) \tag{3.3.34}$$

for all $T \in \mathcal{T}^{(l)}$ with a constant c only depending on the space dimension d and shape regularity σ of $\mathcal{T}^{(l)}$, see, e.g. [28, Chapter 3]. Finally, proceeding similarly to the stability proof of $\Pi_{\mathcal{S}_K}$ in Corollary 3.2.38 and estimating the jump contributions in analogy to Lemma 3.2.35 leads to (3.3.33) with a constant $c_{\mathcal{I}}$ that only depends on the space dimension d, shape regularity σ of $\mathcal{T}^{(l)}$, the constant δ in (3.1.20), the constant c_0 in (3.2.21), and the material constant $\mathfrak{c}$.

Complexity considerations

Let us consider the highly localized interface network from Example 3.1.1 in two space dimensions. Starting from the partition $\mathcal{T}^{(0)}$ of Ω consisting of two congruent triangles, subsequent triangulations $\mathcal{T}^{(k)}$, $k \geq 1$, resolving $\Gamma^{(k)}$ are obtained by applying two uniform regular refinement steps to $\mathcal{T}^{(k-1)}$.
For given $k < K$, the cell-based schemes require the evaluation of Ritz projections to the cells $G \in \mathcal{G}^{(l)}$, $k \leq l \leq K$. Note that the cell $G_{\max} \in \mathcal{G}_{\infty}^{(1)}$ with the largest diameter is present in every $\mathcal{G}^{(l)}$, since it will not be split by any finer interfaces Γ_l, $l > 1$, and covers more than half of the domain. Because of (3.1.20), solving the cell problem corresponding to the Ritz projection to $G_{\max}$ for a single subspace correction is asymptotically as costly as solving the entire problem.
A single iteration step of one of the patch based schemes with $k \leq K$ has the optimal algorithmic complexity of a multigrid V-cycle, i.e. $O(N)$, where N is the number of vertices in the triangulation $\mathcal{T}^{(K)}$ of the finest level.

Numerical experiments

Naturally, there is a plethora of problem and solver parameters for which the performance of the numerical approach can be assessed and optimized. In an effort to confirm the theoretical findings from the previous sections, the focus will be on an evaluation of the convergence behavior of the various subspace corrections methods in the context of progressively more elaborate interface network geometries, that satisfy fewer and fewer assumptions and are less and less covered by theory. An example inspired by geophysical, spatial structures illustrates their applicability in settings beyond the presented theoretical framework. The implementation is based on the **D**istributed and **U**nified **N**umerics **E**nvironment (DUNE) [12, 17, 117], written in C++ and available as the separate module dune-faultnetworks[1].

In the remainder, let us consider the finite element discretization (3.1.21) of the fractal interface problem (3.1.10) with $\Omega = (0,1)^2 \subset \mathbb{R}^2$, $\mathfrak{c} = 1$, the identity matrix $A = I \in \mathbb{R}^{d\times d}$, $B = 1$ and three different fractal interface network geometries, whose construction will be described shortly. Numerical approximations will be obtained resting on discrete analogues of the cg iteration with basic iterates from (3.3.28) and (3.3.29) and block Jacobi and Gauß-Seidel smoothers induced by the multilevel cell- and patch-based splittings (3.3.15) and (3.3.18), respectively, with coarse space $\mathcal{S}_k = \mathcal{S}_1$ and fine space $\mathcal{S}_K$ corresponding to the discrete solution space $\mathcal{S}_K$, $K = 1, \dots, K_{\max}$. All experiments start with an initial iterate $u^{(0)} = u_{\mathcal{S}_1}$, that is given by the finite element approximation on the coarse grid $\mathcal{T}^{(1)}$. In particular, the following methods will be investigated:

(MG) standard multigrid V-cycle with Gauß-Seidel smoother induced by the multilevel patch-based splitting (3.3.18) with 3 pre- and post-smoothing steps on each level

(patch-JA) cg method preconditioned with block Jacobi smoother induced by the multilevel patch-based splitting (3.3.18)

[1] `https://git.imp.fu-berlin.de/podlesny/dune-faultnetworks`

(patch-GS) cg method preconditioned with block Gauß-Seidel smoother induced by the multilevel patch-based splitting (3.3.18)

(cell-JA) cg method preconditioned with block Jacobi smoother induced by the multilevel cell-based splitting (3.3.15)

(cell-GS) cg method preconditioned with block Gauß-Seidel smoother induced by the multilevel cell-based splitting (3.3.15)

In order to assess the convergence properties of the numerical methods, two computationally feasible quantities will be examined. First, let us consider the minimal number of iteration steps ν_{stop} needed to reduce the algebraic error below discretization accuracy on the finest grid. It is computed according to the hierarchical error estimate [80]

$$\left\| u_{\mathcal{S}_K} - u_{\mathcal{S}_K}^{(\nu_{\text{stop}})} \right\|_{\mathcal{H}} \leq \left\| u_{\mathcal{S}_{K+1}} - u_{\mathcal{S}_K} \right\|_{\mathcal{H}} \leq \| u - u_{\mathcal{S}_K} \|_{\mathcal{H}} \,. \tag{3.3.35}$$

Here, the last estimate follows by best-approximation of the discretization error $\|u - u_{\mathcal{S}_K}\|_{\mathcal{H}}$ in $\mathcal{S}_{K+1}$. The number of iterations ν_{stop} governs the computational efficiency of the individual methods and characterizes their convergence speed in practice as well as their robustness with respect to the scale K. Second, the error reduction factors

$$\rho_K^{(\nu)} = \frac{\left\| u_{\mathcal{S}_K} - u_{\mathcal{S}_K}^{(\nu)} \right\|_{\mathcal{H}}}{\left\| u_{\mathcal{S}_K} - u_{\mathcal{S}_K}^{(\nu-1)} \right\|_{\mathcal{H}}}, \qquad \nu = 1, \dots, 9,$$

and their geometric mean ρ_K approximate the convergence rates for the respective methods and levels $K = 1, \dots, K_{\max}$.

Highly localized interface network. The first experimental setup features the highly localized fractal interface network introduced in Example 3.1.1, see Figure 3.3 for an illustration.

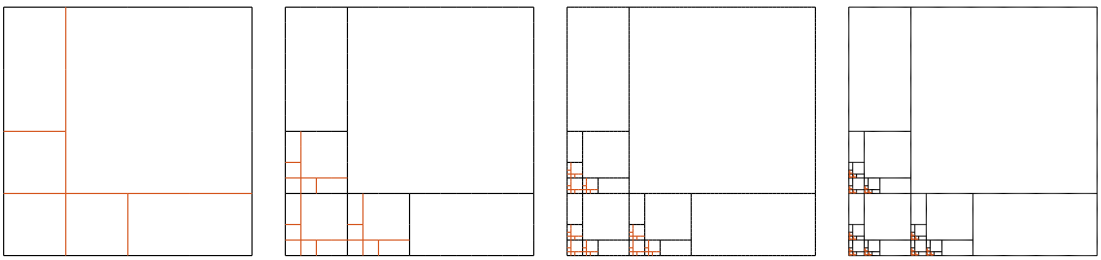

Figure 3.3: Highly localized interface network: Construction of $\Gamma^{(K)}$ with Γ_K (orange) in $d = 2$ space dimensions for $K = 1, \dots, 4$ from left to right.

Recall, that $d_k = \sqrt{2}\, 4^{-k}$, $C_k = 2^{k+1}$, and $r_k = 2^{-k}$ hold. Thus, all assumptions on the interface geometry from Section 3.1.1 and in particular (3.1.3), (3.1.6) are fulfilled. Moreover, the conditions (3.2.17) and (3.2.21) are satisfied for $\mathfrak{c} = 1$, see Example 3.2.27.
Starting from the partition $\mathcal{T}^{(0)}$ of Ω consisting of two congruent triangles, the

initial triangulation $\mathcal{T}^{(1)}$ resolving $\Gamma^{(1)}$ is obtained by two uniform regular refinement steps thereof, while subsequent triangulations $\mathcal{T}^{(k+1)}$ result from two uniform regular refinement steps applied to $\mathcal{T}^{(k)}$, $k \geq 1$. By construction, it holds $h_k = \sqrt{2}\,4^{-k}$, therefore (3.1.20) is satisfied with $\delta = 1$ and the refinement factor from (3.3.21) is bounded by $c_r = 4$. The number of neighboring cells of $G \in \mathcal{G}^{(k)}$ from $\mathcal{G}^{(k)}$ is uniformly bounded by $c_N = 6$, $k \in \mathbb{N}$.
Hence, for this specific fractal interface network, all conditions for the uniform approximation and stability properties of the projections $\Pi_{\mathcal{S}_k}$, $k \in \mathbb{N}$, stated in Corollary 3.2.33 and Corollary 3.2.38, as well as the uniform convergence results in Theorem 3.3.14 and Theorem 3.3.15 are fulfilled.

ν	$K=2$	$K=3$	$K=4$	$K=5$
1	0.291	0.326	0.329	0.337
2	0.352	0.410	0.423	0.442
3	0.387	0.446	0.461	0.489
4	0.400	0.457	0.475	0.511
5	0.404	0.461	0.480	0.526
6	0.406	0.463	0.482	0.540
7	0.406	0.464	0.484	0.553
8	0.406	0.464	0.485	0.565
9	0.406	0.464	0.485	0.575
ρ_K	0.382	0.437	0.453	0.498

Table 3.1: Highly localized interface network: Error reduction factors and geometric mean ρ_K of (MG).

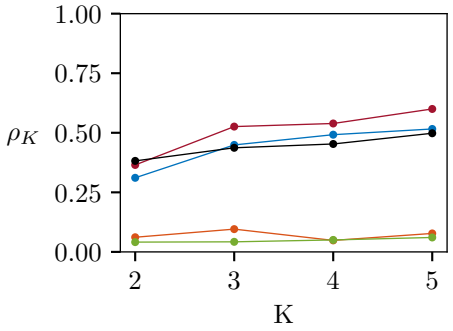

Figure 3.4: Highly localized interface network: Geometric means ρ_K of error reduction factors $\rho_K^{(\nu)}$, $\nu = 1, \ldots, 9$, for the methods MG, patch-JA, patch-GS, cell-JA, cell-GS.

Table 3.1 shows the error reduction factors $\rho_K^{(\nu)}$ of (MG) for the iteration steps $\nu = 1, \ldots, 9$ and the corresponding geometric mean ρ_K, $K = 2, \ldots, 5$. On each level K, the error reduction factors converge to the level specific convergence rate and appear to be bounded away from 1 for increasing K. The other, cg-based methods exhibit a qualitatively similar behavior, however, their error reduction factors are not monotonically increasing as the iteration scheme is nonlinear. Figure 3.4 illustrates the geometric means ρ_K of the reduction factors $\rho_K^{(\nu)}$ for all considered methods with respect to the scale $K = 2, \ldots, 5$. Generally, one observes faster convergence for sequential versions of the respective algorithms. For (cell-JA), they seem to saturate at 0.70, which is also a rough estimate on the upper bound for (patch-JA) and (MG), while 0.15 is a bound for the sequential variants. This finding suggests mesh- and scale-independent convergence of all considered methods.

The discretization accuracy according to (3.3.35) is reached with fewer iteration steps of the sequential methods than the parallel variants, see Table 3.2. Moreover, the parallel methods (cell-JA) and (patch-JA) as well as (MG) seem to scale slightly worse with K, however, they still appear to be rather robust in this regard. Naturally, this observation agrees with the significantly smaller reduction factors for the sequential versions.

K	patch-GS	cell-GS	MG	patch-JA	cell-JA
2	1	1	1	2	1
3	1	1	2	4	3
4	1	1	3	5	5

Table 3.2: Highly localized interface network: Number ν_{stop} of iterations until criterion (3.3.35) is satisfied.

Cantor-type interface network Next, let us consider a Cantor set proposed in [126] and later investigated in the context of fractal homogenization in [61]. It is constructed similarly to the highly localized interface network from Example 3.1.1, that was considered in the last numerical experiment.
Let $\Omega = (0,1)^2 \subset \mathbb{R}^2$ denote the unit square, $\{e_1, e_2\}$ the canonical basis in $\mathbb{R}^2$ and construct the sequence of interfaces $(\Gamma_k)_{k\in\mathbb{N}}$ inductively as follows. Set $\Gamma^{(0)} = \Gamma_0 = \partial\Omega$ and, for given $\Gamma^{(k)}$, $k \geq 0$, define

$$\tilde{\Gamma}_{k+1} = \Gamma^{(k)} \cup \{e_1 + \Gamma^{(k)}\} \cup \{e_2 + \Gamma^{(k)}\}$$

as well as $\Gamma_{k+1} = \frac{1}{2}\tilde{\Gamma}_{k+1} \setminus \Gamma^{(k)}$, see Figure 3.5 for an illustration.

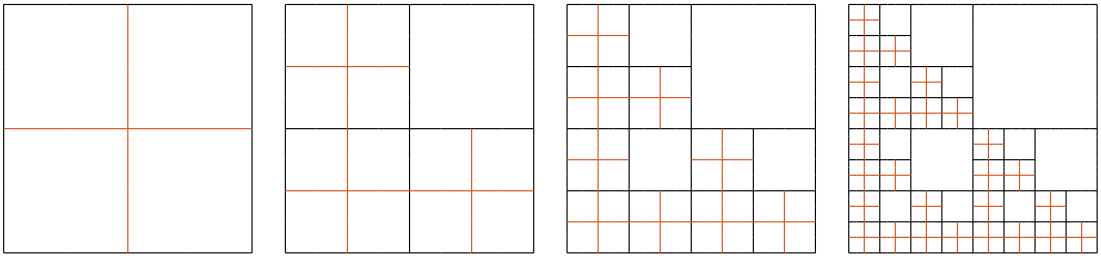

Figure 3.5: Cantor interface network: Construction of $\Gamma^{(K)}$ with Γ_K (orange) in $d = 2$ space dimensions for $K = 1, \ldots, 4$ from left to right.

The resulting fractal interface network Γ is self-similar by construction and the associated geometric quantities are given by $d_k = \sqrt{2}\,2^{-k}$, $C_k = 2^k$, and $C_{k,l} = C_{l-k}$, $l > k$. Thus, it holds $r_k = 2^{-k}$ and $C_0 = 1$ in (3.1.6). Therefore, all assumptions on the interface geometry from Section 3.1.1 and in particular (3.1.3), (3.1.6) are fulfilled. Moreover, condition (3.2.17), which leads to the uniform approximation property of the considered projections is satisfied for $\mathfrak{c} = 1$. However, there is no $\mathfrak{c} > 0$, such that (3.2.21) holds. Consequently, the stability results for the projections and the convergence theory derived therewith cannot be applied. In the context of cell-based subspace decompositions, the geometry of the interface network induces another, prohibitive issue, since there is no uniform bound c_N on the number of neighboring cells of $G \in \mathcal{G}^{(k)}$ from $\mathcal{G}^{(k)}$, $k \in \mathbb{N}$. Strictly speaking, the convergence theory, that was previously developed, cannot be applied to this interface network. Still, most assumptions are satisfied and there is hope that the considered methods perform similarly well.

The simplicial triangulations $\mathcal{T}^{(k)}$ resolving $\Gamma^{(k)}$ are constructed by partitioning Ω uniformly into squares of edge length 2^{-k} and subsequently subdividing each square into two triangles. Note that any such triangulation $\mathcal{T}^{(K)}$ resolves the Cantor level

ν	$K=3$	$K=4$	$K=5$	$K=6$	$K=7$	$K=8$	$K=9$
1	0.486	0.506	0.506	0.505	0.504	0.504	0.504
2	0.527	0.592	0.597	0.596	0.596	0.596	0.596
3	0.544	0.649	0.668	0.668	0.668	0.669	0.669
4	0.551	0.682	0.722	0.724	0.724	0.725	0.725
5	0.555	0.700	0.760	0.766	0.766	0.767	0.767
6	0.557	0.710	0.786	0.798	0.798	0.798	0.799
7	0.558	0.715	0.804	0.822	0.823	0.823	0.823
8	0.558	0.719	0.816	0.840	0.842	0.842	0.842
9	0.559	0.721	0.823	0.854	0.857	0.857	0.857
ρ_K	0.543	0.662	0.712	0.721	0.721	0.721	0.721

Table 3.3: Cantor interface network: Error reduction factors and geometric mean ρ_K of (MG).

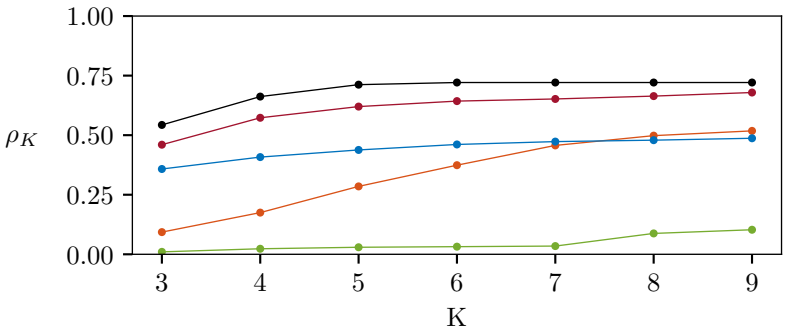

Figure 3.6: Cantor interface network: Geometric means ρ_K of the error reduction factors $\rho_K^{(\nu)}$, $\nu = 1, \dots, 9$, for the methods MG, patch-JA, patch-GS, cell-JA, cell-GS.

interface network $\Gamma^{(k)}$, $K > k$. By construction, it holds $h_k = \sqrt{2}\, 2^{-k}$ and (3.1.20) is satisfied with $\delta = 1$. The refinement factor from (3.3.21) is bounded by $c_r = 2$.

As is demonstrated in Table 3.3, the error reduction factors $\rho_K^{(\nu)}$ of (MG) converge to the level specific convergence rates and appear to be bounded away from 1 for increasing K, $K = 3, \dots, 9$. The cg-based methods show a qualitatively similar behavior, although their error reduction factors are not monotonically increasing as the iteration scheme is nonlinear. Again, the geometric means ρ_K of the reduction factors $\rho_K^{(\nu)}$ with respect to the scale $K = 3, \dots, 9$ illustrate, that sequential versions converge faster than their parallel counterparts, see Figure 3.6. The error reduction factors for all methods seem to saturate with increasing K, suggesting mesh- and scale-independent convergence.

The discretization accuracy according to (3.3.35) is reached with fewer iteration steps of the sequential methods than the parallel variants, see Table 3.4. Moreover, the parallel methods (cell-JA) and (patch-JA) as well as (MG) appear to scale worse

K	patch-GS	cell-GS	MG	patch-JA	cell-JA
3	1	1	2	2	3
5	1	2	5	4	6
7	1	2	> 10	6	10
9	1	3	> 10	8	> 10

Table 3.4: Cantor interface network: Number ν_{stop} of iterations until criterion (3.3.35) is satisfied.

with K, while the others remain rather robust in this regard. In comparison to the previous numerical experiment with the highly localized interface network, the overall convergence behavior is slightly worse but still highly efficient and robust with respect to the mesh size as well as scale K.

Geologically inspired interface network The last interface network mimics a fractal crystalline structure. It is constructed using an algorithm with certain random components first published in [78] and produces geometries, that are reminiscent of microstructures observed in the geosciences, e.g. Quartz grain deformation patterns or during subgrain rotation recrystallization. The triangulation $\mathcal{T}^{(1)}$ results from applying four uniform regular refinement steps to the initial partition $\mathcal{T}^{(0)}$ consisting of two congruent triangles. Moreover, any further triangulation $\mathcal{T}^{(k+1)}$ ensues from uniform regular refinement of $\mathcal{T}^{(k)}$, $k \geq 1$. The level-k interfaces are constructed inductively as follows.

Let $G_0 = \Omega$ denote the initial cell with center $c = (0.5, 0.5)^T$ and midpoints $l, t, r, b \in \mathbb{R}^2$ of its left, top, right, and bottom boundary. The level-1 interface Γ_1, as shown in the left picture of Figure 3.7, then consists of four connected paths of edges in $\mathcal{E}^{(1)}$ starting with l, t, r, b and ending with c. The edges are selected randomly with strong bias towards the straight line connecting the corresponding start and end points under the constraint, that the four paths do not self-intersect and meet in and only in c. Thus, $\Gamma^{(1)} = \Gamma_1$ splits G_0 into four level-1 subcells $G_i \in \mathcal{G}^{(1)}$, $1 \leq i \leq 4$, whose "centers" $c_i^{(1)}$ are given by $\frac{1}{2}(l+t)$, $\frac{1}{2}(t+r)$, $\frac{1}{2}(r+b)$, $\frac{1}{2}(b+l)$. The "midpoints" for their left, top, right, and bottom boundaries are derived from their respective $c_i^{(1)}$ by selecting appropriate points in $\Gamma^{(1)} \cap \{c_i^{(1)} + se_1 \,:\, s \in \mathbb{R}\}$ and $\Gamma^{(1)} \cap \{c_i^{(1)} + se_2 \,:\, s \in \mathbb{R}\}$. Each cell $G_i \in \mathcal{G}^{(1)}$ is either marked for refinement now or will remain invariant forever. Marking a cell for refinement or setting $G_i \in \mathcal{G}_\infty^{(1)}$ is done randomly according to the probability $\mathcal{P}(\min\{c_{i,1}, c_{i,2}\})$ with density $\rho(\xi) = 2(1-\xi)$, $\xi \in (0,1)$, i.e., with a linear bias towards the left and the lower boundary of Ω. The cells $G_i \in \mathcal{G}^{(1)} \setminus \mathcal{G}_\infty^{(1)}$, that are to be refined, are split into four subcells by four, randomly generated paths of edges in $\mathcal{E}^{(2)}$ starting with midpoints of its left, top, right, and bottom boundary and ending in c_i similarly to the splitting of the initial cell G_0. The union of all these paths constitutes the level-2 interface Γ_2. Repeating these steps inductively leads to all further interface networks Γ_k, $k = 2, \ldots, 6$ (see Figure 3.7).

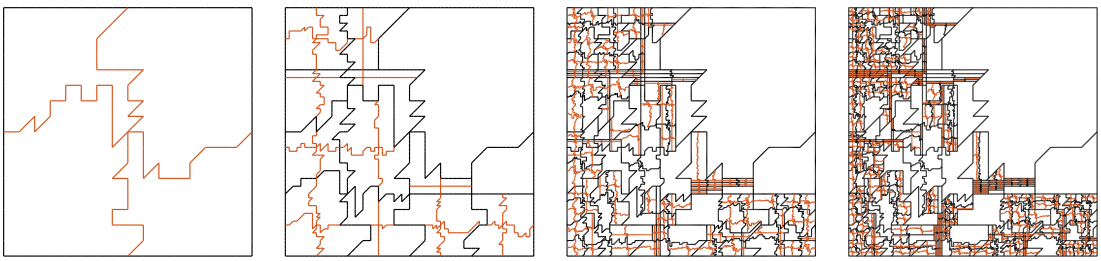

Figure 3.7: Geologically inspired interface network: Construction of $\Gamma^{(K)}$ with Γ_K (orange) in $d = 2$ space dimensions for $K = 1, 3, 5, 6$.

By construction, the resulting interface network satisfies $d_k \to 0$ for $k \to \infty$. Yet, it is not obvious how sharp estimates for the geometric quantities from Section 3.1.1,

namely d_k, C_k, and r_k, $k \geq 1$, turn out. For the ensuing numerical computations, C_k from the Cantor interface network will be used. In general, the interface network does not fulfill the conditions stated in Corollary 3.2.33 and Corollary 3.2.38 that finally lead to the convergence results developed in this section.

ν	$K=2$	$K=3$	$K=4$	$K=5$	$K=6$
1	0.598	0.614	0.582	0.545	0.519
2	0.637	0.695	0.690	0.668	0.652
3	0.660	0.742	0.748	0.733	0.721
4	0.676	0.773	0.789	0.780	0.769
5	0.688	0.795	0.818	0.817	0.805
6	0.698	0.810	0.840	0.845	0.833
7	0.706	0.821	0.857	0.868	0.856
8	0.713	0.829	0.870	0.885	0.875
9	0.719	0.835	0.879	0.899	0.890
ρ_K	0.676	0.765	0.780	0.774	0.759

Table 3.5: Geologically inspired interface network: Error reduction factors and geometric mean ρ_K of (MG).

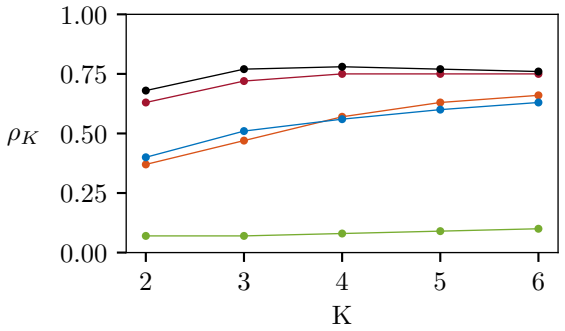

Figure 3.8: Geologically inspired interface network: Geometric means ρ_K of the error reduction factors $\rho_K^{(\nu)}$, $\nu = 1, \ldots, 9$, for the methods MG, patch-JA, patch-GS, cell-JA, cell-GS.

Nevertheless, the error reduction factors $\rho_K^{(\nu)}$ of (MG) as displayed in Table 3.5 converge to the level specific convergence rates, appear to be bounded away from 1 for increasing K, $K = 3, \ldots, 9$ and only moderately deteriorate in comparison with the highly localized and Cantor-type cases. The cg-based methods demonstrate a qualitatively similar behavior. Sequential versions converge faster than their parallel counterparts as the geometric means ρ_K of the error reduction factors $\rho_K^{(\nu)}$ with respect to $K = 2, \ldots, 6$ depicted in Figure 3.8 show. For all methods, the error reduction factors seem to saturate with increasing K, suggesting mesh- and scale-independent convergence.

According to (3.3.35), the discretization accuracy is reached with fewer iteration steps of the sequential methods than the parallel variants, see Table 3.6. Moreover, the parallel methods (cell-JA) and (patch-JA) appear to scale slightly worse with K, while the others remain rather robust for increasing K.
Evidently, the numerical methods are not only very robust with respect to the mesh size and the scale K, but also with regard to the geometry of the interface network.

Although only the first, highly localized interface network satisfies all conditions to apply the presented convergence theory, the performance of the investigated algorithms deteriorates only slightly for the other interface networks and the same qualitative behavior is observed.

K	patch-GS	cell-GS	MG	patch-JA	cell-JA
2	1	1	1	1	1
4	1	1	2	3	4
6	1	2	4	6	8

Table 3.6: Geologically inspired interface network: Number ν_{stop} of iterations until criterion (3.3.35) is satisfied.

4 Application to geological fault networks

In this concluding chapter of the thesis, the discretization approach and algorithmic approximation of layered fault systems, that was developed in Chapter 2, will be put to the test in a series of numerical experiments. All considered setups consist of a deformable body of St. Venant Kirchhoff material in $d = 2$ space dimensions, that is split into m sub-bodies with corresponding reference domains Ω_i, $i = 1, \dots, m$, by $m - 1$ planar faults. In particular, the dynamics of the systems and solver performance will be investigated over the time interval $[0, T]$ with final time $T = 60\,\mathrm{s}$. Some of the findings presented hereafter are subject of an upcoming publication [54].

The implementation is based on the **D**istributed and **U**nified **N**umerics **E**nvironment (DUNE) [12, 17, 117], written in C++ and available as the separate module dune-tectonic[1]. DUNE is a modular software framework for solving partial differential equations with widely used grid-based methods, e.g. finite element, finite volume and finite difference methods. One important design feature is the separation of concerns, i.e. data structures and functionality, through slim, template dependent interfaces. This leads to a very flexible, efficient (both with respect to scientific computations and implementation time) and extendable framework. Apart from the available core and grid modules, the implementation depends on additional ones providing finite element assemblers (dune-fufem), solvers (dune-solvers, dune-tnnmg), data structures (dune-matrix-vector), and dual mortar coupling (dune-contact), that are developed and maintained at Freie Universität Berlin[2]. Note that dune-contact makes use of the dune-grid-glue library [11], which provides infrastructure for the coupling of two unrelated DUNE grids[3].

4.1 Discretization and algebraic solution

Time stepping strategies In the subsequent experiments, time discretization will be carried out using two different strategies for time step size selection. The first is given by a straightforward partition of the interval $[0, T]$ into N uniform time steps of length $\tau = T/N$.
However, the seismic cycle postulates strongly varying dynamics of stick-slip systems ranging from phases of slow interseismic loading to fast coseismic periods. In this light, one expects to benefit from adaptive time step size selection in terms of shorter

[1] `https://git.imp.fu-berlin.de/podlesny/dune-tectonic`
[2] `https://git.imp.fu-berlin.de/agnumpde`
[3] `https://gitlab.dune-project.org/extensions/dune-grid-glue`

computation times while maintaining accuracy. This is pursued by the following standard, adaptive strategy and based on the assumption that the dynamics can be resolved efficiently with only slightly varying, subsequent time step sizes.
For given approximate solution of the coupled spatial Problem 2.6.4 at time $t_n \in [0, T)$, that was obtained with the time step size τ_{n-1}, choose $\tau_n^* = \tau_{n-1}$ for $n \geq 0$ and $\tau_{-1} = 10^{-4}\, T$ as an initial guess for the new time step size τ_n. Then, compute an approximate solution $(\dot{u}_{n+1}^{(C)}, \alpha_{n+1}^{(C)})$ of the coupled spatial Problem 2.6.4 at $t_n + 2\tau_n^*$ with one time step of size $2\tau_n^*$ and another solution $(\dot{u}_{n+1}^{(R)}, \alpha_{n+1}^{(R)})$ with two time steps of size τ_n^*. If the criterion

$$\|\alpha_{n+1}^{(C)} - \alpha_n^{(R)}\|_{L^2(\Gamma^F)} \leq \delta_\tau \, \mathrm{m}^{1/2} \tag{4.1.1}$$

is fulfilled for a suitable tolerance δ_τ, then the time step is coarsened by setting $\tau_n^* := 2\tau_n^*$ and the above coarsening procedure repeated until (4.1.1) is no longer satisfied. If coarsening the time step size is not feasible, i.e. the criterion (4.1.1) is violated for the initial guess $\tau_n^* = \tau_{n-1}$, then proceed similarly to refine it. Refinement is performed by successive bisection of the time step size $\tau_n^* := \tau_n^*/2$ until (4.1.1) is met for the first time. The last accepted time step size candidate τ_n^* determines the new time step size $\tau_n = \tau_n^*$. The tolerance δ_τ is fixed in alignment with the prescribed accuracy of the inner fixed point iteration and is specified below.

Triangulations The ensuing spatial problems, that have to be solved in each time step, are discretized with respect to triangulations $\mathcal{T}_i^{(K)}$ resulting from K refinement steps applied to initial triangulations $\mathcal{T}_i^{(0)}$ of the domains Ω_i, $i = 1, \ldots, m$. Their generation varies for the individual experiments and will be detailed in their respective, dedicated sections. These triangulations give rise to an associated hierarchy of finite element spaces, which are basis for the construction of the algebraic solvers and in particular the TNNMG method.

Fixed point iteration A major building block of the proposed solution algorithm is decoupling the spatial rate-and-state Problem 2.6.4 by means of the fixed point iteration (2.6.8). The relaxation parameter is set to $\omega = 1/2$ and the iteration is terminated once the stopping criterion

$$\|\alpha_{n,\mathcal{B}}^{\nu} - \alpha_{n,\mathcal{B}}^{\nu-1}\|_{L^2(\Gamma^F)} \leq 10^{-1} \delta_\tau \, \mathrm{m}^{1/2} \tag{4.1.2}$$

is satisfied. The required number of fixed point iterations ν_{stop} to meet the criterion is crucial to the feasibility of this approach in practice. The tolerance parameter δ_τ is the same as in the adaptive time stepping strategy (4.1.1), selected to ensure a comparable accuracy of fixed point iteration and time stepping, and intended to be in the range of the discretization error. This choice and its actual value $\delta_\tau = 10^{-5}$ are motivated by systematic trial and error optimizing computational efficiency in the setting of unilateral frictional contact, cf. [101, Section 3.3]. Similar efforts could be undertaken in the present setting, but are not part of this thesis.

Algebraic solution of the parametrized rate and state problems The algebraic solution of the discrete state problem (2.6.6) with given rate for Dieterich's aging law is approximated using pointwise bisection until the pointwise error is uniformly bounded by the threshold 10^{-12}.
The algebraic solution of the discrete rate problem (2.6.5) with given state is computed using the Truncated Nonsmooth Newton Multigrid (TNNMG) method described in Section 2.7. The initial iterate is given by the final iterate of the preceding step in the fixed point iteration. In each TNNMG step, the truncated, linear correction is determined with 5 iteration steps of a standard multigrid V-cycle with 3 pre- and 3 post-smoothing steps, i.e. the linear solver (MG) employed for the scalar, multiscale interface problems from the numerical experiments in Section 3.3.2 that demonstrated rapid, mesh- and scale-independent convergence rates. The iteration is terminated once the stopping criterion

$$\left\| \dot{u}^{\nu} - \dot{u}^{\nu-1} \right\|_n \leq 10^{-8}\,\mathrm{W}^{1/2}\mathrm{m}^{1/2} \tag{4.1.3}$$

is fulfilled, where $\|\cdot\|_n = a_n(\cdot,\cdot)^{1/2}$ denotes the time-dependent energy norm with $a_n(\cdot,\cdot)$ from (2.5.4). This way, the error of the inner multigrid iteration is reduced several orders of magnitude below the error of the outer fixed point iteration.

4.2 Spring slider with deformable foundation

As a first application, let us consider a spring slider experiment similar to the one presented in [102], but featuring a deformable instead of a rigid foundation. It consists of two bodies each with dimensions $5\,\mathrm{m} \times 1\,\mathrm{m}$, whose reference domains are given by $\Omega_1 = (-2.5, 2.5) \times (-1, 0)$ and $\Omega_2 = (-2.5, 2.5) \times (0, 1)$ with contact interface $\Gamma^F = (-2.5, 2.5) \times \{0\}$. The bodies are subject to gravity, i.e. the body force f is constant and given by $f = -\rho g \cdot e_2$, where g denotes the gravitational constant. On the vertical boundaries Γ_i^N of the reference configurations Ω_i, $i = 1, 2$, let us impose homogeneous Neumann conditions $f^N = 0$. The foundation is fixed along its lower boundary Γ_1^D via homogeneous Dirichlet conditions $u(\,\cdot\,, t) = \dot{u}(\,\cdot\,, t) = 0$, $0 \leq t \leq T$. Along the upper Dirichlet boundary Γ_2^D of the slider, the condition $\dot{u}(\,\cdot\,, t) = v_D\, \xi(t) \cdot e_1$ prescribes a smooth transition of the velocities from zero to a regime with constant loading speed $v_D = 2 \times 10^{-4}\,\mathrm{m/s}$ using

$$\xi(t) = \begin{cases} \frac{1}{2}(1 - \cos(4\pi t/T)), & \text{if } t \leq T/4 \\ 1 & \text{otherwise.} \end{cases} \tag{4.2.1}$$

At the friction boundary Γ^F between foundation and slider, rate-and-state friction conditions hold with Dieterich's aging law. See Figure 2.1 for an illustration of the experimental setup.

At $t = 0$, the initial deformation $u(\cdot, 0)$ is determined by one step of the fixed point iteration associated with the stationary problem (2.4.6) and thus approximates the equilibrium configuration. Furthermore, the initial velocity field is set to $\dot{u}(\,\cdot\,, 0) = 0$ on Ω, which is consistent with the Dirichlet conditions and the initial state field is

bulk parameter	value	friction parameter	value
bulk modulus E	4.12×10^7 Pa	ref. velocity V_0	1×10^{-6} m/s
Poisson ratio ν	0.3	ref. friction coeff. μ_0	0.6
mass density ρ	5×10^3 kg/m^2	a	0.010
gravity g	9.81 N/kg	b	0.015
		charact. slip dist. L	1×10^{-5} m

Table 4.1: Material parameters.

defined as $\alpha(\,\cdot\,, 0) = -10$ on Γ^F. The remaining material parameters are selected in accordance to Table 4.1.

The initial triangulations $\mathcal{T}_i^{(0)}$ of the domains Ω_i, $i = 1, 2$, are shown in the left picture of Figure 4.1. For the upcoming experiments, various final triangulations $\mathcal{T}_i^{(K)}$, $i = 1, 2$, resulting from $K = 2, \ldots, 5$ steps of global red refinement, i.e. bisection of all edges of all triangles $T \in \mathcal{T}_i^{(k)}$ to obtain the refined triangulation $\mathcal{T}_i^{(k+1)}$, $k = 0, \ldots, K-1$, will be considered. The right picture of Figure 4.1 depicts the triangulations $\mathcal{T}_i^{(3)}$, $i = 1, 2$.

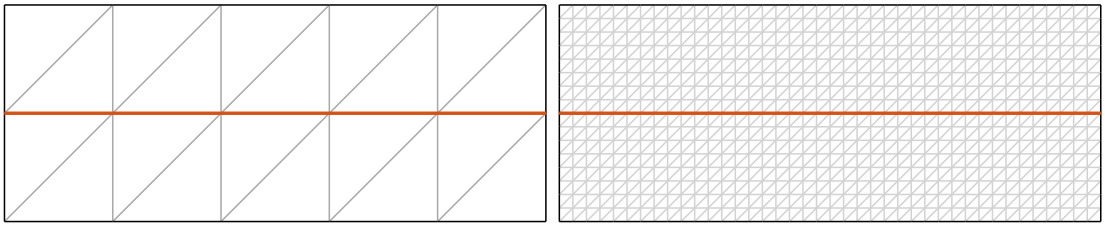

Figure 4.1: Spring slider: Initial triangulations $\mathcal{T}_i^{(0)}$ (left) and uniformly refined triangulations $\mathcal{T}_i^{(K)}$ with $K = 3$ (right), $i = 1, 2$. The fault is shown in orange.

Simulation results

Next, let us examine the qualitative dynamics of the deformed bodies during the time interval $[0, T]$. For this purpose, Figure 4.2 shows the mean value of the approximate relative velocity $|[\dot{u}_{n,\mathcal{S}}]^{u_{n-1},\mathcal{S}}|$ over the entire fault Γ^F for each time instant $t_n \in [0, T]$. One observes that the behavior of the system is characterized by slider and foundation undergoing an initial loading phase, until at roughly $t_n = 24$ s it transitions into a pattern of almost periodic peaks in relative velocity indicating the occurrence of slip events. Here, the periodicity of slip events is slightly perturbed in relation to the one discovered in numerical experiments with a rigid foundation [102].

The spatial propagation of individual slip events along the entire fault is illustrated in Figure 4.3. Choosing a uniform time step size of $\tau = T/10^6$ and final triangulations $\mathcal{T}_i^{(4)}$, $i = 1, 2$, it depicts isolines of approximate relative velocities on the fault Γ^F (horizontal axis) offset by the loading velocity evolving over various short time intervals (vertical axis) corresponding to the first six slip events (top left to bottom right). The first slip event represents a bilateral rupture, i.e. it nucleates at the center of Γ^F and spreads towards both its edges. This behavior is qualitatively similar to the one observed in the case of unilateral contact in [102]. Moreover, symmetric

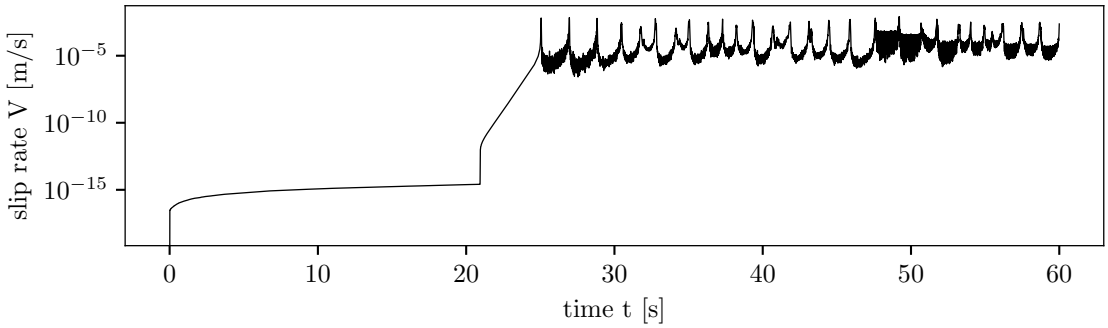

Figure 4.2: Spring slider: Initial loading phase and almost periodic slip events evidenced by the mean value of relative velocities over the entire fault Γ^F for each time instant $t_n \in [0, T]$ computed with uniform time step sizes $\tau = T/10^6$ and final triangulations $\mathcal{T}_i^{(4)}$, $i = 1, 2$.

aftershocks occur where the primary wave ran out towards the edges of the fault. The second slip event features symmetric foreshocks situated approximately where the aftershocks of the previous slip event took place before the fault ruptures along most of its length. Again, it is followed by aftershocks in a similar location. Both of these events appear to be spatially symmetric with respect to the center of the fault.

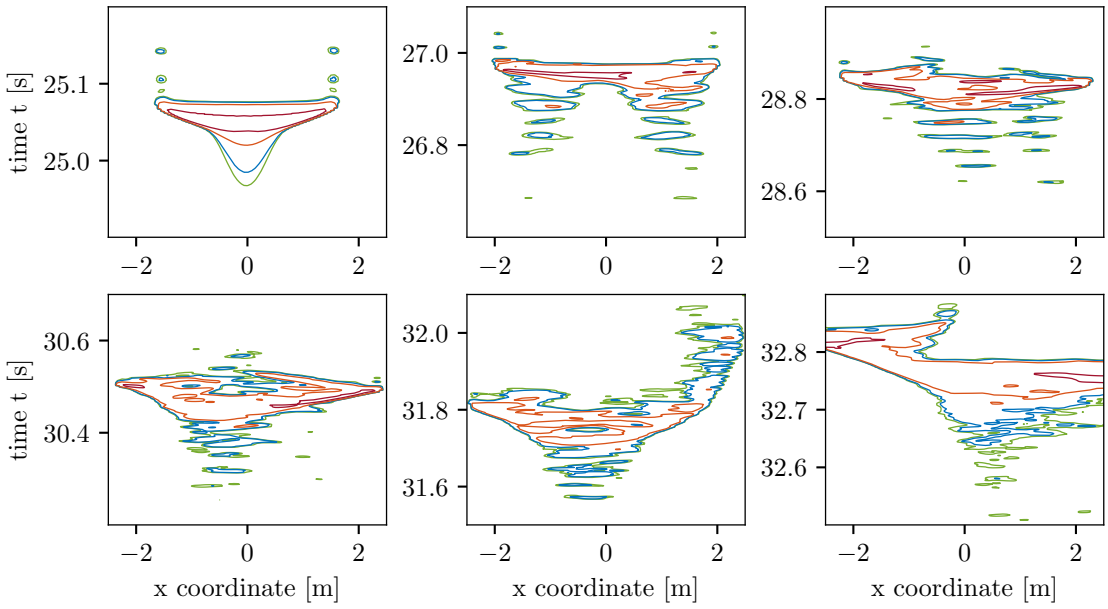

Figure 4.3: Spring slider: Isolines (10^1 µm/s green, 10^2 µm/s blue, 10^3 µm/s orange, 10^4 µm/s red) of relative velocities along Γ^F over different time intervals resolving the first 6 slip events (top left to bottom right).

In contrast, the other shown events do not possess this symmetry, but nucleate close to the center and spread bilaterally across the entire fault nonetheless. Especially event 5 and 6 display more pronounced dynamics to the right and left of Γ^F, respectively. Generally, primary ruptures seem to be preceded by foreshocks located mainly towards the center of the fault, where subsequently the slip events emerge. Furthermore, aftershocks can be observed typically wherever the primary rupture last subsided. These characteristics are considerably different from the purely periodic behavior observed in simulations of a subduction zone with rigid foundation [101].

The next objective is to investigate the behavior in the stick-slip regime and assess properties of the time discretization, fixed-point iteration and performance of the algebraic solver.

Convergence properties of the time discretization

Focusing on the beginning of the strike-slip regime and the first 6 slip events, let us take a closer look at the mean value of the approximate relative velocity $|[\dot{u}_{n,\mathcal{S}}]^{u_{n-1,\mathcal{S}}}|$ over the entire fault Γ^F during the time interval $[24.7, 33.5]$. While the final triangulations $\mathcal{T}_0^{(K)}$ and $\mathcal{T}_1^{(K)}$ remain fixed with $K = 4$, a series of experiments using the classical Newmark scheme with uniform step sizes $\tau_j = T/N_j$, $N_j = 10^{4+j}$, $j = 0, 1, 2$, is conducted, see Figure 4.4. For decreasing time step sizes, the resulting approximate relative velocity seems to converge.

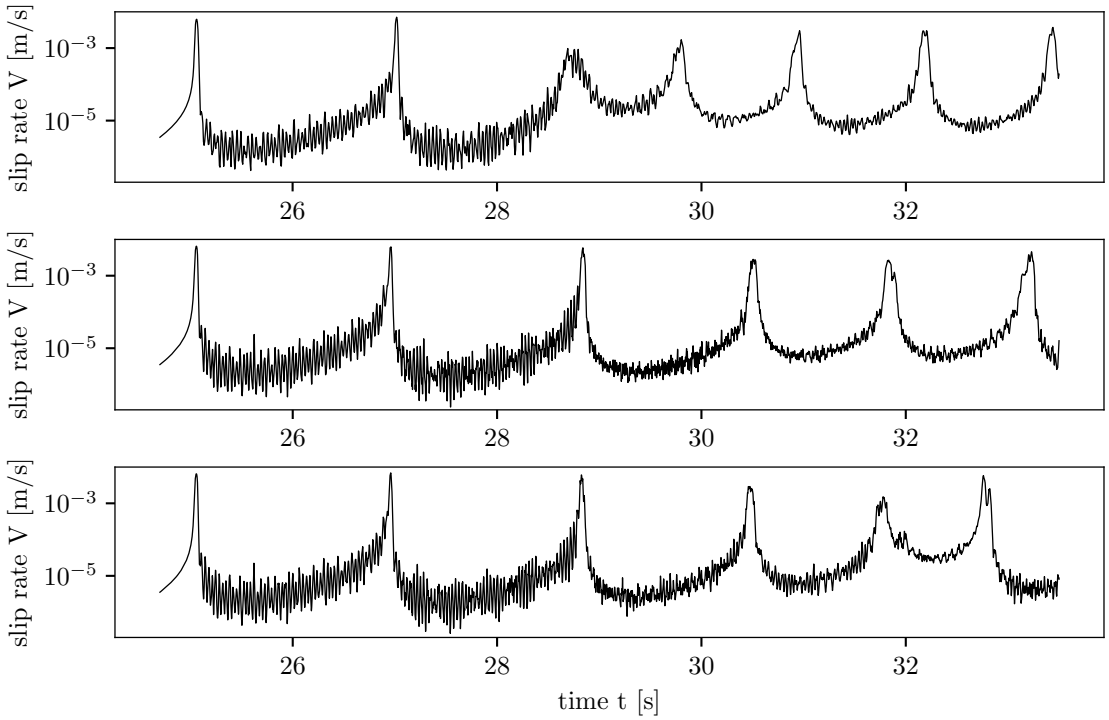

Figure 4.4: Spring slider: Mean approximate relative velocities over the fault Γ^F with final triangulations $\mathcal{T}_i^{(4)}$, $i = 1, 2$, and uniform Newmark time stepping using decreasing sizes $\tau_j = T/N_j$, $N_j = 10^{4+j}$, $j = 0, 1, 2$ (top to bottom).

However, one observes highly oscillatory behavior on much smaller time scales than the low frequency stick-slip process, that persists through refinement of the time step. The cause of this phenomenon is twofold.
Similar, high frequency oscillations turn out utilizing the dissipative backward Euler method and sufficiently fine time steps $\tau = T/10^6$, see Figure 4.5. In comparison to the Newmark discretization, cf. the bottom picture in Figure 4.4, the resulting amplitudes appear to be smaller. This suggests a physical origin for some of the oscillatory behavior, which is supported by findings from simulations for unilateral frictional contact [102].

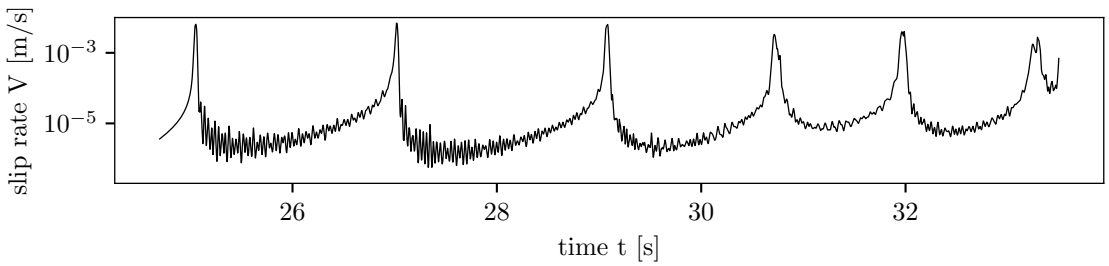

Figure 4.5: Spring slider: Mean approximate relative velocities over the fault Γ^F with final triangulations $\mathcal{T}_i^{(4)}$, $i = 1, 2$, and uniform backward Euler time stepping with step size $\tau = T/10^6$.

Secondly, high frequency oscillations and instability are numerical artifacts attributed to known shortcomings of the classical Newmark scheme in the context of (frictional) contact problems, see Section 2.5 for a detailed discussion. In the established literature, several modifications are suggested to overcome these drawbacks (see Krause & Walloth [82] and the references cited therein for an overview and comparison).

Adaptive time stepping

The bottom picture of Figure 4.6 shows the mean approximate relative velocity using adaptive time stepping with minimal step size $\tau_{\min} = 1.5\,T/10^6$ (black) and unrestricted step size selection leading to minimal step sizes of $\tau_{\min} = 9.8\,T/10^8$ (blue). In the following, the version with unrestricted step size selection serves as an approximation of the exact solution. The evolution of the depicted velocities appears to be identical except for the last peak suggesting convergence and a certain robustness with respect to the temporal resolution of the slip events on the considered time interval.

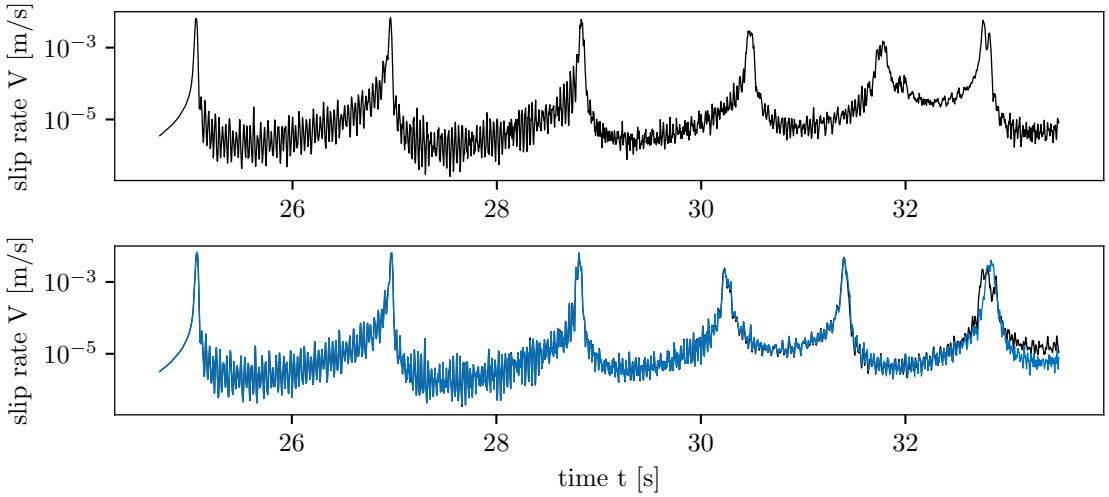

Figure 4.6: Spring slider: Mean approximate relative velocities over the fault Γ^F with final triangulations $\mathcal{T}_i^{(4)}$, $i = 1, 2$, using uniform Newmark time stepping with step size $\tau = T/10^6$ (top) and adaptive time stepping (bottom) with minimal step size $\tau_{\min} = 1.5\,T/10^6$ (black) and unrestricted step size selection (blue).

Moreover, the mean velocities computed with restricted, adaptive time stepping seem closer to the exact solution (blue) than the ones obtained with uniform Newmark time stepping with a comparable step size, see the top picture of Figure 4.6. On one hand, this is rather surprising as the approach with uniform time steps possesses a much finer resolution of the interseismic phase in addition to a similar resolution of coseismic dynamics. Unfortunately, the improved temporal resolution does not lead to more accurate solutions in the interseismic phase, but adds unnecessarily computed time steps in which numerical instabilities accumulate. This explains the observed phenomenon.

Convergence properties of the fixed point iteration

Discretizing $[0, T]$ uniformly in time with 10^4 steps, the average and maximum number of fixed point iterations per time step for spatial problems arising from the final triangulations $\mathcal{T}_0^{(K)}$ and $\mathcal{T}_1^{(K)}$, $K = 2, \dots, 6$, is depicted in Figure 4.2. The average number of required iterations seems to saturate indicating mesh-independent convergence of the fixed point iteration. In case of unilateral contact, this claim is supported by theoretical results [99] and practical experience [102].
The maximum number of fixed point iterations is attained during slip events indicating that the utilized time step size $\tau = T/10^4$ is too coarse to resolve the dynamics during ruptures accurately. The suggested adaptive time step size selection is a suitable remedy as the next section demonstrates.

K	2	3	4	5	6
max	30	36	47	53	56
avg	3.76	4.14	4.05	4.10	4.05

Table 4.2: Spring slider: Average and maximum number of fixed point iterations per 10^4 uniform time steps depending on the number of grid refinements K.

Adaptive time stepping and performance of the algebraic solver

Last, let us assess the adaptive selection of time steps as well as the performance of the algebraic solver that is composed of the fixed point iteration (2.6.8) decoupling rate and state and the TNNMG method for the solution of the rate problem as described in Section 2.7. The top picture of Figure 4.7 shows the adaptively selected time step sizes τ_n for the time instants $t_n \in [24, T]$ starting shortly before the end of the loading phase. Note that the time step size is reduced by about 2 orders of magnitude, whenever slip events occur, to maintain accuracy. Consequently, resolving slip events with sufficiently small time steps leads to few fixed point iterations required to satisfy the stopping criterion (4.1.2). As opposed to a uniform time step size in the previous section, here, usually 2 - 4 fixed point iterations suffice for adaptively selected time steps, see the middle picture. In each step of the outer fixed point iteration, the sum of all inner TNNMG iterations necessary to fulfill the stopping criterion (4.1.3) ranges from 5 to 23 as the bottom picture demonstrates.

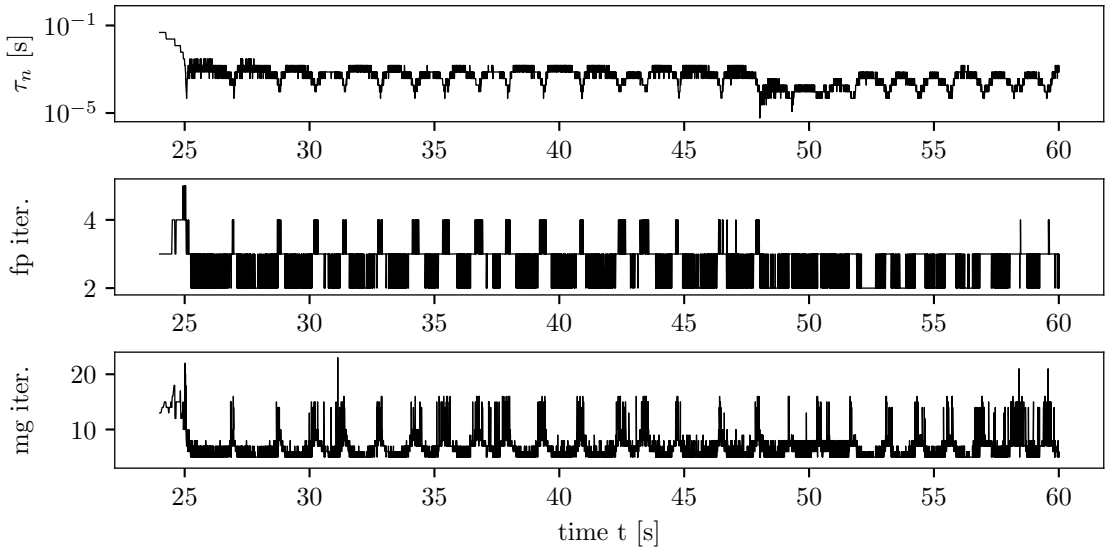

Figure 4.7: Spring slider: Adaptive time step selection and performance of the algebraic solver in terms of computed outer fixed point (fp) iterations per time step and corresponding sum of inner TNNMG (mg) iterations.

4.3 Layered fault system

The last application involves the layered fault system introduced as the mathematical model problem in section 2.3 and accompanied us throughout the rest of the exposition. It is an extension of the 2-body spring slider setup to multiple spatial scales.
The various experimental setups considered here consist of $m = 2, \dots, 5$ layered bodies with dimensions $5\,\mathrm{m} \times 0.3^{s_i}\,\mathrm{m}$, $i = 1, \dots, m$, where

$$s_i = \begin{cases} i-1, & \text{if } i < 1 + m/2 \\ m-i, & \text{otherwise} \end{cases}$$

and associated reference configurations Ω_i resulting from the decomposition of $\Omega = (-2.5, 2.5) \times (0, \sum_{i=1}^{m} 0.3^{s_i})$ by the faults

$$\Gamma^F = \bigcup_{i=1}^{m-1} \Gamma^F_{i,i+1} = \bigcup_{i=1}^{m-1} (-2.5, 2.5) \times \left\{ \textstyle\sum_{j=1}^{i} 0.3^{s_j} \right\}.$$

This construction leads to a layering such that the height of bodies shrinks exponentially from bottom and top towards the center of the stack of bodies, see Figure 2.3. For $m = 2$, the spring slider configuration from the previous section is recovered.

Similar to the spring slider setting in Section 4.2, the layered fault system is fixed by homogeneous Dirichlet conditions $u(\cdot, t) = \dot{u}(\cdot, t) = 0$, $0 \le t \le T$ at the bottom boundary Γ^D_1 of the bottom body Ω_1. At the upper Dirichlet boundary Γ^D_m of the top body Ω_m, $m = 2, \dots, 5$, the condition $\dot{u}(\cdot, t) = v_D\, \xi(t) \cdot e_1$ prescribes the same smooth transition from zero velocity to a regime of constant loading, cf. (4.2.1). Otherwise, the material parameters, body force, bodywise homogeneous Neumann boundary conditions and rate-and-state friction conditions with Dieterich's aging

law on Γ^F as well as the initial deformation, velocity and state fields are chosen in analogy to the ones introduced in Section 4.2.

For all experiments performed in this section, time discretization and the selection of time step sizes is controlled by the adaptive procedure described in Section 4.1. The ensuing spatial problems occurring in each time step are discretized with respect to triangulations $\mathcal{T}_i^{(K)}$ resulting from K refinement steps applied to initial triangulations $\mathcal{T}_i^{(0)}$ of the domains Ω_i, $i = 1, \dots, m$. The initial triangulations $\mathcal{T}_i^{(0)}$ are determined by partitioning Ω_i into $M = \lfloor 5/0.3^{s_i} \rfloor$ rectangles of dimensions $5/M$ m $\times\, 0.3^{s_i}$ m and then splitting each rectangle into two triangles, e.g., see the left picture of Figure 4.8 for the resulting initial triangulations for $m = 5$.

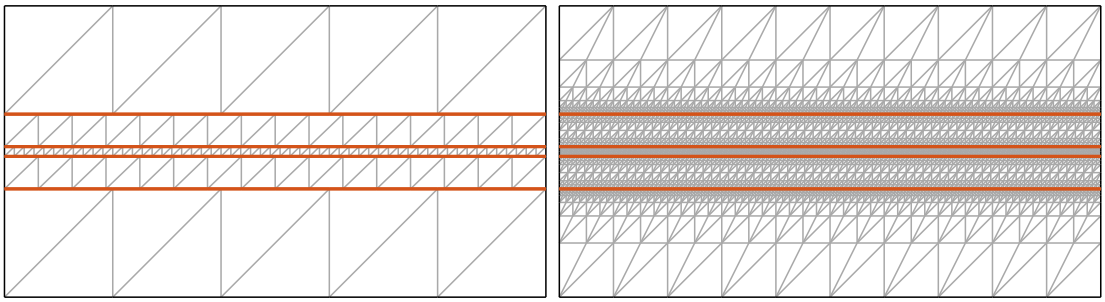

Figure 4.8: Initial triangulations $\mathcal{T}_i^{(0)}$ (left) and adaptively refined final triangulations $\mathcal{T}_i^{(5)}$ (right) for $m = 5$ bodies, $i = 1, \dots, m$. The $m - 1$ faults are shown in orange.

Subsequently, a priori red-green refinement is concentrated at the faults and achieved by the following adaptive procedure. Starting with $\mathcal{T}_i^{(0)}$, regular (red) refinement, i.e. bisection of all edges, is applied to all triangles $T \in \mathcal{T}_i^{(k)}$, $k \geq 0$, whose diameter h_T violates the criterion

$$h_T < (1 + 80\, d(T, \Gamma^F)\, h_{\min}, \tag{4.3.1}$$

where $d(T, \Gamma^F)$ denotes the distance of T to Γ^F and $h_{\min} = 6.25$ cm. Afterwards, the triangles, for which two or three edges have been bisected by previous red refinement, are marked and refined regularly until only those with no or only one bisected edge remain. The latter ones are refined by (green) closures connecting the midpoint of the bisected edge with the opposite vertex. By this procedure, the resulting triangulation $\mathcal{T}_i^{(k+1)}$ is conforming. In order not to jeopardize shape regularity, the (green) closures are removed before another step of red-green refinement is applied [9]. This strategy for a priori, adaptive refinement terminates with $K = k$, once the criterion (4.3.1) is satisfied for all triangles $T \in \mathcal{T}_i^{(k)}$ and all $i = 1, \dots, m$. For $m = 5$, the final triangulations $\mathcal{T}_i^{(K)}$ after $K = 5$ refinement steps are shown in the right picture of Figure 4.8.
For each number of bodies $m = 2, \dots, 5$, Table 4.3 summarizes the total number of grid vertices as well as bounds on the triangle diameters h_T, $T \in \mathcal{T}_i^{(K)}$, $i = 1, \dots, m$, generated by this procedure.

m	2	3	4	5
no. vertices	1274	2113	2952	4057
$\min(h_T)$ in cm	4.4	4.4	4.4	3.2
$\max(h_T)$ in cm	70.8	70.8	70.8	70.8

Table 4.3: Fault system: Total number of (no.) grid vertices and bounds on the triangle diameters h_T, $T \in \mathcal{T}_i^{(K)}$, $i = 1, \ldots, m$ depending on the number of bodies $m = 2, \ldots, 5$ in the layered fault system.

Simulation results

As in the spring slider experiment, let us examine the mean value of approximate relative velocities on the faults Γ^F. The layered fault system with $m = 3$ bodies exhibits an initial loading phase and stick-slip pattern consisting of almost periodic slip events on the top fault $\Gamma^F_{2,3}$, see the top picture of Figure 4.9, that are qualitatively similar to the one observed for a single fault in the spring slider experiment. The bottom fault $\Gamma^F_{1,2}$ reveals a highly oscillatory loading phase, for which it is currently not understood whether these oscillations are physical, e.g. caused by the fixed foundation of Ω_1, or numerical artifacts. Afterwards, at about 48.0 s, there is a jump in mean relative velocity that seems to saturate, albeit with isolated perturbances, and may transition to steady creep or lead to later slip events.

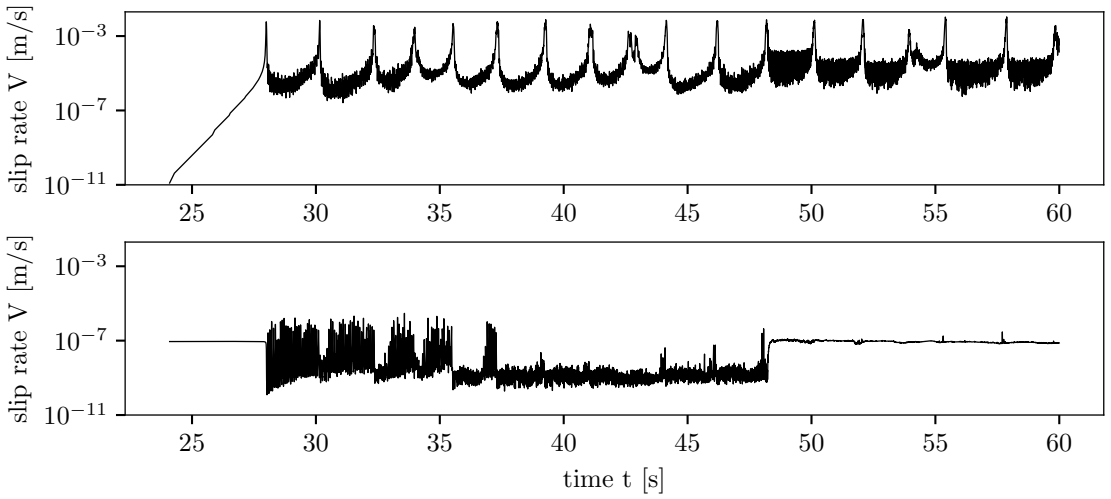

Figure 4.9: Layered fault system: Mean relative velocities over the faults $\Gamma^F_{2,3}$ (top) and $\Gamma^F_{1,2}$ (bottom) for the layered fault system with $m = 3$ bodies.

Interestingly, these overall dynamics at the top and bottom fault are retained for the layered fault system with $m = 5$ bodies, cf. Figure 4.10 showing the mean relative velocities on the top fault $\Gamma^F_{m-1,m}$ in the top picture and on the bottom fault $\Gamma^F_{1,2}$ in the bottom picture. On the top fault, the stick-slip process seems to possess a similar frequency and amplitude. Again, the bottom fault is host to a highly oscillating loading phase before saturating at about 57.5 s. The middle two faults $\Gamma^F_{3,4}$ and $\Gamma^F_{2,3}$ show comparable mean relative velocities, see the middle two pictures of Figure 4.10. The same jump in mean relative velocity at about 57.5 s as for the bottom fault is present. Subsequently, mean relative velocities may continue to saturate and

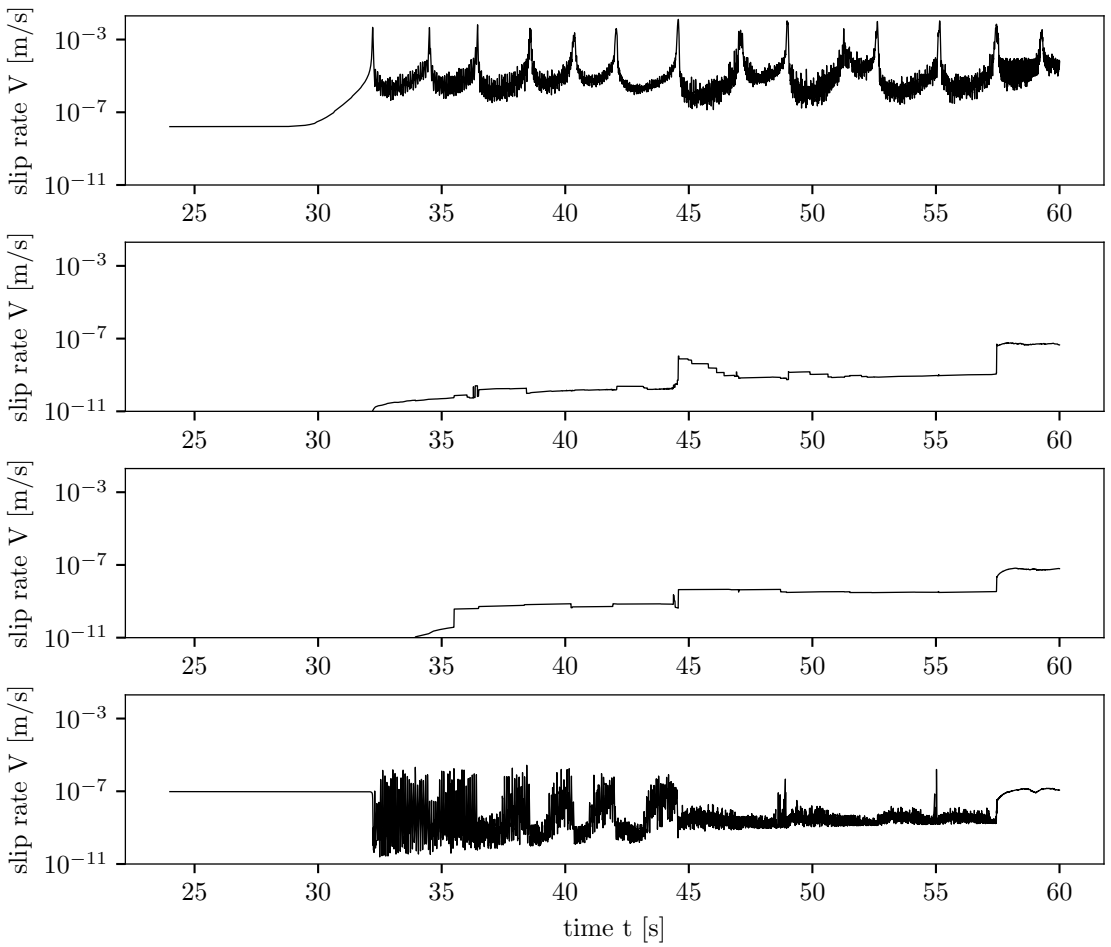

Figure 4.10: Layered fault system: Mean relative velocities over the faults $\Gamma^F_{i,i+1}$, $i = 1, \ldots, 4$, from $\Gamma^F_{4,5}$ (top) to $\Gamma^F_{1,2}$ (bottom) for the layered fault system with $m = 5$ bodies.

transition to steady creep or lead to future slip events.
Studying the time of first rupture on the top fault $\Gamma^F_{m-1,m}$, i.e. identified by the first peak in mean relative velocity, one notices that it increases monotonically with the number of bodies $m = 2, \ldots, 5$ from 25.2 s to 32.2 s, see Table 4.4. Intuitively, this observation is expected since there is more bulk material available to accommodate strain and growing opportunity for stress release along more faults for an increasing number of bodies.

m	2	3	4	5
t_{first} in s	25.2	28.0	31.2	32.2

Table 4.4: Layered fault system: Time of first rupture t_{first} on the top fault $\Gamma^F_{m-1,m}$ identified by the first peak in mean relative velocity depending on the number of bodies $m = 2, \ldots, 5$ in the layered fault system.

The spatial propagation of individual slip events along the top fault $\Gamma^F_{m-1,m}$ for the layered fault network with $m = 5$ bodies is illustrated in Figure 4.11. It lays out isolines of approximate relative velocities on the fault (horizontal axis) offset by the loading velocity evolving over various short time intervals (vertical axis)

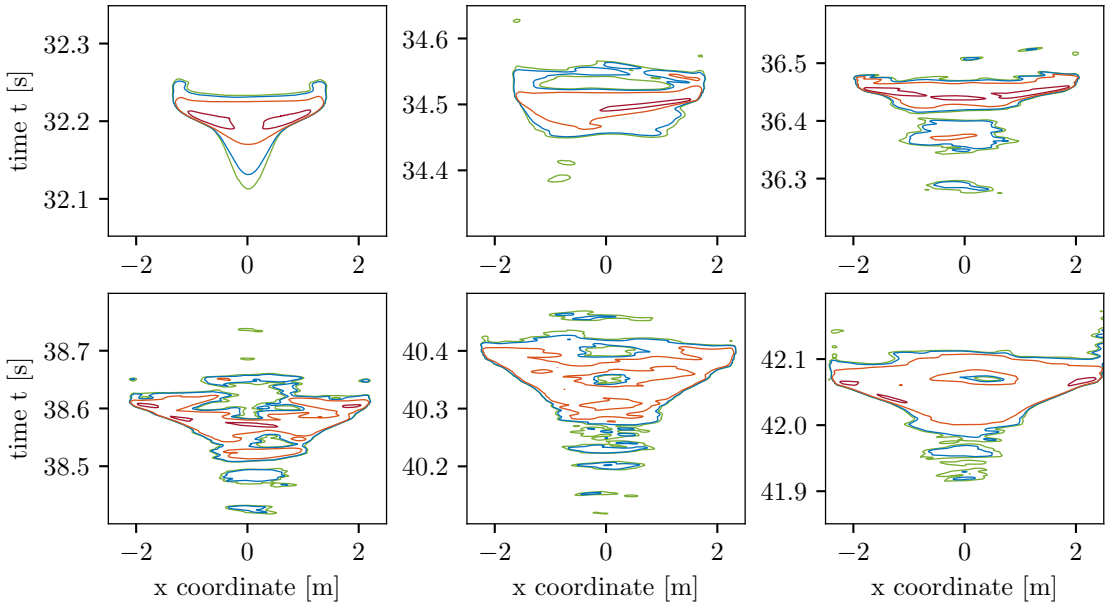

Figure 4.11: Layered fault system: Isolines (10^1 µm/s green, 10^2 µm/s blue, 10^3 µm/s orange, 10^4 µm/s red) of relative velocities along the top fault $\Gamma^F_{m-1,m}$ of the layered fault system with $m = 5$ bodies over different time intervals resolving the first 6 slip events (top left to bottom right).

corresponding to the first six slip events (top left to bottom right). Except for the first and second slip event, which feature either no foreshocks or asymmetrical ones on the left side of $\Gamma^F_{m-1,m}$, respectively, ruptures are preceded by foreshocks located in the middle of $\Gamma^F_{m-1,m}$ that trigger bilateral events. Moreover, most slip events are followed by small aftershocks. Qualitatively, the characteristics of these ruptures are very similar to the ones discovered with the spring slider setup, cf. Figure 4.3.

Performance and scaling properties of the algebraic solver

As Figure 4.12 indicates, the performance of adaptive time step selection and of the algebraic solver is essentially the same for the layered fault system with $m = 5$ bodies as in the spring slider experiment. Once more, the adaptive time stepping procedure reduces time step sizes by about 2 orders of magnitude in order to resolve slip events on the top fault $\Gamma^F_{m-1,m}$. As in the spring slider experiment, the number of outer fixed point iterations takes values between 2 to 4 and the sum of all inner TNNMG iterations in each of these steps is bounded by 19 during the stick-slip phase except for slightly larger values around the first slip event and the event at 57.5 s, where the relative velocities jump on all faults simultaneously.
This not only holds for $m = 5$, but also for layered fault systems with $m = 2, 3, 4$ bodies, see Table 4.5. However, for $m = 2$, there is one outlier time step during the loading phase requiring unusually many fixed point iterations. Excluding this single instance, one recovers characteristic iteration numbers as for the other experiments. This issue could be addressed by refining the time step size, if the number of fixed point iterations increases beyond a reasonable threshold. Furthermore, it strongly suggests that the building blocks of the algebraic solver, i.e. the outer fixed point and inner TNNMG iteration, and their convergence properties are independent of scaling

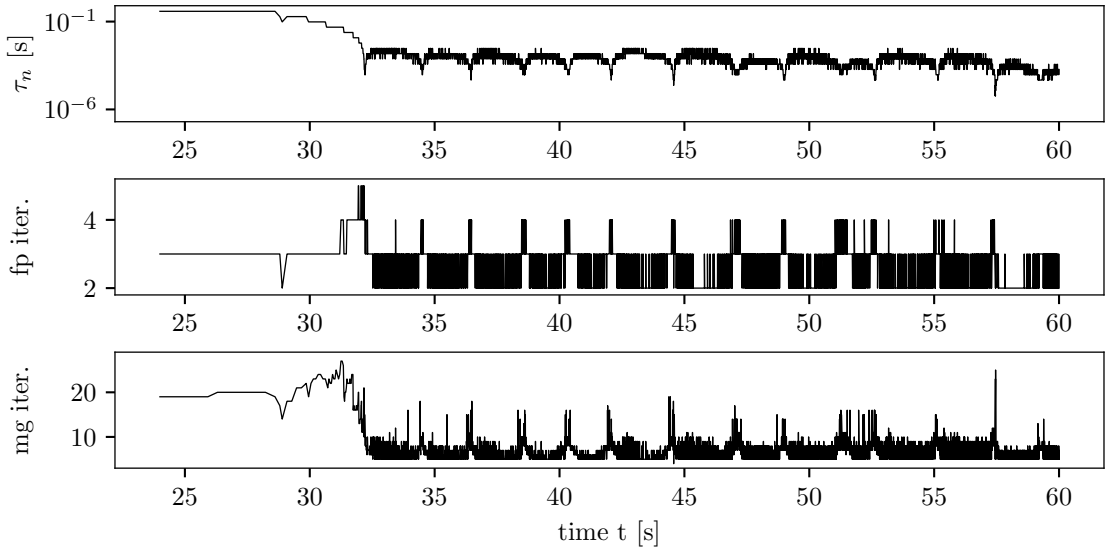

Figure 4.12: Fixed point (fp) iterations, total number of TNNMG (mg) iterations over all fixed point iterations and absolute time step size τ as determined by the adaptive time stepping procedure (top to bottom) of the numerical solver.

m	2	3	4	5
$\tau_{\max}$ in s	6.1	3.1	3.1	3.1
$\tau_{\min}$ in s	2.9×10^{-6}	5.9×10^{-6}	5.9×10^{-6}	5.9×10^{-6}
fp iter. max	15 (5)	5	5	5
fp iter. avg	2.72	2.67	2.63	2.68
mg iter. max	106 (21)	21	27	35
mg iter. avg	6.95	6.71	6.62	6.78

Table 4.5: Layered fault system: Smallest ($\tau_{\min}$) and largest time step size ($\tau_{\max}$) selected by adaptive time stepping, maximum and average number of fixed point (fp) as well as TNNMG (mg) iterations performed by the algebraic solver depending on the number of bodies $m = 2, \ldots, 5$ in the layered fault system. The values in parentheses for $m = 2$ denote the individual values when excluding the one time step with the maximum number of fixed point iterations.

phenomena induced by the number of bodies and faults in the layered fault system. These results attest to the robustness and efficiency of this solution approach.

Although the numerical algorithm and its implementation are highly efficient, this kind of experimental setup and choice of parameters is the limit of what is currently achievable in a single threaded environment with reasonable computation times of less than a week. Higher spatiotemporal resolution, problems in three space dimensions, longer final simulation times T or otherwise added complexity require parallelization of the algorithm and implementation, preferably both in space and time, to guarantee feasible running times.

Bibliography

[1] A. Abdulle, E. Weinan, B. Engquist, and E. Vanden-Eijnden. "The heterogeneous multiscale method". In: *Acta Numerica* 21 (2012), pp. 1–87. DOI: 10.1017/S0962492912000025.

[2] G. Allaire. "Homogenization and two-scale convergence". In: *SIAM Journal on Mathematical Analysis* 23.6 (1992), pp. 1482–1518. DOI: 10.1137/0523084.

[3] G. Allaire and M. Briane. "Multiscale convergence and reiterated homogenisation". In: *Proceedings of the Royal Society of Edinburgh Section A: Mathematics* 126.2 (1996), pp. 297–342. DOI: 10.1017/S0308210500022757.

[4] D. J. Andrews. "A numerical study of tectonic stress release by underground explosions". In: *Bulletin of the Seismological Society of America* 63.4 (1973), pp. 1375–1391. DOI: 10.1785/BSSA0630041375.

[5] J.-P. Avouac. "From Geodetic Imaging of Seismic and Aseismic Fault Slip to Dynamic Modeling of the Seismic Cycle". In: *Annual Review of Earth and Planetary Sciences* 43.1 (2015), pp. 233–271. DOI: 10.1146/annurev-earth-060614-105302.

[6] L. Baffico, C. Grandmont, Y. Maday, and A. Osses. "Homogenization of elastic media with gaseous inclusions". In: *Multiscale Modeling & Simulation* 7.1 (2008), pp. 432–465. DOI: 10.1137/070705714.

[7] W. Bangerth, J. Dannberg, M. Fraters, R. Gassmoeller, A. Glerum, T. Heister, and J. Naliboff. *ASPECT: Advanced Solver for Problems in Earth's Convection, User Manual*. July 2021.

[8] R. E. Bank, T. F. Dupont, and H. Yserentant. "The hierarchical basis multigrid method". In: *Numerische Mathematik* 52.4 (1988), pp. 427–458. DOI: 10.1007/BF01462238.

[9] R. E. Bank, A. H. Sherman, and A. Weiser. "Some refinement algorithms and data structures for regular local mesh refinement". In: *Scientific Computing, Applications of Mathematics and Computing to the Physical Sciences* 1 (1983), pp. 3–17.

[10] S. Barbot, N. Lapusta, and J.-P. Avouac. "Under the hood of the earthquake machine: Toward predictive modeling of the seismic cycle". In: *Science* 336.6082 (2012), pp. 707–710. DOI: 10.1126/science.1218796.

[11] P. Bastian, G. Buse, and O. Sander. "Infrastructure for the coupling of Dune grids". In: *Numerical Mathematics and Advanced Applications 2009*. Springer, 2010, pp. 107–114. DOI: 10.1007/978-3-642-11795-4_10.

[12] P. Bastian, M. Blatt, A. Dedner, N.-A. Dreier, C. Engwer, R. Fritze, C. Gräser, C. Grüninger, D. Kempf, R. Klöfkorn, M. Ohlberger, and O. Sander. "The Dune framework: Basic concepts and recent developments". In: *Computers & Mathematics with Applications* 81 (2021). Development and Application of Open-source Software for Problems with Numerical PDEs, pp. 75–112. DOI: 10.1016/j.camwa.2020.06.007.

[13] K.-J. Bathe and A. Chaudhary. "A solution method for planar and axisymmetric contact problems". In: *International Journal for Numerical Methods in Engineering* 21 (1 1985). DOI: 10.1002/nme.1620210107.

[14] Y. Ben-Zion. "Collective behavior of earthquakes and faults: Continuum-discrete transitions, progressive evolutionary changes, and different dynamic regimes". In: *Reviews of Geophysics* 46.4 (2008). DOI: 10.1029/2008RG000260.

[15] C. Bernardi, Y. Maday, and A. T. Patera. "Domain Decomposition by the Mortar Element Method". In: *Asymptotic and Numerical Methods for Partial Differential Equations with Critical Parameters*. Ed. by H. G. Kaper, M. Garbey, and G. W. Pieper. Dordrecht: Springer Netherlands, 1993, pp. 269–286. ISBN: 9789401047982. DOI: 10.1007/978-94-011-1810-1_17.

[16] J. Bey. "Simplicial grid refinement: on Freudenthal's algorithm and the optimal number of congruence classes". In: *Numerische Mathematik* 85.1 (2000), pp. 1–29. DOI: 10.1007/s002110050475.

[17] M. Blatt, A. Burchardt, A. Dedner, C. Engwer, J. Fahlke, B. Flemisch, C. Gersbacher, C. Gräser, F. Gruber, C. Grüninger, D. Kempf, R. Klöfkorn, T. Malkmus, S. Müthing, M. Nolte, M. Piatkowski, and O. Sander. "The Distributed and Unified Numerics Environment, Version 2.4". In: *Archive of Numerical Software* 4.100 (2016), pp. 13–29. DOI: 10.11588/ans.2016.100.26526.

[18] R. I. Borja and C. D. Foster. "Continuum mathematical modeling of slip weakening in geological systems". In: *Journal of Geophysical Research: Solid Earth* 112.B4 (2007). DOI: 10.1029/2005JB004056.

[19] D. Braess and W. Hackbusch. "A new convergence proof for the multigrid method including the V-cycle". In: *SIAM Journal on Numerical Analysis* 20.5 (1983), pp. 967–975. DOI: 10.1137/0720066.

[20] S. C. Brenner. "Two-level additive Schwarz preconditioners for nonconforming finite elements". In: *Contemporary Mathematics* 180 (1994), pp. 9–14.

[21] S. C. Brenner. "Two-Level Additive Schwarz Preconditioners for Nonconforming Finite Element Methods". In: *Mathematics of Computation* 65 (215 1996). DOI: 10.1090/S0025-5718-96-00746-6.

[22] C. Carstensen. "Clément interpolation and its role in adaptive finite element error control". In: *Partial differential equations and functional analysis* (2006), pp. 27–43. DOI: 10.1007/3-7643-7601-5_2.

[23] C. Carstensen. "Weighted Clément-type interpolation and a posteriori analysis for FEM". In: *Berichtsreihe des Mathematischen Seminars Kiel, Technical report*. 1997, pp. 97–119.

[24] C. Carstensen and S. A. Funken. "Constants in Clément-interpolation error and residual based a posteriori estimates in finite element methods". In: *East-West J. Numer. Math.* 8.3 (2000), pp. 153–175.

[25] C. Carstensen and R. Verfürth. "Edge residuals dominate a posteriori error estimates for low order finite element methods". In: *SIAM Journal on Numerical Analysis* 36.5 (1999), pp. 1571–1587. DOI: 10.1137/S003614299732334X.

[26] J. Chen and C. J. Spiers. "Rate and state frictional and healing behavior of carbonate fault gouge explained using microphysical model". In: *Journal of Geophysical Research: Solid Earth* 121.12 (2016), pp. 8642–8665. DOI: 10.1002/2016JB013470.

[27] P. G. Ciarlet. *Mathematical Elasticity: Volume I: Three-dimensional elasticity*. North-Holland, 1988. ISBN: 9780080875415.

[28] P. G. Ciarlet. *The Finite Element Method for Elliptic Problems*. Society for Industrial and Applied Mathematics, 2002. DOI: 10.1137/1.9780898719208.

[29] P. Clément. "Approximation by finite element functions using local regularization". In: *Revue francaise d'automatique, informatique, recherche opérationnelle. Analyse numérique* 9.R2 (1975), pp. 77–84. DOI: 10.1051/m2an/197509R200771.

[30] A. Cochard and R. Madariaga. "Dynamic faulting under rate-dependent friction". In: *Pure and Applied Geophysics* 142.3 (1994), pp. 419–445. DOI: 10.1007/BF00876049.

[31] L. Dal Zilio, Y. van Dinther, T. V. Gerya, and C. C. Pranger. "Seismic behaviour of mountain belts controlled by plate convergence rate". In: *Earth and Planetary Science Letters* 482 (2018), pp. 81–92. DOI: 10.1016/j.epsl.2017.10.053.

[32] S. M. Day, L. A. Dalguer, N. Lapusta, and Y. Liu. "Comparison of finite difference and boundary integral solutions to three-dimensional spontaneous rupture". In: *Journal of Geophysical Research: Solid Earth* 110.B12 (2005). DOI: 10.1029/2005JB003813.

[33] P. Deuflhard and A. Hohmann. *Numerische Mathematik 1: Eine algorithmisch orientierte Einführung*. De Gruyter, 2018. ISBN: 9783110614329. DOI: 10.1515/9783110614329.

[34] P. Deuflhard, R. Krause, and S. Ertel. "A contact-stabilized Newmark method for dynamical contact problems". In: *International Journal for Numerical Methods in Engineering* 73.9 (2008), pp. 1274–1290. DOI: 10.1002/nme.2119.

[35] J. H. Dieterich. "Applications of Rate- and State-Dependent Friction to Models of Fault Slip and Earthquake Occurrence". In: vol. 4. Dec. 2007, pp. 107–129. ISBN: 9780444519283. DOI: 10.1016/B978-044452748-6.00065-1.

[36] J. H. Dieterich. "Modeling of rock friction: 1. Experimental results and constitutive equations". In: *Journal of Geophysical Research* 84 (B5 1979). DOI: 10.1029/JB084iB05p02161.

[37] J. H. Dieterich. "Modeling of rock friction: 2. Simulation of preseismic slip". In: *Journal of Geophysical Research* 84 (B5 1979). DOI: 10.1029/JB084iB05p02169.

[38] J. H. Dieterich. "Time-dependent friction and the mechanics of stick-slip". In: *Pure and Applied Geophysics* 116 (4-5 1978). DOI: 10.1007/978-3-0348-7182-2_15.

[39] J. H. Dieterich and B. D. Kilgore. "Direct observation of frictional contacts: New insights for state-dependent properties". In: *Pure and Applied Geophysics* 143 (1 1994). DOI: 10.1007/BF00874332.

[40] P. Donato and S. Monsurro. "Homogenization of two heat conductors with an interfacial contact resistance". In: *Analysis and Applications* 2.03 (2004), pp. 247–273. DOI: 10.1142/S0219530504000345.

[41] M. Dryja and O. B. Widlund. "Some domain decomposition algorithms for elliptic problems". In: *Iterative methods for large linear systems*. Elsevier, 1990, pp. 273–291. DOI: 10.1016/B978-0-12-407475-0.50022-X.

[42] M. Dryja and O. B. Widlund. *Towards a unified theory of domain decomposition algorithms for elliptic problems*. New York University, Courant Institute of Mathematical Sciences, 1989.

[43] T. Dupont and R. Scott. "Polynomial approximation of functions in Sobolev spaces". In: *Mathematics of Computation* 34.150 (1980), pp. 441–463. DOI: 10.1090/S0025-5718-1980-0559195-7.

[44] W. E, B. Engquist, et al. "The heterogeneous multiscale method". In: *Communications in Mathematical Sciences* 1.1 (2003), pp. 87–132.

[45] Y. Efendiev and T. Y. Hou. *Multiscale finite element methods: Theory and applications*. Vol. 4. Springer Science & Business Media, 2009. ISBN: 9780387094960.

[46] L. C. Evans and R. F. Gariepy. *Measure Theory and Fine Properties of Functions, Revised Edition*. Textbooks in Mathematics. CRC Press, 2015. ISBN: 9780429161483. DOI: 10.1201/b18333.

[47] P. Galvez, J.-P. Ampuero, L. A. Dalguer, S. N. Somala, and T. Nissen-Meyer. "Dynamic earthquake rupture modelled with an unstructured 3-D spectral element method applied to the 2011 M9 Tōhoku earthquake". In: *Geophysical Journal International* 198.2 (2014), pp. 1222–1240. DOI: 10.1093/gji/ggu203.

[48] X. Gao and K. Wang. "Strength of stick-slip and creeping subduction megathrusts from heat flow observations". In: *Science* 345.6200 (2014), pp. 1038–1041. DOI: 10.1126/science.1255487.

[49] A. Glerum, C. Thieulot, M. Fraters, C. Blom, and W. Spakman. "Nonlinear viscoplasticity in ASPECT: benchmarking and applications to subduction". In: *Solid Earth* 9.2 (2018), pp. 267–294. DOI: 10.5194/se-9-267-2018.

[50] R. Glowinski. *Numerical methods for non-linear variational problems*. Springer Verlag, 1984.

[51] C. Goldfinger, Y. Ikeda, R. S. Yeats, and J. Ren. "Superquakes and Supercycles". In: *Seismological Research Letters* 84.1 (2013), pp. 24–32. DOI: 10.1785/0220110135.

[52] C. Gräser. "Convex Minimization and Phase Field Models". PhD thesis. Free University Berlin, 2011.

[53] C. Gräser and R. Kornhuber. "Multigrid methods for obstacle problems". In: *Journal of Computational Mathematics* 27.1 (2009), pp. 1–44. URL: https://www.jstor.org/stable/43693490.

[54] C. Gräser, R. Kornhuber, and J. Podlesny. "Numerical simulation of multiscale fault systems with rate- and state-dependent friction". In: *arXiv* (2021). DOI: 10.48550/ARXIV.2110.14429.

[55] C. Gräser, U. Sack, and O. Sander. "Truncated Nonsmooth Newton Multigrid Methods for Convex Minimization Problems". In: *Domain Decomposition Methods in Science and Engineering XVIII*. Berlin, Heidelberg: Springer Berlin Heidelberg, 2009, pp. 129–136. DOI: 10.1007/978-3-642-02677-5_12.

[56] C. Gräser and O. Sander. "Truncated nonsmooth Newton multigrid methods for block-separable minimization problems". In: *IMA Journal of Numerical Analysis* 39 (1 2019), pp. 454–481. DOI: 10.1093/imanum/dry073.

[57] D. S. Grebenkov, M. Filoche, and B. Sapoval. "Mathematical basis for a general theory of Laplacian transport towards irregular interfaces". In: *Physical Review E* 73.2 (2006), p. 021103. DOI: 10.1103/PhysRevE.73.021103.

[58] W. Hackbusch. *Multi-grid Methods and Applications*. Computational Mathematics Series. Springer, Berlin, Heidelberg, 1985. ISBN: 9780387127613.

[59] E. Hairer, C. Lubich, and G. Wanner. *Geometric Numerical Integration: Structure-Preserving Algorithms for Ordinary Differential Equations*. 2nd. Vol. 31. Springer-Verlag Berlin Heidelberg, 2006. ISBN: 9783642051579. DOI: 10.1007/3-540-30666-8.

[60] G. P. Hayes et al. *Tectonic summaries of magnitude 7 and greater earthquakes from 2000 to 2015*. Tech. rep. 2016-1192. U.S. Geological Survey, 2017.

[61] M. Heida, R. Kornhuber, and J. Podlesny. "Fractal homogenization of multiscale interface problems". In: *Multiscale Modeling & Simulation* 18.1 (2020), pp. 294–314. DOI: 10.1137/18M1204759.

[62] A. Heinecke, A. Breuer, S. Rettenberger, M. Bader, A.-A. Gabriel, C. Pelties, A. Bode, W. Barth, X.-K. Liao, K. Vaidyanathan, M. Smelyanskiy, and P. Dubey. "Petascale High Order Dynamic Rupture Earthquake Simulations on Heterogeneous Supercomputers". In: *SC '14: Proceedings of the International Conference for High Performance Computing, Networking, Storage and Analysis*. IEEE. 2014, pp. 3–14. DOI: 10.1109/SC.2014.6.

[63] R. Herrendörfer, Y. Van Dinther, T. Gerya, and L. A. Dalguer. "Earthquake supercycle in subduction zones controlled by the width of the seismogenic zone". In: *Nature Geoscience* 8.6 (2015), pp. 471–474. DOI: 10.1038/ngeo2427.

[64] F. Heslot, T. Baumberger, B. Perrin, B. Caroli, and C. Caroli. "Creep, stick-slip, and dry-friction dynamics: Experiments and a heuristic model". In: *Physical Review E* 49 (6 1994). DOI: 10.1103/PhysRevE.49.4973.

[65] S. Hüeber and B. I. Wohlmuth. "An Optimal A Priori Error Estimate for Nonlinear Multibody Contact Problems". In: *SIAM journal on numerical analysis* 43.1 (2005), pp. 156–173. DOI: 10.1137/S0036142903436678.

[66] T. J. R. Hughes, R. L. Taylor, J. L. Sackman, A. Curnier, and W. Kanoknukulchai. "A finite element method for a class of contact-impact problems". In: *Computer Methods in Applied Mechanics and Engineering* 8 (3 1976). DOI: 10.1016/0045-7825(76)90018-9.

[67] T. J. Hughes, G. R. Feijóo, L. Mazzei, and J.-B. Quincy. "The variational multiscale method–a paradigm for computational mechanics". In: *Computer Methods in Applied Mechanics and Engineering* 166.1-2 (1998), pp. 3–24. DOI: 10.1016/S0045-7825(98)00079-6.

[68] V. V. Jikov, S. M. Kozlov, and O. A. Oleinik. *Homogenization of differential operators and integral functionals*. Springer Science & Business Media, 2012. ISBN: 9783642846595.

[69] C. Kane, E. A. Repetto, M. Ortiz, and J. Marsden. "Finite element analysis of nonsmooth contact". In: *Computer Methods in Applied Mechanics and Engineering* 180 (1-2 1999). DOI: 10.1016/S0045-7825(99)00034-1.

[70] M. Käser, C. Castro, V. Hermann, and C. Pelties. "SeisSol – A Software for Seismic Wave Propagation Simulations". In: *High Performance Computing in Science and Engineering, Garching/Munich 2009*. Ed. by S. Wagner, M. Steinmetz, A. Bode, and M. M. Müller. Springer Berlin Heidelberg, 2010, pp. 281–292. DOI: 10.1007/978-3-642-13872-0_24.

[71] V. Kim. *Japan damage could reach $235 billion, World Bank estimates*. Accessed: 08.06.2021. 2011. URL: https://www.latimes.com/business/la-fg w-japan-quake-world-bank-20110322-story.html.

[72] C. Klapproth. "The contact-stabilized Newmark method: consistency error of a spatiotemporal discretization". In: *Numerische Mathematik* 131 (2015), pp. 59–82. DOI: 10.1007/s00211-014-0686-1.

[73] C. Klapproth, A. Schiela, and P. Deuflhard. "Adaptive timestep control for the contact-stabilized Newmark method". In: *Numerische Mathematik* 119 (2011), pp. 49–81. DOI: 10.1007/s00211-011-0374-3.

[74] C. Klapproth, A. Schiela, and P. Deuflhard. "Consistency results on Newmark methods for dynamical contact problems". In: *Numerische Mathematik* 116 (2010), pp. 65–94. DOI: 10.1007/s00211-010-0300-0.

[75] R. Kornhuber, R. Krause, O. Sander, P. Deuflhard, and S. Ertel. "A monotone multigrid solver for two body contact problems in biomechanics". In: *Computing and Visualization in Science* 11 (2008), pp. 3–15. DOI: 10.1007/s 00791-006-0053-6.

[76] R. Kornhuber, D. Peterseim, and H. Yserentant. "An analysis of a class of variational multiscale methods based on subspace decomposition". In: *Mathematics of Computation* 87.314 (2018), pp. 2765–2774. DOI: 10.1090/mcom/3302.

[77] R. Kornhuber, J. Podlesny, and H. Yserentant. "Direct and iterative methods for numerical homogenization". In: *Domain decomposition methods in science and engineering XXIII*. Springer, 2017, pp. 217–225. DOI: 10.1007/978-3-319-52389-7_21.

[78] R. Kornhuber, J. Podlesny, and H. Yserentant. "Numerical Homogenization of Fractal Interface Problems". In: *arXiv* (2020). DOI: 10.48550/ARXIV.2007.11479.

[79] R. Kornhuber and H. Yserentant. "Multilevel methods for elliptic problems on domains not resolved by the coarse grid". In: *Contemporary Mathematics* 180 (1994), pp. 49–60.

[80] R. Kornhuber and H. Yserentant. "Numerical Homogenization of Elliptic Multiscale Problems by Subspace Decomposition". In: *Multiscale Modeling & Simulation* 14.3 (2016), pp. 1017–1036. DOI: 10.1137/15M1028510.

[81] R. Krause. "A Nonsmooth Multiscale Method for Solving Frictional Two-Body Contact Problems in 2D and 3D with Multigrid Efficiency". In: *SIAM Journal on Scientific Computing* 31.2 (2009), pp. 1399–1423. DOI: 10.1137/070682514.

[82] R. Krause and M. Walloth. "Presentation and comparison of selected algorithms for dynamic contact based on the Newmark scheme". In: *Applied Numerical Mathematics* 62.10 (2012), pp. 1393–1410. DOI: 10.1016/j.apnum.2012.06.014.

[83] M. Kronbichler, T. Heister, and W. Bangerth. "High Accuracy Mantle Convection Simulation through Modern Numerical Methods". In: *Geophysical Journal International* 191 (2012), pp. 12–29. DOI: 10.1111/j.1365-246X.2012.05609.x.

[84] M. R. Lancia. "A transmission problem with a fractal interface". In: *Zeitschrift für Analysis und ihre Anwendungen* 21.1 (2002), pp. 113–133. ISSN: 02322064.

[85] N. Lapusta, J. R. Rice, Y. Ben-Zion, and G. Zheng. "Elastodynamic analysis for slow tectonic loading with spontaneous rupture episodes on faults with rate-and state-dependent friction". In: *Journal of Geophysical Research: Solid Earth* 105.B10 (2000), pp. 23765–23789. DOI: 10.1029/2000JB900250.

[86] T. A. Laursen and J. C. Simo. "A continuum-based finite element formulation for the implicit solution of multibody, large deformation-frictional contact problems". In: *International Journal for Numerical Methods in Engineering* 36 (20 1993). DOI: 10.1002/nme.1620362005.

[87] T. Laursen. *Computational Contact and Impact Mechanics: Fundamentals of Modeling Interfacial Phenomena in Nonlinear Finite Element Analysis*. Springer Berlin Heidelberg, 2013. ISBN: 9783662048641.

[88] M. F. Linker and J. H. Dieterich. “Effects of variable normal stress on rock friction: Observations and constitutive equations”. In: *Journal of Geophysical Research* 97 (B4 1992). DOI: 10.1029/92JB00017.

[89] A. Målqvist and D. Peterseim. “Localization of elliptic multiscale problems”. In: *Mathematics of Computation* 83.290 (2014), pp. 2583–2603. DOI: 10.1090/S0025-5718-2014-02868-8.

[90] C. Marone. “Laboratory-derived friction laws and their application to seismic faulting”. In: *Annual Review of Earth and Planetary Sciences* 26 (1 May 1998).

[91] A. Mielke. “Three Examples Concerning the Interaction of Dry Friction and Oscillations”. In: *Trends in Applications of Mathematics to Mechanics*. Ed. by E. Rocca, U. Stefanelli, L. Truskinovsky, and A. Visintin. Cham: Springer International Publishing, 2018, pp. 159–177. ISBN: 9783319759395. DOI: 10.1007/978-3-319-75940-1_8.

[92] A. Mielke and T. Roubíček. “Rate-independent elastoplasticity at finite strains and its numerical approximation”. In: *Mathematical Models and Methods in Applied Sciences* 26.12 (2016), pp. 2203–2236. DOI: 10.1142/S0218202516500512.

[93] H. Nagahama and K. Yoshii. “Scaling laws of fragmentation”. In: *Fractals and Dynamic Systems in Geoscience*. Springer, 1994, pp. 25–36. ISBN: 9783662073063. DOI: 10.1007/978-3-662-07304-9_2.

[94] O. Oncken, D. Boutelier, G. Dresen, and K. Schemmann. “Strain accumulation controls failure of a plate boundary zone: Linking deformation of the Central Andes and lithosphere mechanics”. In: *Geochemistry, Geophysics, Geosystems* 13.12 (2012). DOI: 10.1029/2012GC004280.

[95] P. Oswald. “On a BPX-preconditioner for P1 elements”. In: *Computing* 51.2 (1993), pp. 125–133. DOI: 10.1007/BF02243847.

[96] C. Pelties, J. De la Puente, J.-P. Ampuero, G. B. Brietzke, and M. Käser. “Three-dimensional dynamic rupture simulation with a high-order discontinuous Galerkin method on unstructured tetrahedral meshes”. In: *Journal of Geophysical Research: Solid Earth* 117.B2 (2012). DOI: 10.1029/2011JB008857.

[97] D. Peterseim. “Variational multiscale stabilization and the exponential decay of fine-scale correctors”. In: *Building Bridges: Connections and Challenges in Modern Approaches to Numerical Partial Differential Equations*. Ed. by G. R. Barrenechea, F. Brezzi, A. Cangiani, and E. H. Georgoulis. Springer International Publishing, 2016, pp. 343–369. ISBN: 9783319416403. DOI: 10.1007/978-3-319-41640-3_11.

[98] D. Peterseim and M. Schedensack. “Relaxing the CFL Condition for the Wave Equation on Adaptive Meshes”. In: *Journal of Scientific Computing* 72.3 (Sept. 2017), pp. 1196–1213. DOI: 10.1007/s10915-017-0394-y.

[99] E. Pipping. “Dynamic problems of rate-and-state friction in viscoelasticity”. PhD thesis. Free University Berlin, 2014.

[100] E. Pipping. "Existence of long-time solutions to dynamic problems of viscoelasticity with rate-and-state friction". In: *ZAMM-Journal of Applied Mathematics and Mechanics/Zeitschrift für Angewandte Mathematik und Mechanik* 99.11 (2019), e201800263. DOI: 10.1002/zamm.201800263.

[101] E. Pipping, R. Kornhuber, M. Rosenau, and O. Oncken. "On the efficient and reliable numerical solution of rate-and-state friction problems". In: *Geophysical Journal International* 204.3 (Feb. 2016), pp. 1858–1866. DOI: 10.1093/gji/ggv512.

[102] E. Pipping, O. Sander, and R. Kornhuber. "Variational formulation of rate- and state-dependent friction problems". In: *ZAMM - Journal of Applied Mathematics and Mechanics / Zeitschrift für Angewandte Mathematik und Mechanik* 95.4 (2015), pp. 377–395. DOI: 10.1002/zamm.201300062.

[103] A. Popov and S. V. Sobolev. "SLIM3D: A tool for the three-dimensional thermomechanical modeling of the lithospheric deformation with elasto-visco-plastic rheology". In: *Physics of the Earth and Planetary Interiors* 171.1-4 (2008), pp. 55–75. DOI: 10.1016/j.pepi.2008.03.007.

[104] J. de la Puente, J.-P. Ampuero, and M. Käser. "Dynamic rupture modeling on unstructured meshes using a discontinuous Galerkin method". In: *Journal of Geophysical Research: Solid Earth* 114.B10 (2009). DOI: 10.1029/2008JB006271.

[105] M. A. Puso and T. A. Laursen. "A mortar segment-to-segment contact method for large deformation solid mechanics". In: *Computer Methods in Applied Mechanics and Engineering* 193.6 (2004), pp. 601–629. DOI: 10.1016/j.cma.2003.10.010.

[106] M. A. Puso and T. A. Laursen. "Mesh tying on curved interfaces in 3D". In: *Engineering Computations* 20.3 (2003), pp. 305–319. DOI: 10.1108/02644400310467225.

[107] E. Rabinowicz. *Friction and wear of materials*. Wiley, New York, 1965.

[108] E. Rabinowicz. "Stick and Slip". In: *Scientific American* 194 (5 1956). URL: http://www.jstor.org/stable/26122743.

[109] E. Rabinowicz. "The Nature of the Static and Kinetic Coefficients of Friction". In: *Journal of Applied Physics* 22 (11 1951). DOI: 10.1063/1.1699869.

[110] K. Ranjith and J. R. Rice. "Stability of quasi-static slip in a single degree of freedom elastic system with rate and state dependent friction". In: *Journal of the Mechanics and Physics of Solids* 47.6 (1999), pp. 1207–1218. DOI: 10.1016/S0022-5096(98)00113-6.

[111] H. F. Reid. *The California earthquake of April 18, 1906: The mechanics of the earthquake*. Report of the state earthquake investigation commission. Carnegie Institution of Washington, 1910.

[112] J. R. Rice, N. Lapusta, and K. Ranjith. "Rate and state dependent friction and the stability of sliding between elastically deformable solids". In: *Journal of the Mechanics and Physics of Solids* 49.9 (2001), pp. 1865–1898. DOI: 10.1016/S0022-5096(01)00042-4.

[113] E. Rothe. “Zweidimensionale parabolische Randwertaufgaben als Grenzfall eindimensionaler Randwertaufgaben”. In: *Mathematische Annalen* 102.1 (1930), pp. 650–670.

[114] A. Ruina. “Slip instability and state variable friction laws”. In: *Journal of Geophysical Research* 88 (B12 1983). DOI: 10.1029/JB088iB12p10359.

[115] J. B. Rundle, D. L. Turcotte, R. Shcherbakov, W. Klein, and C. Sammis. “Statistical physics approach to understanding the multiscale dynamics of earthquake fault systems”. In: *Reviews of Geophysics* 41.4 (2003). DOI: 10.1029/2003RG000135.

[116] C. G. Sammis, R. H. Osborne, J. L. Anderson, M. Banerdt, and P. White. “Self-similar cataclasis in the formation of fault gouge”. In: *Pure and Applied Geophysics* 124.1 (1986), pp. 53–78. DOI: 10.1007/BF00875719.

[117] O. Sander. *Dune–The Distributed and Unified Numerics Environment*. Vol. 140. Springer Nature, 2020. ISBN: 9783030597023.

[118] O. Sander. “Multidimensional Coupling in a Human Knee Model”. PhD thesis. Free University Berlin, 2008.

[119] C. H. Scholz. “Earthquakes and friction laws”. In: *Nature* 391.6662 (Jan. 1998), pp. 37–42. DOI: 10.1038/34097.

[120] L. R. Scott and S. Zhang. “Finite element interpolation of nonsmooth functions satisfying boundary conditions”. In: *Mathematics of computation* 54.190 (1990), pp. 483–493. DOI: 10.1090/S0025-5718-1990-1011446-7.

[121] L. Slobodeckij. “Generalized Sobolev spaces and their application to boundary problems for partial differential equations”. In: *Leningrad. Gos. Ped. Inst. Ucen. Zap* 197 (1958), pp. 54–112.

[122] S. V. Sobolev and I. Muldashev. “Modeling Seismic Cycles of Great Megathrust Earthquakes Across the Scales With Focus at Postseismic Phase”. In: *Geochemistry Geophysics Geosystems (G3)* 18.12 (2017), pp. 4387–4408. DOI: 10.1002/2017GC007230.

[123] A. Tiero. “On Korn’s Inequality in the Second Case”. In: *Journal of Elasticity* 54 (3 Mar. 1999). DOI: 10.1023/A:1007549427722.

[124] V. A. Titarev and E. F. Toro. “ADER: Arbitrary High Order Godunov Approach”. In: *Journal of Scientific Computing* 17.B12 (1 2002), pp. 609–618. DOI: 10.1023/A:1015126814947.

[125] M. Tur, F. J. Fuenmayor, and P. Wriggers. “A mortar-based frictional contact formulation for large deformations using Lagrange multipliers”. In: *Computer Methods in Applied Mechanics and Engineering* 198 (37-40 2009). DOI: 10.1016/j.cma.2009.04.007.

[126] D. L. Turcotte. “Crustal deformation and fractals, a review”. In: *Fractals and Dynamic Systems in Geoscience*. Springer, 1994, pp. 7–23. ISBN: 9783662073063. DOI: 10.1007/978-3-662-07304-9_1.

[127] T. Ulrich, A.-A. Gabriel, J.-P. Ampuero, and W. Xu. "Dynamic viability of the 2016 Mw 7.8 Kaikōura earthquake cascade on weak crustal faults". In: *Nature communications* 10.1 (2019), pp. 1–16. DOI: 10.1038/s41467-019-09125-w.

[128] C. Uphoff, S. Rettenberger, M. Bader, E. H. Madden, T. Ulrich, S. Wollherr, and A.-A. Gabriel. "Extreme Scale Multi-Physics Simulations of the Tsunamigenic 2004 Sumatra Megathrust Earthquake". In: *Proceedings of the International Conference for High Performance Computing, Networking, Storage and Analysis*. SC '17. Denver, Colorado: Association for Computing Machinery, 2017, pp. 1–16. DOI: 10.1145/3126908.3126948.

[129] R. Verfürth. "Error estimates for some quasi-interpolation operators". In: *ESAIM: Mathematical Modelling and Numerical Analysis* 33.4 (1999), pp. 695–713. DOI: 10.1051/m2an:1999158.

[130] B. Wohlmuth. "Variationally consistent discretization schemes and numerical algorithms for contact problems". In: *Acta Numerica* 20 (May 2011), pp. 569–734. DOI: 10.1017/S0962492911000079.

[131] B. I. Wohlmuth. "A mortar finite element method using dual spaces for the Lagrange multiplier". In: *SIAM journal on numerical analysis* 38.3 (2000), pp. 989–1012. DOI: 10.1137/S0036142999350929.

[132] B. I. Wohlmuth. *Discretization Methods and Iterative Solvers Based on Domain Decomposition*. Vol. 17. Lecture Notes in Computational Science and Engineering. Springer, 2001. ISBN: 9783540410836. DOI: 10.1007/978-3-642-56767-4.

[133] B. I. Wohlmuth and R. H. Krause. "Monotone Multigrid Methods on Nonmatching Grids for Nonlinear Multibody Contact Problems". In: *SIAM journal on scientific computing* 25.1 (2003), pp. 324–347. DOI: 10.1137/S1064827502405318.

[134] J. Xu. "Iterative Methods by Space Decomposition and Subspace Correction". In: *SIAM Review* 34 (4 1992), pp. 581–613. DOI: 10.1137/1034116.

[135] D. M. Young. "Iterative methods for solving partial differential equations of elliptic type". PhD thesis. Cambridge, MA: Harvard University, 1950.

[136] H. Yserentant. "Old and new convergence proofs for multigrid methods". In: *Acta numerica* 2 (1993), pp. 285–326. DOI: 10.1017/S0962492900002385.

[137] V. V. Zhikov and A. Pyatnitskii. "Homogenization of random singular structures and random measures". In: *Izvestiya: Mathematics* 70.1 (2006), pp. 19–67.

Zusammenfassung

Die Akkumulation von Deformationen und der Abbau von Spannungen entlang multiskaliger, geologischer Störungsnetzwerke sind fundamentale Bestandteile der Dynamik von Erdbeben- und Bruchprozessen in der Lithosphäre. Solche Störungen werden nach ihrer Relativbewegung an der Grenzfläche klassifiziert und reichen von Subduktionszonen wie dem japanischen Inselbogen, über Transformstörungen wie der San Andreas Verwerfung bis hin zu mehrskaligen Störungssystemen wie der Atacama-Region. Aufgrund langer Phasen seismischer Ruhe und kurzer, plötzlicher Erdbeben findet das mechanische Verhalten über eine große Spanne von Zeitskalen statt, was zu einer unzureichenden Datenlage aus Naturbeobachtungen führt und das Gewinnen von geophysikalischen Einblicken erschwert. Ziel dieser Arbeit ist es einen Beitrag zur Schließung dieser Lücke mittels mathematischer Modellierung und numerischer Analysis zu leisten sowie geophysikalisch relevante, numerische Simulationen von Störungsnetzwerken zu entwickeln.
Zunächst wird ein mathematisches Modell für die Deformation eines geologischen Systems mit Störungen, die sich nicht schneiden, eingeführt, das aus geschichteten, viskoelastischen Körpern besteht und mit einem Dieterich-Ruina Modell von raten- und zustandsabhängiger Reibung auf den Kontaktflächen versehen ist. Hierbei werden die körperinternen Deformationen als klein angenommen, während große Relativverschiebungen zugelassen sind. Dann führt die Zeitdiskretisierung einer Variationsformulierung des Modellproblems mit der klassischen Newmark Methode in jedem Zeitschritt zu einem gekoppelten System von nicht-glatten, konvexen Minimierungsproblemen für die Raten und Zustände. Dieses System wird mit einer Fixpunktiteration entkoppelt und im Raum durch einen Mortar-Ansatz und stückweise konstante Finite-Elemente diskretisiert. Das daraus resultierende, parametrisierte Raten-Problem kann anschließend mit einer nicht-glatten Mehrgittermethode (TNNMG) effizient algebraisch gelöst werden. Die Konvergenzgeschwindigkeit dieses Verfahrens hängt wesentlich von einer effizienten Fehlerminimierung in einem dazugehörigen linearen Korrekturschritt ab.
Der zweite Teil beschäftigt sich mit der numerischen Homogenisierung von elliptischen Variationsproblemen auf fraktalen Interface-Netzwerken, die den linearen Problemen im Korrekturschritt des TNNMG Verfahrens strukturell ähneln. Anders als im ersten Teil wird hier der volle Umfang räumlicher Skalen geologischer Störungsnetzwerke in Form von fraktalen Multiskalen-Geometrien abgebildet. Hierfür stellt die Konstruktion von Projektionsoperatoren mit geeigneten Stabilitäts- und Approximationseigenschaften den wichtigsten Beitrag dieser Arbeit dar. Die Existenz dieser Projektionen ermöglicht die Anwendung etablierter Ansätze wie der lokalisierten, orthogonalen Zerlegungen (LOD) zur Konstruktion von Multiskalen-Diskretisierungen mit optimaler a priori Schätzung des Diskretisierungsfehlers oder wie Teilraumkorrekturmethoden, die zu algebraischen Lösern mit gitter- und skalenunabhängigem Konvergenzverhalten führen.
Abschließend illustrieren numerische Simulationen mit einer Einzelstörung und dem geschichteten, mehrskaligen Störungssystem sowohl die Eigenschaften des mathematischen Modells als auch die Effizienz, Zuverlässigkeit und Skalenunabhängigkeit des algebraischen Lösers.